Identification of equilibrium and irradiation-induced defects in nuclear ceramics: electronic structure calculations of defect properties and positron annihilation characteristics

Julia Wiktor

▶ **To cite this version:**

Julia Wiktor. Identification of equilibrium and irradiation-induced defects in nuclear ceramics: electronic structure calculations of defect properties and positron annihilation characteristics. Condensed Matter [cond-mat]. Aix-Marseille Université, 2015. English. NNT : . tel-01403492

HAL Id: tel-01403492
https://theses.hal.science/tel-01403492

Submitted on 26 Nov 2016

HAL is a multi-disciplinary open access archive for the deposit and dissemination of scientific research documents, whether they are published or not. The documents may come from teaching and research institutions in France or abroad, or from public or private research centers.

L'archive ouverte pluridisciplinaire **HAL**, est destinée au dépôt et à la diffusion de documents scientifiques de niveau recherche, publiés ou non, émanant des établissements d'enseignement et de recherche français ou étrangers, des laboratoires publics ou privés.

Aix-Marseille Université
École Doctorale : Physique et Sciences de la Matière

THÈSE DE DOCTORAT

pour obtenir le grade de
DOCTEUR DE L'UNIVERSITÉ AIX-MARSEILLE
Spécialité : Matière condensée, Nanosciences
par

Julia WIKTOR

Identification of equilibrium and irradiation-induced defects in nuclear ceramics: electronic structure calculations of defect properties and positron annihilation characteristics

Soutenue le 02 octobre 2015

Jury :

Martti PUSKA	Président du jury
Grégory GENESTE	Rapporteur du jury
David KEEBLE	Membre du jury
Marjorie BERTOLUS	Directrice de thèse
Marie-France BARTHE	Co-directrice de thèse
Gérald JOMARD	Co-encadrant CEA

CEA Cadarache 2012–2015

Acknowledgements

This manuscript is the conclusion of a three-year PhD thesis at the French Alternative Energies and Atomic Energy Commission (CEA). First, I would like to thank the Departament of Fuel Studies (DEC), the Section of Fuel Behavior Studies and Simulation (SESC) and the Laboratory of Fuel Behavior Laws (LLCC) for allowing me to carry out this project in the best conditions.

I would like to thank the people who supervised this work. I am grateful to Gérald Jomard for passing on the engaging subject of positron annihilation to me, for generosity in teaching me all I needed to know during my Master's internship in the Laboratory of Fuel Behavior Simulation (LSC) and for the continous help during this PhD project later in LLCC. I always enjoyed working with him and greately appricitated our discussions and his immidiate understanding.

I would like to thank Marjorie Bertolus, for all the support and encouragement. Supervising a PhD project isn't an easy task, so I am very grateful to her for always being able to provide the needed resources and for devoting time to make the corrections of all the papers, projects, applications, presentations and many more. She always made sure that everything was of the highest quality.

This thesis wouldn't be complete if it wasn't for the collaboration with experimentalists. I am grateful to Marie-France Barthe for sharing her insight into positron annihilation spectroscopy measurements and for all the discussions, allowing us to make the link between calculations and experimental results. I believe that an ability to cooperate with researchers performing experiments is crucial for a theorist and I have learnt this useful skill thanks to her.

This thesis wouldn't be possible without contributions of numerous people. I am especially grateful to Marc Torrent for his help with the ABINIT development. I enjoyed the time we spent together working on the code, I am very thankful for all I could learn from him and I am sure that this project wouldn't work without him. I would like to also thank Boris Dorado for sharing his experience and knowledge, and for his support. I am also grateful to Ilja Makkonen for his insights and for receiving me, together with Filip Tuomisto, in their group at Aalto

University. I also want to thank Michel Freyss, Philip Garcia, Guillaume Martin and Fabien Bruneval for all the discussions and help.

I would like to thank Martti Puska and Grégory Geneste for carefully reviewing this manuscript and David Keeble for agreeing to be a jury member during my defence.

I am grateful to the present and former members of the LLCC laboratory for all the pleasant moments we shared during these three years.

I would like to thank the L'Oréal Foundation and UNESCO for awarding me the L'Oréal-UNESCO *For Women in Science* fellowship. It not only allowed me to attend enriching conferences and finance my visit at the Aalto University, but also gave me an opportunity to meet some great young female scientists and to promote science among french high school students.

Finally, I would like to thank my mom Hania, dad Józef, brothers Kuba and Józik, and my gorgeous husband Michał for everything.

Contents

Introduction

The knowledge of the behavior of the materials used in nuclear reactors is essential for the safety and efficiency of the power plants. During irradiation in a reactor the fission of actinide nuclei causes the creation of large amounts of defects, which affect the physical and chemical properties of materials inside the reactor, in particular fuel and structural materials. An active field of research is the improvement of the knowledge of the basic mechanisms that induce the modification of materials under irradiation. This can be done by so called separate effects experiments, which aim at uncoupling the combined phenomena happening in the reactor, as well as by modeling at different scales. Joining these experimental and modeling approaches is the strategy of the Fuel behavior law laboratory (LLCC) at CEA Cadarache, France, where this thesis was carried out.

An important question for understanding the behavior of nuclear materials under irradiation is the beginning of the formation of rare gas bubbles. Small aggregates of vacancy defects, which can trap gaseous fission products, such as Kr or Xe, are particularly interesting from the point of view of the investigation of bubble formation mechanisms. Additionally, the point defects themselves, empty or containing fission products, can affect thermochemical and thermomechanical properties of the materials, hence need to be studied.

One of the non-destructive methods that can be used to characterize these defects is the positron annihilation spectroscopy (PAS). This experimental technique involves detecting the radiation generated during electron-positron annihilation in a sample and deducing the properties of the material studied. PAS is based on the fact that when a positron diffuses in a sample, it can be trapped in open volume defects, what changes its annihilation characteristics. There are two positron annihilation characteristics that allow one to detect defects in materials: the first one, the positron lifetime, is mostly sensitive to the open volume of defects. Second, the Doppler broadening of the annihilation radiation, carries information on the chemical environment in which positron annihilate. However, positron annihilation spectroscopy results do not provide a direct link between the signal and the type of the defect. Therefore, the interpretation

of experimental data often requires comparisons with other experimental techniques or with electronic structure calculations.

This work is dedicated to the modeling at the atomic scale of nuclear materials containing defects and to calculating their annihilation characteristics in order to contribute to the interpretation of experimental results obtained by PAS and to the identification of the defects. The materials considered in this work are silicon carbide, a ceramic considered as a possible alternative to zirconium alloys used as fuel cladding in current reactors as well as tubes for the fuel assembly envelopes, and uranium dioxide, the standard fuel in pressurized water reactors. The contribution to the identification of the defects can be done directly through calculations of the annihilation characteristics of the defects, but can also be supported by additional modeling, for instance of the defects charge states. The positron annihilation spectroscopy is sensitive to the charge states of the defects and their prediction can, therefore, facilitate the identification of defects.

In this work, positron lifetime were calculated using the implementation of the two component density functional theory (TCDFT) in the ABINIT code. Then the methods needed to calculate the second positron annihilation characteristic, the Doppler broadening of the annihilating pairs, were implemented in the code. This part was done in collaboration with Marc Torrent from CEA DAM/DIF.

The second part of this work was dedicated to adapting the different methods used in calculations of positron annihilation characteristics and formation energies of charged defects to silicon carbide and uranium dioxide. Effort has been made to perform the most up-to-date calculations of positron lifetimes, i.e. using fully self-consistent calculations schemes and taking into account the effect of the changes of the atomic positions in the simulated defects, due to the vacancy creation and the positron localization inside the defect. The combined results of the formation energies, positron lifetime and Doppler broadening calculations are then used to identify defects experimentally detected in silicon carbide and uranium dioxide in the CNRS-CEMHTI laboratory in Orléans, France.

Chapter 1

Literature review

1.1 Nuclear materials considered

1.1.1 Silicon carbide

Silicon carbide is a ceramic with a high melting point, a good chemical stability and a low neutron absorption. These properties make it a possible cladding material in high temperature fission reactors [1] and in the Accident Tolerant Fuels (ATF) in generation II and III reactors [2, 3]. Additionally, its mechanical properties as a composite material make it an interesting material for fuel assembly envelopes [4]. Moreover, as a wide band gap semiconductor, it is envisaged as an alternative for silicon in microelectronic devices [5].

Silicon carbide can exist in about 250 crystalline forms, all of which have the same planar arrangement of carbon and silicon atoms, but different sequences of these planes. $6H$-SiC, which can be formed at temperatures higher than 1700°C, is the most common polytype of silicon carbide, with six planes in each sequence and a hexagonal crystal structure. Another hexagonal polytype is $4H$-SiC with four planes in each sequence. At temperatures lower than 1700°C, a cubic form, with three planes in a sequence, $3C$-SiC, is formed. In this work, the $3C$-SiC and $6H$-SiC polytypes were studied. The stacking sequences of these two polytypes are shown in the Fig. 1.1. As for the band structure, silicon carbide is an indirect gap semiconductor. The gap size depends on the polytype, for $3C$-SiC and $6H$-SiC it is equal to 2.36 and 3.0 eV [6], respectively.

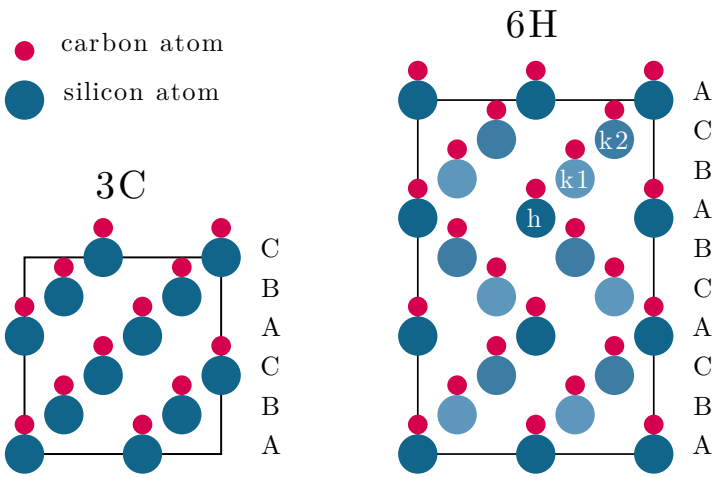

Figure 1.1: *Stacking sequences in the [1120] plane of the two studied polytypes, cubic 3C and hexagonal 6H. In 6H-SiC atoms occupy three different sites - hexagonal h and two quasicubic - k_1 and k_2.*

In its application as a cladding material in nuclear reactors, the role of silicon carbide is to ensure the heat transfer from the fuel to the coolant and to act as a barrier for fission products. If used as a hexagonal tube, its role would be to provide the structural integrity to the fuel assembly and to guide the flow of the coolant. In the case of both these applications it is essential to understand the effects of the irradiation on the thermomechanical and thermochemical properties of silicon carbide, for instance through defects creation and their interaction with fission products. Defects in silicon carbide have already been studied in numerous works, for instance in Ref. [7], [8], [9] and [10].

1.1.2 Uranium dioxide

Uranium dioxide (UO_2) is currently the most widely used fuel material in pressurized water reactors (PWR). It has been chosen as a fuel material because of its high melting temperature (3120 K [11]) and chemical stability, in particular low chemical reactivity with water. Since during irradiation in the reactor the properties of UO_2 evolve, for example due to the creation of defects in the lattice, it is important to be able to predict which types of defects can be expected and wthat is their influence on the material.

At atmospheric pressure UO_2 have two stable crystalline structures, with a phase transition at Néel temperature T_N=30.8 K. Below T_N an antiferromagnetic Jahn-Teller distorted phase is the stable one. Above T_N uranium dioxide is a paramagnetic Mott insulator with a cubic fluorite crystal structure (see Fig. 1.2) [12, 13] and a lattice parameter of 5.473 Å [14]. Uranium dioxide

is an ionic material, in which the uranium cations (U^{4+}) in UO_2 form a face centered cubic (fcc) structure and oxygen anions (O^{2-}) occupy the tetrahedral sites. Various experimental studies determined the gap of UO_2 between 2.14 and 2.5 eV [15–17]. Moreover, the $5f$ electrons of uranium in UO_2 are strongly correlated and localized close to the nuclei [18–20]. As a consequence, the theoretical methods that need to be used to model uranium dioxide have to be carefully chosen. These methods will be further discussed in Chapter 2. Further details on crystalline phases and defects in UO_2 can be found in earlier PhD theses on the subject [21, 22].

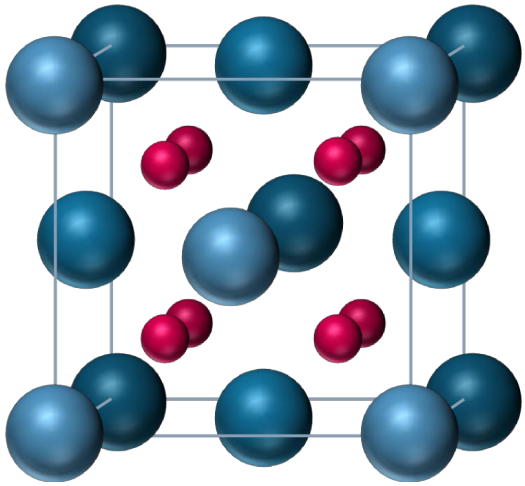

Figure 1.2: *Fluorite structure CaF_2. Blue and red spheres represent cations and anions, respectively (in the case of UO_2, uranium and oxygen atoms).*

1.1.3 Irradiation effects in nuclear materials

During reactor operation, uranium 235 atoms can absorb a neutron that leads to its splitting into two smaller nuclei, which masses are usually close to each other (e.g Ba and Kr or Sr and Xe) and to emission of two or three neutrons. The two fission products carry an important kinetic energy (around 65–95 MeV). This energy can be lost through two different processes. First, at high energy, the energy is transferred through inelastic interactions with the atoms of the fuel material, such as electronic excitations. These interactions can lead to displacement of the atoms located along the fission product trajectory. Then, at lower energies, the energy loss through ballistic collisions between atoms dominates. In this case, displacement cascades can be formed and lead to defects creation and migration within a larger region.

Defects created due to the energy loss of the fission products or neutrons, such as vacancies and vacancy clusters, can induce a significant evolution of the physical properties of the fuel and cladding materials. An important question concerning defects in nuclear materials is their

evolution as function of varying temperature and irradiation. In some cases these effects can lead to the disappearing of defects, in others to their aggregation and growth. In the later case, small aggregates of vacancy defects, which can trap gaseous fission products, such as Kr or Xe, are particularly interesting for the investigation of bubble formation mechanisms. Moreover, the point defects themselves, empty or containing fission products, can affect thermochemical and thermomechanical properties of the materials, hence need to be studied. The importance of the insight into the defects in both silicon carbide and uranium oxide is reflected in the number of theoretical and experimental studies concerning this aspect. The energetics and migration of defects in these two materials have been widely studied using the electronic structure calculations [9, 22–31]. Additionally various experimental methods have been used to investigate the defects in SiC and UO_2, such as electron paramagnetic resonance (EPR) [32–39], Raman spectroscopy [40], X-ray absorption spectroscopy (XAS) [41] or photoluminescence spectroscopy (PL) [42, 43]. Another experimental method that can be used to characterize these defects is the positron annihilation spectroscopy (PAS).

1.2 Positrons to probe matter: principle of positron annihilation spectroscopy

Positron annihilation spectroscopy (PAS) is a non-destructive characterization technique, which can probe materials on the atomic scale and can be used to identify open volume defects such as vacancies. Positron as the antiparticle of the electron annihilate quickly in solids, which leads to the emission of gamma rays. PAS consists in recording these radiations and deducing the properties of the positrons and the electrons with which they have annihilated. There are two positron annihilation characteristics that allow one to characterize defects in materials: the positron lifetime and the Doppler broadening of the annihilation radiation..

The positrons used in PAS experiments are usually generated by a Na^{22} source, along with a 1.27 MeV γ ray, in a β^+ decay

$$^{22}\mathrm{Na} \rightarrow {}^{22}\mathrm{Ne} + \mathrm{e}^+ + \nu_\mathrm{e} + \gamma. \tag{1.2.1}$$

In positron lifetime measurements the initial 1.27 MeV γ ray can be detected to mark the birth of the positron.

The positrons emitted from this source have a broad kinetic energy distribution up to 540 keV. The majority of this energy is lost when the positrons enter the sample and thermalize. During

this process positrons travel from 100 to a few 100 μm into the sample depending on its density [44]. It means that positrons can probe the bulk of a solid. After diffusing in the sample, the positron can annihilate with an electron in the perfect lattice, around a negative ion or get trapped in a neutral or negative vacancy-type defect and annihilate inside it. The annihilation can be observed as two γ rays of approximately 511 keV are generated and can be detected. In Fig. 1.3 the main interactions of the positrons with solids are shown.

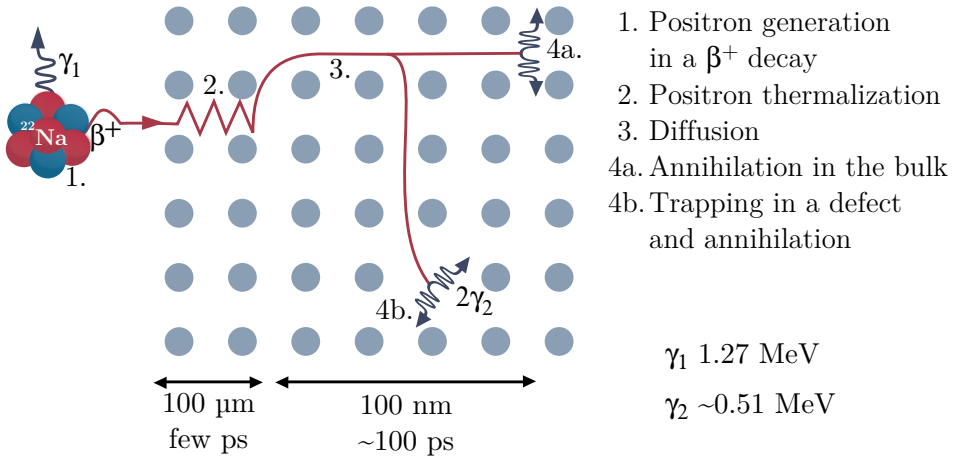

Figure 1.3: *Scheme of the main positron-solid interactions.*

The time difference between the detection of the γ ray emitted during the β^+ decay and those coming from the annihilation is used to determine the lifetime of the positron in the material. This characteristic depends mostly on the free volume the positron occupies and is longer for the positrons trapped in vacancies than for those which annihilate from a delocalized state in the perfect lattice (which has its specific annihilation characteristics). The results yielded by a lifetime experiment take the form of a positron decay spectrum, as illustrated in Fig. 1.4a. As represented in the figure, the spectrum can be a sum of different components, each characterized by its positron lifetime τ_i and contributing to the spectrum with a given intensity I_i. The spectra can be decomposed using non-linear fitting to obtain I_i and τ_i. It is worth noting that if the lifetime measurements are performed as a function of temperature, the evolution of the intensity corresponding to a defect can sometimes yield information on its charge state. This is because for negative vacancies the positron trapping decreases when the measurement temperature rises, while for the neutral ones it remains constant (see Sec. 1.2.1.1).

The second annihilation characteristic that can be measured, the Doppler broadening, is related to the energy difference ΔE_γ between the two photons emitted during the annihilation process. Due to the conservation of the momentum of the electron-positron annihilation pair the two

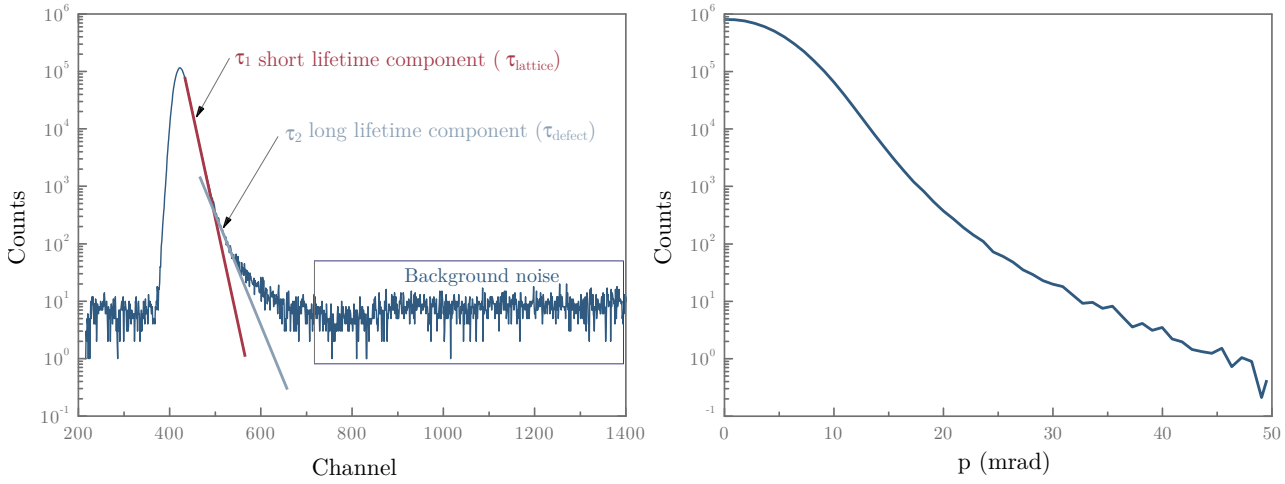

(a) *Lifetime spectrum* ***(b)*** *Momentum spectrum*

Figure 1.4: *Illustrations of lifetime and momentum distributions of annihilation radiation spectra.*

photons have the energy of 511 keV$-\Delta E_\gamma$ and 511 keV$+\Delta E_\gamma$, with

$$\Delta E_\gamma = \frac{1}{2} c p_L, \tag{1.2.2}$$

where p_L is the longitudinal projection of the electron-positron pair momentum. Considering that the momentum of the thermalized positron can be neglected, the Doppler broadening of the annihilation radiation gives information about the distribution of the momenta of the electrons with which the positron annihilates, making it possible to detect vacancy defects and to obtain information e.g. on their chemical environment. Experimentally, the number of counts as a function of p_L is measured, resulting in a Doppler spectrum as illustrated in Fig. 1.4b. Two types of data analysis are the most commonly used. The first consists of plotting ratios of Doppler spectra to reference data (perfect lattice or reference material). The second way is to compare integrated low- and high-momentum contributions to the momentum distribution. It can be done by calculating the so-called S (low-momentum) and W (high-momentum) parameters, being defined, respectively, as the ratio of the counts in the regions close to and far from the 511 keV value to the total number of the counts. The schematic representation of these two parameters is shown in Fig. 1.5. As presented in the figure, positron trapping in a vacancy usually results in an increase of S and a decrease of W. This is due to the fact that when a positron is localized in the vacancy its annihilation probability with valence electrons increases (corresponding mostly to low momenta) while there is less interaction between the positron and the core electrons, which results in a decrease of the high momentum contribution.

It is worth noting that in experiments both lifetime components and S and W parameters can sometimes be related to en ensemble of defects, for instance when the annihilation characteristics of the defects are very close.

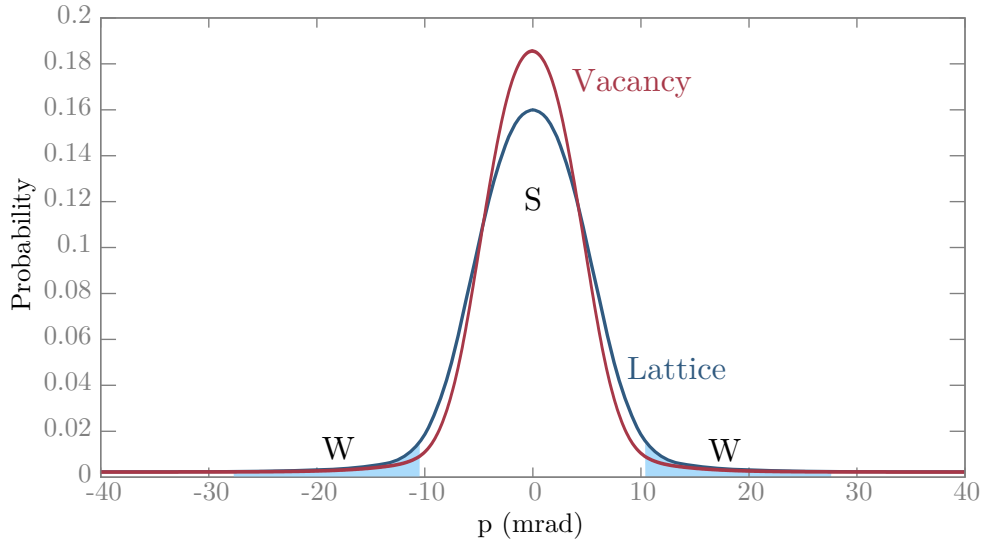

Figure 1.5: *Schematic representation of the relative S and W parameters.*

1.2.1 Methods used in PAS results interpretation

The interpretation of the measurements performed using PAS is not always straightforward. In the case of the positron lifetimes measurements, first decompositions of the spectra must be performed, which can be problematic when several types of defects are present [45]. Moreover, the PAS measurements themselves do not provide a direct link between the signal and the defects type. In order to facilitate the defects identification, one can for instance use the positron trapping model to verify the detected annihilation states, to determine the lifetimes of the defects and their concentration. The model also allows the determination of the charge state of the defects present in the studied samples. The results can be also compared with other experimental methods or modeled annihilation features to identify the detected defects.

1.2.1.1 Positron trapping model

The evolution of the positron annihilation characteristics as a function of the measurement temperature can be analyzed using a positron trapping model [46–53]. In this model, the description of the positron trapping and annihilation from different states (from the delocalized

state in the lattice and from N different defects) is obtained through solving a set of rate equations [54]:

$$\frac{dn_{\mathrm{L}}}{dt} = -(\lambda_{\mathrm{L}} + \sum_j \kappa_j) n_{\mathrm{L}} + \sum_j \delta_j n_{\mathrm{D}j}, \tag{1.2.3}$$

$$\frac{dn_{\mathrm{D}j}}{dt} = \kappa_j n_{\mathrm{L}} - (\lambda_{\mathrm{D}j} + \delta_j) n_{\mathrm{D}j} \ (j = 1, \ldots, N), \tag{1.2.4}$$

where n_{L} is the probability of a positron being in the free state, $n_{\mathrm{D}j}$ is the probability of being trapped in a given defect. λ_{L}, $\lambda_{\mathrm{D}j}$, κ_j and δ_j are the annihilation, trapping and detrapping rates, respectively.

The trapping rate is related to the defect concentration c_j through the relation $\kappa_j = \mu_{\mathrm{D}j} c_{\mathrm{D}j}$, where $\mu_{\mathrm{D}j}$ is the specific trapping coefficient.

For neutral defects $\mu_{\mathrm{D}j}$ is temperature independent. The trapping coefficient of the negative vacancies is higher at low temperatures, due to a long-range attractive Coulomb potential created by these defect and then it varies as $T^{-1/2}$, since when the temperature rises the positrons gain energy allowing them to escape from this additional potential. A positron can be trapped not only in open volume defects, but also by hydrogen-like Rydberg states around negative non-vacancy defects, caused by the long-range Coulomb potential. The positron trapping rate at the Rydberg states also varies as $T^{-1/2}$ [50].

1.2.1.2 Comparison with other experimental methods and modeling results

In order to fully exploit the results of the positron annihilation spectroscopy experiments, one needs to be able to attribute the detected signal to a type of defect. This relation is not always possible to deduce based on PAS measurements only. Comparison with other experimental methods, for instance electron paramagnetic resonance (EPR) spectroscopy and photoluminescence spectroscopy (PL) or theoretically calculated positron annihilation characteristics can be especially helpful in defects identification. In this study we focus on the modeling contribution to the PAS experiments interpretation. The positron annihilation characteristics, the positron lifetime and the momentum distribution of electron-positron pairs, can be calculated in the two-component density functional theory, which will be presented in Sec. 2.3.

1.3 Overview of positron annihilation results available in the materials studied

Positron annihilation spectroscopy has been widely used to study defects in semiconductors, including silicon carbide. On the other hand, few theoretical positron annihilation studies exist for this material. As far as uranium dioxide is concerned, a limited number of experimental studies exist, while no calculation of annihilation characteristics has been published to the best of our knowledge.

1.3.1 Silicon carbide

1.3.1.1 Theoretical studies

The lattice positron lifetime of silicon carbide was calculated in several studies. In these calculations various methods were used. These results and the methods used are summarized in Tab. 1.1.

It can be noticed in Tab. 1.1 that the calculations using no correction to take into account the imperfect screening in SiC yield lattice lifetimes much shorter than the experimental ones for $3C$-SiC and $6H$-SiC, which are around 140 ps [55, 56]. When the semiconductor correction (SC) or gradient correction (GC) are applied, the results are in better agreement with experimental values, especially when the pseudopotential method is used. It seems that both ways of taking into account the reduced screening can be used in the case of SiC.

Positron lifetimes for defects have been calculated by Brauer *et al.* [58, 59], Kawasuso *et al.* [63] and Staab *et al.* [64]. The results obtained for various defects are presented in Tab. 1.2. In these calculations several important approximations were made. First, the authors used the 'conventional' scheme (see Sec. 2.3.2), which does not take into account the effect of the localized positron on the electronic density. Second, these studies were performed for unrelaxed defects (Brauer *et al.* and Staab *et al.*) or using geometries that had been relaxed without the positron (Kawasuso *et al.* and Staab *et al.*).

Doppler broadening calculations for silicon carbide have been performed by Kawasuso *et al.* [63]. Like in the case of positron lifetimes, the conventional scheme was used and the full relaxation (due to the defect creation and positron localization inside the defect) was not taken

Table 1.1: *Synthesis of the calculated lattice positron lifetimes in 3C silicon carbide available in literature. The type of correction taking into account the imperfect screening in silicon carbide (SC – semiconductor correction, GC – gradient correction) and of basis set representation used in calculations are indicated.*

	Corr.	Basis set representation	Lifetime (ps)
Puska *et al.* [57]	SC	Atomic superposition	134
Brauer *et al.* [58]	SC	Atomic superposition	141
Brauer *et al.* [59]	SC	TB-LMTO	138
Barbiellini *et al.* [60]	none	LMTO-ASA	124
	GC	LMTO-ASA	139
	none	Atomic superposition	121
	GC	Atomic superposition	134
Panda *et al.* [61]	none	Pseudopotentials	130
	GC	Pseudopotentials	145
Panda *et al.* [62]	GC	Pseudopotentials	145
	GC	Pseudopotentials	144
	GC	LMTO-ASA	138
	GC	LMTO-ASA	138
Kawasuso *et al.* [63]	SC	Pseudopotentials	143

Table 1.2: *Synthesis of the positron lifetimes calculated for vacancies in SiC available in literature. Ranges of lifetimes are indicated in cases where various polytypes and defect geometries were considered in the study.*

	Lifetime (ps)		
Defect	Brauer *et al.* [58, 59]	Kawasuso *et al.* [63]	Staab *et al.* [64]
V_C	150-153	145	137-144
V_{Si}	185-194	190-196	180–195
V_C+C_{Si}		168–184	
V_C+V_C	160–161		
V_{Si}+V_{Si}	194-196		
V_C+V_{Si}	212–216	208–215	209-216
$(V_C+V_{Si})_2$	254	240	
$(V_C+V_{Si})_3$	286	282	
$(V_C+V_{Si})_4$	321	299	
$(V_C+V_{Si})_6$		329	

into account. The relative S_{rel} and W_{rel} parameters, determined for various defects in SiC in this study are presented in Tab. 1.3. These parameters are defined as:

$$S_{\mathrm{rel}} = \frac{S_{\mathrm{defect}}}{S_{\mathrm{lattice}}} \tag{1.3.1}$$

Table 1.3: *Synthesis of the relative S_{rel} and W_{rel} parameters (see text) calculated for vacancies in 3C and 4H-SiC by Kawasuso et al. [63]. The S_{rel} and W_{rel} parameters were calculated in 0–3 and 15–30 mrad windows, respectively, using data convoluted with a Gaussian function with FWHM of 3.92 mrad. The ranges of S_{rel} and W_{rel} are given if different results were found for various sites and polytypes.*

Defect	S_{rel}	W_{rel}
V_C	1.005–1.006	0.975–0.977
V_{Si}	1.031–1.037	0.651–0.715
V_C+C_{Si}	1.018–1.034	0.658–0.747
V_C+V_{Si}	1.057	0.590
$(V_C+V_{Si})_2$	1.122	0.463
$(V_C+V_{Si})_3$	1.160	0.346
$(V_C+V_{Si})_4$	1.198	0.312
$(V_C+V_{Si})_6$	1.227	0.297

and

$$W_{\mathrm{rel}} = \frac{W_{\mathrm{defect}}}{W_{\mathrm{lattice}}}. \tag{1.3.2}$$

1.3.1.2 Experimental studies

Positron annihilation spectroscopy has been widely used to study defects in $3C$, $4H$ and $6H$ silicon carbide. Samples exhibiting various doping levels and irradiation conditions have been examined. We will list here some of the results and interpretations presented in these studies.

Kerbiriou *et al.* [32] observed a positron lifetime varying with temperature from 210 ps up to 220 ps in 800 keV electron irradiated n-type $3C$-SiC. The authors concluded that the lifetimes were coming from at least two vacancy-type defects - V_{Si} and V_C+V_{Si}. This identification was based on the calculation results by Brauer *et al.* [58, 59]. Kerbiriou *et al.* also examined the sample using electron paramagnetic resonance (EPR) and identified the T1 signal, attributed to V_{Si}^{1-} [32, 35, 65, 66].

Kawasuso *et al.* [56] also studied n-type $3C$-SiC irradiated with 1 MeV electrons and detected a lifetime component of 188 ps, which they attributed to the silicon vacancy. The T1 signal observed in Kerbiriou *et al.* study, indicating the presence of V_{Si}^{1-}, was detected by EPR in the same sample. The lifetime component of 188 ps was hence attributed to the silicon monovacancy.

Concerning $6H$-SiC, no defect was observed by PAS in p-type samples in the majority of published studies [55, 67, 68]. A long lifetime component corresponding to open volume defects

was, however, observed in p-type samples irradiated at high fluences of 12 MeV proton (above 10×10^{16} cm^{-2} by Barthe *et al.* As for the n-type 6*H*-SiC, several groups of lifetimes were observed. Shorter experimental positron lifetimes, of 176 ps [69], 183 ps [67], 174 ps and 176 ps [70] were observed and assigned to the silicon vacancy based on the calculations of Brauer *et al.* The second group of experimental lifetimes observed in n-type 6*H*-SiC contained lifetimes of 210 ps [69], 202 ps [55], 210 ps and 220 ps [68]. These lifetimes are usually attributed to the V_C+V_{Si} divacancy.

Longer positron lifetimes were also detected in other studies. For instance Barthe *et al.* [71] observed lifetimes of 257 ps and 281 ps lifetimes in n-type 6*H*-SiC irradiated with low-energy protons and annealed at 900°C and 1300°C, respectively. These lifetimes were attributed to the $(V_C+V_{Si})_2$ and $(V_C+V_{Si})_3$ vacancy defects. Aavikko *et al.* [72] studied undoped SiC samples annealed at 1600°C. They observed long lifetime components of 261, 283 and 284 ps, which were attributed to clusters containing four and five vacancies, respectively.

Finally, Brauer *et al.* [58] studied 6*H*-SiC samples irradiated with 200 keV Ge^+ ions, at fluences varying from 10^{16} to 10^{19} m^{-2}. For the lowest fluence, a long lifetime component of 235 ps was observed and attributed to the divacancy, even though it was longer than what Brauer *et al.* had calculated for this type of defect. The authors indicated that the discrepancy between the measured and calculated lifetimes could come from the fact that the relaxation effects were not taken into account. For the 10^{19} m^{-2} fluence, Brauer *et al.* observed a lifetime component of 305 ps and attributed it to a defect containing six vacancies.

It can be noticed that there are discrepancies in the literature between the positron lifetimes attributed for example to the silicon monovacancy. This problem has been discussed for instance by Lam *et al.* [45]. The authors suppose that the decomposition of the experimental spectra can be incorrect when several types of defects are present in the samples. Another issue might be the fact that theoretical studies on positron annihilation characteristics were limited in number and that too strong approximations had been made in the available ones. These inconsistencies in the defect identification in silicon carbide are one of the motivations behind the present work.

In addition to the positron lifetime measurements, numerous Doppler broadening spectroscopy studies were published [68–71, 73–78]. Ohshima *et al.* [73] studied n-type 6*H*-SiC samples implanted with 200 keV phosphorous ions and then annealed up to 1500°C. In the as-implanted samples the relative S_{rel} parameter of 1.067 was detected and attributed to a defect with a size similar to V_C+V_{Si}. After annealing, the increase of S was interpreted as the formation of clusters such as $(V_C+V_{Si})_2$ and $(V_C+V_{Si})_3$. The V_C+V_{Si} divacancy was also identified in the PhD thesis of Laurent Henry [77] with $S_{rel} = 1.068$ and $W_{rel} = 0.866$ in 6*H*-SiC. Barthe *et al.* [71] also studied the annealing of defects in 6*H*-SiC, implanted with low-energy protons. After

annealing at 900°C a cluster with $S_{\mathrm{rel}} = 1.088$ and $W_{\mathrm{rel}} = 0.766$ was detected and identified as $(\mathrm{V_C}+\mathrm{V_{Si}})_2$, also based on its lifetime of 257 ps.

Kawasuso *et al.* [74–76] measured the Doppler broadening of three polytypes of silicon carbide, $3C$, $4H$ and $6H$. The samples were n-doped and irradiated with 1-2 MeV electrons. The authors identified the silicon vacancies, with the relative S_{rel} parameter of 1.028–1.033, as the predominant defects in the samples.

Rempel *et al.* [69] studied n-type $6H$-SiC samples irradiated with 2.5 MeV electrons. Based on the shape of ratios between diamond, silicon and silicon carbide lattice spectra they identified vacancies on the two sublattices, C vacancies, Si vacancies and Si-Si divacancies. Another study performed to identify defects on the two SiC sublattices was performed by Arpiainen *et al.* [68]. The n-type $6H$-SiC samples were irradiated by electrons and protons with various energies. The authors attributed the signals detected after 0.8 MeV electron and 12 MeV proton irradiation to carbon and silicon vacancies, respectively. Dannefaer *et al.* [70] also studied electron irradiated n-type $6H$-SiC samples and determined $S_{\mathrm{rel}} = 1.00$ and $W_{\mathrm{rel}} = 1.00$ for $\mathrm{V_C}$, $S_{\mathrm{rel}} = 1.05$ and $W_{\mathrm{rel}} = 0.90$ for $\mathrm{V_{Si}}$ and $S_{\mathrm{rel}} = 1.03$ and $W_{\mathrm{rel}} = 1.0$ for $\mathrm{V_C}+\mathrm{C_{Si}}$.

It is worth keeping in mind that a direct comparison between the different published momentum distribution measurements is not always possible. The ratio curves and relative valence and core contributions (S and W parameters) depend on the experimental resolution. The windows within which the S and W parameters are integrated might also differ between the studies and it can strongly affect their values.

1.3.1.3 Experimental results of X. Kerbiriou

In this work we will analyze, among others, the experimental results obtained for silicon carbide during X. Kerbiriou's thesis at the CEMHTI Laboratory (Orléans, France). The interpretation of these measurements has been the basis of our collaboration and the subject of publication [79], therefore the experimental data is presented in detail here and will be discussed further in Sec. 4.4 in view of the calculation results obtained during this study.

In the study by X. Kerbiriou, the $6H$-SiC samples were cut from a low nitrogen-doped single crystal wafer ($n_{\mathrm{D}} - n_{\mathrm{A}} = 1.9{\times}10^{17}$ cm^{-3}, 385 μm thick). It was a commercial CREE research (0001)-oriented $6H$-SiC wafer grown using the modified Lely method. The characterization using positron annihilation spectroscopy was performed on of these crystals before irradiation and reported in Ref. [55]. It showed that these samples contained negatively charged non-vacancy defects.

Proton irradiation was performed at room temperature at the CEMHTI laboratory using a cyclotron. The crystals were irradiated under vacuum with 12 MeV protons at a fluence of 4×10^{16} cm^{-2} on a water-cooled sample support. The maximum flux used during irradiation was maintained close to 2×10^{13} $H^+cm^{-2}s^{-1}$ in order to avoid sample warming. SRIM [80] calculations reported in Ref. [55] showed that 12 MeV protons go through the whole crystal and that the vacancy defect distribution is almost homogeneous as a function of depth. A 20 minute isochronal annealing, from 100°C (EPR study) or 300°C (PAS study) up to 1050°C by 50°C steps - was performed in a rapid thermal annealing furnace under argon atmosphere. Both PAS and EPR spectra were recorded as a function of the sample temperature before annealing and after the various annealing steps.

Electron paramagnetic resonance (EPR) measurements

The electron paramagnetic resonance (EPR) measurements were performed using an EMX BRUKER spectrometer at 80 and 300 K. This technique allows one to probe defects in solids exhibiting unpaired electrons. It is based on the fact that in the presence of an external magnetic field the energy level of an unpaired electron is split into two. The electron magnetic moment is then either parallel or antiparallel to the field. The information about the defect type can be obtained by measuring the energy absorbed by the material due to transitions of the electron between these two levels.

The EPR spectra obtained by X. Kerbiriou for the SiC samples were decomposed into different Lorentzian type components using numerical simulation. The spin numbers in the irradiated crystals were determined by comparison with a $CuSO_4$ standard sample measured at the same time. The absorption intensity measured in the SiC sample and the standard sample were determined by fitting the signal with a sum of Lorentzian functions. The number of spin in the sample is therefore given by the relation as follows

$$[N_{\text{spin}}]_{\text{sample}} = \frac{3}{4S(S+1)} \frac{I_{\text{sample}}}{I_{\text{standard}}} \frac{\rho}{m} N_{\text{standard}}, \tag{1.3.3}$$

where ρ is the volumic mass of the sample, m its weight, N_{standard} the number of spin centers in the standard sample, I_{sample} and I_{standard} the EPR signal intensities in the sample and in the standard sample, respectively. S is the spin of the centers detected in the sample. The defect concentrations given in the following are average values on the whole crystal volume.

The spectra are described by the parameters of the Hamiltonian as follows:

$$\mathcal{H} = \mu_{\mathbf{B}}\mathbf{B}\cdot\mathbf{g}\cdot\mathbf{S} + \mathbf{S}\cdot D\cdot\mathbf{S} + \sum_j A_j\mathbf{S}\cdot\mathbf{I}_j \tag{1.3.4}$$

with $\mu_{\mathbf{B}}$ being the Bohr magneton, $\mathbf{B}$ the magnetic field, $\mathbf{S}$ the effective spin of the defect, $\mathbf{g}$ the g tensor, which accounts for the coupling between the orbital and spin angular momentum of the electrons, D the Zero Field Splitting (ZFS), A_j the hyperfine (HF) interaction constant with the nuclear spin of the neighbor atom j and $\mathbf{I}_j$ the nuclear spin of the neighbor atom j. The first derivative of the EPR spectra is presented in Fig. 1.6a and 1.6b for ease of interpretation.

PAS measurements

The evolution of the lifetime components as a function of the measurement temperature for various annealing temperatures is plotted in Fig. 1.7a. For each annealing temperature, the values of the average positron lifetime $\tau_{\text{av.}}$, the long lifetime component τ_2 and its relative intensity I_2 are plotted as a function of measurement temperature. The data shown correspond to the measurements performed before and after annealing at 300°C, 750°C, 850°C and 1000°C. These annealing temperatures were chosen because the evolution of the positron lifetime parameters as a function of the measurement temperature is representative of the general behavior.

For all annealing temperatures, $\tau_{\text{av.}}$ and τ_2 vary with the measurement temperature. This indicates that at least one negative defect is detected. Moreover, since the long lifetime component depends on the annealing temperature, several types of vacancy defects are probably detected and their concentrations change during annealing. The same spectra are therefore presented also as a function of annealing temperature for three characteristic measurement temperatures - 35 K, 215 K and 555 K (see Fig. 1.7b). The low (35 K) and high (575 K) measurement temperatures allow one to obtain information on the negatively charged and the neutral vacancy defects detected in the crystals, respectively. For a better accuracy, the values presented for 35 K are in fact an average for 15 K, 35 K and 55 K, the values for 215 K are an average for 195 K, 215 K and 235 K and the values for 555 K are an average for 535 K, 555 K and 575 K.

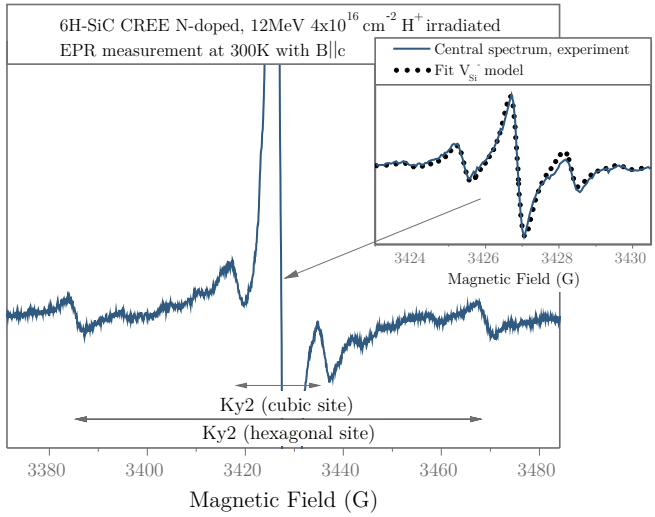

(a)

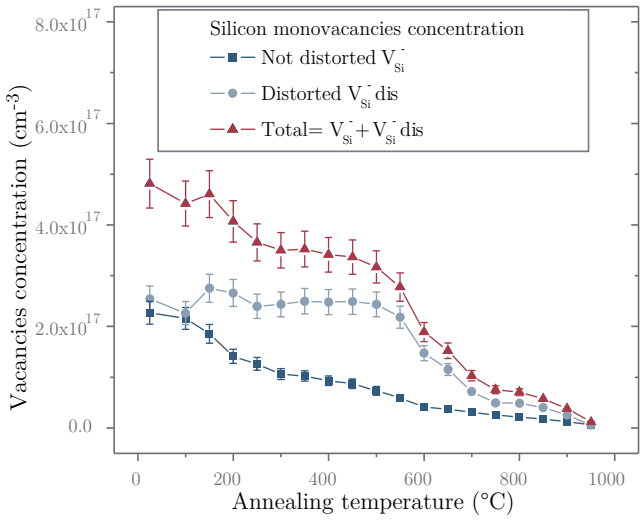

(b)

Figure 1.6: *(a) EPR spectrum obtained at 300 K in the proton irradiated 6H-SiC CREE crystal before annealing. The inset shows the central spectrum and its fit using the V_{Si}^{1-} model. (b) Silicon vacancies concentration (not distorted, distorted, sum) as a function of the annealing temperature in the 6H-SiC H^+ 12 MeV irradiated crystal.*

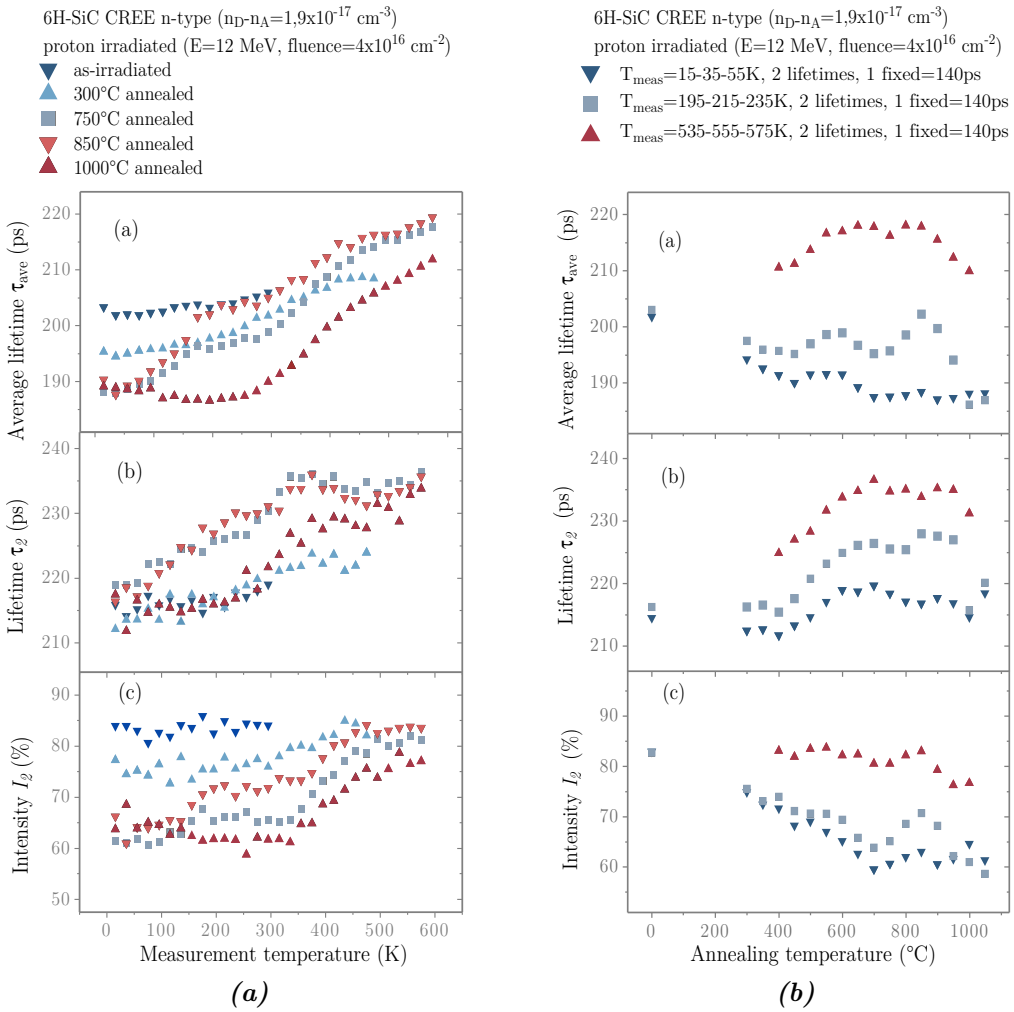

(a) ***(b)***

Figure 1.7: *(a) Measurement and annealing temperature dependence of the positron lifetime components obtained for the 12-MeV proton irradiated crystals. In both figures the average lifetime $\tau_{av.}$ (a), long lifetime component τ_2 (b) and its intensity I_2 (c), are shown.*

1.3.2 Uranium dioxide

Several experimental PAS studies on uranium dioxide are available in literature. In the study of Barthe *et al.* [81] a lattice lifetime of 169±1 ps was measured in polished and annealed samples. The samples were then irradiated with electrons and α particles at various fluences. No defect was detected after irradiation with 1 MeV electrons. It is consistent with the fact that this irradiation should create defects in the oxygen sublattice only and that the positive oxygen vacancies should not be detected by the positrons. In the other samples, irradiated with 45 MeV α particles of 2.5 MeV electrons the long lifetime components between 301±7 and 307±3 ps were observed. Since the PAS measurements on irradiated UO_2 presented in Ref. [81] were performed at constant temperature (300 K), the charge state of the defect could not be deduced.

In the study of Roudil *et al.* [82] α self-irradiated actinide-doped UO_2 samples were examined by PAS. In samples with 0.2% plutonium weight content a long lifetime component of 313 ps was detected. In the case of 27% Pu-doped UO_2 a lifetime of 340 ps was observed.

The Doppler broadening of the annihilation radiation in UO_2 was also measured [83–87]. Barthe *et al.* [83] studied the annealing behavior of near surface vacancy defects in sintered polished UO_2 samples. In as-polished disks a vacancy with $S_{\mathrm{rel}} = 1.12 - 1.13$ and $W_{\mathrm{rel}} = 0.78 - 0.79$ was detected. During annealing an increase of the size of this defect was observed. Labrim *et al.* [84, 85] examined helium implanted UO_2 and attributed $S_{\mathrm{rel}} = 1.076$ and $W_{\mathrm{rel}} = 0.88$ to a complex containing uranium vacancies. Doppler broadening spectroscopy was also used to study Xe implantation in uranium dioxide by Djourelov *et al.* [86, 87]. The authors observed that in the stoichiometric samples at $10{\times}10^{15}$ and $10{\times}10^{16}$ cm^{-2} fluences low concentration of bubbles was created and it increased after annealing. In hyper-stoichiometric samples the Xe bubbles could be already observed in as-irradiated samples and their concentration increased during annealing. It was also shown that the bubbles were stable at 1673 K, while at 1873 K the release of Xe from the bubbles was observed after 16 h of annealing.

In addition to the already published studies mentioned above , in this work we will also analyze some unpublished PAS results for UO_2. These measurements have been performed by M.-F. Barthe *et al.* at the CEMHTI laboratory and are presented below.

The evolution of the annihilation characteristics as a function of the measurement temperature in 45 MeV α irradiated UO_2 disks is presented in Fig. 5.17. For all measurement temperatures two positron lifetimes were extracted from the experimental spectrum decomposition, indicating presence of an open volume defect. The measurement temperature dependence of the short lifetime component τ_1, the long lifetime component τ_2, the average positron lifetime $\tau_{\mathrm{av.}}$ and

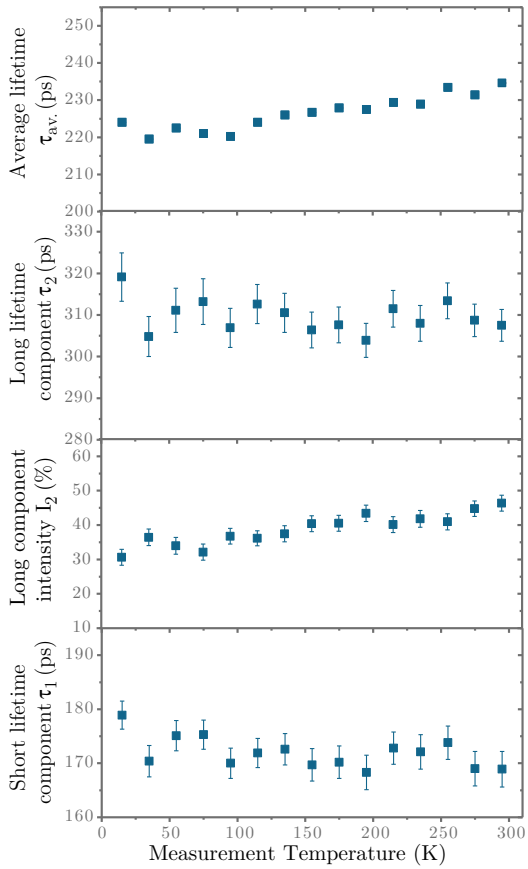

Figure 1.8: *Evolution of the average positron lifetime $\tau_{av.}$, short and long lifetime components τ_1 and τ_2 and the intensity I_2, detected in UO_2 crystals irradiated with 45 MeV α particles at a fluence of 2×10^{16} cm^{-2}, as a function of the measurement temperature.*

the intensity I_2 corresponding to τ_2 are shown in Fig. 1.8. These experimental results will be discussed and analyzed in Sec. 5.4.

1.4 Conclusions

The importance of comprehension of the point defects behavior led to extensive experimental studies on both silicon carbide and uranium dioxide. Positron annihilation spectroscopy is one of the most powerful methods that can be used to study open volume defects in solids, which is why it has been widely used to investigate unirradiated and irradiated SiC and UO_2. The interpretation of the PAS measurements, however, is not straightforward, which is reflected for example in discrepancies between the positron lifetimes attributed to silicon monovacancy-related defects in the literature. Additionally, theoretical studies on positron annihilation characteristics are limited in number for SiC and are not available in literature for UO_2. In the case of silicon

carbide, several computational studies have been published [58, 59, 63, 64], but using significant approximations. No fully self-consistent calculations, taking into account the relaxation of the atoms due to the defect creation and positron localization have been performed up to now. The aim of this thesis is therefore to perform state-of-the-art positron calculations for SiC and UO_2 and to contribute to the identification of defects in these materials.

Chapter 2

Computational methods

The goal of this thesis is to support the identification of signals observed by PAS in both uranium dioxide and silicon carbide by means of first-principles modeling. For both positron annihilation characteristics and formation energies determining, electronic structure calculations are necessary. We explain here the principles of electronic calculations and in particular the framework used, the density functional theory (DFT) and the two-component density functional theory (TCDFT).

2.1 Density functional theory

Electronic structure calculations enable one to describe matter at the atomic scale. At this scale systems consist of interacting nuclei and electrons. The basic equation for this type of problem is the Schrödinger equation, which can be written as

$$\hat{H}\Psi \equiv \left[\hat{T}_{\mathrm{n}} + \hat{T}_{\mathrm{e}} + \hat{V}_{\mathrm{nn}} + \hat{V}_{\mathrm{ne}} + \hat{V}_{\mathrm{ee}}\right]\Psi = E\Psi, \tag{2.1.1}$$

where $\hat{H}$ is the Hamiltonian, Ψ is the total wavefunction of the system, $\hat{T}_{\mathrm{n}}$, $\hat{T}_{\mathrm{e}}$ are the kinetic energies of nuclei and electrons and $\hat{V}_{\mathrm{nn}}$, $\hat{V}_{\mathrm{ne}}$ and $\hat{V}_{\mathrm{ee}}$ describe nucleus-nucleus, nucleus-electron and electron-electron interactions and E is the total energy of the system.

Eq. (2.1.1) is not possible to solve analytically for a complex system and approximations and numerical methods are necessary. Density functional theory is a type of quantum mechanical methods, which allows one to model the electronic structure of many body systems, such as

atoms, molecules and condensed matter phase thanks to the use of several simplifications. This method was formulated by Hohenberg and Kohn [88] based on the Thomas-Fermi model [89, 90]. In DFT the electronic density, $n(\mathbf{r})$, is the basic parameter describing the system, which means that all the properties of the system can be expressed as functionals of the density. This approach simplifies the calculations, as the problem of N electrons with $3N$ spatial coordinates is reduced to a problem of a global charge density with 3 spatial coordinates only. We present here the main approximations, theorems and methods used in the density functional theory.

2.1.1 Born-Oppenheimer approximation

The first approximation that can be made to solve Eq. (2.1.1) was proposed by Born and Oppenheimer [91]. As the masses of nuclei are much larger than those of electrons, the nuclei can be considered as fixed. It means that their kinetic energy, T_{n}, can be neglected. Additionally, the total wavefunction can be separated into electronic and ionic parts, $\Psi = \Psi_{\mathrm{ions}} \times \Psi_{\mathrm{electrons}}$. Therefore, the Schrödinger equations corresponding to electrons and nuclei can be solved independently. We will consider the electronic part only in the following expressions. The effect of the nuclei presence on the electrons is represented by an external potential $v(\mathbf{r})$, which is sensed by moving electrons. For electrons, it reduces the Eq. (2.1.1) to

$$\hat{H}\Psi \equiv \left[T_{\mathrm{e}} + \sum_{i}^{N} v(\mathbf{r}_i) + V_{\mathrm{ee}} \right] \Psi = E\Psi, \tag{2.1.2}$$

where N is the number of electrons in the system.

2.1.2 Electronic density

Eq. (2.1.2), even though already simplified, is still a problem of N electrons with $3N$ spatial coordinates. The idea behind DFT is to represent the system using the charge density only. This density, for a normalized wavefunction Ψ, is defined as:

$$n(\mathbf{r}) = N \int \mathrm{d}\mathbf{r}_2 \, d\mathbf{r}_3 \, \ldots \, d\mathbf{r}_N \, \left|\Psi(\mathbf{r}, \mathbf{r}_2, \ldots, \mathbf{r}_n)\right|^2 . \tag{2.1.3}$$

The wavefunction normalization leads to

$$\int \mathrm{d}\mathbf{r} \, n(\mathbf{r}) = N. \tag{2.1.4}$$

In the density functional theory all operators describing a given system can be expressed as functionals of the density described above, thanks to the Hohenberg-Kohn theorems.

2.1.3 Hohenberg-Kohn theorems

The first Hohenberg-Kohn theorem states that the external potential $v(\mathbf{r})$, as well as the total energy of the system, are unique functionals of the electronic density. It means that the system of electrons can be described by

$$T_{\mathrm{e}}[n] + \int \mathrm{d}\mathbf{r}\, v(\mathbf{r}) n(\mathbf{r}) + U_{\mathrm{ee}}[n] = E_v[n], \tag{2.1.5}$$

where $E_v[n]$ is the energy of the system for a given potential $v(\mathbf{r})$, $T_{\mathrm{e}}[n]$ is the kinetic energy of the electrons and $U_{\mathrm{ee}}[n]$ is a functional describing the electron-electron interactions. In the expression above we can regroup the terms independent of the external potential in a universal functional

$$F[n] = T_{\mathrm{e}}[n] + U_{\mathrm{ee}}[n]. \tag{2.1.6}$$

According to the second Hohenberg-Kohn theorem, the density functional $E_v[n]$ is minimized for the ground state of the electronic density in the given potential $v(\mathbf{r})$. It means that the ground-state energy can be found through the functional minimization,

$$E_g[n] = \min \left\{ \int \mathrm{d}\mathbf{r}\, v(\mathbf{r}) n(\mathbf{r}) + F[n] \right\}. \tag{2.1.7}$$

with a constraint put on the density variation:

$$\mathrm{d}\mathbf{r}\, \delta n(\mathbf{r}) = 0. \tag{2.1.8}$$

2.1.4 Kohn-Sham approach

The Hohenberh-Kohn theorems themselves are not enough to determine the $n(\mathbf{r})$ density, because a direct formulation of the $F[n]$ functional for a system of interacting electrons does not exist. To overcome this issue, the Kohn-Sham approach, which consists in replacing a complex system of interacting electrons by a system of independent electrons moving in an effective potential V_{eff} that yields the same density, can be used. In this approach the $F[n]$ functional can

be divided into three parts:

$$F[n] = T_{\mathrm{s}}[n] + V_{\mathrm{H}}[n] + E_{\mathrm{XC}}[n], \tag{2.1.9}$$

where T_{s} is the kinetic energy of the non-interacting electrons, V_{H} is the classical electrostatic (Hartree) energy, related to the Coulomb repulsion between the electrons. E_{XC} is the exchange-correlation energy, which contains the difference between the kinetic energies of the interacting and non-interacting systems and the non-classical electrostatic interaction energy. The separation of the $F[n]$ functional is done in this way, because the first two terms are simple to deal with, while the more complex effects are contained in the third part.

Treating each electron i separately, one obtains the Kohn-Sham (KS) equations:

$$-\frac{\hbar^2}{2m}\nabla^2\psi_i(\mathbf{r}) + V_{\mathrm{eff}}(\mathbf{r})\psi_i(\mathbf{r}) = \epsilon_i\psi_i(\mathbf{r}). \tag{2.1.10}$$

Energies ϵ_i are the Lagrange multipliers of the problem and are called KS energies and ψ_i orbitals are referred to as KS orbitals. It should be noted that the KS energies are not the energies of the real electrons and the KS orbitals are not their wavefunctions. These are only the parameters used to find the ground state of the system. For N orbitals with the lowest energy, the electronic density can be expressed as:

$$n(\mathbf{r}) = \sum_{i=1}^{N} |\psi_i(\mathbf{r})|^2. \tag{2.1.11}$$

For an interacting system the effective potential V_{eff} can be divided in three parts: the part coming from the interactions with nuclei, $v(\mathbf{r})$, the part describing the Coulomb interaction between electrons and the exchange-correlation part, μ_{XC}. Equation (2.1.10) can be written as:

$$\left\{-\frac{\hbar^2}{2m}\nabla^2 + v(\mathbf{r}) + \mathrm{d}\mathbf{r}'\,\frac{n(\mathbf{r}')}{|\mathbf{r}-\mathbf{r}'|} + \mu_{\mathrm{XC}}(n)\right\}\psi_i(\mathbf{r}) = \epsilon_i\psi_i(\mathbf{r}), \tag{2.1.12}$$

with

$$\mu_{\mathrm{XC}}(n) = \frac{\delta E_{\mathrm{XC}}}{\delta n(\mathbf{r})}. \tag{2.1.13}$$

The $E_{\mathrm{XC}}[n]$ functional is, however, known exactly only for the free electron gas, while in other cases, approximations need to be made. The choice of this approximation will decide in large part the accuracy of the method. In general $E_{\mathrm{XC}}[n]$ is expressed as:

$$E_{\mathrm{XC}}[n] = \int \mathrm{d}\mathbf{r}\, e_{\mathrm{XC}}(\mathbf{r}, [n(\mathbf{r}')])n(\mathbf{r}), \tag{2.1.14}$$

where $e_{\mathrm{XC}}(\mathbf{r}, [n(\mathbf{r}')])$ represents the exchange-correlation energy in the point of space $\mathbf{r}$, per particle. In this work, two approximations of the exchange-correlation energy are used, the LDA (Local Density Approximation) and the GGA (General Gradient Approximation).

2.1.5 Exchange-correlation functionals

2.1.5.1 Local density approximation

LDA is the simplest approximation of the exchange-correlation interaction functional, in which we use the energy dependence on the density is calculated as in the uniform electron gas:

$$E_{\mathrm{XC}}^{\mathrm{LDA}}[n] \simeq \int \mathrm{d}\mathbf{r}\, e_{\mathrm{XC}}[n(\mathbf{r})] n(\mathbf{r}), \tag{2.1.15}$$

where e_{XC} is the exchange-correlation energy per unit volume, per particle, calculated for a homogeneous electron gas with the $n(\mathbf{r})$ density. In the local density approximation the exchange part is given explicitly:

$$e_{\mathrm{X}}^{\mathrm{hom}} = -\frac{3}{4}\left(\frac{3}{\pi}\right)^{1/3} n^{4/3}, \tag{2.1.16}$$

in atomic units. The correlation part can be estimated using Monte Carlo methods, as it has been done e.g. by Wigner [92] or Ceperley and Alder [93].

LDA is a good approximation in systems where the electronic density does not vary much, which is usually not true for molecular and ionic systems. Nevertheless, in many systems LDA can still provide satisfactory results. A well-known problem of this approximation, however, is that it overestimates binding energies and underestimates bond lengths [94].

2.1.5.2 Generalized gradient approximation

The generalized gradient approximation is an improvement of the LDA. In this approach, the exchange-correlation energy is not only based on the electronic density, but also on its gradient $|\nabla n(\mathbf{r})|$. The exchange-correlation functional in the GGA is given by:

$$E_{\mathrm{XC}}^{\mathrm{GGA}} = \int \mathrm{d}\mathbf{r}\, e_{\mathrm{X}}^{\mathrm{hom}}[n(\mathbf{r})] F_{\mathrm{XC}}[n(\mathbf{r}), |\nabla n(\mathbf{r})|] n(\mathbf{r}), \tag{2.1.17}$$

where $e_{\mathrm{X}}^{\mathrm{hom}}$ is the exchange energy of a homogeneous electron gas, given in Eq. (2.1.16) and F_{XC} is a dimensionless function. Numerous formulations of F_{XC} exist, among which the ones

provided by Perdew, Burke and Ernzerhof (PBE) [95] and Perdew and Wang (PW91) [96] are the most used for solid systems. In this work we used the PBE formulation.

2.1.6 DFT+U

Even though standard DFT provides satisfactory results for a wide range of systems, it is known to fail to describe some classes of materials, such as actinide oxides, containing strongly correlated electrons, localized close to nuclei. In order to model properties of such materials, methods beyond DFT are necessary. Several methods can be used to improve the description of strongly correlated electrons, such as DFT+U [97], Self-interaction correction (SIC) [98], hybrid functionals [99] and the combination of DFT and DFT+DMFT (dynamic mean field theory) [100]. In this study we use the DFT+U method to model uranium oxide since it yields good results for bulk UO_2 and is the only method currently tractable for systems containing defects.

DFT+U is a correction that can be applied to standard DFT functionals, LDA and GGA. In this method, a Hubbard-like term E_{Hub} is added to the energy of the correlated electrons to describe their enhanced interactions. This term is related to two types of interactions, the Coulomb interaction, represented by a parameter U and exchange interaction, represented by a parameter J. The energy in DFT+U consists of three terms:

$$E_{\mathrm{DFT}+U} = E_{\mathrm{DFT}} + E_{\mathrm{Hub}} - E_{\mathrm{DC}}, \tag{2.1.18}$$

where E_{DC} is a double counting term, related to the fact that a part of the correlation energy is already included in the energy calculated in LDA or GGA. The Hubbard-like term E_{Hub} can be expressed in several ways. The most used methods are those proposed by Liechtenstein *et al.* [101], in which the U and J parameters are considered separately, and Dudarev *et al.* [97], in which only the difference $U - J$ is considered. In this study we use the Liechtenstein scheme of the DFT+U method.

2.1.7 Modeling of solids

2.1.7.1 Bloch's theorem

For the simulation of crystalline structures, an infinite material can be replaced by a finite cell repeated periodically. In the corresponding system, the potential sensed by the electrons is

periodic as well. We have, therefore, $U(\mathbf{r}) = U(\mathbf{r}+\mathbf{R})$, where $\mathbf{R}$ is a Bravais lattice vector, being a multiplication of the unitary vectors of the system, $\mathbf{a}_1$, $\mathbf{a}_2$ and $\mathbf{a}_3$,

$$\mathbf{R} = x_1\mathbf{a}_1 + x_2\mathbf{a}_2 + x_3\mathbf{a}_3, \quad (x \in \mathbb{Z}). \tag{2.1.19}$$

According to the Bloch's theorem, the wavefunction $\psi_{n\mathbf{k}}$ of an electron moving in such a periodic potential can be written as a product of a wavelike part $\exp(i\mathbf{k}\cdot\mathbf{r})$ and a lattice periodic part $u_{n\mathbf{k}}(\mathbf{r})$,

$$\psi_{n\mathbf{k}}(\mathbf{r}) = \exp(i\mathbf{k}\cdot\mathbf{r})u_{n\mathbf{k}}(\mathbf{r}), \tag{2.1.20}$$

where n is the band index and $\mathbf{k}$ is a vector of the reciprocal space. The $\mathbf{k}$ vectors are related to the unitary vectors of the reciprocal space $\mathbf{b}_1$, $\mathbf{b}_2$ and $\mathbf{b}_3$ through the relation:

$$\mathbf{k} = y_1\mathbf{b}_1 + y_2\mathbf{b}_2 + y_3\mathbf{b}_3, \quad (y \in \mathbb{R}). \tag{2.1.21}$$

The unitary vectors of the real and reciprocal lattices are related by $\mathbf{a}_i \cdot \mathbf{b}_j = 2\pi\delta_{ij}$. The $\mathbf{k}$ vector is usually constrained to lie within the first Brillouin zone in the reciprocal space, hence the y_i factors are between -1 and 1.

Calculations of many important quantities such as the charge density or the total energy of a system consist of integration over the infinitely extended systems in the real space. This can be replaced by integrals over the finite first Brillouin zone in reciprocal space thanks to the Bloch's theorem. However, the sampling of $\mathbf{k}$-points within the Brillouin zone is crucial for the accuracy of the integration.

2.1.7.2 Plane waves

To determine the electronic wavefunctions numerically, a basis of functions must be chosen. One possibility is to use localized functions, such as Gaussian functions or atomic orbitals. The second choice are plane waves, which are mathematically simple and allow an easy computation of the forces acting on the ions. Additionally, errors caused by the incompleteness of the basis set can be easily reduced by adding more plane waves.

When the plane waves basis is chosen, $u_{n\mathbf{k}}(\mathbf{r})$ from Eq. (2.1.20) can be expanded in a Fourier series:

$$u_{n,\mathbf{k}}(\mathbf{r}) = \Omega^{-1/2}\sum_G c_{n\mathbf{G}} \exp(i\mathbf{G}\cdot\mathbf{r}), \tag{2.1.22}$$

where Ω is the cell volume, $\mathbf{G}$ is the lattice vector and $c_{\mathrm{n}\mathbf{G}}$ are the plane wave coefficients.

The summation in Eq. (2.1.22) goes over all reciprocal space vectors. However, in practice, only a certain number of **G** can be treated. For computational purposes, a limit on the maximal kinetic energy corresponding to the free particle with the wavevector **G** is chosen. This maximal energy is called the cut-off energy. Every vector **G** taken into account in calculations must fulfill the condition

$$\frac{\hbar^2 \left|\mathbf{k}+\mathbf{G}\right|^2}{2m} < E_{\mathrm{cut}}. \tag{2.1.23}$$

Plane wave basis sets are widely used in electronic structure calculations of solids. Nevertheless, when using a reasonable cut-off energy, they fail to describe the strong oscillations of the wave functions near the nuclei. There are several ways to overcome the problem of description of these oscillations. We present here the two main methods, the pseudopotential and projector augmented-wave (PAW) methods.

2.1.7.3 Pseudopotentials

The idea of the pseudopotential method is to get rid of the oscillations of the wavefunction in the region close to nuclei, while keeping a correct description of the valence electrons in all other regions of space. This can be done by smoothing the Coulomb potential up to a certain radius, called cut-off radius. The relation between the all-electron wavefunction and the pseudo wavefunction obtained using the pseudopotential method is presented in Fig. 2.1. Since the resulting pseudo wavefunction has no oscillations, it can be easily described using a reasonable number of plane waves.

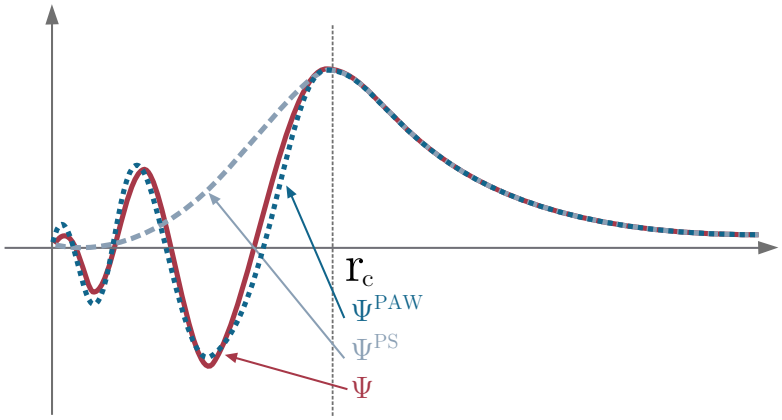

Figure 2.1: *Representation of a wavefunction and its description in pseudopotentials (PS) and PAW methods.*

The pseudopotential method can provide a good description of various materials properties. However, in many cases a higher accuracy is needed. To obtain a precision very close to that

obtained when considering all the electrons of the system, while keeping the simplicity of the pseudopotential method, the projector augmented-wave (PAW) method [102–105] can be used.

2.1.7.4 Projector augmented-wave method

The PAW method combines the pseudopotential and linear augmented-plane-wave methods (LAPW) approaches. In the PAW method the all-electron (AE) wavefunctions Ψ_{nk}, with n and k indexes corresponding to bands and **k**-points, respectively, are obtained from pseudo (PS) wavefunctions, thanks to a linear transformation:

$$\Psi_{nk}(\mathbf{r}) = \tilde{\Psi}_{nk}(\mathbf{r}) + \sum_i \left(\phi_i(\mathbf{r}) - \tilde{\phi}_i(\mathbf{r})\right) \langle \tilde{p}_i | \tilde{\Psi}_{nk} \rangle. \tag{2.1.24}$$

The index i stands for the atomic position $\mathbf{R}$, the angular momentum (l, m) and an additional index n to distinguish different partial waves for the same site and angular momentum. The AE ϕ_i and PS $\tilde{\phi}_i$ partial waves are equal outside an atom centered PAW augmentation region.

Eq. (2.1.24) can be represented schematically as in Fig. 2.2. The all-electron wavefunction is relatively smooth in the inter-atomic region (in gray) and it oscillates around the atoms (in pink). It can be hence decomposed as a sum of a smooth pseudo wavefunction occupying the whole space and all-electron partial waves localized in the PAW augmentation region. The third term, the contribution of pseudo partial waves is removed so that there is no double counting in the atomic region.

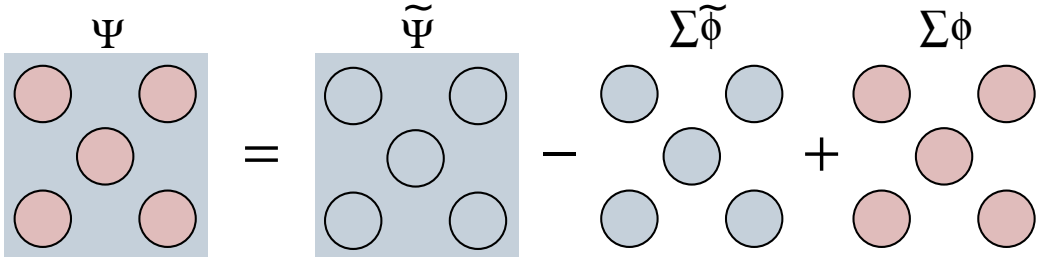

Figure 2.2: *Schematic representation of the PAW method.*

Starting from Eq. (2.1.24) one can show that the total charge density of the electrons can be rewritten as:

$$n(\mathbf{r}) = \tilde{n}(\mathbf{r}) + n^1(\mathbf{r}) - \tilde{n}^1(\mathbf{r}) + n_c(\mathbf{r}), \tag{2.1.25}$$

with n_c being the density of the frozen-core electrons which is kept constant and equal to the

core density of the isolated atom and

$$\begin{cases} \tilde{n}(\mathbf{r}) &= \sum_{nk} f_{nk} \langle \tilde{\Psi}_{nk} \mid \mathbf{r} \rangle \langle \mathbf{r} \mid \tilde{\Psi}_{nk} \rangle \\ n^1(\mathbf{r}) &= \sum_{ij} \rho_{ij} \langle \phi_i \mid \mathbf{r} \rangle \langle \mathbf{r} \mid \phi_j \rangle \\ \tilde{n}^1(\mathbf{r}) &= \sum_{ij} \rho_{ij} \langle \tilde{\phi}_i \mid \mathbf{r} \rangle \langle \mathbf{r} \mid \tilde{\phi}_j \rangle. \end{cases} \tag{2.1.26}$$

In the above, f_{nk} are the occupation factors of the Kohn-Sham wave functions while ρ_{ij} is defined as:

$$\rho_{ij} = \sum_{nk} f_{nk} \langle \tilde{\Psi}_{nk} \mid \tilde{p}_i \rangle \langle \tilde{p}_j \mid \tilde{\Psi}_{nk} \rangle. \tag{2.1.27}$$

From the decomposition of the density given in Eq. (2.1.25) it is possible to write the total energy as a sum of pseudo $\tilde{E}$, partial all-electron E^1 and partial pseudo $\tilde{E}^1$ contributions (the different terms are detailed in Ref. [105]):

$$E = \tilde{E} + E^1 - \tilde{E}^1. \tag{2.1.28}$$

The relation between the all-electron wavefunction and the wavefunction obtained using the PAW method is presented in Fig.2.1. As presented in the figure, the PAW method yields a much better description of the wavefunction that the pseudopotential method.

2.1.7.5 Supercells

To model an infinite material, unitary cells containing one or a few atoms are periodically repeated in the three dimensions of space, as shown in Fig. 2.3a. If a defect is introduced into the unitary cell, it will interact with its images in the repeated cells, leading to errors in the calculations. To minimize this interaction, unitary cells with relatively large numbers of atoms, called supercells, are used. The supercells method is presented in Fig. 2.3. The first image shows a perfect lattice obtained by repeating a unitary cell containing one atom. The second image shows a 2×2 supercell containing a defect (presented in red) and its images (in pink). The third image represents a 4×4 supercell containing a defect. It can be seen that increasing the size of the supercell increases the distance between the defect and its images and therefore minimizes the interactions. To obtain the most accurate calculations, very large supercells should be used,

however, the maximal number of atoms that can be taken into account is determined by the computational resources. The supercells used in the study of defects in silicon carbide and uranium dioxide in this work are presented in Fig. 2.4. We used a supercell containing 216 atomic sites to model defects in $3C$-SiC, 192 atomic sites in the case of $6H$-SiC and 96 atomic sites for UO_2.

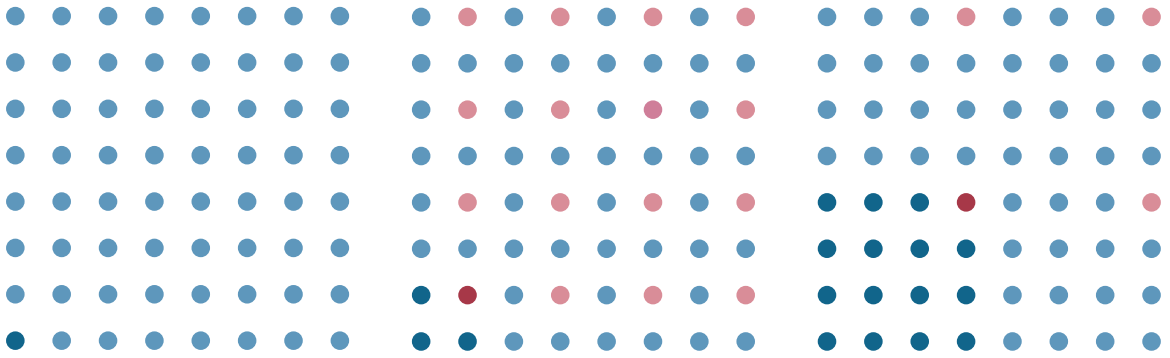

(a) Unitary cell *(b) 2×2 supercell with a defect* *(c) 4×4 supercell with a defect*

Figure 2.3: *Two-dimiensional scheme of the supercell method.*

2.2 Calculations of formation energies of charged defects

The charge of a defect determines if it can be detected by PAS. Positive vacancies should not be observed as they create a long-range repulsive Coulomb potential, which results in a small

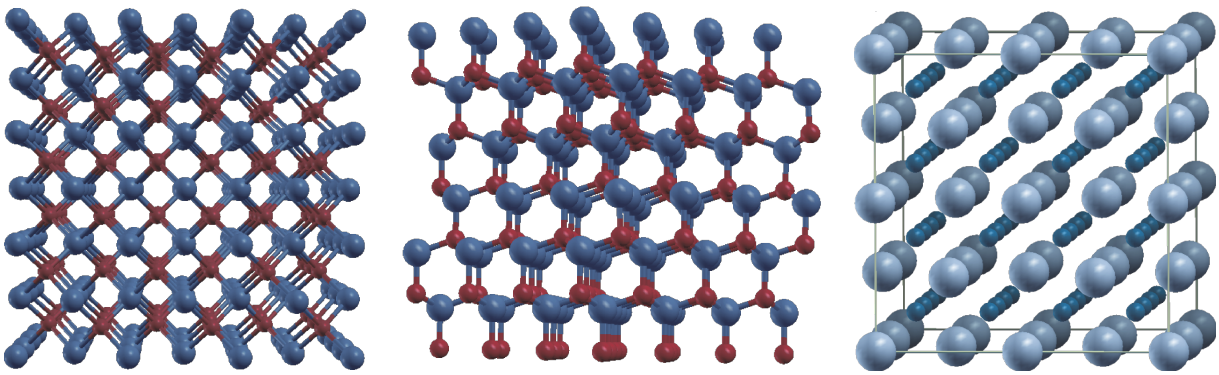

(a) 3C-SiC supercell *(b) 6H-SiC supercell* *(c) UO_2 supercell*

Figure 2.4: *Supercells used to model defects in this work. The 3C-SiC, 6H-SiC and UO_2 supercells contain 216, 192 and 96 atomic sites, respectively.*

positron trapping coefficient [44]. Negative and neutral vacancies, on the contrary, can be observed and distinguished as the trapping coefficient of the former decreases with temperature while it is constant for the latter. It is therefore important to consider the various possible charge states of each defect.

The basic equation describing the formation energy of a vacancy defect E_f reads [9]:

$$E_\mathrm{f}(V_\mathrm{X}, q) = E_\mathrm{tot}(V_\mathrm{X}, q) - \sum_i n_i \mu_i + q\mu_\mathrm{e}, \tag{2.2.1}$$

where $E_\mathrm{tot}(V_\mathrm{X}, q)$ is the total energy of the supercell, n_i is the number of atoms of the i type in the cell, μ_i is the chemical potentials of the i atom, q is the charge of the defect and μ_e is the electron chemical potential, which can vary from the bottom to the top of the band gap. Since the classical supercell approach fails in providing accurate formation energies for charged supercells, approximations need to be introduced to Eq. (2.2.1). Even if a large number of atoms is used in calculations, the defects cannot be considered as isolated because of the long range electrostatic interactions. Various schemes of energy correction were proposed [106–108]. The first correction that should be made is a simple electrostatic correction. The Madelung correction ΔE_el, which was proposed by Leslie and Gillan [106], can be added to the formation energy. This correction is expressed as:

$$\Delta E_\mathrm{el} = \frac{\alpha q^2}{2\epsilon_0 L}, \tag{2.2.2}$$

where α is the Madelung lattice constant, ϵ is the static dielectric constant and L is the length of the supercell edge. ΔE_el tends to overestimate the correction, as it takes into account only the monopole term of the electrostatic interaction. An improved scheme proposed by Lany and Zunger [107], which contains only 2/3 of the Madelung term, along with a potential alignment ΔV, can be also used. The potential alignment is related to the fact that the electronic states can be shifted in a cell containing a defect compared to a perfect system. Several methods of calculating the potential alignment exist. In this study we use a method proposed by Taylor and Bruneval [108], taking

$$\Delta V = \langle v_\mathrm{KS}^\mathrm{bulk} \rangle - \langle v_\mathrm{KS}^\mathrm{defect} \rangle. \tag{2.2.3}$$

$\langle v_\mathrm{KS}^\mathrm{bulk} \rangle$ and $\langle v_\mathrm{KS}^\mathrm{defect} \rangle$ are the average Kohn-Sham potentials calculated for the cell without and with the defect, respectively.

2.3 Two component density functional theory

In order to calculate the characteristics of the positron annihilation in a solid, one needs to determine the electronic and positronic densities and wavefunctions in the considered system. These quantities can be computed in the two component density functional theory (TCDFT) [44, 109, 110], which is a generalization of the density functional theory.

The total energy in TCDFT can be written in a similar way as in DFT,

$$\begin{aligned} E[n^+, n^-] = E[n^+] + E[n^-] + \int \mathrm{d}\mathbf{r}\, V_{\mathrm{ext}}(\mathbf{r})[n^-(\mathbf{r}) - n^+(\mathbf{r})] \\ - \int \mathrm{d}\mathbf{r} \int \mathrm{d}\mathbf{r}'\, \frac{n^-(\mathbf{r})n^+(\mathbf{r})}{|\mathbf{r}-\mathbf{r}'|} + E_{\mathrm{c}}^{\mathrm{e-p}}[n^+, n^-], \end{aligned} \tag{2.3.1}$$

where $E[n^+]$ and $E[n^-]$ are the one-component functionals for positron and electrons, V_{ext} is an external potential, the fourth term correspond to the Hartree interaction and $E_{\mathrm{c}}^{\mathrm{e-p}}$ is an electron-positron correlation functional. Various approximations can be made for the $E_{\mathrm{c}}^{\mathrm{e-p}}$ term leading to several calculation schemes which will be described in Sec. 2.3.2. It is worth noting that in the above expression both electron and positron densities are positive, while the signs of the external potential acting on the positron and of the electron-positron Hartree interaction are negative.

2.3.1 Momentum distribution and positron lifetime

The two positron annihilation characteristics usually measured experimentally, the positron lifetime and the momentum distribution of the annihilating electron-positron pair (see Sec. 1.2) can be calculated using the positron and electron densities and wavefunctions yielded by TCDFT. The momentum distribution can be expressed as [44]:

$$\rho(\mathbf{p}) = \pi r_e^2 c \sum_i \left| \int \mathrm{d}\mathbf{r}\, e^{-i\mathbf{p}\cdot\mathbf{r}} \Psi_i^{\text{e-p}}(\mathbf{r}) \right|^2, \tag{2.3.2}$$

where $\Psi_i^{\text{e-p}}$ is the two-particle wavefunction in the state i and $\mathbf{p}$ is a given momentum, r_{e} is the classical electron radius and c is the speed of light. If we consider that the electron and positron are independent (independent particle model, IPM) we can rewrite $\Psi_i^{\text{e-p}}$ as a product of the electronic and positronic wavefunctions:

$$\Psi_i^{\text{e-p}} = \Psi^+(\mathbf{r})\Psi_i^-(\mathbf{r}). \tag{2.3.3}$$

To take into account the correlation effects between the electrons and the positron, one can introduce the position-dependent enhancement factor $\sqrt{g(n^-, n^+)}$ [111], corresponding to the increase in annihilation due to the short-range screening of the positron by the electrons. It is worth noting that often, an enhancement factor that depends only on the electronic density is considered and expressed as $\sqrt{\gamma(n^-)}$. However, in this study, we will also use the enhancement factors depending on both the electron and positron densities. Including the enhancement factor leads to the expression

$$\rho(\mathbf{p}) = \pi r_e^2 c \sum_{ij} \left| \int \mathrm{d}\mathbf{r}\, e^{-i\mathbf{p}\cdot\mathbf{r}} \Psi_i^+(\mathbf{r}) \Psi_j^-(\mathbf{r}) \sqrt{g(n^-, n^+)} \right|^2 \tag{2.3.4}$$

Since in the above expression the enhancement factor depends only on the position $\mathbf{r}$ (through densities) and not on the electronic state i, the corresponding method is called the *state-independent scheme*, or less often the *position-dependent scheme*.

The positron lifetime is calculated as the inverse of the total annihilation rate, which can be obtained by integrating $\rho(\mathbf{p})$ over the momenta:

$$\lambda = \frac{1}{\tau} = \frac{1}{(2\pi)^3} \int \mathrm{d}\mathbf{p}\, \rho(\mathbf{p}). \tag{2.3.5}$$

The annihilation rate can be also calculated using the electron and positron densities $n^-(\mathbf{r})$ and $n^+(\mathbf{r})$,

$$\lambda = \pi r_\mathrm{e}^2 c \int \mathrm{d}\mathbf{r}\, n^-(\mathbf{r}) n^+(\mathbf{r}) g(n^-, n^+). \tag{2.3.6}$$

The momentum distribution can be also calculated in the *state-dependent scheme* [112]. According to Makkonen *et al.* [113] the correlation effects in the state-independent scheme are overestimated, however, since the enhancement factor $\sqrt{\gamma(n^-(\mathbf{r}))}$ describes the distortion of the electron-positron wavefunction due to the short-range screening, while the wavefunction is distorted in the whole space. The state-dependent scheme, uses a constant enhancement factor γ_j for each electronic state described by the index j. In this method the momentum distribution is expressed as

$$\rho(\mathbf{p}) = \pi r_e^2 c \sum_{ij} \gamma_j \left| \int \mathrm{d}\mathbf{r}\, e^{-i\mathbf{p}\cdot\mathbf{r}} \Psi_i^+(\mathbf{r}) \Psi_j^-(\mathbf{r}) \right|^2, \tag{2.3.7}$$

where $\gamma_j = \lambda_j / \lambda_j^{\mathrm{IPM}}$. λ_j is the total annihilation rate calculated for the electronic state j,

$$\lambda_j = \pi r_\mathrm{e}^2 c \int \mathrm{d}\mathbf{r}\, n_j^-(\mathbf{r}) n^+(\mathbf{r}) \gamma(n^-(\mathbf{r})), \tag{2.3.8}$$

and λ_j^{IPM} is the annihilation rate calculated for the same state within the IPM, hence using $\gamma = 1$. When the formulation of the enhancement factor depending on both electron and positron densities ($g(n^-, n^+)$) is used, the above expression will be replaced by:

$$\lambda_j = \pi r_{\mathrm{e}}^2 c \int \mathrm{d}\mathbf{r}\, n_j^-(\mathbf{r}) n^+(\mathbf{r}) g(n^-, n^+), \tag{2.3.9}$$

Makkonen *et al.* [113] showed that the Doppler spectra calculated using the state-independent scheme are in slightly better agreement with the experimental measurements, while the state-dependent scheme overestimates the distribution for high momenta. However, they point out that when ratios of Doppler spectra to a reference spectrum are considered the state-dependent scheme yields better results. As the comparison with experiments is usually made using Doppler spectra ratios and parameters extracted from them, we decided to implement and use the state-dependent scheme only.

2.3.2 Calculation schemes

When determining the electrons and positron wavefunctions and densities, one can choose various formulations of the electron-positron correlation energy ($E_{\mathrm{c}}^{\mathrm{e-p}}$ in Eq. (2.3.1)) and make several assumptions. This leads to several calculations schemes. In all of them, the ground state electron density is first calculated using DFT. Taking into account this density, the potential $v^+(\mathbf{r})$ sensed by a positron is computed. The positron density can then be found by solving the Kohn-Sham equations, which in this case take form:

$$-\frac{\hbar^2}{2m}\nabla^2\psi_i^+(\mathbf{r}) + v^+(\mathbf{r})\psi_i^+(\mathbf{r}) = \epsilon_i^+\psi_i^+(\mathbf{r}). \tag{2.3.10}$$

Taking the positron ground state wavefunction $\psi^+(\mathbf{r})$, for which the lowest energy ϵ^+ is obtained, the positron density is found, according to

$$n^+(\mathbf{r}) = |\psi^+(\mathbf{r})|^2. \tag{2.3.11}$$

At this point, an approximation considering that the positron density is too small to affect the electronic density is sometimes made, leading to the simplest positron calculation scheme, called conventional (CONV). This assumption is well justified in the case of a delocalized positron in a perfect lattice. When this approximation is made, the calculation is stopped after one electronic and one positronic calculation step (see Fig. 2.5). In this method a LDA zero-positron density

limit of the electron-positron correlation functional parametrized for the positron density tending to zero (zero-positron-density limit) is used. This functional was parametrized by Boroński and Nieminen [110] using the data provided by Arponen and Pajanne [114]. Despite its simplicity, the conventional scheme works well in the cases of perfect crystals and has been widely used in studies of positrons localized in vacancies [58, 59, 63, 113, 115–118].

A second calculation scheme, using the same parametrization as in CONV, but in which the electron and positron densities are calculated self-consistently, was proposed by Gilgien, Galli, Gygi and Car [119] and is called GGGC.

A third scheme, called PSN, uses a full LDA electron-positron correlation functional provided by Puska, Seitsonen, and Nieminen [120] and an enhancement factor depending on both the electron and the positron densities. This scheme was based on the Boroński and Nieminen method [110]. The three positron calculation schemes, mentioned above are illustrated in Figure 2.5.

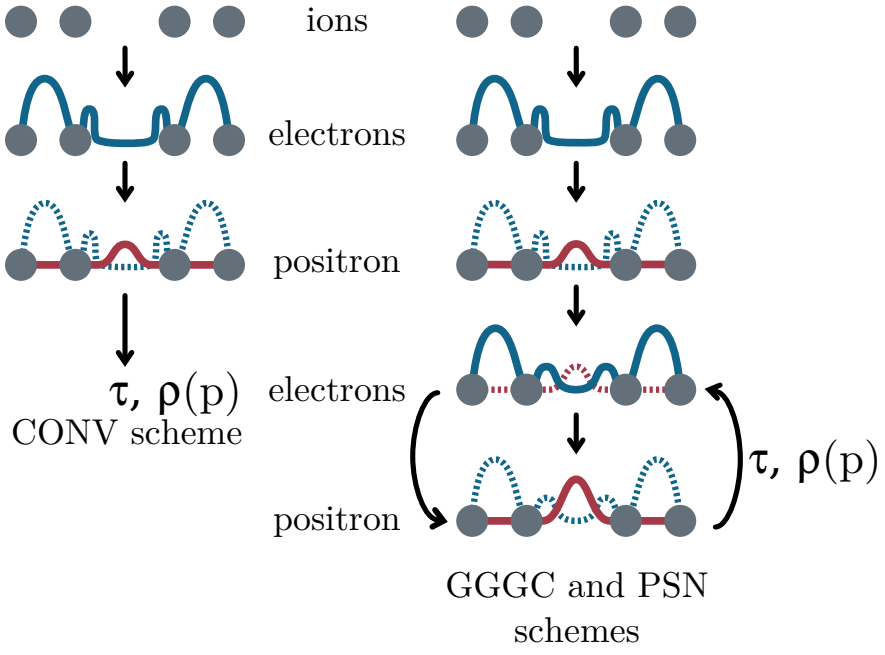

Figure 2.5: *Two-component calculation schemes. To the left, the CONV scheme, in which the electronic structure is first calculated, then the positronic one. After those two steps, the positron lifetime and Doppler broadening can be calculated. To the right PSN and GGGC schemes, in which several repetitions of the electronic and positronic steps are made until convergence on the densities is reached.*

2.3.2.1 Enhancement factors in the GGGC scheme

Various expressions for the enhancement factor γ are used in the GGGC and the PSN schemes, which can strongly affect the calculated positron lifetime. In GGGC, the formula proposed by Boroński and Nieminen [110], for a zero-positron-density limit, is used. It is based on the interpolation of many-body calculations by Arponen and Pajanne [114] and takes the form:

$$\gamma(n^-) = \pi c r_0^2 n \left[1 + 1.23 r_\mathrm{s} + 0.8295 r_\mathrm{s}^{3/2} - 1.26 r_\mathrm{s}^2 + 0.3286 r_\mathrm{s}^{5/2} + \frac{1}{6} r_\mathrm{s}^3\right], \tag{2.3.12}$$

where r_s is a density parameter equal to the radius of a sphere containing one electron:

$$\frac{4}{3}\pi r_\mathrm{s}^3 n^- = 1, \tag{2.3.13}$$

for a electronic density n^-.

2.3.2.2 Enhancement factors in the PSN scheme

In the PSN scheme the expression for the enhancement factor proposed by Puska, Seitsonen and Nieminen [120] is used. The form of the positron lifetime is the one proposed by Boroński and Nieminen [110],

$$\frac{1}{\tau} = \pi r_\mathrm{e}^2 \int \mathrm{d}\mathbf{r}\; n^+(\mathbf{r}) n(\mathbf{r}) g(0; n^+, n), \tag{2.3.14}$$

where $g(0; n^+, n)$ replaces the enhancement factor γ and is the electron-positron pair correlation function at the origin. The form of this factor was obtained by fitting Lantto's results of hypernetted-chain calculations of the pair-correlation functions [121], quoted by Boroński and Nieminen [110], while using the interpolating functional:

$$g(0; n^+, n) = a(n_>) n_<^3 + b(n_>) n_<^2 + c(n_>) n_< + g_0(n_>), \tag{2.3.15}$$

where $n_>$ ($n_<$) stands for the positron or electron density, depending on which is larger (smaller). The parametrizing functions $a(n)$, $b(n)$ and $c(n)$ are expressed as:

$$a(n) = \frac{1}{n^3}\left[2k(n) - 6g_1(n) + 8g_2(n) - 2g_0(n)\right], \tag{2.3.16}$$

$$b(n) = \frac{1}{n^2}\left[-3k(n) + 11g_1(n) - 16g_2(n) + 5g_0(n)\right] \tag{2.3.17}$$

and

$$c(n) = \frac{1}{n}\left[k(n) - 4g_1(n) + 8g_2(n) - 4g_0(n)\right]. \tag{2.3.18}$$

The $g_0(r_s)$, $g_1(r_s)$ and $g_2(r_s)$ are the functions interpolating and extrapolating the data obtained by Lantto in the hypernetted-chain approximation of many-body theory,

$$g_0(r_s) = 1 + 1.2300r_s + 0.9889r_s^{3/2} - 1.4820r_s^2 + 0.3956r_s^{5/2} + \frac{1}{6}r_s^3, \tag{2.3.19}$$

$$g_1(r_s) = 1 + 2.0286r_s - 3.3892r_s^{3/2} - 3.0547r_s^2 - 1.0540r_s^{5/2} + \frac{1}{6}r_s^3 \tag{2.3.20}$$

and

$$g_2(r_s) = 1 + 0.2499r_s + 0.2949r_s^{3/2} + 0.6944r_s^2 - 0.5339r_s^{5/2} + \frac{1}{6}r_s^3, \tag{2.3.21}$$

with

$$\frac{4}{3}\pi r_{\mathrm{s}}^3 n = 1. \tag{2.3.22}$$

2.3.2.3 Ways of correcting the imperfect screening of the positron in semiconductor and insulators

The enhancement factor γ or g is used to take into account the increase in the electron density at a positron site due to the screening of the positron by electrons. However, the positron calculation schemes were first developed to model metallic materials and they assume a perfect screening of the positron by the electrons. In semiconductors and insulators corrections have to be used to take into account the existence of the gap in the electronic states. Two types of corrections are available: A semiconductor correction (SC) can be implemented in the enhancement factor as proposed by Puska [122]. Alternatively, a gradient correction (GC) proposed by Barbiellini *et al.* [60] can be implemented in both the enhancement factor and the electron-positron correlation energy. It is worth noting that the gradient correction can be applied not only for semiconductors, but also other materials in which the description of the positron is difficult, for instance in alkali metals.

Semiconductor correction

In order to take into account the increase in the enhancement factor due to the screening of the positron by electrons, a semiempirical model was proposed by Puska *et al.* [57]:

$$\gamma(n_-) = \pi r_{\mathrm{e}}^2 cn\left[1 + 1.23r_{\mathrm{s}} + 0.8295r_{\mathrm{s}}^{3/2} - 1.26r_{\mathrm{s}}^2 + 0.3286r_{\mathrm{s}}^{5/2} + \frac{1}{6}(1 - 1/\epsilon_\infty)r_{\mathrm{s}}^3\right], \tag{2.3.23}$$

where ϵ_∞ is the dielectric constant of the considered material.

The semiconductor correction in the PSN scheme was not available. For the purpose of the study on silicon carbide we implemented it in the PSN method, as presented in Sec. 3.1.2.

Gradient correction

Another way of correcting the enhancement factor was proposed by Barbiellini *et al.* [60, 123]. This method is called the gradient correction (GC) and introduces

$$\gamma_{\mathrm{GGA}} = 1 + (\gamma_{\mathrm{LDA}} - 1)e^{-\alpha\epsilon}, \tag{2.3.24}$$

where γ_{GGA} and γ_{LDA} are the GGA and LDA formulations of the enhancement factor, respectively, ϵ is a parameter chosen to best reproduce lattice lifetimes of various materials and $\epsilon = |\nabla \ln n|^2/q_{\mathrm{TF}}^2$, with $1/q_{\mathrm{TF}}^2$ is the local Thomas-Fermi screening length.

2.3.2.4 Other formulations of the enhancement factor

Several other formulations of the enhancement factor, aiming at improving the prediction of the positron lifetimes, have been also proposed. Stachowiak and Lach [124] suggested a LDA form of γ within perturbed the hypernetted-chain approximation (called PHCLDA):

$$\gamma_{\mathrm{PHCLDA}} = 1 + 1.23r_{\mathrm{s}} - 0.137r_{\mathrm{s}}^2 + \frac{1}{6}r_{\mathrm{s}}^3. \tag{2.3.25}$$

Boroński [125] proposed a GGA version of the PHC enhancement factor:

$$\gamma_{\mathrm{PHCGGA}} = 1 + (\gamma_{\mathrm{PHCLDA}} - 1)e^{-\alpha\epsilon}, \tag{2.3.26}$$

with $\alpha = 0.10$. Kuriplach and Barbiellini [126] suggested LDA and GGA forms of the enhancement factor, based on a fit to quantum Monte Carlo data obtained by Drummond *et al.* [127]:

$$\gamma_{\mathrm{QMCLDA}} = 1 + 1.23r_{\mathrm{s}} - 0.22r_{\mathrm{s}}^2 + \frac{1}{6}r_{\mathrm{s}}^3 \tag{2.3.27}$$

and

$$\gamma_{\mathrm{QMCGGA}} = 1 + (\gamma_{\mathrm{QMCLDA}} - 1)e^{-\alpha\epsilon}, \tag{2.3.28}$$

with $\alpha = 0.05$. The assessment of the positron lifetimes obtained using various forms of the enhancement factor has been presented by Kuriplach and Barbiellini in Ref. [126] and Zhang

et al. in Ref. [128]. According to Kuriplach and Barbiellini, even though the use of PHCGGA and QMCGGA methods improves the description of the positron annihilation, it is difficult to decide which one should be used and additional precise experiments should be performed to help solving the matter.

2.4 TCDFT implementation in ABINIT

In the present study we use the two-component density functional theory implementation available in the ABINIT package [129]. In this section we briefly present the ABINIT project and the practical implementation of the TCDFT in the code, in particular within the projector augmented-wave method.

2.4.1 ABINIT

ABINIT [129–131] is an open-source package allowing one to find the total energy, charge density and electronic structure of systems made of electrons and nuclei within the density functional theory. It uses pseudopotentials and a planewave or wavelet basis. ABINIT also allows geometry optimizations according to the DFT forces and stresses and to perform molecular dynamics simulations using these forces. ABINIT is distributed under GNU General Public Licence (GPL) and can be freely used, modified and distributed, hence the developments made in the present study are also available for other groups studying positron annihilation in materials.

2.4.2 Self-consistency

In practice the TCDFT in ABINIT is implemented as a double loop on the electronic and positronic densities: during each subloop, one of the two densities (and Hamiltonians) is kept constant while the other is being converged (see Fig. 2.6). If the CONV scheme is performed (e.g. for perfect lattice) the calculation is stopped after two subloops, one electronic and one positronic, and the positron lifetime and momentum distribution are calculated. If a self consistent scheme is used, the electronic and positronic steps are repeated until the convergence criterion is reached. Additionally, the forces acting on atoms, including contributions from the electrons and the positron, can be calculated and the calculation continued for the new atomic configuration. To decrease the computational time when atomic relaxation is performed, each

new ionic step can be started with an electronic calculation taking into account the potential due to the positron from the last calculation, which can help to decrease significantly the number of iterations.

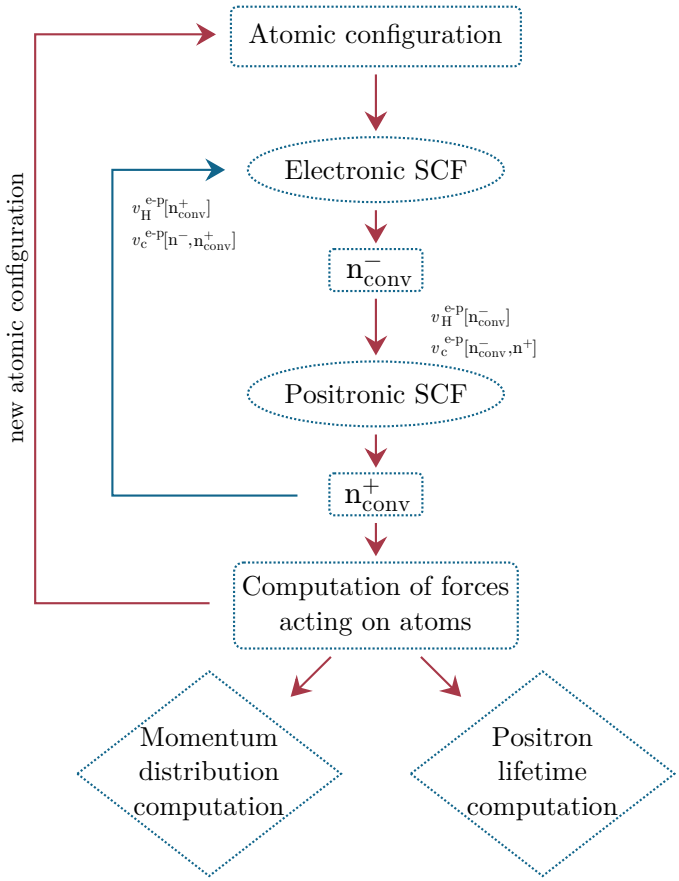

Figure 2.6: *Illustration of the fully self-consistent two-component density functional theory calculations in* ABINIT. n^-_{conv} *and* n^+_{conv} *refer to converged electronic and positronic densities, respectively.*

2.4.3 TCDFT in the PAW formalism

The TCDFT method has been implemented in ABINIT in a unified formalism for the positron and the electrons: the wavefunctions of the electrons and the positron in the system are expressed on the same mixed PAW basis set (planewaves and atomic orbitals). The choice to use the PAW formalism to represent both the positronic and electronic wavefunctions and densities allows one to, for example, use techniques able to treat strongly-correlated system (DFT+U) and to calculate energies and forces of the positron-electron system self-consistently. Additionally, this implementation results in calculations that can be performed as a single run, using the same dataset for electrons and a positron. On the other hand, it needs to be kept in mind that the

standard PAW datasets are not always suited for the description of the positron wavefunction. The corresponding issues are addressed in Sec. 3.2.1.3.

In order to be able to calculate the positron lifetimes and the Doppler spectra using the PAW method, the expression for the energy of an interacting electrons-positron system, the positron lifetime and the momentum distribution (Eq. (2.3.1), Eq. (2.3.2) and (2.3.6), respectively) had to be rewritten in this formalism. Some of the main equations of the PAW method have been presented in Sec. 2.1.7.4. We will also use notations introduced in Ref. [105]. The formulations for the energies and positron lifetime will be presented below, while the development of the expression for the momentum distribution, will be presented in Sec. 3.2.1.

2.4.3.1 Energies

First, the expressions for the total energy of a system containing electrons and a positron will be written within the PAW formalism. The conventions used in Ref. [105] are used in the following. We can introduce superscripts '$-$' and '$+$' in order to refer to the electron- and positron-related quantities. The energy then consists of three parts: one coming from the valence electrons and the ions E^-, one related to the positron E^+ and one to the electron-positron interactions E^{+-},

$$E = E^- + E^+ + E^{+-}. \tag{2.4.1}$$

E^- has the same expression as in Sec. 2.1.7.4 or in Sec. 2.3 in Ref. [105]. The contribution to total energy coming from the positron can be similarly divided into three parts:

$$E^+ = \tilde{E}^+ + E^{1+} - \tilde{E}^{1+}, \tag{2.4.2}$$

where

$$\begin{cases} \tilde{E}^+ &= \langle\tilde{\Psi}^+| - \frac{\Delta}{2}|\tilde{\Psi}^+\rangle - \int \mathrm{d}\mathbf{r}\, v_{\mathrm{H}}[\tilde{n}_{Zc}](\tilde{n}^+ + \hat{n}^+) \\ E^{1+} &= \sum_{ij} \rho^+_{ij}\langle\phi_i| - \frac{\Delta}{2}|\phi_j\rangle - \int_{\Omega_{\mathrm{R}}} \mathrm{d}\mathbf{r}\, v_{\mathrm{H}}[n_{Zc}](n^{1+}) \\ \tilde{E}^{1+} &= \sum_{ij} \rho^+_{ij}\langle\tilde{\phi}_i| - \frac{\Delta}{2}|\tilde{\phi}_j\rangle - \int_{\Omega_{\mathrm{R}}} \mathrm{d}\mathbf{r}\, v_{\mathrm{H}}[\tilde{n}_{Zc}](\tilde{n}^{1+} + \hat{n}^+) \end{cases} \tag{2.4.3}$$

The ρ^+_{ij} are the occupancies of each (i,j) channel, defined as $\rho^+_{ij} = \langle\tilde{\Psi}^+ \mid \tilde{p}_i\rangle\langle\tilde{p}_j \mid \tilde{\Psi}^+\rangle$ and v_{H} is the Hartree potential of the corresponding density. n_{Zc} and $\tilde{n}_{Zc}$ are the sums of the

nucleus and core electron charge densities and pseudized densities, respectively. $\hat{n}^+$ is the positron compensation charge density, which is added to soft charge densities $\tilde{n}^+$ and $\tilde{n}^{1+}$ to reproduce the correct multipole moment of the charge density, similarly to what is done for the electronic density [103]. In the above, the self-interaction correction as described by Boroński and Nieminen in Ref. [110] (Appendix B) is used. There is therefore no positron-positron Hartree and exchange-correlation interaction.

The last contribution to total energy, E^{+-}, which is due to interactions between the positron and the electrons, can also be divided into three parts:

$$E^{+-} = \tilde{E}^{+-} + E^{1+-} - \tilde{E}^{1+-}, \tag{2.4.4}$$

where

$$\begin{cases} \tilde{E}^{+-} &= -\int \mathrm{d}\mathbf{r}\, v_{\mathrm{H}}[\tilde{n}^- + \hat{n}^- + \tilde{n}_c](\tilde{n}^+ + \hat{n}^+) \\ &+ E_{\mathrm{c}}[(\tilde{n}^- + \hat{n}^- + \tilde{n}_c), (\tilde{n}^+ + \hat{n}^+)] \\ E^{1+-} &= -\int_{\Omega_{\mathrm{R}}} \mathrm{d}\mathbf{r}\, v_{\mathrm{H}}[n^{1-} + n_c](n^{1+}) \\ &+ E_{\mathrm{c}}[(n^{1-} + n_c), n^{1+}] \\ \tilde{E}^{1+-} &= -\int_{\Omega_{\mathrm{R}}} \mathrm{d}\mathbf{r}\, v_{\mathrm{H}}[\tilde{n}^{1-} + \hat{n}^- + \tilde{n}_c](\tilde{n}^{1+} + \hat{n}^+) \\ &+ E_{\mathrm{c}}[(\tilde{n}^{1-} + \hat{n}^- + n_c), (\tilde{n}^{1+} + \hat{n}^+)]. \end{cases} \tag{2.4.5}$$

2.4.3.2 Positron lifetime

The positron lifetime is calculated using positron and electron densities. One can hence represent it in the PAW formalism by introducing Eq. (2.1.25) into Eq. (2.3.6). In the following it is considered that the density of core electrons n_c is included in n^1 and the pseudo-density of core electrons $\tilde{n}_c$ in $\tilde{n}$ and $\tilde{n}^1$. Introducing the PAW formulations of the electron and positron densities, we obtain the expression:

$$\begin{aligned} \lambda &= \pi r_{\mathrm{e}}^2 c \int \mathrm{d}\mathbf{r} \Big([\tilde{n}^-(\mathbf{r}) + n^{1-}(\mathbf{r}) - \tilde{n}^{1-}(\mathbf{r})] \\ &* [\tilde{n}^+(\mathbf{r}) + n^{1+}(\mathbf{r}) - \tilde{n}^{1+}(\mathbf{r})] \\ &* g(\tilde{n}^- + n^{1-} - \tilde{n}^{1-}, \tilde{n}^+ + n^{1+} - \tilde{n}^{1+}) \Big). \end{aligned} \tag{2.4.6}$$

The integral in the above can be divided in two parts: the first over the augmentation region and the second outside it, leading to:

$$\begin{aligned}\lambda_{\mathbf{r}\in\Omega_\mathrm{R}} &= \pi r_\mathrm{e}^2 c \int_{\mathbf{r}\in\Omega_\mathrm{R}} \mathrm{d}\mathbf{r} \Big([\tilde{n^-}(\mathbf{r}) + n^{1-}(\mathbf{r}) - \tilde{n}^{1-}(\mathbf{r})] \\ &* \quad [\tilde{n}^+(\mathbf{r}) + n^{1+}(\mathbf{r}) - \tilde{n}^{1+}(\mathbf{r})] \\ &* \quad g(\tilde{n}^- + n^{1-} - \tilde{n}^{1-}, \tilde{n}^+ + n^{1+} - \tilde{n}^{1+}) \Big)\end{aligned} \tag{2.4.7}$$

and

$$\begin{aligned}\lambda_{\mathbf{r}\notin\Omega_\mathrm{R}} &= \pi r_\mathrm{e}^2 c \int_{\mathbf{r}\notin\Omega_\mathrm{R}} \mathrm{d}\mathbf{r} \Big([\tilde{n}^-(\mathbf{r}) + n^{1-}(\mathbf{r}) - \tilde{n}^{1-}(\mathbf{r})] \\ &* \quad [\tilde{n}^+(\mathbf{r}) + n^{1+}(\mathbf{r}) - \tilde{n}^{1+}(\mathbf{r})] \\ &* \quad g(\tilde{n}^- + n^{1-} - \tilde{n}^{1-}, \tilde{n}^+ + n^{1+} - \tilde{n}^{1+}) \Big).\end{aligned} \tag{2.4.8}$$

Inside the augmentation region, if the partial wave and plane-waves basis sets are complete, $\tilde{n} = \tilde{n}^1$ and $\tilde{n}^+ = \tilde{n}^{1+}$, which leads to:

$$\lambda_{\mathbf{r}\in\Omega_\mathrm{R}} = \pi r_\mathrm{e}^2 c \int_{\mathbf{r}\in\Omega_\mathrm{R}} \mathrm{d}\mathbf{r}\, n^{1-}(\mathbf{r}) n^{1+}(\mathbf{r}) g(n^{1-}, n^{1+}). \tag{2.4.9}$$

Outside the augmentation region $n^1 - \tilde{n}^1 = 0$ and $n^{1+} - \tilde{n}^{1+} = 0$, which leads to:

$$\lambda_{\mathbf{r}\notin\Omega_\mathrm{R}} = \pi r_\mathrm{e}^2 c \int_{\mathbf{r}\notin\Omega_\mathrm{R}} \mathrm{d}\mathbf{r}\, [\tilde{n}^-(\mathbf{r})(\mathbf{r})] \tilde{n}^+(\mathbf{r}) g(\tilde{n}^-, \tilde{n}^+). \tag{2.4.10}$$

Inside the augmentation region we can also write the subtraction of two equal integrals, which will allow us to simplify the expression for the annihilation rate:

$$\begin{aligned}&\int_{\mathbf{r}\in\Omega_\mathrm{R}} \mathrm{d}\mathbf{r}\, \tilde{n}^-(\mathbf{r}) \tilde{n}^+(\mathbf{r}) g(\tilde{n}^-, \tilde{n}^+) \\ &- \int_{\mathbf{r}\in\Omega_\mathrm{R}} \mathrm{d}\mathbf{r}\, \tilde{n}^{1-}(\mathbf{r}) \tilde{n}^{1+}(\mathbf{r}) g(\tilde{n}^{1-}, \tilde{n}^{1+}) = 0.\end{aligned} \tag{2.4.11}$$

By adding the two integrals from Eq. (2.4.11) to the decomposed λ from Eq. (2.4.9) and (2.4.10)

we obtain:

$$\begin{aligned}\lambda &= \pi r_e^2 c \left(\int_{\mathbf{r}\notin\Omega_R} \mathrm{d}\mathbf{r}\, \tilde{n}^-(\mathbf{r})\tilde{n}^+(\mathbf{r}) g(\tilde{n}^-,\tilde{n}^+) \right. \\ &+ \int_{\mathbf{r}\in\Omega_R} \mathrm{d}\mathbf{r}\, \tilde{n}^-(\mathbf{r})\tilde{n}^+(\mathbf{r}) g(\tilde{n}^-,\tilde{n}^+) \\ &+ \int_{\mathbf{r}\in\Omega_R} \mathrm{d}\mathbf{r}\, n^{1-}(\mathbf{r}) n^{1+}(\mathbf{r}) g(n^{1-},n^{1+}) \\ &- \left. \int_{\mathbf{r}\in\Omega_R} \mathrm{d}\mathbf{r}\, \tilde{n}^{1-}(\mathbf{r})\tilde{n}^{1+}(\mathbf{r}) g(\tilde{n}^{1-},\tilde{n}^{1+}) \right).\end{aligned} \tag{2.4.12}$$

We can put the first two integrals together and extend the intervals of the last two to the whole space, since they are equal to zero outside the augmentation region. This leads to the final expression for the annihilation rate decomposed in three terms:

$$\lambda = \tilde{\lambda} + \lambda^1 - \tilde{\lambda}^1, \tag{2.4.13}$$

where

$$\begin{cases} \tilde{\lambda} &= \pi r_e^2 c \int \mathrm{d}\mathbf{r}\, \tilde{n}^-(\mathbf{r})\tilde{n}^+(\mathbf{r}) g(\tilde{n}^-,\tilde{n}^+) \\ \lambda^1 &= \pi r_e^2 c \int_{\Omega_R} \mathrm{d}\mathbf{r}\, n^{1-}(\mathbf{r}) n^{1+}(\mathbf{r}) g(n^{1-},n^{1+}) \\ \tilde{\lambda}^1 &= \pi r_e^2 c \int_{\Omega_R} \mathrm{d}\mathbf{r}\, \tilde{n}^{1-}(\mathbf{r})\tilde{n}^{1+}(\mathbf{r}) g(\tilde{n}^{1-},\tilde{n}^{1+}). \end{cases} \tag{2.4.14}$$

It is worth noting that it is only possible to obtain the equation above if the partial waves and plane-waves basis are complete, which is an assumption usually made in the PAW formalism.

2.5 Conclusions

In this chapter we presented the methods that can be used to calculate the formation energies and positron annihilation characteristics of defects in solids. We briefly presented the density functional theory (DFT). We further described the calculation of the formation energies of defects and the two-component density functional theory (TCDFT), in the framework of which the positron annihilation features can be computed. Finally, the implementation of TCDFT in the ABINIT code was presented. As described in this chapter, in both density functional theory and two-component density functional theory, various approximations can be made and different functionals used. This implies that tests need to be performed to determine which methods are the most appropriate for the studied materials.

Chapter 3

Code tests and development

In this chapter we first present the methods that have been used in the positron lifetime calculations, the tests of the ABINIT implementation and the derivation of parameters that we will use in the further study. We then show the derivation of the equations allowing us to implement the momentum distribution calculations within the PAW formalism and present the way in which the equations have been implemented in the code. Finally, results of the tests of Doppler broadening calculation implementation are presented.

3.1 Calculations of positron lifetime

3.1.1 Test of the implementation of positron lifetime calculation in the PAW formalism in the ABINIT code

Positron lifetime calculation in the PAW method had been only recently implemented in the ABINIT code [129]. Therefore, we firstly needed to test this development. We chose to do it by comparing results on silicon with the ones obtained by Takenaka *et al.* [132], who used the all-electron full-potential linearized augmented plane wave method (FLAPW), the most accurate implementation of DFT available up to now. We decided to perform tests in similar conditions to those used by Takenaka *et al.* Therefore, we did not use the semiconductor correction and took the the experimental volume of Si. We used the same parametrization as in Reference [132], which is equivalent to our CONV scheme. The calculation was performed using a PAW

dataset for silicon with $2s$, $2p$, $3s$ and $3p$ valence states, hence with 12 valence electrons and we obtained a lifetime of 209 ps, which is close to the results of Takenaka *et al.* of 211 ps.

To test the case of a trapped state for the positron, we performed calculations for V_{Si} in bulk Si. Using the CONV scheme we obtained 217 ps for the silicon vacancy relaxed without the positron (8.3% inward relaxation in D_{2d} geometry) and 241 ps for the unrelaxed vacancy. Then we fully relaxed the defect in the GGGC scheme and found a lifetime of 271 ps. These results are consistent with those of Makkonen *et al.* [113, 115], who also used the PAW method to describe the electronic wavefunctions and densities (215 ps and 272 ps for the vacancy relaxed without and with the positron, respectively). The small differences between our results and those from the reference studies indicate that the positron lifetime calculation implementation in ABINIT is reliable.

In our calculations the same basis set is used for the description of both electron and positron wavefunctions. However, since the natures of the electron-ion and positron-ion interactions are different, the shapes of the corresponding wavefunctions are not the same. As a result, in some cases, the basis set used for the electron wavefunctions representation can be inappropriate for the positron distribution description. For example, the silicon PAW dataset with $3s$ and $3p$ valence states only can be successfully used for electronic structure calculations. Yet, using this PAW dataset, we calculated the lattice lifetime of bulk Si of 223 ps, which is much longer than the lifetime obtained with $2s$, $2p$, $3s$ and $3p$ valence states (209 ps). It indicates that the basis set with $3s$ and $3p$ valence states may not be complete enough to properly describe the positron wavefunction. We therefore performed another calculation using a PAW dataset treating 4 valence electrons, but containing additional $2s$ and $2p$ projectors. This yielded the same lattice lifetime as in the 12 valence electrons calculation. It means that the large lifetime discrepancy between cases with 4 and 12 valence electrons is due to the basis set incompleteness. This problem will be further discussed in Sec. 3.2.1.3.

3.1.2 Implementation of the semiconductor correction in the PSN scheme

For the purpose of the study on silicon carbide we implemented the semiconductor correction in the PSN scheme, in a similar way to what was done for the GGGC method (see Sec. 2.3.2.3). The expression for the enhancement factor in the PSN scheme was presented in Sec. 2.3.2.2. To take into account the semiconductor correction in the PSN scheme, we modified functions $g_0(n)$, $g_1(n)$ and $g_2(n)$ in Equations (2.3.19) to (2.3.21), in analogy to what was done in the $g(n)$

factor of CONV and GGGC. As a result, the interpolating functions occurring in the model of Puska *et al.*, now expressed as a function of r_s, take the form

$$g_0(r_s) = 1 + 1.2300r_s + 0.9889r_s^{3/2} - 1.4820r_s^2 + 0.3956r_s^{5/2} + \frac{1}{6}(1 - 1/\epsilon_\infty)r_s^3, \tag{3.1.1}$$

$$g_1(r_s) = 1 + 2.0286r_s - 3.3892r_s^{3/2} - 3.0547r_s^2 - 1.0540r_s^{5/2} + \frac{1}{6}(1 - 1/\epsilon_\infty)r_s^3 \tag{3.1.2}$$

and

$$g_2(r_s) = 1 + 0.2499r_s + 0.2949r_s^{3/2} + 0.6944r_s^2 - 0.5339r_s^{5/2} + \frac{1}{6}(1 - 1/\epsilon_\infty)r_s^3, \tag{3.1.3}$$

with

$$\frac{4}{3}\pi r_s^3 n = 1. \tag{3.1.4}$$

It has to be noted, that this modification is done only when the electron density is higher than the density of the positron, i.e. when it enters Eq. 2.3.15 as $n_>$. When the positron density is the larger one, the functions $g_0(n)$, $g_1(n)$ and $g_2(n)$ keep their original form with $1/\epsilon_\infty = 0$.

3.1.3 Implementation of the gradient correction in the PSN scheme

The gradient correction in the PSN scheme did not exist either in literature. For the purposes of this study, we decided to implement the gradient correction in the PSN method. Firstly, we implemented the correction, taking an adjustable parameter $\alpha = 0.22$, as proposed by Barbiellini *et al.* [60], in both the enhancement factor g and the correlation energy. However, the implementation of the gradient correction in the correlation energy led to some inconsistent results. Both Barbiellini *et al.* in Ref. [60] and Kuriplach *et al.* in their recent work [126] showed that the gradient correction has a significant influence on the enhancement factor while the positron density remains almost unaffected. We decided, therefore, to apply the gradient correction only on the g function in the PSN scheme, by taking

$$g_{\mathrm{GGA}}^{\mathrm{PSN}} = 1 + (g_{\mathrm{LDA}}^{\mathrm{PSN}} - 1)e^{-\alpha\epsilon}, \tag{3.1.5}$$

where ϵ is a parameter, $\epsilon = |\nabla \ln n|^2/q_{\mathrm{TF}}^2$, with $1/q_{\mathrm{TF}}^2$ being the local Thomas-Fermi screening length.

3.1.4 Parameters of positron lifetime calculations

3.1.4.1 Silicon carbide

The effect of the number of considered valence electrons and the basis set completeness on the positron lifetimes calculated in Si, which was mentioned in Sec. 3.1.1, had to be verified as well in the case of SiC. For that purpose we compared results obtained using 4 and 12 valence electrons in the Si dataset (while considering all electrons in the valence state for carbon). We also studied the effect of the approximation taken for the electron-electron interaction. In the GGA and LDA calculations we used the theoretical lattice parameters of 3C-SiC of 4.39 and 4.33 Å respectively, and 6.52 for the experimental high frequency dielectric constant ϵ_∞ in the semiconductor correction. The calculations were performed using cells containing 8 atomic sites. The results of this preliminary study are presented in Table 3.1.

Table 3.1: *Comparison of positron lifetimes obtained in 3C-SiC for lattice and carbon vacancy using different PAW datasets. Relative lifetimes for the carbon vacancy were calculated according to Eq. (3.1.6).*

	e-e x-c approx.	Si valence electrons	Schema	Lifetime (ps)	Relative lifetime
Lattice	LDA	4	CONV	149	
Lattice	LDA	12	CONV	144	
V_C	LDA	4	GGGC	211	42%
V_C	LDA	12	GGGC	204	42%

In the case of SiC the differences caused by the number of electrons included in the frozen core are smaller than for Si (see Sec. 3.1.1). The lattice positron lifetimes is only 5 ps smaller for 12 than for 4 valence electrons. The difference is slightly larger for the carbon vacancy than in the case of lattice (7 ps), but the ratio between vacancy lifetime and lattice lifetime is the same for the two PAW datasets. It means that for calculations in SiC the use of 4 valence electrons for silicon is satisfactory. However, in the PSN calculations the use of 4 valence electrons in the Si PAW dataset did not permit to obtain calculation convergence. A more complete basis set had to be used in that case.

We studied the effect of the approximation used for the electron-electron exchange-correlation interaction on the obtained lifetimes. We performed calculations using LDA and GGA for monovacancies. Results can be seen in Table 3.2. Each time the equilibrium volume yielded by the corresponding method is used. The lifetimes obtained in LDA are only slightly shorter than in GGA as the corresponding lattice parameter is smaller. The type of the electron-electron interaction functional and the size of the PAW dataset used in calculations affect all

Table 3.2: *Comparison of positron lifetimes obtained in 3C-SiC for carbon and silicon vacancies. Different schemes, electron-electron exchange-correlation functionals and PAW datasets are used. Relative lifetimes were calculated according to Eq. (3.1.6).*

	e-e x-c approx.	Si valence electrons	Scheme	Lifetime (ps)	Relative lifetime
Lattice	LDA	4	CONV	149	
Lattice	GGA	4	CONV	153	
Lattice	LDA	12	CONV	144	
Lattice	GGA	12	CONV	148	
V_C	LDA	4	GGGC	211	42%
V_C	GGA	4	GGGC	217	42%
V_C	LDA	12	PSN	195	35%
V_C	GGA	12	PSN	200	35%
V_{Si}	LDA	4	GGGC	224	51%
V_{Si}	GGA	4	GGGC	231	51%
V_{Si}	LDA	12	PSN	227	58%
V_{Si}	GGA	12	PSN	236	59%

the obtained lifetimes. As we showed before in the case of different numbers of valence electrons, these differences have only a slight effect on the ratio between the lifetimes of defects and that of the lattice. Therefore, to be able to correctly compare the results obtained using the various methods, we present not only the absolute lifetimes, but also relative lifetimes f_{rel}, calculated according to

$$f_{\mathrm{rel}} = \frac{\tau_{\mathrm{defect}} - \tau_{\mathrm{lattice}}}{\tau_{\mathrm{lattice}}}, \tag{3.1.6}$$

where τ_{lattice} is the lattice lifetime obtained using the same method and parametrization as for the considered defect.

Since the GGA approximation of the exchange-correlation interaction between electrons yields better energies than LDA [133], the best scenario would be to use GGA in both the GGGC and PSN calculations. However, since in the PSN scheme 12 valence electrons must be considered in the Si PAW dataset, using GGA approximation leads to a very high computational cost. As seen in Table 3.2, the differences in relative positron lifetimes obtained in PSN+GGA and PSN+LDA are smaller than 1%. The absolute lifetimes calculated in PSN+LDA are shorter mainly due to a smaller lattice parameter used. Based on that, we decided to perform PSN calculations in LDA. For the GGGC scheme GGA is used as the computational cost remains reasonable in this case.

Additionally, in the case of the carbon vacancy we have studied the effect of the initial geometry on the positron localization. In some theoretical studies it was found that this defect is not a

positron trap [57, 63], which is still controversial. To be sure that our result is not a consequence of the starting point, we performed two calculations. In the first one we started with the perfect atomic positions, while in the second one we began with a vacancy that was already relaxed without a positron. The carbon vacancy itself relaxes inwards in a D_{2d} symmetry [10] due to the formation of dimer-like bonds between the silicon atoms surrounding the defect. A smaller volume of V_C could prevent the positron localization. However, both calculations eventually yield an outward relaxation, in very similar T_d geometries. It probably means that the positron can break the bonds between silicon atoms. A similar effect was found for a silicon vacancy in Si [134].

3.1.4.2 Uranium dioxide

We studied the effect of the parameters used in the calculations on the positron lifetime of perfect UO_2. We compared the results obtained in GGA and GGA+U methods, when:

- using various cell volumes,
- taking two types of positron lifetime calculation schemes,
- applying different corrections to the enhancement factor g,
- considering or neglecting the spin polarization.

The results of these tests are presented in Tab. 3.3. We used two different calculations schemes, PSN and GGGC. GGGC+SC and PSN+SC in Tab. 3.3 refer to schemes in which the semiconductor correction, based on the one proposed by Puska [122] and described in Sec. 3.1.2, was used. We took the experimental high-frequency dielectric constant of UO_2 equal to 5.1 [135] in the semiconductor correction. GGGC+GC and PSN+GC refer to schemes in which the gradient correction, proposed by Barbiellini *et al.* [60], was used. It is worth noting that in the GGGC+GC scheme this correction is applied on both the enhancement factor and the electron-positron correlation functional, while in the PSN+GC method it is only implemented in the enhancement factor g, as described in Sec. 3.1.3. In Tab. 3.3 we present the lattice positron lifetimes calculated using various volumes. $V^{\text{exp.}}$ refers to the experimental volume, corresponding to a lattice parameter of 5.47 Å [14]. $V^{\text{eq.}}$ refers to the equilibrium volume yielded by calculations using given parameters. We can notice that the lifetimes obtained using the semiconductor correction, both using the PSN and GGGC schemes, are systematically shorter than the ones calculated with the gradient correction. Moreover, the GGGC and PSN schemes yield

Table 3.3: *Lattice positron lifetime of UO_2 calculated using various computational parameters.*

	GGA				GGA+U			
	no spin		spin		no spin		spin	
	$V^{\text{eq.}}$	$V^{\text{exp.}}$	$V^{\text{eq.}}$	$V^{\text{exp.}}$	$V^{\text{eq.}}$	$V^{\text{exp.}}$	$V^{\text{eq.}}$	$V^{\text{exp.}}$
PSN+SC	151 ps	157 ps	155 ps	157 ps	152 ps	157 ps	160 ps	156 ps
GGGC+SC	149 ps	155 ps	150 ps	154 ps	154 ps	155 ps	158 ps	154 ps
PSN+GC	156 ps	162 ps	161 ps	162 ps	158 ps	162 ps	167 ps	162 ps
GGGC+GC	157 ps	164 ps	159 ps	164 ps	163 ps	164 ps	168 ps	163 ps

similar lattice positron lifetimes, both when the semiconductor and the gradient correction is used. Additionally, the results obtained using the gradient correction are in better agreement with the experimental lattice lifetime obtained for UO_2 of 169±1 ps [81]. It suggests that the schemes using the gradient correction are more suitable for the description of positron lifetimes in uranium dioxide, hence we choose to use them in the present study. We decided to use both GGGC+GC and PSN+GC schemes in our further study of defects positron lifetimes. First, we do it in order to avoid the misinterpretation of experimental results, which could result from possible errors of one of the calculation methods. Second, since the studies in which different self-consistent schemes are used are scarce, we wish to compare those two methods and verify the influence of the scheme choice on the defect identification.

In Tab. 3.3 we also observe that when the experimental volume is considered, we obtain similar results for all schemes using different descriptions of the electrons in the system. No effect of the functional used for the electron-electron exchange-correlation functional description or of the spin polarization is observed. In particular, it is worth noting that the U parameter does not affect directly the calculated positron lifetimes. The difference between the lifetimes calculated in GGA and GGA+U methods is of 1 ps at most, when the experimental volumes are taken. The lifetimes calculated at the equilibrium volumes found using a given method, however, differ more strongly. This is because the positron lifetime is highly sensitive to the free volume. The best agreement between the calculated and experimental lifetime is reached for the calculation using the GGA+U method and spin polarization at the equilibrium volume (168 and 167 ps in the GGGC+GC and PSN+GC schemes, respectively, compared to 169±1 ps measured experimentally). This is, therefore, the set of parameters that we use for the study of defects in UO_2.

3.2 Calculation of Doppler broadening of the annihilation radiation

3.2.1 Implementation of Doppler broadening calculations in the PAW formalism in the ABINIT code

In the calculations of the Doppler broadening of the annihilation radiation we wish to use the fully self-consistent two component calculation schemes implemented in ABINIT. The full self-consistency in this code is possible thanks to the use of the same PAW formalism for both electron and positron wavefunctions. As a consequence, it is necessary to express the equations needed to calculate the electron-positron momentum distribution in the PAW method.

Since the momentum distribution of the annihilating electron-positron pairs is a sum over the electronic states, we can consider the core and valence contributions separately and apply the most convenient approximations and methods for each of them. We will now present the methods used for the valence and core electrons, respectively.

3.2.1.1 Valence electrons

The first step towards expressing the valence contribution to the momentum distribution of the annihilating electron-positron pairs in the PAW formalism is to implement the PAW form of the electron and positron wavefunctions into Eq. (2.3.4). The product of electron and positron wavefunctions needed in this equation takes the form:

$$\begin{aligned} \Psi^{+}(\mathbf{r})\Psi^{-}_{nk}(\mathbf{r}) = & \left(\tilde{\Psi}^{+}(\mathbf{r}) + \sum_{i}\left(\phi_i(\mathbf{r}) - \tilde{\phi}_i(\mathbf{r})\right)\langle\tilde{p}_i|\tilde{\Psi}^{+}\rangle\right) \\ * & \left(\tilde{\Psi}^{-}_{nk}(\mathbf{r}) + \sum_{j}\left(\phi_j(\mathbf{r}) - \tilde{\phi}_j(\mathbf{r})\right)\langle\tilde{p}_j|\tilde{\Psi}^{-}_{nk}\rangle\right). \end{aligned} \tag{3.2.1}$$

Multiplication of the terms in the brackets leads to:

$$\begin{aligned}
\Psi^+(\mathbf{r})\Psi^-_{nk}(\mathbf{r}) &= \tilde{\Psi}^+(\mathbf{r})\tilde{\Psi}^-_{nk}(\mathbf{r}) \\
&+ \tilde{\Psi}^+(\mathbf{r})\sum_j \left(\phi_j(\mathbf{r}) - \tilde{\phi}_j(\mathbf{r})\right)\langle\tilde{p}_j|\tilde{\Psi}^-_{nk}\rangle \\
&+ \tilde{\Psi}^-_{nk}(\mathbf{r})\sum_i \left(\phi_i(\mathbf{r}) - \tilde{\phi}_i(\mathbf{r})\right)\langle\tilde{p}_i|\tilde{\Psi}^+\rangle \\
&+ \sum_{ij}\phi_i(\mathbf{r})\left(\phi_j(\mathbf{r}) - \tilde{\phi}_j(\mathbf{r})\right)\langle\tilde{p}_i|\tilde{\Psi}^+\rangle\langle\tilde{p}_j|\tilde{\Psi}^-_{nk}\rangle \\
&- \sum_{ij}\tilde{\phi}_i(\mathbf{r})\left(\phi_j(\mathbf{r}) - \tilde{\phi}_j(\mathbf{r})\right)\langle\tilde{p}_i|\tilde{\Psi}^+\rangle\langle\tilde{p}_j|\tilde{\Psi}^-_{nk}\rangle.
\end{aligned} \tag{3.2.2}$$

By definition, outside the augmentation region the wavefunction is equal to the pseudo part only, hence $\phi_j(\mathbf{r}) - \tilde{\phi}_j(\mathbf{r})$ is equal to zero. Inside the augmentation region, on the other hand, if the partial wave and plane-wave basis sets are complete, $\tilde{\Psi}^+(\mathbf{r}) = \sum_i \tilde{\phi}_i(\mathbf{r})\langle\tilde{p}_i|\tilde{\Psi}^+\rangle$ and $\tilde{\Psi}^-(\mathbf{r}) = \sum_j \tilde{\phi}_j(\mathbf{r})\langle\tilde{p}_j|\tilde{\Psi}^-\rangle$. We can rewrite the products of the quantities existing in the whole space and those which have non-zero values only inside the PAW augmentation region as:

$$\begin{aligned}
&\tilde{\Psi}^+(\mathbf{r})\sum_j \left(\phi_j(\mathbf{r}) - \tilde{\phi}_j(\mathbf{r})\right)\langle\tilde{p}_j|\tilde{\Psi}^-_{nk}\rangle \\
&= \sum_{ij}\tilde{\phi}_i(\mathbf{r})\left(\phi_j(\mathbf{r}) - \tilde{\phi}_j(\mathbf{r})\right)\langle\tilde{p}_i|\tilde{\Psi}^+\rangle\langle\tilde{p}_j|\tilde{\Psi}^-_{nk}\rangle
\end{aligned} \tag{3.2.3}$$

and

$$\begin{aligned}
&\tilde{\Psi}^-_{nk}(\mathbf{r})\sum_i \left(\phi_i(\mathbf{r}) - \tilde{\phi}_i(\mathbf{r})\right)\langle\tilde{p}_i|\tilde{\Psi}^+\rangle \\
&= \sum_{ij}\tilde{\phi}_j(\mathbf{r})\left(\phi_i(\mathbf{r}) - \tilde{\phi}_i(\mathbf{r})\right)\langle\tilde{p}_i|\tilde{\Psi}^+\rangle\langle\tilde{p}_j|\tilde{\Psi}^-_{nk}\rangle.
\end{aligned} \tag{3.2.4}$$

This leads to:

$$\begin{aligned}
&\Psi^+(\mathbf{r})\Psi^-_{nk}(\mathbf{r}) = \tilde{\Psi}^+(\mathbf{r})\tilde{\Psi}^-_{nk}(\mathbf{r}) \\
&+ \sum_{ij}\left(\phi_i(\mathbf{r})\phi_j(\mathbf{r}) - \tilde{\phi}_i(\mathbf{r})\tilde{\phi}_j(\mathbf{r})\right)\langle\tilde{p}_i|\tilde{\Psi}^+\rangle\langle\tilde{p}_j|\tilde{\Psi}^-_{nk}\rangle,
\end{aligned} \tag{3.2.5}$$

therefore

$$\rho_{\mathbf{k}}(\mathbf{p}) = \pi r_e^2 c \sum_n \Bigg| \int \mathrm{d}\mathbf{r}\, e^{-i\mathbf{p}\cdot\mathbf{r}} \tilde{\Psi}^+(\mathbf{r}) \tilde{\Psi}^-_{nk}(\mathbf{r}) + \int \mathrm{d}\mathbf{r}\, e^{-i\mathbf{p}\cdot\mathbf{r}} \sum_{ij} \Big(\phi_i(\mathbf{r})\phi_j(\mathbf{r}) - \tilde{\phi}_i(\mathbf{r})\tilde{\phi}_j(\mathbf{r}) \Big) * \langle \tilde{p}_i | \tilde{\Psi}^+ \rangle \langle \tilde{p}_j | \tilde{\Psi}^-_{nk} \rangle \Bigg|^2 . \tag{3.2.6}$$

We can see that inside the squared modulus above, we obtain a sum of two separate integrals: one containing the pseudo wavefunctions and one containing partial waves. We can consider each of them separately.

We can further transform the second integral in Eq. (3.2.6). By separating the partial waves into angular and radial parts we obtain

$$\phi_i(\mathbf{r}) = \frac{\phi_i(r)}{r} S_{l_i m_i}(\hat{r}) \tag{3.2.7}$$

and

$$\tilde{\phi}_j(\mathbf{r}) = \frac{\tilde{\phi}_j(r)}{r} S_{l_j m_j}(\hat{r}), \tag{3.2.8}$$

where $S_{l_i m_i}(\hat{r})$ are the real spherical harmonics. We can also express the exponential $e^{-i\mathbf{p}\cdot\mathbf{r}}$ as:

$$e^{-i\mathbf{p}\cdot\mathbf{r}} = 4\pi \sum_{LM} (-i)^L S_{LM}(\hat{p}) S_{LM}(\hat{r}) j_L(pr). \tag{3.2.9}$$

Separation of the angular and radial parts of the second integral from Eq. (3.2.6), using $d\mathbf{r} = r^2 dr d\Omega$, leads to:

$$\int \mathrm{d}\mathbf{r}\, e^{-i\mathbf{p}\cdot\mathbf{r}} \sum_{ij} \Big(\phi_i(\mathbf{r})\phi_j(\mathbf{r}) - \tilde{\phi}_i(\mathbf{r})\tilde{\phi}_j(\mathbf{r}) \Big) \langle \tilde{p}_i | \tilde{\Psi}^+ \rangle \langle \tilde{p}_j | \tilde{\Psi}^-{}_{nk} \rangle = 4\pi \sum_{ij} \langle \tilde{p}_i | \tilde{\Psi}^+ \rangle \langle \tilde{p}_j | \tilde{\Psi}^-{}_{nk} \rangle$$
$$* \sum_{LM} S_{LM}(\hat{p}) (-i)^L \left(\int \mathrm{d}\Omega\, S_{l_i m_i}(\hat{r}) S_{l_j m_j}(\hat{r}) S_{LM}(\hat{r}) \right) \left(\int \mathrm{d}r\, \Big(\phi_i(r)\phi_j(r) - \tilde{\phi}_i(r)\tilde{\phi}_j(r) \Big) j_L(pr) \right). \tag{3.2.10}$$

By introducing the real Gaunt coefficients $\mathcal{G}$ (see Ref. [105]),

$$\mathcal{G}^{LM}_{l_i m_i l_j m_j} = \int \mathrm{d}\Omega\, S_{l_i m_i}(\hat{r}) S_{l_j m_j}(\hat{r}) S_{LM}(\hat{r}), \tag{3.2.11}$$

we finally obtain the expression

$$\int \mathrm{d}\mathbf{r}\, e^{-i\mathbf{p}\cdot\mathbf{r}} \sum_{ij} \left(\phi_i(\mathbf{r})\phi_j(\mathbf{r}) - \tilde{\phi}_i(\mathbf{r})\tilde{\phi}_j(\mathbf{r})\right) \langle\tilde{p}_i|\tilde{\Psi}^+\rangle\langle\tilde{p}_j|\tilde{\Psi^-}_{nk}\rangle = 4\pi \sum_{ij} \langle\tilde{p}_i|\tilde{\Psi}^+\rangle\langle\tilde{p}_j|\tilde{\Psi^-}_{nk}\rangle$$
$$* \sum_{LM} S_{LM}(\hat{p})(-i)^L \mathcal{G}^{LM}_{l_i m_i l_j m_j} \int \mathrm{d}r \, \left(\phi_i(r)\phi_j(r) - \tilde{\phi}_i(r)\tilde{\phi}_j(r)\right) j_L(pr). \tag{3.2.12}$$

Introducing the above into Eq. (3.2.6) we can write the final expression of the valence contribution to the momentum distribution calculated at a given **k**-point:

$$\begin{aligned} \rho_{vk}(\mathbf{p}) &= \pi r_e^2 c \sum_n \left| \int \mathrm{d}\mathbf{r} e^{-i\mathbf{p}\cdot\mathbf{r}} \tilde{\Psi}^+(\mathbf{r}) \tilde{\Psi^-}_{nk}(\mathbf{r}) + 4\pi \sum_{ij} \langle\tilde{p}_i|\tilde{\Psi}^+\rangle\langle\tilde{p}_j|\tilde{\Psi^-}_{nk}\rangle \right. \\ &* \left. \sum_{LM} S_{LM}(\hat{p})(-i)^L \mathcal{G}^{LM}_{l_i m_i l_j m_j} \int \mathrm{d}r \left(\phi_i(r)\phi_j(r) - \tilde{\phi}_i(r)\tilde{\phi}_j(r)\right) j_L(pr) \right|^2 . \end{aligned} \tag{3.2.13}$$

3.2.1.2 Core electrons

The core contribution to the momentum distribution is expressed as:

$$\rho_{\mathrm{c}}(\mathbf{p}) = \pi r_e^2 c \sum_{j_{\mathrm{c}}} \left| \int \mathrm{d}\mathbf{r}\, e^{-i\mathbf{p}\cdot\mathbf{r}} \Psi^+(\mathbf{r}) \Psi^-_{j_{\mathrm{c}}}(\mathbf{r}) \right|^2 , \tag{3.2.14}$$

where the summation goes over all the core electronic states j_{c}.

To adapt this equation, we express the positron wavefunction in the PAW formalism, and for the core electrons, we assume that the core electrons are unaffected by the crystal formation which means that their wavefunctions are equal to those of the isolated atom (frozen core approximation),

$$\Psi^-_{j_{\mathrm{c}}}(\mathbf{r}) = \phi_{j_{\mathrm{c}}}(\mathbf{r}). \tag{3.2.15}$$

This leads to the form as follows for the core contribution to the momentum distribution:

$$\rho_{\mathrm{c}}(\mathbf{p}) = \pi r_e^2 c \sum_{j_{\mathrm{c}}} \left| \int \mathrm{d}\mathbf{r}\, e^{-i\mathbf{p}\cdot\mathbf{r}} \left(\tilde{\Psi}^+(\mathbf{r}) + \sum_i (\phi_i(\mathbf{r}) - \tilde{\phi}_i(\mathbf{r})) < \tilde{p}_i|\tilde{\Psi}^+ > \right) \phi_{j_{\mathrm{c}}}(\mathbf{r}) \right|^2 \tag{3.2.16}$$

We consider then that the core electron wavefunctions are contained inside the augmentation region. This approximation seems reasonable in the majority of considered cases and can be

easily verified. If the pseudo partial waves $\tilde{\phi}_k(\mathbf{r})$ form a complete basis sets for the pseudo-wavefunction $\tilde{\Psi}^+(\mathbf{r})$ we have:

$$\int \mathrm{d}\mathbf{r}\, e^{-i\mathbf{p}\cdot\mathbf{r}} \left(\tilde{\Psi}^+(\mathbf{r}) - \sum_k < \tilde{p}_k|\tilde{\Psi}^+ > \tilde{\phi}_k(\mathbf{r}) \right) \phi_{j_\mathrm{c}}(\mathbf{r}) = 0, \tag{3.2.17}$$

which leads to:

$$\rho_\mathrm{c}(\mathbf{p}) = \pi r_e^2 c \sum_{j_\mathrm{c}} \left| \int \mathrm{d}\mathbf{r}\, e^{-i\mathbf{p}\cdot\mathbf{r}} \sum_k < \tilde{p}_k|\tilde{\Psi}^+ > \phi_k(\mathbf{r})\phi_{j_\mathrm{c}}(\mathbf{r}) \right|^2 . \tag{3.2.18}$$

Further, we separate the partial waves into angular and radial parts and transform the equations in the same way as was done for the valence contribution. This leads to the final expression for the core contribution to the momentum distribution:

$$\rho_\mathrm{c}(\mathbf{p}) \;=\; \pi r_e^2 c \sum_{j_\mathrm{c}} \left| 4\pi \sum_i < \tilde{p}_i|\tilde{\Psi}^+ > \sum_{LM} S_{LM}(\hat{p})(-i)^L \mathcal{G}^{LM}_{l_i m_i l_j m_{j_\mathrm{c}}} \int dr\, \phi_i(r)\phi_{j_\mathrm{c}}(r) j_L(pr) \right|^2 . \tag{3.2.19}$$

3.2.1.3 PAW basis set completeness for positron wavefunction

To obtain both Eq. (3.2.13) and (3.2.19) we considered that the PAW basis set is complete enough to describe the positron wavefunction inside the augmentation region. The PAW datasets, however, are generated in order to describe electronic wavefunctions and not the positronic ones. The nature of the electron-ion and positron-ion interactions and, hence, the shapes of the corresponding wavefunctions differ strongly. Therefore, in some cases, a standard PAW dataset can be inappropriate for the positron description. This can affect the calculated positron lifetimes, but the effect is less significant than in the Doppler spectra calculations, since in the former case the annihilation rate is integrated over the whole space and the errors in the core region can be covered by the valence contribution. In Doppler broadening calculations this issue needs to be monitored more carefully.

In Fig. 3.1 we illustrate the effect of the choice of the PAW dataset on the positron wavefunction in a Si lattice. In this figure we present the decomposition to the total positronic wavefunction (all-electron, 'AE') into three components–pseudo ('PS'), partial all-electron ('partial AE') and partial pseudo ('partial PS')–according to Eq. (2.1.7.4).

First, we used a standard Si PAW dataset with 4 valence electrons ($3s$ and $3p$ basis set orbitals). With a complete basis set we should have $\tilde{\Psi}^+(\mathbf{r}) = \sum_i \tilde{\phi}_i(\mathbf{r})\langle\tilde{p}_i|\tilde{\Psi}^+\rangle$ inside the PAW

augmentation region (here up to $r = 1.5$ bohr). However, it can be seen in Fig. 3.1a that the corresponding pseudo ('PS') and partial pseudo ('partial PS') contributions are not equal in this range. Additionally, we can observe a peak at the (0,0,0) point, which corresponds to the center of a silicon atom, where the positron wavefunction should be equal to zero. This dataset is clearly not appropriate for the positron wavefunction representation.

In Fig. 3.1b we present the positron wavefunction obtained using a PAW dataset with 12 valence electrons ($2s$, $2p$, $3s$ and $3p$ basis set orbitals). In this case the 'PS' and 'partial PS' are equal inside the augmentation region, which means that the basis set is complete. There is still a non-zero value of the all-electron wavefunction at the (0,0,0) point, but it is much smaller than the one yielded by the 4 valence electrons dataset. It is worth pointing out that we could also enlarge the PAW dataset by including projectors corresponding to excited states. However, our test showed that a better description of the positron was always achieved when adding the semicore electron orbitals.

Fig. 3.1 shows clearly that by adding additional states in the PAW dataset we obtain a better description of the positron wavefunction. However, increasing the number of the valence electrons taken into account for a given element leads to more time consuming calculations. In the cases when large supercells are required (when modeling defects) the computational cost can become too high. We decided to test if it is possible to add the partial waves corresponding to the semicore electrons in the basis set used only for the positron wavefunction description, while keeping the initial number of valence electrons. For instance, in the case of Si, we would like to still consider only 4 valence electrons, but add the $2s$ and $2p$ states in the positron wavefunction basis set. In practice, we generate a PAW datasets (using a modified version of the Atompaw generator [104]) in which we add the partial waves and projectors corresponding to these additional states after the initial functions. During the self-consistent calculation, when the electronic step is performed, we put to zero all quantities corresponding to these additional states, so that the wavefunction basis set for the electrons is equal to the one calculated with 4 valence electrons. This allows us to obtain a better description of the positron wavefunction without a significant increase of the computational cost. The positron wavefunction obtained for the Si lattice using the PAW dataset with 4 valence electrons and added $2s$ and $2p$ states is presented in Fig. 3.2 and compared with those calculated using standard datasets with 4 and 12 valence electrons. The positron wavefunctions obtained using a dataset containing on one hand 12 valence electrons and on the other hand 4 valence electrons and added $2s$ and $2p$ states are equal, which suggests that both including the semicore electrons in the valence and adding the corresponding states only to the positron wavefunction basis set equally improves the positron description. The effect of the choice of the PAW dataset on the Doppler spectrum will be discussed in Sec. 3.2.3.

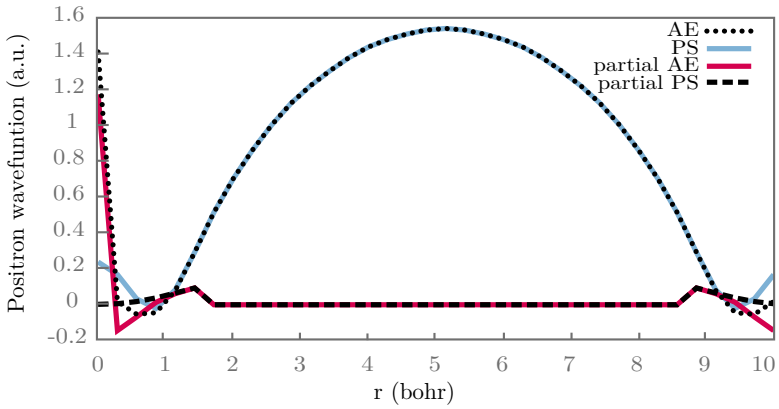

(a) *4 valence electrons*

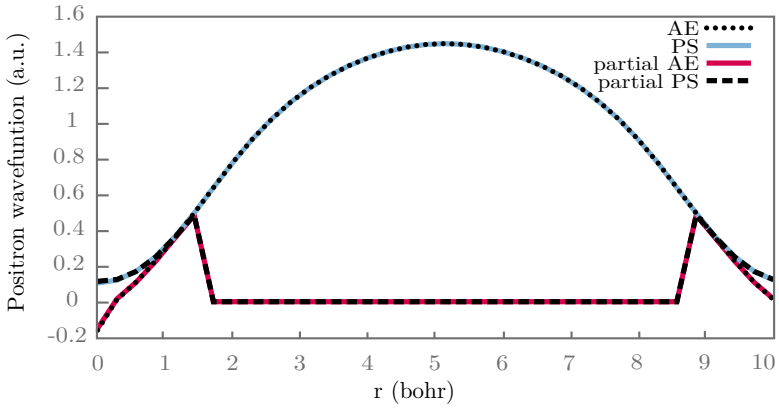

(b) *12 valence electrons*

Figure 3.1: *Positron wavefunctions in Si lattice obtained using PAW datasets containing 4 (a) and 12 (b) valence electrons. The wavefunctions are plotted between two Si atoms at (0,0,0) and (0,0,1) reduced coordinates. All electron (AE), pseudo (PS), partial all electron (partial AE) and partial pseudo (partial PS) contributions are presented.*

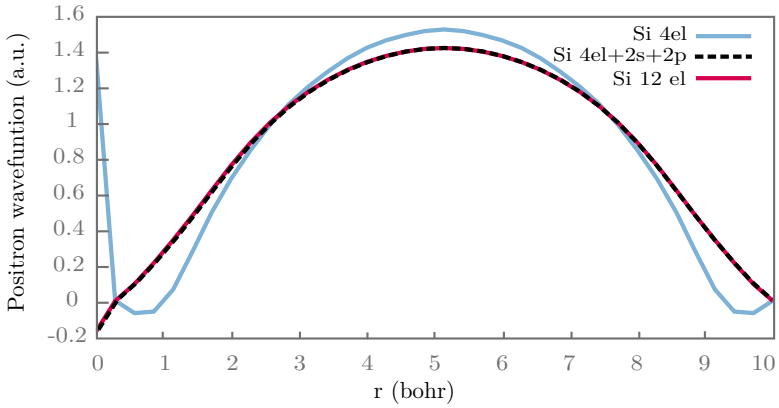

Figure 3.2: *Positron wavefunctions in a Si lattice obtained using PAW datasets containing 4, 12 valence electrons and a dataset with 4 valence electrons and added 2s and 2p states. The wavefunctions are plotted between two Si atoms at (0,0,0) and (0,0,1) reduced coordinates.*

3.2.2 Numerical solutions used in momentum distribution calculations

The momentum distribution of annihilating electron-positron pairs can be considered as a Fourier transform of the product of the electrons and the positron wavefunctions. To calculate the 'pseudo' part of the equation for the momentum distribution we decided to use the Fast Fourier transform (FFT) routines as implemented in ABINIT. The FFT in these routines is performed between real and reciprocal space grids of equal sizes. The grid on which the momentum distribution will be given must, therefore, be the same as the one used to express the wavefunctions in the reciprocal space (called the 'FFT grid').

3.2.2.1 Momentum grid

The relation between the real and reciprocal grids used in the code is presented in Fig. 3.3. In this two-dimensional scheme a_1 and a_2 are the lengths of the cell used in the calculation and nfft_1 and nfft_2 are numbers of points of the real grid in each direction. The spacing of the reciprocal grid is proportional to the inverse of a_1 and a_2 and its size to nfft_1 and nfft_2.

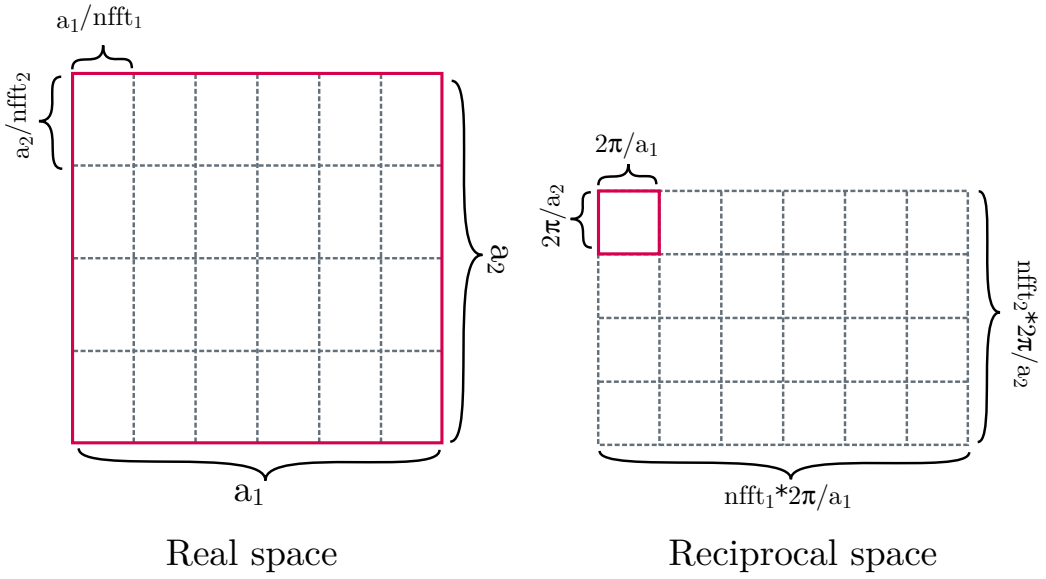

Figure 3.3: *Two-dimensional scheme of real and reciprocal space grids.*

In order to obtain the correct Doppler spectrum, spaces between the points of the momentum grid must be small enough. Since the reciprocal grid spacing is inversely proportional to the cell size, increasing the number of atoms used in the calculation will lead to a finer momentum grid.

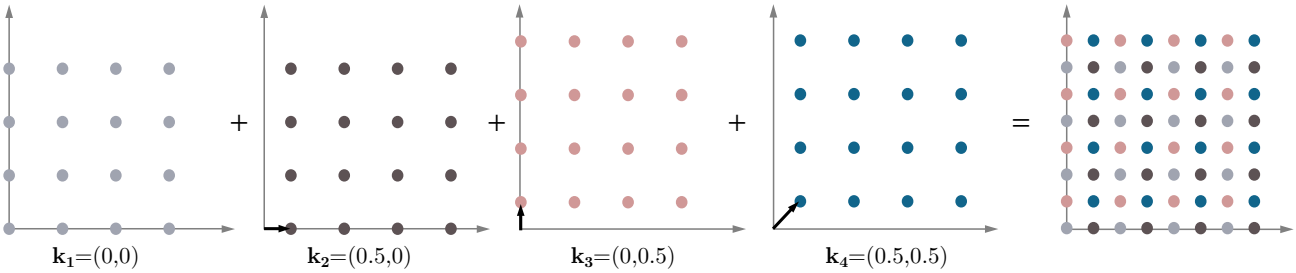

Figure 3.4: *Schematic two-dimensional representation of the shifted momentum grids used in momentum distribution calculations.*

This cannot, however, always be done, since calculations performed using very large supercells are too time consuming. Another way to increase the sampling of the reciprocal space is to perform the FFT several times, each time on a grid shifted by a vector $\mathbf{k}$, with coordinates varying between -1 and 1. This is equivalent to the use of several $\mathbf{k}$-points in the first Brillouin zone mentioned in Sec. 2.1.20. For example, as shown in the two-dimenstional scheme in Fig. 3.4, one can double the accuracy by performing the FFT on four different grids (eight for a three-dimensional grid), shifted by $\mathbf{k} = (0, 0)$, $\mathbf{k} = (0, 0.5)$, $\mathbf{k} = (0.5, 0)$ and $\mathbf{k} = (0.5, 0.5)$.

The core and PAW valence contributions to the momentum distribution, Eq. (3.2.13) and Eq. (3.2.19), are expressed on a radial grid in the real space. The FFT routines could not be used in this case, since we need to perform a Fourier transform between this radial grid and a rectangular grid in the momentum space. The Fourier transform of the wavefunctions product between radial and rectangular grids was written from scratch in our implementation, hence the choice of the momentum grid was arbitrary. We chose, however, to use the same grid as used to perform the FFT to facilitate the summation of the pseudo, PAW and core contributions to the momentum distribution.

3.2.2.2 Parallelization

The momentum distribution calculations can be time and memory consuming. In order to be able to perform calculations using large supercells, necessary for defect studying, the code needed to be parallelized. We implemented the parallelization on three levels, allowing one to use the Locally Optimal Block-preconditioned Conjugate Gradient (LOBPCG) [136] or the Chebyshev filtering algorithm [137]. That means that the processors can be distributed between the $\mathbf{k}$-points (in our case also between the shifted momentum grids), bands and FFT grid points during the density, lifetime and momentum distribution calculations. If the parallelization over bands is used, the wavefunction of the positron, which occupies one band, is known to some of the

processors only. Therefore, before the momentum distribution calculation the processors need to exchange the positron wavefunction. Then, each processor performs a calculation only for given **k**-points (grids), electronic bands and FFT points. After that, summation over the band processors is performed and the results for different **k**-points are gathered. Finally, processors holding in memory different FFT points write out the results in parallel.

3.2.2.3 Post-processing

The output of the Doppler broadening calculation is a momentum density on a three dimensional grid. The experimental results are usually presented as one dimensional projections of the momentum density or as integrals over the low- and high-momentum regions (S and W parameters, respectively) of the Doppler spectrum (see Fig. 1.5). Therefore, the three dimensional results need to be processed before they can be exploited. First, the projections are calculated. That can be done in the [001], [011] or [111] directions. The next step is related to the fact that the resolution of the experimental momentum distribution measurements is finite. In order to mimic the corresponding effects and, hence, to be able to make a meaningful comparison between the experiments and calculations, one needs to convolve the theoretical results with a Gaussian function with the FWHM (full width at half maximum) corresponding to the experimental resolution. Therefore, after the projections, the convolution is performed in the post-processing. Presenting ratios of Doppler spectra to reference data (perfect lattice or reference material) is a convenient way of presenting the results. To calculate the ratios, the considered spectra must be given on the same grid and normalized in the same way. The last step of the post-processing is, therefore, the interpolation of the data and its normalization. We decided to use a grid with 0.1 mrad spacing and to normalize the spectra to unity.

3.2.3 Testing of the implementation

To validate our implementation of the Doppler broadening calculations we compared results obtained using ABINIT with theoretical and experimental spectra published in literature. Following Makkonen *et al.* [115] we first compare ratios between spectra of perfect materials. To be able to compare our results with those of Makkonen *et al.* we perform calculations for Si, Al, Fe and Cu. Additionally, we perform tests for SiC and C in order to be able to make a comparison with the ratios of the experimental Doppler spectra of diamond, Si and SiC of Rempel *et al.* [69]. We also test our implementation for the case of the monovacancy in silicon. In the following tests the calculation results for the [001], [011] and [111] directions are averaged

(unless stated otherwise), in order to achieve the best agreement with experiments, in which the directions cannot usually be distinguished. In the tests we use the state-dependent scheme with the LDA electron-positron correlation functional, since according to Makkonen *et al.* [113] these methods give better results than the state-independent scheme or the GGA approximation. We do not use the semiconductor correction, since we observed that it had no significant influence on the normalized Doppler spectra.

The first tests have been performed on the perfect silicon lattice. In this case various PAW datasets containing different numbers of valence electrons can be used. These datasets have been discussed in Sec. 3.2.1.3. The first dataset tested included the $3s$ and $3p$ states in the valence and the $1s$, $2s$ and $2p$ states in core. The corresponding Doppler spectrum is presented in Fig. 3.5 (blue line). We can see that the results obtained using this dataset are incorrect. We observe an unphysically high probability at high momenta in the spectrum. This is related to the errors in the positron wavefunction obtained using this dataset (see Fig. 3.1a). There was a peak in the core region, where the positron wavefunction should disappear. As a result, for instance in Eq. 3.2.19 we multiply the core contribution by a high value, instead of a one tending to zero, which explains the high probability at high momenta. It is worth noting that there was also a non-zero value in the positron wavefunction calculated using the two more complete datasets, however, the error and the affected region was smaller. We suppose, hence, that the corresponding errors in the Doppler spectrum will appear at momenta above the range that is usually compared with experiments of around 40 mrad.

The Doppler spectra obtained using the PAW datasets with 12 valence electrons and with 4 valence electrons and additional $2s$ and $2p$ states in the basis set are presented in black and red, respectively, in Fig. 3.5. We can see that in both cases the behavior at high momenta is greatly improved. The spectra are compared with the theoretical results of Makkonen *et al.* and experimental data by Ranki *et al.* [138]. Our results are in very good agreement with those of Makkonen and slightly above the experimental data at high momenta. The latter is characteristic for the calculations using the state-dependent scheme [113].

The next test consisted of calculating Si lattice to SiC lattice ratio curves (Fig. 3.6). For Si we used the PAW datasets with 12 valence electrons as well as with 4 valence electrons and additional $2s$ and $2p$ states in the basis set. For carbon, we use a dataset including all 6 electrons in the valence state. The ratio curves are compared with the experimental results of Rempel *et al.* [69] for $6H$-SiC. The theoretical results obtained using both PAW datasets are in very good agreement with the experimental data. In the figure we present the results obtained for both $3C$-SiC and $6H$-SiC. It can be seen that the momentum distributions of the silicon carbide lattice are very similar for the two polytypes.

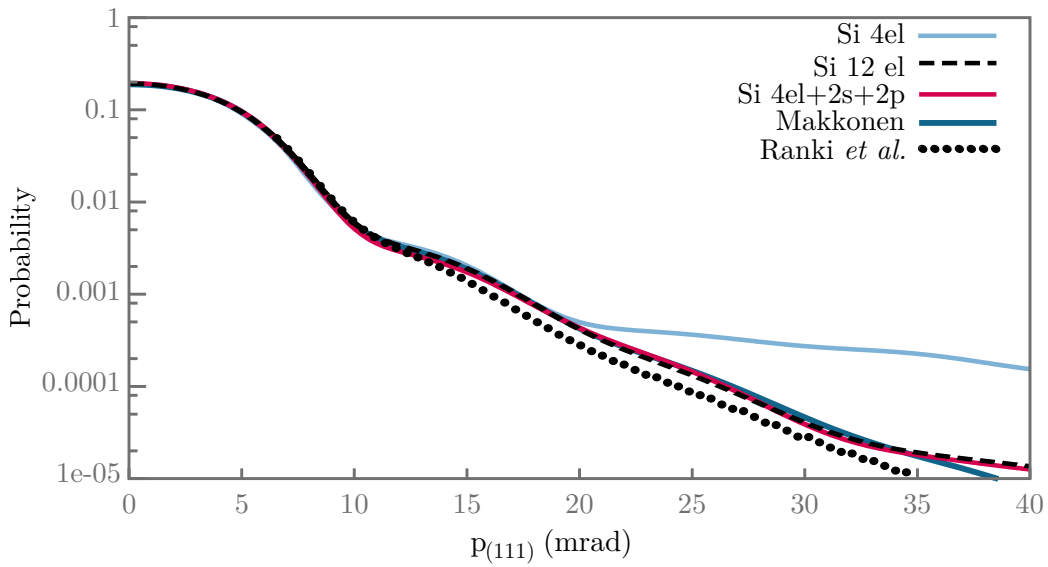

Figure 3.5: *Doppler spectra of Si perfect lattice calculated using different partial waves basis sets. Spectra are convoluted with a Gaussian function with a FWHM of 3.7 mrad. The results are compared with a theoretical spectrum given by Makkonen [139] and experimental data obtained by Ranki et al. [138].*

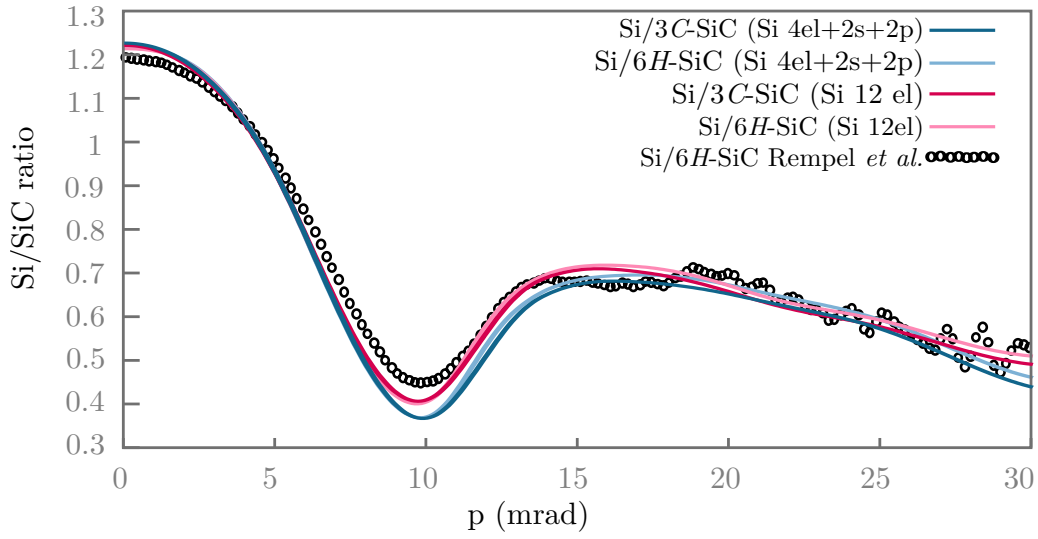

Figure 3.6: *Si lattice/SiC lattice ratio curves of momentum distribution of annihilation radiation. The theoretical results obtained using different silicon PAW datasets are compared with experimental data obtained by Rempel et al. [69]. The theoretical curves are convoluted with a Gaussian function with a FWHM of 3.6 mrad.*

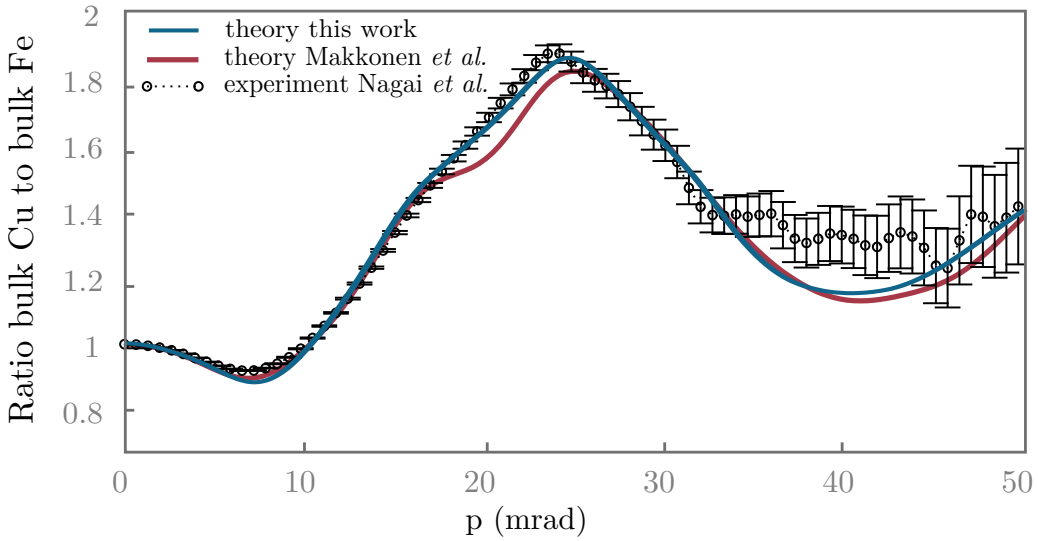

Figure 3.7: *Cu lattice/Fe lattice ratio curves of momentum distributions of annihilation radiation. The result obtained in this study is compared with experimental data obtained by Nagai et al. [140] and with theoretical results of Makkonen et al. [115]. The theoretical curves are convoluted with a Gaussian function with a FWHM of 4.7 mrad.*

We further test our implementation of Doppler broadening calculations in the ABINIT code by repeating some of the tests performed by Makkonen *et al.* in Ref. [115]. In Fig. 3.7 we plot the Cu lattice to Fe lattice momentum distribution ratio curves. In this calculation for Cu we used a PAW dataset containing 19 valence electrons ($3s$, $3p$, $3d$, $4s$ and $4p$) and $2s$ and $2p$ states added in the positron wavefunction basis set. In the case of Fe we used 16 valence electrons ($3s$, $3p$, $3d$ and $4s$) and $2s$ and $2p$ states added in the positron wavefunction basis set. We compare our ratio curve with the theoretical results of Makkonen *et al.* and with the experimental data obtained by Nagai *et al.* [140]. The reference results were extracted from Ref. [115]. We can see that our results are in very good agreement with both theoretical and experimental reference data.

In Fig. 3.8 we plot the Cu lattice to Al lattice momentum distribution ratio curves. In this calculation we used a PAW dataset with 11 valence electrons ($2s$, $2p$, $3s$ and $3p$). In Fig. 3.9 we plot the Si lattice to Fe lattice and Al lattice to Fe lattice ratio curves. For Si we use the PAW dataset with 4 valence electrons and additional $2s$ and $2p$ states in the basis set, as described previously. We observe that the ratio curves obtained using our implementation are in very good agreement with the calculations of Makkonen *et al.* Also, both calculations agree qualitatively to the experimental data of Nagai *et al.* It can be observed, however, that the experimental ratios at low momenta are smaller than the calculated values for both Si and Al. Since the discrepancies are similar for Si and Al, the problem might be due to the Fe spectrum. It is possible that the experimental conditions did not completely correspond to those considered in

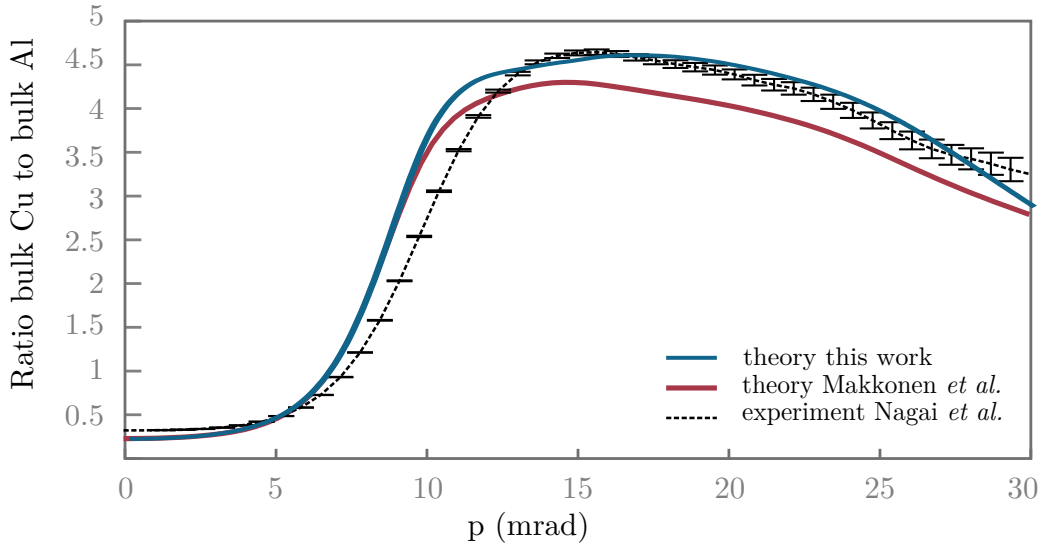

Figure 3.8: *Cu lattice/Al lattice ratio curves of momentum distributions of annihilation radiation. The result obtained in this study is compared with experimental data obtained by Nagai et al. [141] and with theoretical results of Makkonen et al. [115]. The theoretical curves are convoluted with a Gaussian function with a FWHM of 4.3 mrad.*

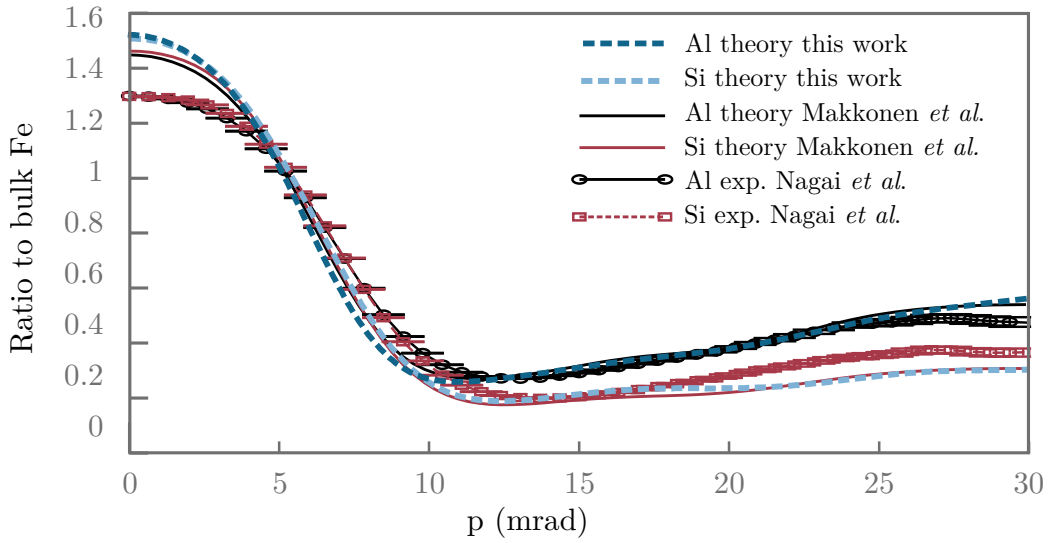

Figure 3.9: *Si attice/Fe lattice and Al lattice/Fe lattice ratio curves of momentum distributions of annihilation radiation. The result obtained in this study is compared with experimental data obtained by Nagai et al. [140] and with theoretical results of Makkonen et al. [115]. The theoretical curves are convoluted with a Gaussian function with a FWHM of 4.7 mrad.*

the calculations or that the sample contained some defects.

Finally, we tested our implementation on the case of a neutral monovacancy in Si. We performed calculations using a 216 atom supercell, taking the PAW dataset with 4 valence electrons and $2s$ and $2p$ states added in the positron wavefunction basis set. The results presented in Fig. 3.10

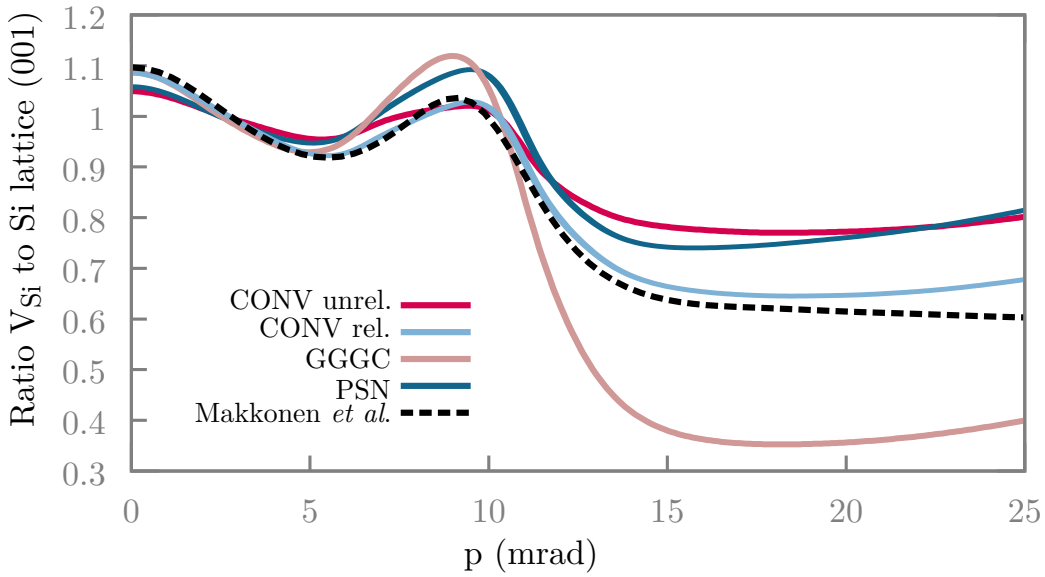

Figure 3.10: *V_{Si}/Si lattice ratio curves of momentum distributions of annihilation radiation in [001] direction. The results obtained in this study are compared with the results of Makkonen et al. [115]. The theoretical curves are convoluted with a Gaussian function with a FWHM of 3.7 mrad.*

were obtained using three different calculation schemes, CONV, GGGC and PSN. The vacancy was relaxed using the PSN and GGGC schemes. In the case of the CONV method we performed a calculation first taking unrelaxed positions and then taking the relaxed positions from the GGGC calculation. The results are compared with the results of Makkonen *et al.* [115]. First, we can observe that the low momentum regions are similar in all calculations and that a maximum near 10 mrad is always found. However, the high-momenta ratios differ strongly. The GGGC scheme yields the lowest high momentum ratio, which corresponds to the fact that this scheme overestimates the localization of the positron in the defect and thus predicts a lower positron density in the core region. As the positron localization is weaker in the PSN scheme, the ratio curve obtained using this method is closer to one. The calculation performed for the relaxed monovacancy using the CONV scheme can be compared with the result of Makkonen *et al.*, since they used a similar method in their study. The spectra are in rather good agreement up to 20 mrad, with a slightly higher high-momentum ratio yielded by our calculation. Above 20 mrad the agreement is not as good. This can be due to the fact that the methods used in these two calculations are slightly different.

In experimental studies, relative S_{rel} and W_{rel} parameters are often considered. In Tab. 3.4 we present these quantities calculated for the silicon monovacancy using the four methods described above. The S_{rel} and W_{rel} parameters were calculated as ratios of the vacancy and lattice Doppler spectra in [001] direction integrated from 0 to 3 mrad and from 10.7 to 27.4 mrad. It is worth noting there is no experimental Doppler broadening data available in literature, so that the

comparison with measurements is not possible for this defect.

Table 3.4: *Relative S_{rel} and W_{rel} parameters of silicon monovacancy obtained using different calculations schemes (CONV, GGGC and PSN). The relaxation, calculated as a percentage of the nearest neighbor distance compared with the ideal vacancy.*

Scheme	S_{rel}	W_{rel}	rel. (%)
CONV unrel.	1.027	0.830	0.0
CONV rel.	1.050	0.723	+7.4
GGGC	1.046	0.526	+7.4
PSN	1.030	0.802	+5.0

To be able to make a comparison with experimental measurements in Si, we also performed a test for a negatively charged silicon divacancy, since this defect has been observed for instance by Kauppinen *et al.* [142]. We convoluted the spectra with a Gaussian function with a FWHM of 4.7 mrad to mimic the experimental resolution in the reference study and calculated the S and W parameters in ranges from 0 to 3 mrad and from 11 to 20 mrad. The S_{rel} and W_{rel} parameters calculated using our implementation and the PSN scheme, 1.050 and 0.72, respectively, are in good agreement with 1.052±0.003 and 0.78±0.02 obtained experimentally.

3.3 Conclusions

In this chapter we first presented the tests performed to validate the implementation of the positron lifetime calculations in the ABINIT code. Then, we determined the optimal parameters for the calculations of positron annihilation characteristics of defects in SiC and UO_2. Third, we described the implementation of the methods needed to calculate the momentum distribution of the annihilation electron-positron pairs in the ABINIT code. The derivation of equations used to calculate the momentum distribution of annihilation radiation in the PAW formalism and their implementation in the ABINIT code was presented. Fourth, the problem of the positron wavefunction basis set completeness was identified and addressed. We presented the numerical solutions used in calculations of Doppler spectra, such as the choice of the grid in the reciprocal space, code parallelization and post-processing of the results. Finally, we described the tests performed to validate this new implementation and compared the computation results obtained for several materials with the data available in literature. These tests showed that our implementation yields results in good agreement with the reference data when complete enough PAW datasets are used. We thus consider that our various implementations are validated.

Chapter 4

Results on silicon carbide

To support the identification of defects in silicon carbide using positron annihilation spectroscopy, we performed three types of calculations: we calculated the formation energy to determine the most stable charges of various defects, the positron lifetimes and the momentum distributions. In this chapter we will present the results of these calculations and the analysis of the experimental data that can be made using the obtained results. The results described in this chapter have been partly published in Ref. [79], [143] and [144].

4.1 Formation energies and charge states of defects

Defect formation energy calculations were performed in two polytypes of SiC, $3C$-SiC and $6H$-SiC, for monovacancies and vacancy clusters, with charge states varying from -2 to $+2$. This was done to predict if a given vacancy can be detected by PAS and to know which charge state can be expected in the examined samples. We will first describe the methods used in the formation energy calculations and then present the results.

4.1.1 Methods used in formation energy calculations

The methods commonly used in formation energy calculations were already described in Sec. 2.2. To calculate the formation energy of charged defects in SiC we used a formula based on a standard formalism for semiconductors proposed by Zhang and Northrup [145] and adapted

by Zywietz, Furthmüller and Beckstedt [10] for SiC. The basic equation describing the defect formation energy E_{f} reads [9]:

$$E_{\mathrm{f}}(V_{\mathrm{X}}, q) = E_{\mathrm{tot}}(V_{\mathrm{X}}, q) - n_{\mathrm{C}}\mu_{\mathrm{C}} - n_{\mathrm{Si}}\mu_{\mathrm{Si}} + q\mu_{\mathrm{e}}, \tag{4.1.1}$$

where $E_{\mathrm{tot}}(V_{\mathrm{X}}, q)$ is the total energy of the supercell, n_{C} and n_{Si} are the numbers of carbon and silicon atoms in the cell, μ_{C} and μ_{Si} are the chemical potentials of the carbon and the silicon atoms in SiC, q is the charge of the defect and μ_{e} is the electron chemical potential, which varies from the bottom to the top of the band gap. We cannot, however, directly use Eq. (4.1.1) and approximations have to be used to determine the formation energy. Firstly, because the chemical potentials of carbon and silicon atoms in SiC are not known. Their values can be expressed in respect to the chemical potentials of C and Si in bulk diamond and silicon, $\mu_{\mathrm{C}}^{\mathrm{bulk}}$ and $\mu_{\mathrm{Si}}^{\mathrm{bulk}}$, respectively:

$$\mu_{\mathrm{C}} = \mu_{\mathrm{C}}^{\mathrm{bulk}} + \Delta\mu_{\mathrm{C}}, \tag{4.1.2}$$

$$\mu_{\mathrm{Si}} = \mu_{\mathrm{Si}}^{\mathrm{bulk}} + \Delta\mu_{\mathrm{Si}}. \tag{4.1.3}$$

The ranges of $\Delta\mu_{\mathrm{C}}$ and $\Delta\mu_{\mathrm{Si}}$ are determined by the formation enthalpy ΔH_{f} calculated as

$$\Delta H_{\mathrm{f}}(\mathrm{SiC}) = \mu_{\mathrm{SiC}}^{\mathrm{bulk}} - \mu_{\mathrm{Si}}^{\mathrm{bulk}} - \mu_{\mathrm{C}}^{\mathrm{bulk}}, \tag{4.1.4}$$

where $\mu_{\mathrm{SiC}}^{\mathrm{bulk}}$ is the energy per SiC pair in a perfect material. Considering the accessible ranges of $\Delta\mu_{\mathrm{C}}$ and $\Delta\mu_{\mathrm{Si}}$ (ΔH_{f}=0.58 eV) and the fact that the variations of stoichiometry in SiC are usually small, we choose to set $\Delta\mu_{\mathrm{C}} = \Delta\mu_{\mathrm{Si}} = \frac{1}{2}\Delta H_{\mathrm{f}}$ in our calculations.

The classical supercell approach fails in providing accurate formation energies for charged supercells, hence a second correction needs to be made in Eq (4.1.1). Even if a large number of atoms is used in calculations, the defects cannot be considered as isolated because of the long range electrostatic interactions. Various schemes of energy correction were proposed [106–108]. To minimize the numerical errors and to approximate the values of μ_{C} and μ_{Si} we chose to use the formula as follows to calculate the formation energy:

$$\begin{aligned} E_{\mathrm{f}}(V_{\mathrm{X}}, q) = \quad & E_{\mathrm{tot}}(V_{\mathrm{X}}, q) - n_{\mathrm{C}}\mu_{\mathrm{SiC}}^{\mathrm{bulk}} \\ & -(n_{\mathrm{Si}} - n_{\mathrm{C}})(\mu_{\mathrm{Si}}^{\mathrm{bulk}} + \frac{1}{2}\Delta H_{\mathrm{f}}(\mathrm{SiC})) \\ & +q(E_{\mathrm{VBM}} + \mu_{\mathrm{e}} + \Delta V) + \frac{2}{3}\Delta E_{\mathrm{el}}(q), \end{aligned} \tag{4.1.5}$$

where E_{tot} is the energy of the supercell with a defect. E_{VBM} is the energy of the valence band maximum in the perfect cell. ΔE_{el} is known as the Madelung correction, which was proposed

by Leslie and Gillan [106]. It is a simple electrostatic correction, introducing a monopole term ΔE_{el},

$$\Delta E_{\mathrm{el}} = \frac{\alpha q^2}{2\epsilon_0 L}, \tag{4.1.6}$$

where α is the Madelung lattice constant, ϵ_0 is the static dielectric constant and L is the length of the supercell edge. ΔE_{el} tends to overestimate the correction, as it takes into account only the monopole term of the electrostatic interaction. Therefore, we used an improved scheme proposed by Lany and Zunger [107], which contains only 2/3 of the Madelung term, along with a potential alignment ΔV. To calculate the ΔV, the method proposed by Taylor and Bruneval [108] taking

$$\Delta V = \langle v_{\mathrm{KS}}^{\mathrm{bulk}} \rangle - \langle v_{\mathrm{KS}}^{\mathrm{defect}} \rangle, \tag{4.1.7}$$

was used. $\langle v_{\mathrm{KS}}^{\mathrm{bulk}} \rangle$ and $\langle v_{\mathrm{KS}}^{\mathrm{defect}} \rangle$ are the average Kohn-Sham potentials calculated for the cell without and with the defect, respectively.

The formation energies of charged defects change with the electron chemical potential μ_{e}, but standard DFT is known to fail in predicting its range. Some authors vary μ_{e} up to the experimental conduction band minimum. We chose to plot our results only up to the theoretical band gap edge to be consistent with the method used. Our μ_{e} cannot hence be directly compared with the experimental one. It is rather an indication of the position of the chemical potential in the band gap and cannot be used as a quantitative estimation of i.e. the ionisation levels of the vacancies.

4.1.2 Computational details

The calculations of formation energies were performed using the ABINIT code. The PAW datasets were generated by the *atompaw* code [104]. In the carbon PAW dataset we treated $2s$ and $2p$ levels as valence states (level $1s$ included in the frozen core region), while for silicon we considered the $3s$ and $3p$ levels as valence states (levels $1s$, $2s$ and $2p$ included in the frozen core region), which corresponds to 4 valence electrons for both elements. For the electron-electron exchange-correlation, the GGA functional as parametrised by Perdew, Burke and Ernzerhof (PBE) [95] was used. We considered the spin polarization and allowed a full relaxation of the defects, at constant volume (the theoretical equilibrium volume), without symmetry conservation. The parameters used in calculations are presented in Table 4.1. This set of parameters ensured the cell parameters and total energy convergence of less than 10^{-3} Å and 2 meV/atom, respectively. Table 4.1 also lists the parameters needed for the electrostatic correction in Equation (4.1.7). For the relaxation of the defects we used the Broyden-Fletcher-Goldfarb-Shanno

minimisation (BFGS) [146–149]. Relaxation was stopped when all the forces acting on atoms were smaller than 0.005 eV/Å.

Table 4.1: *Parameters used in the calculations of the formation energies of charged defects in the two considered polytypes of silicon carbide. Madelung constants for zinc-blende and wurzite were taken. For the static dielectric constant of 6H-SiC we use an average of experimental values in ordinary and extraordinary directions [150].*

Polytype	3C-SiC	6H-SiC
Atomic sites	216	192
Plane wave E_{cut}	700 eV	700 eV
k-point mesh	2×2×2	4×4×2
Lattice parameters	$a = b = c = 4.39$ Å	$a = b = 3.10$ Å, $c = 15.21$ Å
Band gap energy	1.35 eV	2.01 eV
Madelung constant	1.638	1.641
Dielectric constant ϵ_0	9.72	9.84

4.1.3 Monovacancies

4.1.3.1 3C-SiC

Firstly we studied the formation energies of the V_C, V_{Si} and $V_C + C_{Si}$ defects with various charge states from -2 to $+2$ in 3C-SiC. The results for the considered defects are presented in Figure 4.1. We see that the carbon vacancy is positive for almost all the values of the electron chemical potential. It means that in the 3C polytype the V_C defect should be visible in PAS only in strongly n-doped samples, in which the Fermi level lays close to the conduction band minimum. The $V_C + C_{Si}$ complex should not be observed at all in 3C-SiC using PAS. According to our calculations the silicon vacancy should be detected for almost all types of doping if it is present. However, its formation energy is higher than the one of the $V_C + C_{Si}$ complex for all the electron chemical potentials laying in the gap. V_{Si} is thus metastable in 3C-SiC and should not be observed in thermodynamical equilibrium, as was already predicted in previous studies [9, 24]. Nevertheless, this defect can be created by irradiation and remain in the samples, if the temperature is not high enough for the transition between V_{Si} and $V_C + C_{Si}$ to happen.

4.1.3.2 6H-SiC

We also calculated the formation energies in 6H-SiC. In this polytype three nonequivalent atomic sites exist, one hexagonal h and two quasicubic, k_1 and k_2, as shown in Fig. 1.1. For V_C

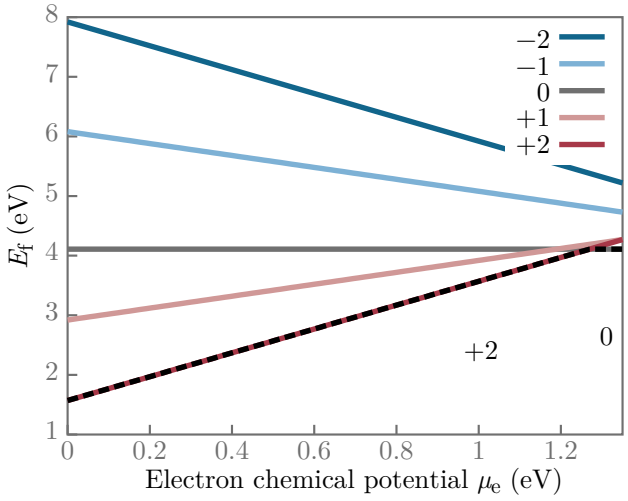

(a) V_C

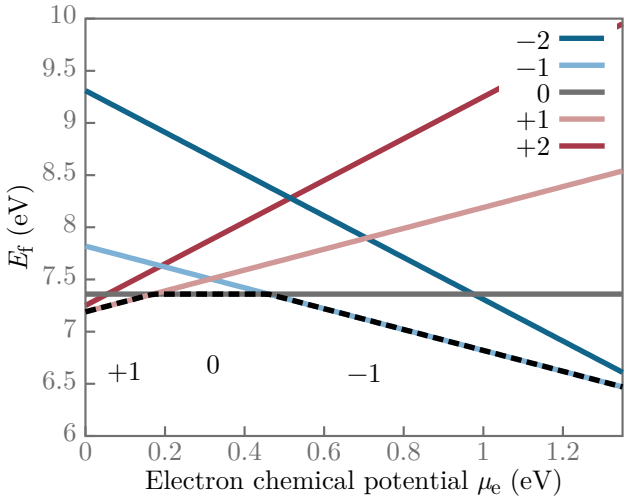

(b) V_{Si}

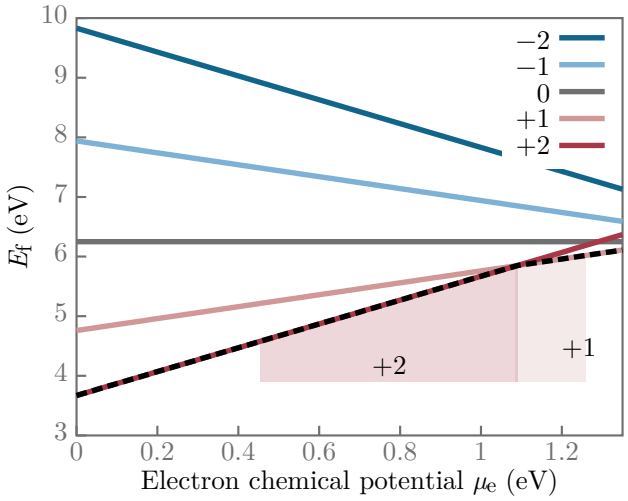

(c) $V_C + C_{Si}$

Figure 4.1: *Formation energies of various charge states of the three monovacancies in 3C-SiC.*

and V_{Si} we considered all three possible configurations. For the $V_C + C_{Si}$ complex we studied only the defects where the vacancy and the antisite atom are both on the same type of sites (k_1-k_1, k_2-k_2 and h-h).

We first performed calculations for the three possible carbon monovacancies. Results are presented in Fig. 4.2. The formation energies for the three sites differ only very slightly. For example for the neutral defects we found the formation energy of 4.23 eV at the h site, 4.15 eV at the k_1 site and 4.10 eV at the k_2 site. Moreover, the general forms of the charge state predominance as a function of μ_e are very similar. In Fig. 4.2 we compare the results obtained in 6H-SiC with the results obtained for 3C-SiC. The energies calculated in the 3C polytype are extrapolated to the edge of the theoretical conduction band minimum of the 6H structure (Fig. 4.2d). We see that the results obtained for 6H-SiC are very close to the extrapolated results obtained in 3C-SiC, especially in the case of the two quasicubic sites. It would be very convenient to be able to predict charge states of the defects in the hexagonal polytype based on the ones obtained in the cubic structure, as the calculations in the latter case are less time-consuming.

We compare the charge states of the V_{Si} and $V_C + C_{Si}$ defects in the 6H structure with the extrapolated results obtained in 3C-SiC. This time we consider only the defects at the hexagonal sites, since it was observed for the carbon vacancy that this case was the most different from the extrapolated results obtained in 3C-SiC. Results are presented in Fig. 4.3 and 4.4. In the case of the silicon vacancy we can observe the largest differences. However, as we are mostly interested in the charge state prediction for PAS experiments interpretation, we can consider that the extrapolation of the results obtained in 3C-SiC is good enough for our purpose.

As for the defect detectability, the case of 6H-SiC is different from the one of 3C-SiC. Due to a larger energy gap higher electron chemical potentials can be reached and defects can get more negative. In this polytype, the carbon vacancy should be visible in the n-type samples. For the $V_C + C_{Si}$ complex, there is a small region where it should be neutral, hence visible. However, unlike in the case of 3C-SiC, the complex is not always stable in 6H-SiC compared to V_{Si}. We show in Figure 4.5 the areas of stability of V_{Si} and $V_C + C_{Si}$. When the $V_C + C_{Si}$ complex is stable, it is positive and cannot therefore be detected by PAS. In n-doped materials, the silicon vacancy is stable, with at least a double negative charge state. The -3 and -4 charge states of this defect were not considered in our calculations but their existence is highly probable in strongly doped n-type 6H-SiC samples.

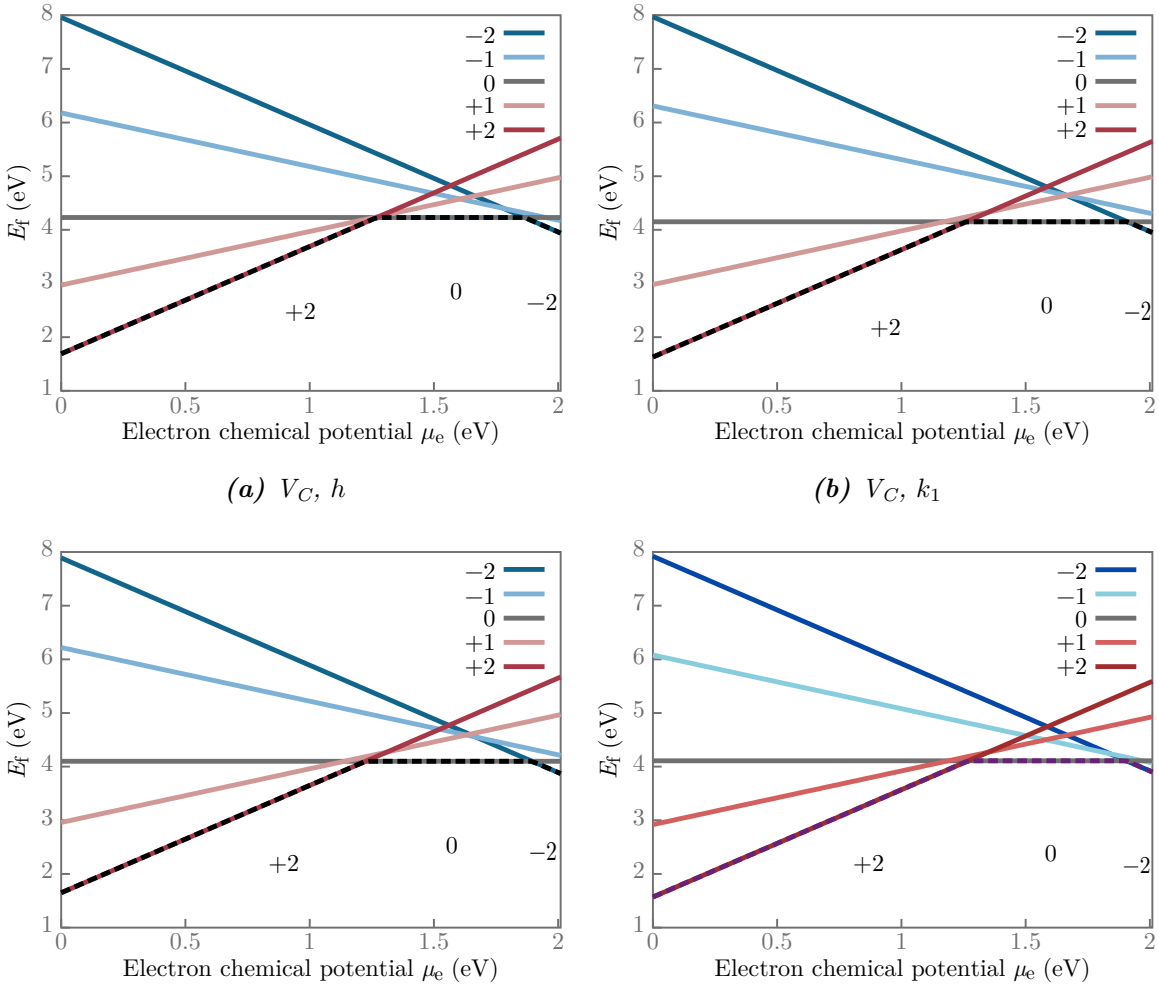

(a) *V_C, h* ***(b)*** *V_C, k_1*

(c) *V_C, k_2* ***(d)*** *Extrapolated 3C results for V_C*

Figure 4.2: *Formation energies of various charge states of the carbon vacancy in 6H-SiC, compared with results obtained in 3C polytype, extrapolated to the 6H-SiC gap end.*

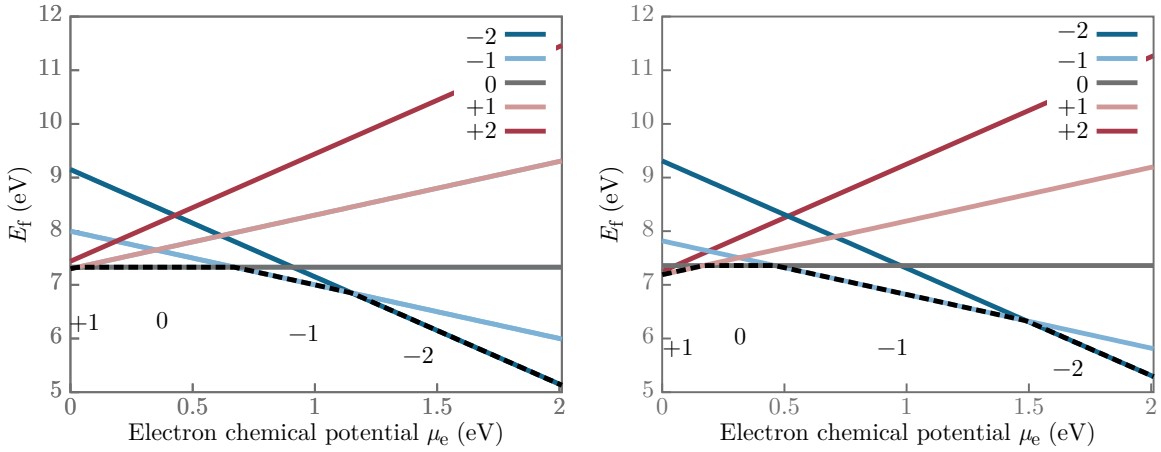

(a) *V_{Si}, h* ***(b)*** *Extrapolated 3C results for V_{Si}*

Figure 4.3: *Formation energies of various charge states of the silicon vacancy in 6H-SiC, compared with results obtained in 3C polytype, extrapolated to the 6H-SiC gap end.*

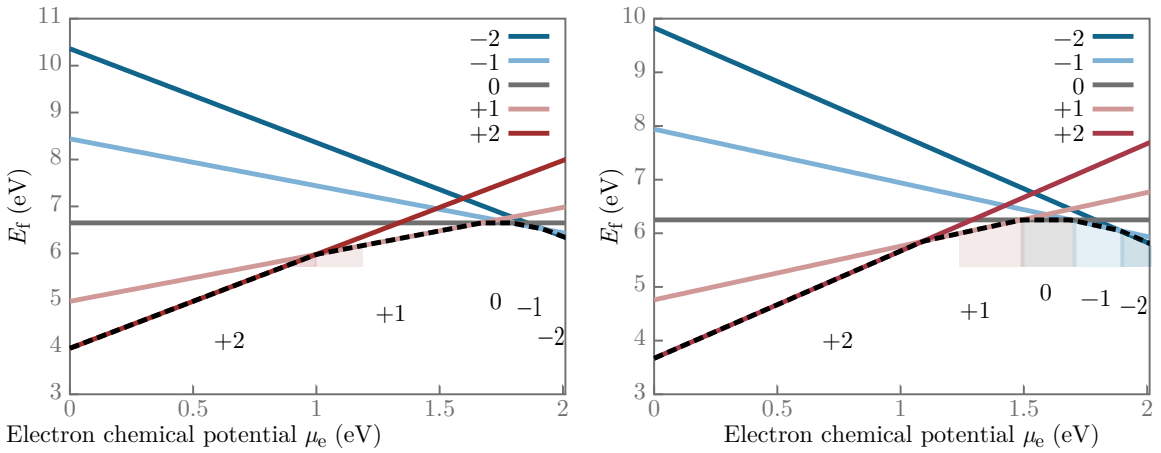

(a) *$V_C + C_{Si}$, h-h* ***(b)*** *Extrapolated 3C results for $V_C + C_{Si}$*

Figure 4.4: *Formation energies of various charge states of the V_C+C_{Si} complex in 6H-SiC, compared with results obtained in 3C polytype, extrapolated to the 6H-SiC gap end.*

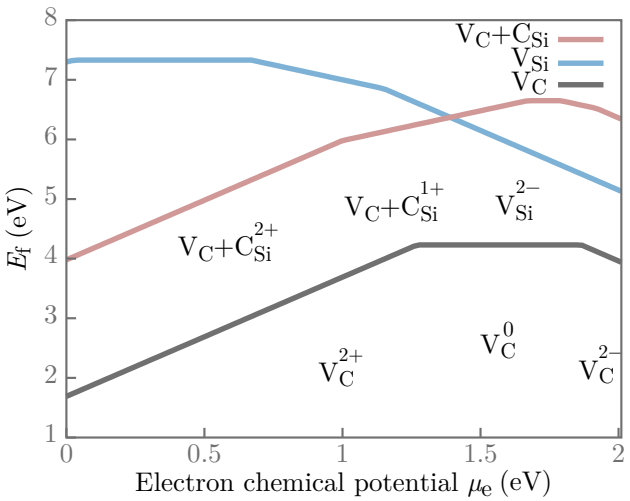

Figure 4.5: *Comparison of the formation energies of three hexagonal defects in 6H-SiC. For V_C+C_{Si} and V_{Si} only the regions where they are stable are coloured.*

4.1.4 Defect clusters

We calculated the formation energies of the vacancy-complexes in 3*C*-SiC, varying the charge from −2 to +2. Calculations were performed for 6 different defects: V_C+V_C, V_C+V_{Si}, V_C+V_{Si}+C_{Si}, V_C+V_{Si}+V_C, V_{Si}+V_C+V_{Si} and $(V_C$+$V_{Si})_2$. Initially we had considered a silicon divacancy V_{Si}+V_{Si}, but during relaxation with a positron, this defect transformed to a V_C+V_{Si}+C_{Si} complex, so we studied it instead.

The evolutions of the formation energies as a function of the electron chemical potential are presented in Figures 4.6a to 4.6f. All results are extrapolated to the theoretical gap edge of 6*H*-SiC (2.01 eV), as it has been shown that the results in the hexagonal polytype can be obtained from those in the 3*C*-SiC using this kind of extrapolation. We can observe that the carbon divacancy, V_C+V_C, has a positive charge for a wide range of Fermi levels. It should thus be difficult to observe this defect in 3*C*-SiC and in the hexagonal polytype it should be only detected in n-type samples. The V_C+V_{Si} divacancy is found to be neutral for a wide range of μ_e, as expected, since this is a stoichiometric defect. This defect should be mostly neutral if detected in 3*C*-SiC, while in 6*H*-SiC it should be neutral for undoped or slightly doped sample and negative in more n-doped samples. The V_{Si}+V_C+C_{Si} complex has a positive charge state only for Fermi levels laying close to the maximum of the valence band and should therefore be possible to detect in undoped and n-type samples in both polytypes. The V_C+V_{Si}+V_C trivacancy should be detected in n-type 3*C*-SiC and in undoped and n-doped 6*H*-SiC. The second trivacancy, V_{Si}+V_C+V_{Si}, is negative for majority of the possible Fermi levels and should, hence, strongly attract the positrons if present in the material. Finally, the $(V_C$+$V_{Si})_2$ tetravacancy, which is

Table 4.2: *Calculated spin states of defect clusters in 3C-SiC.*

Defect	Charge state				
	-2	-1	0	$+1$	$+2$
V_C+V_C	0	1/2	0	1/2	0
V_C+V_{Si}	0	1/2	1	1/2	0
V_{Si}+V_C+C_{Si}	1	1/2	1	1/2	0
V_C+V_{Si}+V_C	1	1/2	2	1/2	1
V_{Si}+V_C+V_{Si}	2	5/2	3	5/2	0
$(V_C$+$V_{Si})_2$	1	3/2	2	3/2	1

also a stoichiometric defect, has a narrower range for neutral charge stability than the divacancy. This defect, however, should be neutral in undoped $3C$-SiC. In $6H$-SiC it can start to have a -1 charge states for Fermi levels close to the middle of the band gap.

To enable the comparison between the studied defects, we present in Figure 4.4 the formation energies of the most stable charge states of all defects. Additionally, we recall in this figure the results obtained for the monovacancies. These results were obtained in the $3C$ polytype and are extrapolated to the theoretical gap edge of $6H$-SiC (2.01 eV).

Several theoretical studies [10, 151, 152] showed that the silicon vacancy in silicon carbide is a high spin defect. Similarly, high spin states are also expected for the vacancy clusters containing V_{Si}. In Tab. 4.2 we present the calculated spin states of the vacancy clusters in $3C$-SiC, which can be useful in the EPR measurements interpretations. The results presented in Tab. 4.2 show that the majority of the defects should have a non-zero spins. It suggests that it should be possible to detect the majority of them in EPR. It is consistent with the fact that several types of defects were detected in SiC using this method [33–38, 153, 154].

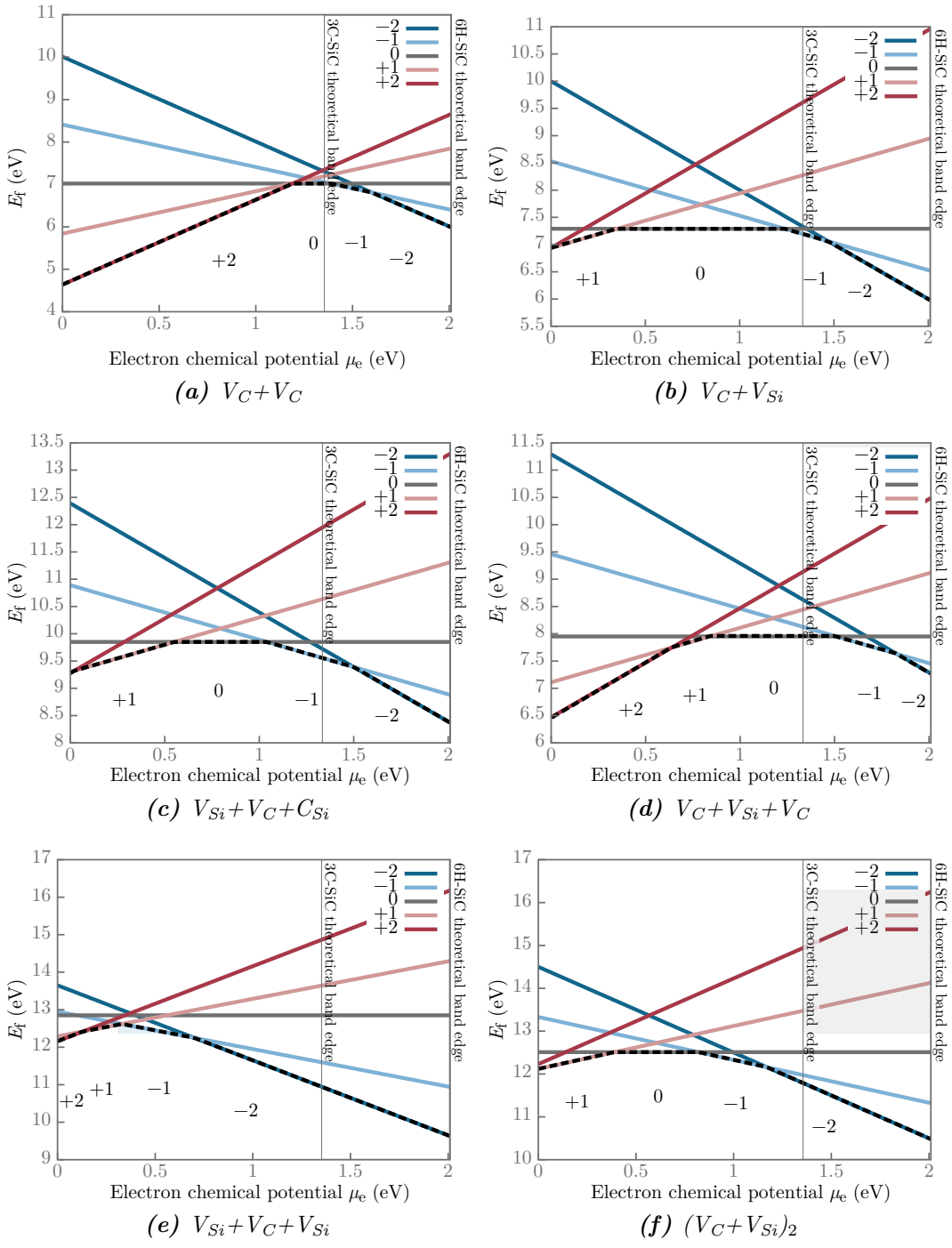

Figure 4.6: *Formation energies of various charge states of vacancy-complexes calculated in 3C-SiC (white background). Results are extrapolated to the 6H-SiC gap end (gray background).*

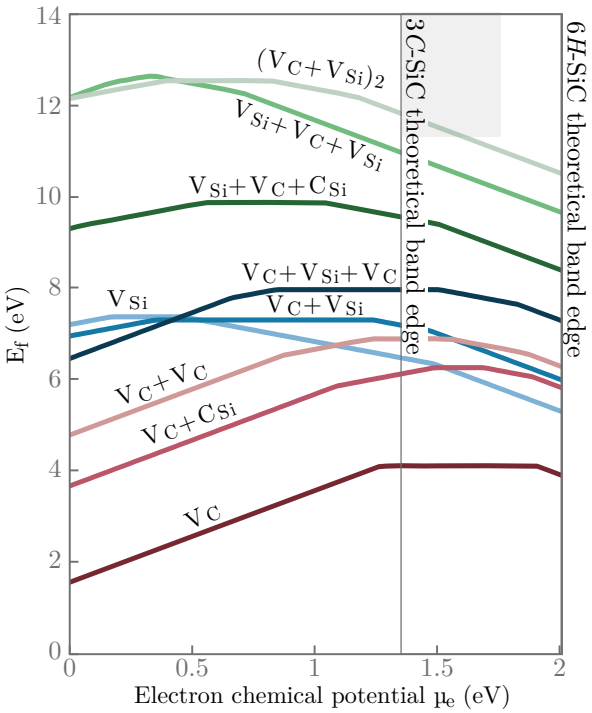

Figure 4.7: *(Formation energies of the most stable charge states of the vacancy complexes studied in stoichiometric 3C-SiC (white background). Results are extrapolated to the top of the 6H-SiC gap (gray background).*

4.2 Positron lifetimes

In this section, the positron lifetimes calculated for neutral and charged vacancies in 3C and 6H-SiC are presented. The tests performed in order to determine the methods used in these calculations are shown in Sec. 3.1.4.

4.2.1 Computational details

The parameters used in positron lifetime calculations in silicon carbide are given in Table 4.3. This set of parameters was sufficient to obtain a structural convergence of less than 10^{-3} Å and an energy precision of less than 2 meV per atom. We permitted a full defect relaxation without conservation of the initial point symmetry at constant volume (the theoretical equilibrium volume). In the formation energy calculations we considered the spin polarization. For the atomic relaxation we used the Broyden-Fletcher-Goldfarb-Shanno minimization scheme (BFGS) [146–149]. Relaxation was stopped when the forces acting on atoms were smaller than 0.005 eV/Å.

In the study on positron lifetimes in 3C-SiC we used supercells with 216 atoms. To verify if this cell is large enough we compared the results obtained for the largest defect considered, the chain hexavacancy (see Sec. 4.2.2.3), in 64, 216 and 512 atoms cells. We obtained 288, 270 and 270 ps, respectively. With a difference between the results obtained in 216 and 512 atom supercells smaller than 1 ps, we assume that the 216 atom cell is large enough for the positron lifetime calculations.

Table 4.3: *Parameters used in the calculations of the positron lifetimes in the two considered polytypes of silicon carbide. For the high-frequency dielectric constant of 6H-SiC we use the average of the experimental values in the ordinary and extraordinary directions.*

Polytype	3C-SiC	6H-SiC
e-e x-c functional	LDA	LDA
Atomic sites	216	192
E_{cut}	600 eV	600 eV
Valence states C	2s, 2p	2s, 2p
Valence states Si	2s, 2p, 3s, 3p	2s, 2p, 3s, 3p
k-point mesh	2×2×2	4×4×2
Lattice parameters	$a = b = c = 4.33$ Å	$a = b = 3.06$ Å
ϵ_∞	6.52 [150]	6.61 [150]

4.2.2 3C-SiC

4.2.2.1 Neutral monovacancies

We first performed calculations for neutral monovacancies in 3C-SiC using three calculations schemes, CONV, GGGC and PSN. Results are presented in Table 4.4 and compared with the lifetimes obtained by Brauer *et al.* [58] Their calculations were done in the conventional scheme including a semiconductor correction. They used the atomic superimposition method in a supercell containing 64 atoms, at the experimental volume and they did not take into account the relaxation effect.

We see that in our study all the defects relax strongly outwards. This leads to much longer lifetimes than the ones predicted by Brauer *et al.* This shows clearly that the effect of the positron on the relaxation cannot be neglected. It can also be observed that the GGGC scheme leads to larger relaxations than PSN. Binding energies (E_b) between the positron and the defect, i.e. the differences between the positron energies in the lattice and in the defect, were also calculated in the three schemes. They are presented in Table 4.5. A positive value of E_b

Table 4.4: *Positron lifetimes calculated in 3C-SiC compared with the results of Brauer et al. [58]. Atomic relaxations are calculated as a relative change in distances between the first neighbours of the defect compared to the perfect defect. Relative lifetimes, calculated using Eq. (3.1.6), are given in parentheses.*

	Lifetime CONV	Lifetime ref. [58]	Lifetime GGGC	Relaxation GGGC	Lifetime PSN	Relaxation PSN
Lattice	153	138	153		144	
V_C	154 (1%)	153 (11%)	217 (42%)	+17%	195 (35%)	+12%
V_{Si}	198 (28%)	191 (38%)	231 (51%)	+12%	227 (58%)	+12%
V_C+C_{Si}	170 (11%)	-	217 (42%)	+27% C-Si +9% Si-Si	203 (41%)	+21% C-Si +7% Si-Si

Table 4.5: *Binding energies between the positron and the defect calculated in various schemes, as a difference between the energy of the positron in lattice and in the defect. Positive values mean positron trapping.*

	E_b CONV (eV)	E_b GGGC (eV)	E_b PSN (eV)
V_C	−0.18	+2.65	+1.07
V_{Si}	+2.41	+5.07	+2.08
V_C+C_{Si}	+0.89	+3.82	+1.61

means that the positron is trapped in the defect. It can be seen that the conventional scheme does not predict the positron trapping in the carbon vacancy, which is found using the GGGC and PSN schemes. Moreover, we found that GGGC yields much larger binding energies than the two other schemes. This is consistent with the overestimation of the positron localization in this scheme, that was already reported by Car *et al.* [119]. Because of this effect, the relaxation predicted in GGGC can be incorrect. Therefore we decided to use the PSN method, which contains more accurate approximations, in further studies.

4.2.2.2 Charged monovacancies

Our study of the charge states of the defects in silicon carbide showed that the neutral defects should not be the only ones to be observed in the PAS experiments. We thus performed calculations for the negatively charged defects as well. We did not consider positive defects as they should not be observed by this experimental technique. Results are presented in Table 4.6. The positron lifetimes of the negative vacancies are slightly shorter than for the neutral ones. It is first due to the fact that the additional negative charges increase the annihilation rate. Secondly, the additional electrons take part in the bonding and reduce the outwards relaxation.

Table 4.6: *Calculated positron lifetimes of negative and neutral monovacancies in 3C-SiC. Results obtained in the PSN scheme are presented. Relative lifetimes are calculated using Eq. (3.1.6).*

	Lifetime PSN (ps)	Relative lifetime	Relaxation PSN
Lattice	144		
V_C^0	195	35%	+12%
V_C^{1-}	193	34%	+10%
V_C^{2-}	188	31%	+10%
V_{Si}^0	227	58%	+12%
V_{Si}^{1-}	225	56%	+11%
V_{Si}^{2-}	222	54%	+11%

However, the differences between the lifetimes of neutral and negative defects are relatively small (around 5 ps).

4.2.2.3 Vacancy clusters

We calculated the positron lifetimes of all neutral vacancy complexes in 3*C*-SiC containing from two to six vacancies. As the lattice lifetime obtained in our calculations is slightly longer than the experimental one (144 ps compared to 140 ps [55]), we also present the lifetimes scaled to this experimental value. The results are presented in Table 4.7 and compared with the results obtained previously by Brauer *et al.* [58, 59]. The superimposed atom model was used and the atomic relaxation and the influence of the positron on the electronic density were not taken into account, as stated in the previous section.

As was shown above the relaxation effect is important in calculations for SiC. We find longer lifetimes than in the study of Brauer *et al.* because all defects relaxed outwards in our study. We can observe that the differences between the two sets of calculations decrease when the cluster size increases. The fact that the relaxation decreases for larger defects is consistent with what was shown for example for vacancy clusters in Si [134, 155, 156].

It can be noticed that in some cases, the positron lifetimes can be very similar for different defects. For V_C, V_C+C_{Si} and V_C+V_C we find lifetimes of 195, 203 and 201 ps, respectively. This can be explained by the fact that, in all of these defects, the positron density is localized at one empty carbon atomic site, as shown in Fig. 4.8. Additionally, it is worth noting that in the V_C+V_C divacancy the positron is localized in one of the two defects. It means that this

Table 4.7: *Positron lifetimes of the relaxed neutral defect clusters in 3C-SiC. The results are presented along with the lattice and monovacancies lifetimes from Ref. [143] and compared with results of Brauer et al. [58, 59] Additionally to the calculated values we present the lifetimes scaled to the experimental lattice lifetime of 140 ps. [55]*

Defect	Lifetime PSN (ps)	Scaled lifetime (ps)	Lifetime ref. [58, 59]
Lattice	144	140	141
V_C	195	190	150
V_{Si}	227	221	185
V_C+C_{Si}	203	197	
V_C+V_C	201	195	
V_C+V_{Si}	242	235	216
V_{Si}+V_C+C_{Si}	245	238	
V_C+V_{Si}+V_C	250	243	
V_{Si}+V_C+V_{Si}	269	262	
$(V_C+V_{Si})_2$	269	262	254
$(V_C+V_{Si})_3^{chain}$	270	263	286[1]
$(V_C+V_{Si})_3^{ring}$	304	296	286[1]

[1]In the reference, the configuration of the cluster is not specified.

cluster, in which the two vacancies are second neighbors, is seen as two separated defects by the positron.

Similarly, lifetimes of 242, 245 and 250 ps were found for the V_C+V_{Si}, V_{Si}+V_C+C_{Si} and V_C+V_{Si}+V_C clusters, respectively. All these defects contain one silicon vacancy and the positron density is localized at its site (see Fig. 4.9). Additionally, the density has a similar spherical form in all of these defects and it is almost not affected by the presence of carbon vacancies nor by a carbon atom in the antisite position, in the case of V_{Si}+V_C+C_{Si}.

For the two defects containing two silicon vacancies - V_{Si}+V_C+V_{Si} and $(V_C+V_{Si})_2$ - the same lifetime of 269 ps was found. As in the case of defects with one V_{Si} only, the positron density is not sensitive to the additional carbon vacancy (Fig. 4.10) and is mainly situated between the two silicon vacancies. It is worth noting that for the $(V_C+V_{Si})_2$ defect various configurations are possible, with different distances between the furthest Si and C vacancies. However, for all these configurations the V_{Si}-V_{Si} distance is the same and since the positron is not sensitive to the position of the additional carbon vacancy, the lifetimes of these configurations were found to differ by less than 1 ps.

For the $(V_C+V_{Si})_3$ defect even more different configurations are possible than for $(V_C+V_{Si})_2$. Additionally, in these configurations, the silicon vacancies are not distributed in the same way.

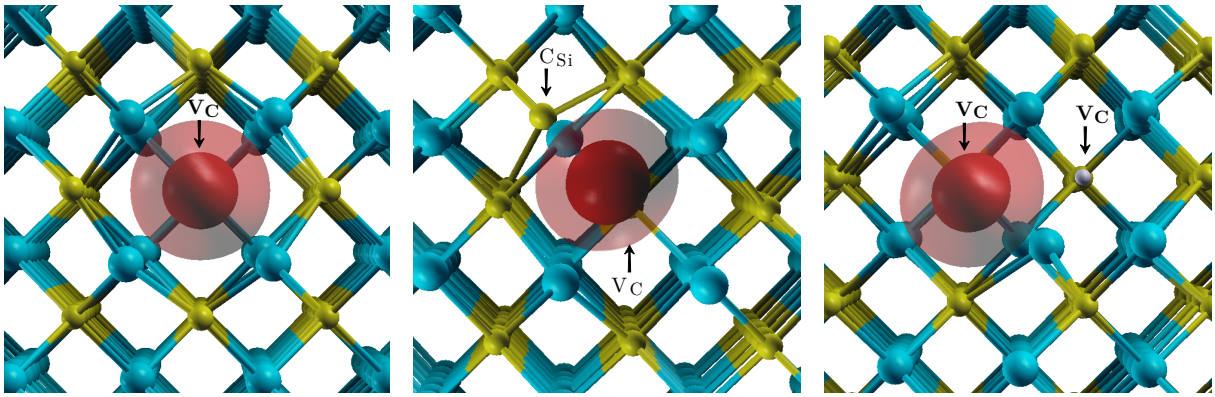

(a) V_C *(b)* V_C+C_{Si} *(c)* V_C+V_C

Figure 4.8: *Positron isodensities (solid traced for 70% of the maximum density, transparent for 30%), in red, in* V_C*,* V_C+C_{Si} *and* V_C+V_C*, in 3C-SiC.*

We studied the two extreme cases, a chain configuration and a ring one (see Fig. 4.11). We found the lifetimes of 270 ps for the chain and 304 ps for ring. In the chain $(V_C+V_{Si})_3$ the three silicon vacancies form a line and the positron is localized in the central silicon vacancy (see Fig. 4.11a). In the ring hexavacancy, the three silicon vacancies form a triangle inside which the positron is localized (see Fig. 4.11b). We can observe that the positron lifetimes calculated for these two configurations of the hexavacancy differ strongly. Moreover, the lifetime calculated for the chain hexavacancy is close to the one calculated for the tetravacancy (269 ps).

To determine which configuration of the hexavacancy is more stable we calculated their formation energies. We found 15.16 eV and 17.79 eV for the neutral charge states of the ring and chain configurations, respectively. It suggests that the ring structure is more stable and will more likely be formed in the material. It has to be kept in mind, however, that the calculations were performed for the neutral charge state only and that the relative stability of these configurations may depend on the charge state and the position of the Fermi level.

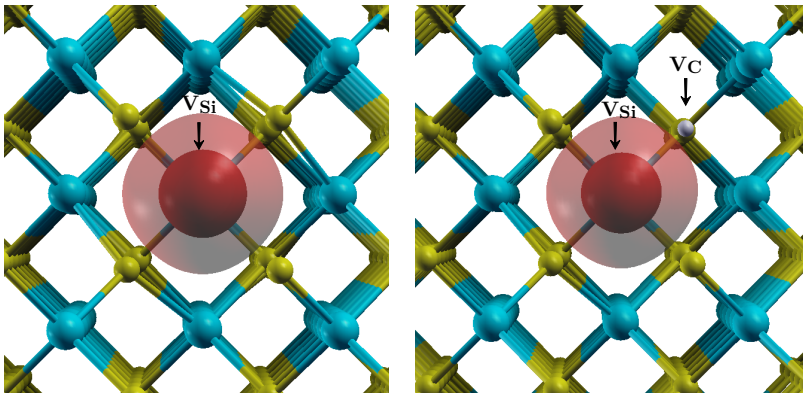

(a) V_{Si} *(b)* V_C+V_{Si}

(c) V_{Si}+V_C+C_{Si} *(d)* V_C+V_{Si}+V_C

Figure 4.9: *Positron isodensities (solid traced for 70% of the maximum density, transparent for 30%), in red, in the defects containing one silicon vacancy, in 3C-SiC. Carbon atoms are presented in yellow, silicon atoms in blue. White spheres represent the carbon vacancies.*

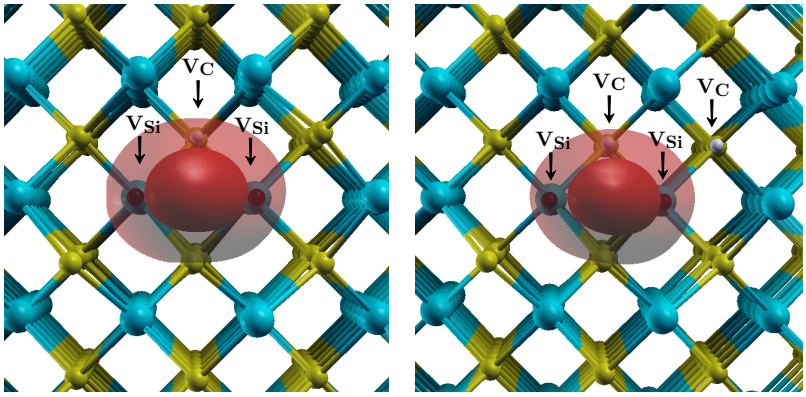

(a) V_{Si}+V_C+V_{Si} *(b)* $(V_C$+$V_{Si})_2$

Figure 4.10: *Positron isodensities (solid traced for 70% of the maximum density, transparent for 30%), in red, in the defects containing two silicon vacancies, in 3C-SiC. Carbon atoms are presented in yellow, silicon atoms in blue. Carbon and silicon vacancies are represented by white and black spheres, respectively.*

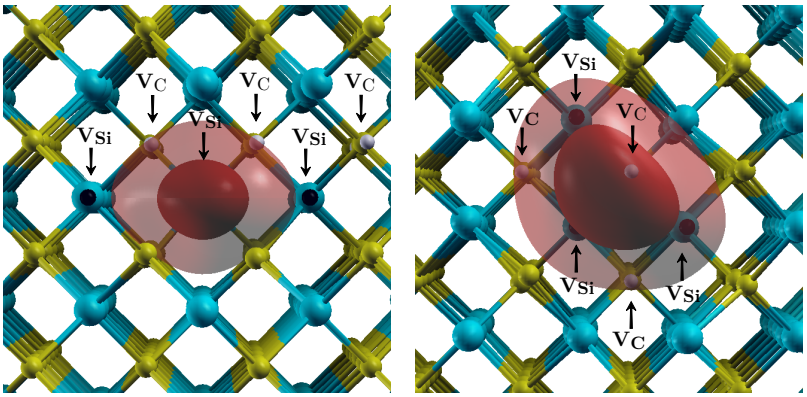

(a) $(V_C{+}V_{Si})_3^{chain}$ **(b)** $(V_C{+}V_{Si})_3^{ring}$

Figure 4.11: *Positron isodensities (solid traced for 70% of the maximum density, transparent for 30%), in red, in two configurations of a hexavacancy, in 3C-SiC. Carbon atoms are presented in yellow, silicon atoms in blue. Carbon and silicon vacancies are represented by white and black spheres, respectively.*

4.2.3 6*H*-SiC

4.2.3.1 Neutral monovacancies

It has been shown in the literature [58, 59] that the positron lifetimes of various defects are similar in different polytypes. However the defect relaxation was not taken into account in the earlier calculations. We performed PSN calculations for selected configurations of the three defects in the hexagonal polytype to verify if the defect free volumes evolve in the same way in 3*C*-SiC and 6*H*-SiC. Results are presented in Table 4.8.

The lattice lifetime obtained for the hexagonal polytype is very close to the one of the cubic structure and in a good agreement with the experimental lifetime of 140 ps [55] obtained for this polytype. We can see from the comparison between Tables 4.4 and 4.8 that the lifetimes of defects at hexagonal sites in 6*H*-SiC are also very similar to those in 3*C*-SiC. Additionally, for the silicon vacancy there are only small differences between the three possible sites and relaxations are also similar. For V_C and $V_C{+}C_{Si}$, however, we find significantly shorter lifetimes when the defect is located at one of the quasicubic sites, which is related to the large differences in the relaxations of k_1-k_1 and k_2-k_2 configurations of $V_C{+}C_{Si}$. The relaxation induced by the positron makes the first neighbors of the vacancy move relatively far from their perfect positions. However, this outward displacement is limited by the second neighbors or even the third neighbors, whose configuration is not the same for each site. The reorganization is different for the two sublattices and this effect is smaller for V_{Si}. This probably explains the differences in

Table 4.8: *Positron lifetimes and atomic relaxations calculated in the PSN scheme. Selected defects of the 6H polytype are considered. Relative lifetimes are calculated using Eq. (3.1.6). The relaxation indicated is calculated as the average relative change in distance between the first neighbors of the defect.*

	Site	Lifetime PSN (ps)	Relative lifetime	Relaxation PSN
Lattice		143		
V_C	h	193	35%	+12%
V_C	k_1	175	22%	+5%
V_C	k_2	173	21%	+6%
V_{Si}	h	226	58%	+11%
V_{Si}	k_1	226	58%	+10%
V_{Si}	k_2	226	58%	+10%
V_C+C_{Si}	h-h	204	43%	+18% C-Si +6% Si-Si
V_C+C_{Si}	k_1-k_1	202	41%	+18% C-Si +4% Si-Si
V_C+C_{Si}	k_2-k_2	188	31%	+11% C-Si +6% Si-Si

lifetimes and relaxations for defects at different sites and the differences with the $3C$-SiC case. In the case of the carbon vacancy, the three possible configurations can be present in the material. Since the corresponding lifetimes are not the same, we can expect that the experimental value corresponds to the mixing weighted by the fraction of the detected defects and their trapping coefficients.

4.2.3.2 Charged monovacancies

We also performed positron lifetime calculations for negative monovacancies in $6H$-SiC. We considered carbon and silicon vacancies with a -2 charge state as these were the only negative defects that should be detected by PAS in this polytype according to our calculations of the formation energies. Results are presented in Table 4.9. Positron lifetimes of all V_{Si} configurations and for the two quasicubic types of V_C are only slightly shorter than for the neutral defects. It is similar to the case of $3C$-SiC. The lifetime of the negative hexagonal carbon vacancy is 13 ps shorter than for the neutral one (shown in Table 4.8), which is caused by a much smaller outward relaxation of this particular defect.

Table 4.9: *Calculated positron lifetimes of monovacancies with a -2 charge state in 6H-SiC. Results obtained in the PSN scheme are presented. Relative lifetimes are calculated using Eq. (3.1.6).*

	Site	Lifetime PSN (ps)	Relative lifetime	Relaxation PSN
Lattice		143		
V_C^{2-}	h	180	26%	+6%
V_C^{2-}	k_1	170	19%	+2%
V_C^{2-}	k_2	171	20%	+3%
V_{Si}^{2-}	h	222	55%	+10%
V_{Si}^{2-}	k_1	223	56%	+11%
V_{Si}^{2-}	k_2	222	55%	+10%

Table 4.10: *Comparison of positron lifetimes of divacancies in 3C-SiC and 6H-SiC. Lifetimes scaled to the experimental lattice lifetime of 140 ps [55] are presented in the last column.*

	Site	Lifetime PSN (ps)	Scaled lifetime (ps)
Lattice	$3C$	144	
V_C+V_{Si}	$3C$	242	235
Lattice	$6H$	143	
V_C+V_{Si}	$6H_{h-h}$	241	236
V_C+V_{Si}	$6H_{k_1-k_1}$	240	235
V_C+V_{Si}	$6H_{k_2-k_2}$	239	234
V_C+V_{Si}	$6H_{k_1-k_2}$	240	235
V_C+V_{Si}	$6H_{h-k_1}$	241	236
V_C+V_{Si}	$6H_{k_2-h}$	241	236

4.2.3.3 Vacancy clusters

In the study on smaller defects we observed that in the case of the carbon vacancy, the positron lifetime differs between the polytypes and between the three possible sites in $6H$-SiC. For the silicon vacancy, these differences were around 1 ps. To verify whether the positron lifetimes of the vacancy complexes depend on the polytype or on the atomic sites in the case of $6H$-SiC, we performed calculations for all possible configurations of the V_C+V_{Si} divacancy in the hexagonal polytype. Results are presented in Tab. 4.10. We observe that the lifetimes of divacancies in $6H$-SiC are very similar, with differences between 1 and 2 ps, and close to the lifetime of this defect in $3C$-SiC. These results suggest that the positron lifetimes calculated for vacancy complexes in $3C$-SiC can be used for the interpretation of the PAS experiments performed on the $6H$-SiC samples.

4.3 Doppler broadening of annihilation radiation

In this section we present the calculations of the momentum distributions of the annihilation radiation calculated for various defects in two silicon carbide polytypes, $3C$ and $6H$.

4.3.1 Computational details

The momentum distribution calculations have been performed using 216 and 192 atom supercells for $3C$-SiC and $6H$-SiC, respectively, using the state-dependent scheme, with the PSN parametrization and in geometries relaxed according to both the electronic and positronic forces. In these calculations the positron wavefuntion has been calculated at two $\mathbf{k}$-points, the Γ point and another one chosen to lie on the edge of the Brilloun zone, to avoid the delocalization of the positron due to the small supercell, as proposed by Korhonen *et al.* [157]. The momentum distributions have been calculated using the wavefunctions corresponding to the Γ point only. We used the cut-off energy of 680 eV, since we found it was enough to obtain Doppler spectra converged up to 40 mrad.

4.3.2 Neutral vacancies in $3C$-SiC

In Fig. 4.12 we present the results obtained for fully relaxed neutral vacancies in $3C$-SiC as ratios to perfect lattice. All the presented spectra have been convolved with a Gaussian function with FWHM=4.7 mrad, which corresponds to the resolution of experiments performed at the CEMHTI laboratory and discussed in the following sections. The results are presented for momenta between 0 and 40 mrad, which are the ranges usually used when presenting experimental data.

We can observe a clear difference between the shapes of the ratio curves obtained for monovacancies on the two different SiC sublattices. The ratio calculated for the carbon vacancy has a maximum of around 1.07 at $p = 0$, decreases below 1 for momenta higher that 4 mrad and exhibits two slight shoulders, one at 11.5 mrad and one around 30 mrad. The form of the ratio calculated for the V_C+V_C divacancy is very similar to that of V_C, with the latter being slightly closer to the perfect lattice.

For V_{Si} we also observe a maximum of around 1.06 at $p = 0$ and the ratio curve drops below 1 at around 4 mrad. Contrary to V_C, at around 11.5 mrad a peak can be observed, with a

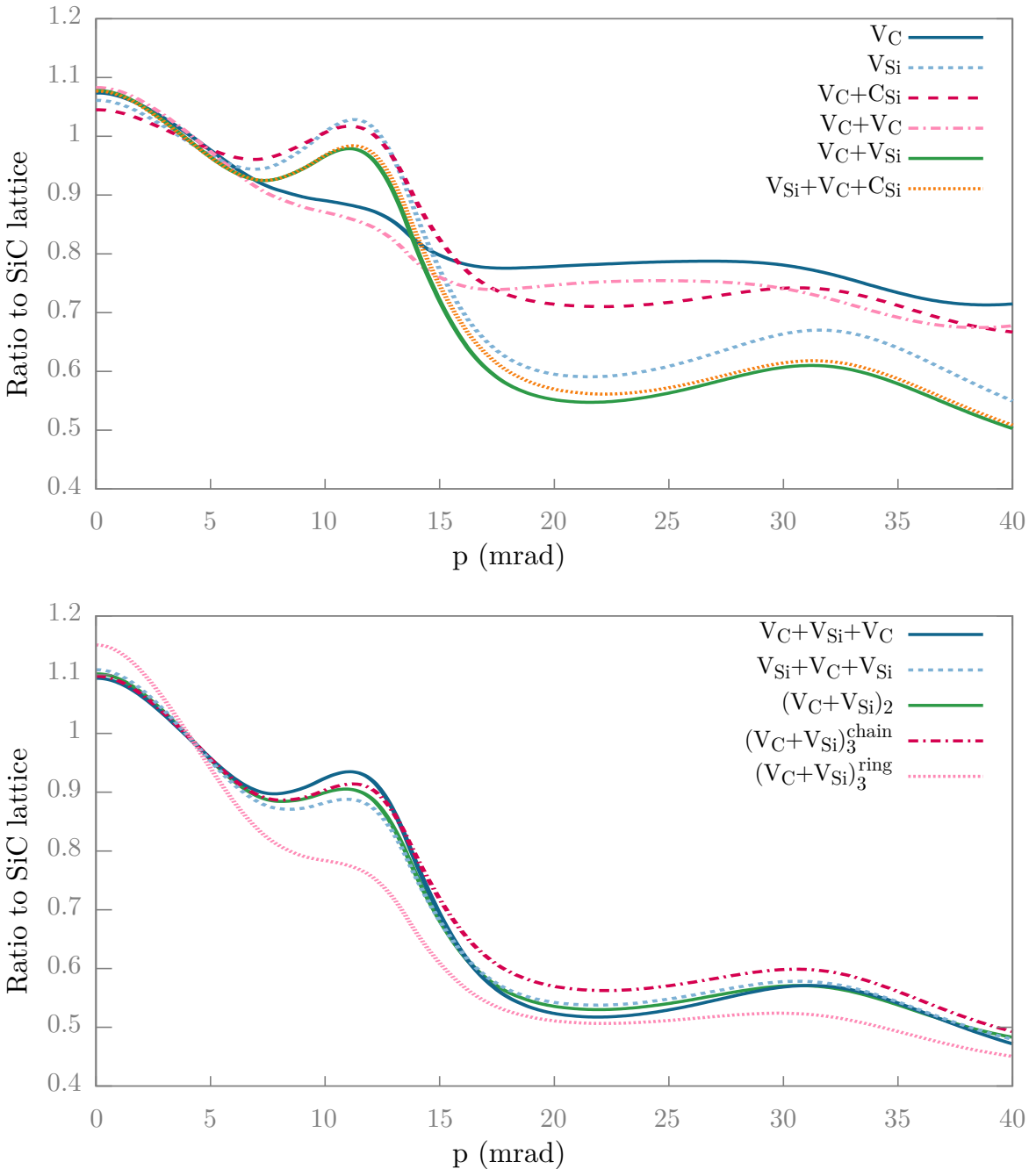

Figure 4.12: *Ratio curves of the calculated momentum distributions of annihilating electron-positron pairs in various vacancies in SiC. All spectra are convoluted with a Gaussian of 4.7 mrad and divided by the lattice spectrum.*

value above 1. This peak can be probably attributed to the annihilation with $2p$ electrons of the carbon atoms, which are expected to be the ones most likely to annihilate with the positron localized at the silicon site. Another peak is observed above 30 mrad with a value around 0.67. The overall shape of the ratio calculated for V_{Si} is in agreement with the previous calculations for this defect performed by Kawasuso *et al.* [63], even if the high-momentum ratio is slightly lower in our calculations (with differences around 0.1). This can be due to the atomic relaxation, which was not fully taken into account in the study of Kawasuso *et al.*

As for the V_C+C_{Si} cluster, the calculated ratio curve has a shape similar to that of the silicon vacancy at low momenta. This can be explained by the fact that even though in this defect the positron is surrounded by one carbon and three silicon atoms, it localizes closer to the antisite C atom (see Fig. 4.8) and the annihilation rate should be the highest with its electrons. The ratio calculated for V_C+C_{Si} is significantly higher at $p > 15$ mrad than the one for V_{Si}, since the volume of the former defect is smaller. This leads to a larger annihilation rate with core electrons.

The ratio curve calculated for the V_C+V_{Si} divacancy has a similar shape to that found for the silicon vacancy. However, since the divacancy has a larger open volume, we observe a higher contribution at the low momenta and a decreased annihilation rate with more energetic electrons.

As far as larger clusters are concerned, similar ratio curves are found for the V_C+V_{Si}+V_C, V_{Si}+V_C+V_{Si}, $(V_C$+$V_{Si})_2$ and $(V_C$+$V_{Si})_3^{chain}$ defects. The result found for the $(V_C$+$V_{Si})_3^{ring}$ hexavacancy can be, however, easily distinguished from the other ones. In this case the value at $p = 0$ is much higher, due to a larger open volume of this defect, and the peak around $p = 11.5$ mrad transforms into a shoulder. It is interesting to notice that the ratio curve of $(V_C$+$V_{Si})_3^{ring}$ has a form which is more similar to that of V_C than to that of V_{Si}, especially at low momenta. It is probably be due to the fact that this defect has a large three-dimensional volume and the localized positron interacts mostly with the Si valence electrons and not with the more localized C electrons.

4.3.3 S and W parameters – effect of the experimental resolution and integration windows

For the interpretation of the experimental studies the S and W parameters are usually analyzed instead of the ratio curves. We therefore calculated these parameters for the considered defects.

In the following sections we will discuss the relative parameters, calculated as:

$$S_{\text{rel}} = \frac{S_{\text{defect}}}{S_{\text{lattice}}} \quad \text{and} \quad W_{\text{rel}} = \frac{W_{\text{defect}}}{W_{\text{lattice}}}. \tag{4.3.1}$$

In the case of S and W it is important to stress the importance of the resolution and the choice of the windows in which these parameters are calculated on the results. In Fig. 4.13 we present the S_{rel} parameter as a function of the W_{rel} parameter plotted for various neutral defects in $3C$-SiC using spectra convoluted with Gaussian functions with different FWHM. We chose two cases corresponding to the experimental measurements using either two Ge detectors in coincidence mode (FWHM=3.6 mrad) or a single Ge detector (FWHM=4.7 mrad). These parameters are calculated using windows of (0–2.86) and (10.58–27.36) mrad for S and W, respectively. We can observe that the results obtained using the higher FWHM are shifted towards the point corresponding to the lattice, (0,0), but the relative positions of the points corresponding to each defect on the plot are conserved for the two resolutions.

The effect of the choice of the windows in which the S and W parameters are integrated is presented in Fig. 4.14. In this case we plotted the results using two windows, $S \in (0, 2.5)$ mrad, $W \in (15.0, 27.36)$ mrad on the one hand and $S \in (0, 2.86)$ mrad, $W \in (10.58, 27.36)$ mrad on the second hand. We observe that the results are much more sensitive to the the high-momentum window than to the low-momentum one. It is interesting to see that when the first set of windows is used, the points are easier to distinguish. In particular, the points corresponding to defects on the carbon sublattice (V_C and V_C+V_C) are well separated from the other ones. When the second set of windows is used, all points are almost exactly aligned on the line passing through the (1,1) point. It means that the choice of the ranges within which the W is calculated can help to distinguish defects in experiments. Another consequence of the high sensitivity of the W parameter to the integration range choice is that the comparison between published data can be difficult, since different windows are usually used for each study.

The S_{rel} and W_{rel} parameters calculated using various resolutions and integration windows, which were used to generate Fig. 4.13 and 4.14 are also presented in Tab. 4.11 for all the considered defects.

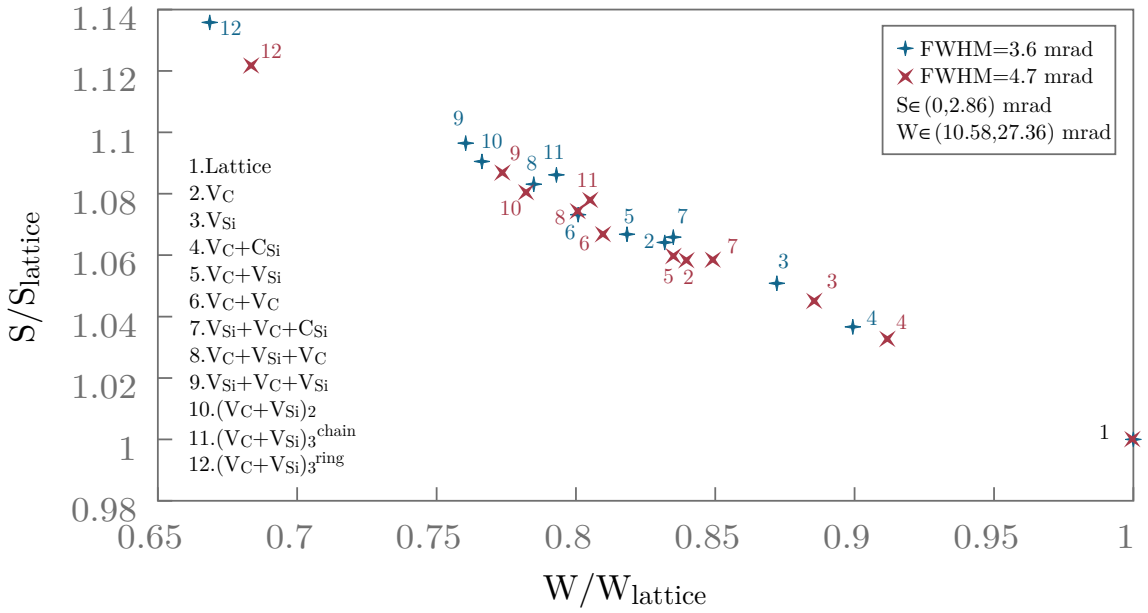

Figure 4.13: *S_{rel} parameter as a function of the W_{rel} parameter plotted for various neutral defects in 3C-SiC using spectra convoluted with Gaussian functions with different FWHM. The parameters are calculated using windows (0,2.86) and (10.58,27.36) mrad for S and W, respectively.*

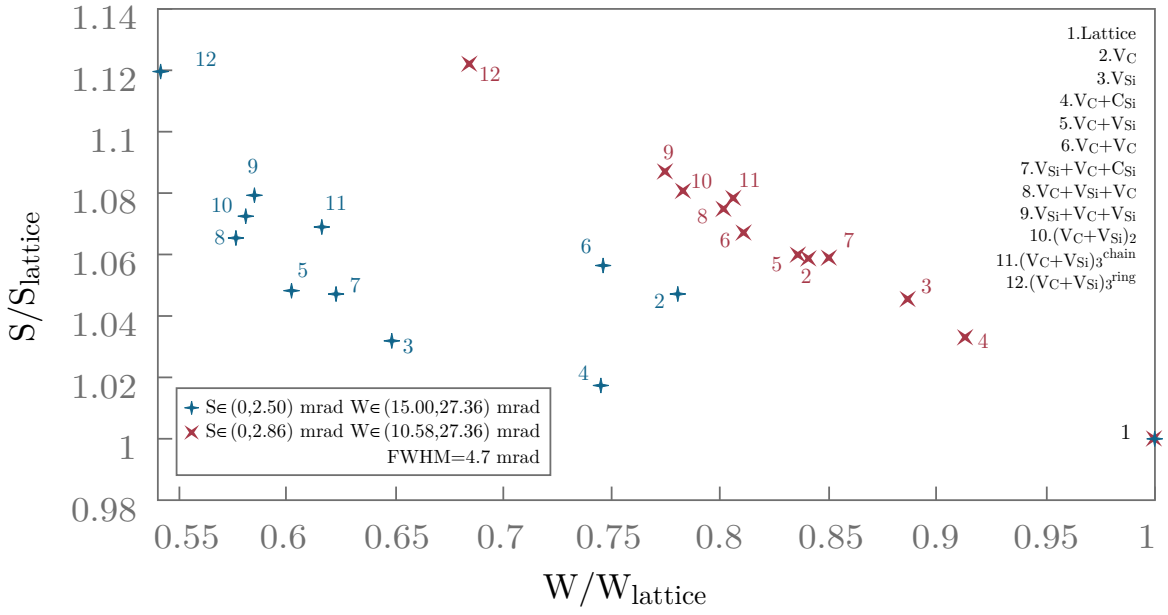

Figure 4.14: *S_{rel} parameter as a function of the W_{rel} parameter plotted for various neutral defects in 3C-SiC using different windows for S and W parameters. The results were obtained using spectra convoluted with a Gaussian function with FWHM=4.7 mrad.*

Table 4.11: *Relative S_{rel} and W_{rel} parameters calculated for various defects in 3C-SiC, using different resolutions and integration.*

	FWHM=3.6 mrad $S \in (0, 2.86)$ mrad $W \in (10.58, 27.36)$ mrad		FWHM=4.7 mrad $S \in (0, 2.86)$ mrad $W \in (10.58, 27.36)$ mrad		FWHM=4.7 mrad $S \in (0, 2.5)$ mrad $W \in (15, 27.36)$ mrad	
Defect	S_{rel}	W_{rel}	S_{rel}	W_{rel}	S_{rel}	W_{rel}
V_C	1.064	0.832	1.058	0.840	1.060	0.780
V_{Si}	1.051	0.871	1.045	0.886	1.048	0.648
V_C+C_{Si}	1.037	0.900	1.033	0.912	1.035	0.744
V_C+V_C	1.073	0.801	1.066	0.810	1.069	0.745
V_C+V_{Si}	1.067	0.818	1.060	0.835	1.063	0.601
V_{Si}+V_C+C_{Si}	1.066	0.835	1.058	0.849	1.061	0.622
V_C+V_{Si}+V_C	1.083	0.785	1.074	0.801	1.078	0.575
V_{Si}+V_C+V_{Si}	1.097	0.760	1.087	0.774	1.091	0.585
$(V_C$+$V_{Si})_2$	1.090	0.766	1.081	0.782	1.085	0.580
$(V_C$+$V_{Si})_3^{\mathrm{chain}}$	1.087	0.792	1.078	0.804	1.081	0.651
$(V_C$+$V_{Si})_3^{\mathrm{ring}}$	1.135	0.669	1.122	0.684	1.127	0.541

4.3.4 Effect of the charge state

We verified the effect of the charge state on the momentum distribution by performing calculations on V_{Si}. We calculated the ratio curves for this defect for 0, −1 and −2 charge states. The results are presented in Fig. 4.15. We can observe that the ratio at $p = 0$ decreases when the negative charge increases. It is due to the fact that the relaxation of the negative vacancies is smaller than for the neutral one (see Tab. 4.6). This is reflected in the corresponding S_{rel} ($S \in (0, 2.86)$ mrad) as shown in Tab. 4.12. The peak close to $p = 10$ mrad rises when the electrons are added to the system, while at the same time the ratio at momenta higher than approximately 17 mrad decreases. Both regions are included in the window used to calculate the W parameter, 10.58–27.36 mrad, however their effects do not cancel each other out and we can observe an increase in W due to an additional negative charge.

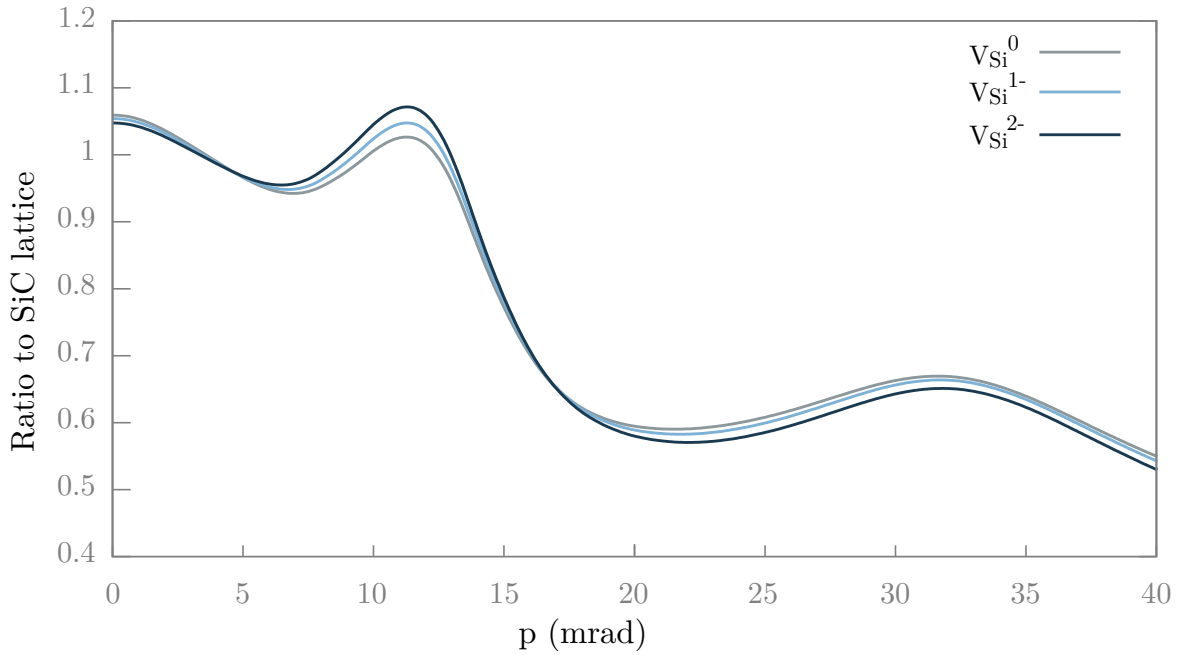

Figure 4.15: *Ratio curves of the calculated momentum distributions of annihilating electron-positron pairs in neutral and charged silicon vacancy in SiC. All spectra are convoluted with a Gaussian function with FWHM=4.7 mrad and divided by the lattice spectrum.*

Table 4.12: *Relative S_{rel} and W_{rel} parameters calculated for various charge states of V_{Si}. The parameters were obtained using windows of 0–2.86 and 10.58–27.36 mrad for S and W, respectively. The spectra were convoluted with a Gaussian function with FWHM=4.7 mrad.*

	S_{rel}	W_{rel}
V_{Si}^{0}	1.045	0.886
V_{Si}^{1-}	1.040	0.899
V_{Si}^{2-}	1.035	0.913

4.3.5 3C and 6H polytypes comparison

In Sec. 3.2.3, while validating our implementation of the calculation methods, we tested the effect of the polytype on the Doppler spectra of the silicon carbide lattice and showed that there was no significant difference between 3C and 6H lattices. The comparison must also be performed for vacancies. In Fig. 4.16 to 4.19 we present the comparisons of the ratio curves obtained for V_C, V_C+C_{Si}, V_{Si} and V_C+V_{Si} defects in silicon carbide. Tab. 4.13 shows the relative S and W parameters calculated for these defects. The definition of the various sites in 6H-SiC, h (hexagonal site), k_1 and k_2 (cubic sites) are given in Fig. 1.1.

In the case of the carbon vacancy (Fig. 4.16) in 6H-SiC we observe a strong dependence of the ratio curve on the site. The result obtained for the h site is quite similar to that calculated in the 3C polytype. For k_1 and k_2 the ratio curves are flatter. It is consistent with what was observed in the calculations of positron lifetimes, where a smaller relaxation and hence a weaker localization of the positron was observed for the cubic sites. It is also reflected in the S_{rel} and W_{rel} parameters which are closer to 1 for k_1 and k_2 (see Tab. 4.13).

The dependence of the calculated ratio on the local geometry is lower for the V_C+C_{Si} complex (Fig. 4.17), but it can still be observed. The positron localization is the strongest in the 3C polytype and in the $h-h$ configuration in 6H-SiC. The weakest relaxation, already observed in the results of the positron lifetimes calculations, is found for the k_2-k_2 configuration, which is reflected in smaller low- and larger high-momentum contributions.

As for the defects in which the positron is localized mostly inside the silicon vacancy, V_{Si} and V_C+V_{Si}, the ratio curves are very similar (see Fig. 4.18 and 4.19). The differences are easier to observe in S_{rel} and W_{rel} parameters (see Tab. 4.13). However, we consider that these differences are probably much lower than the experimental precision, hence not significant when it comes to defect identification.

Based on the small differences between the two polytypes obtained for V_{Si} and V_C+V_{Si}, similarly to what was observed in the positron lifetime calculations, we conclude that the Doppler broadening calculations performed for clusters in 3C-SiC can be used to analyze experimental data obtained for other polytypes as well.

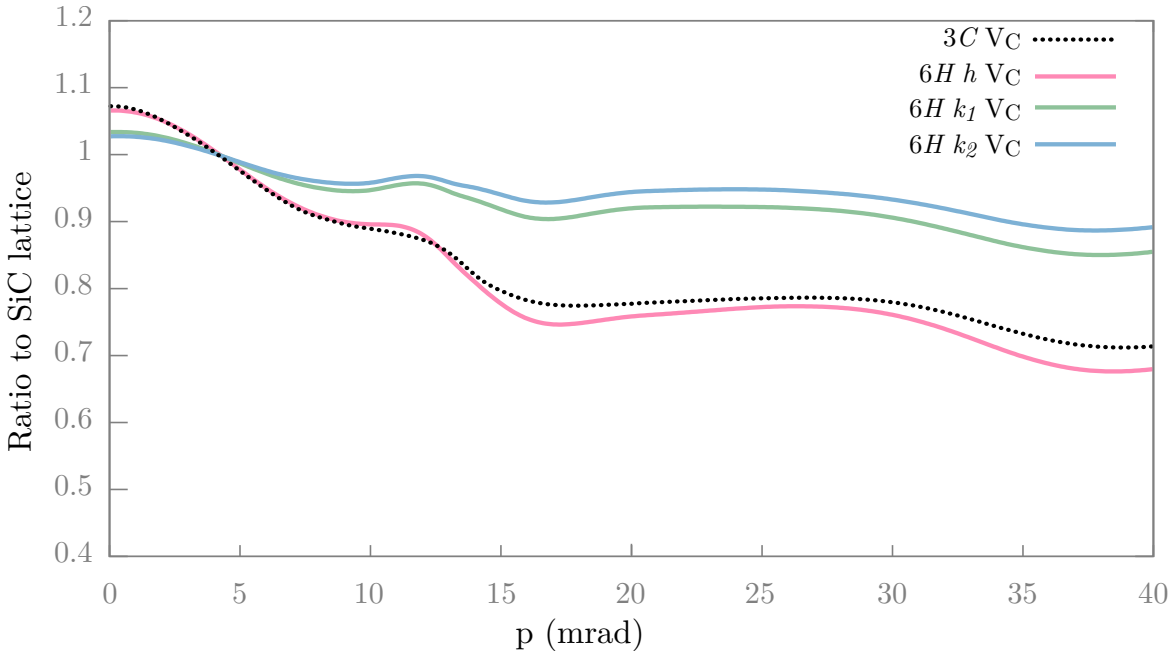

Figure 4.16: *Ratio curves of the calculated momentum distributions of annihilating electron-positron pairs in V_C in 3C and 6H polytypes of silicon carbide. All spectra are convoluted with a Gaussian function with FWHM=4.7 mrad and divided by the lattice spectrum.*

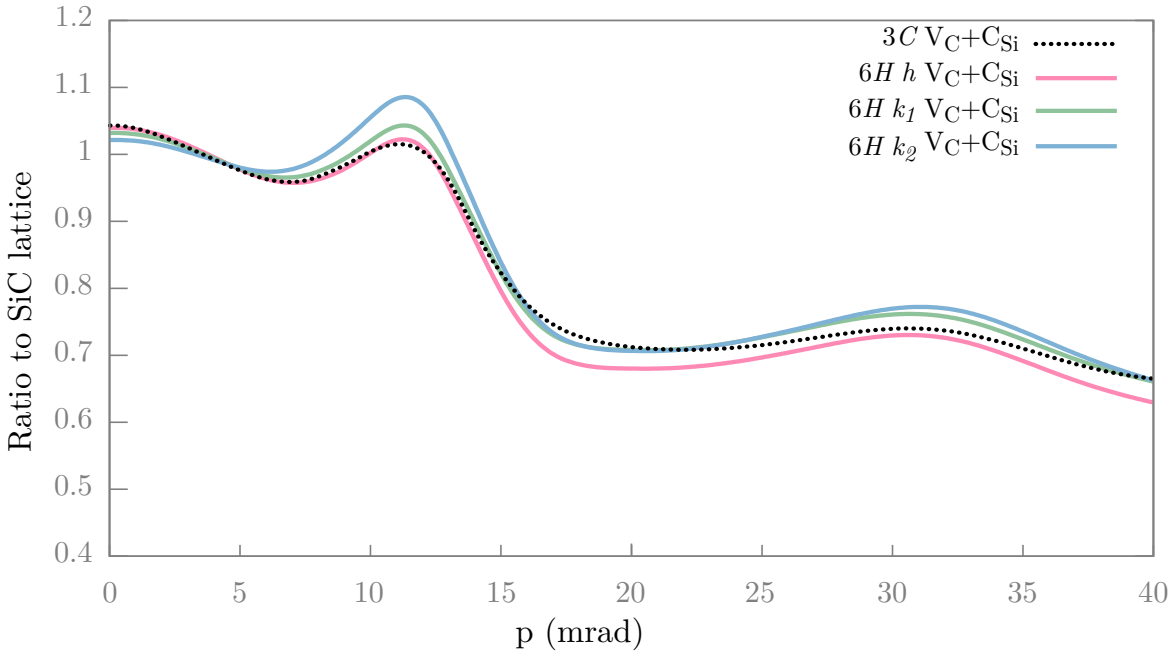

Figure 4.17: *Ratio curves of the calculated momentum distributions of annihilating electron-positron pairs in V_C+C_{Si} complexes in 3C and 6H polytypes of silicon carbide. All spectra are convoluted with a Gaussian function with FWHM=4.7 mrad and divided by the lattice spectrum.*

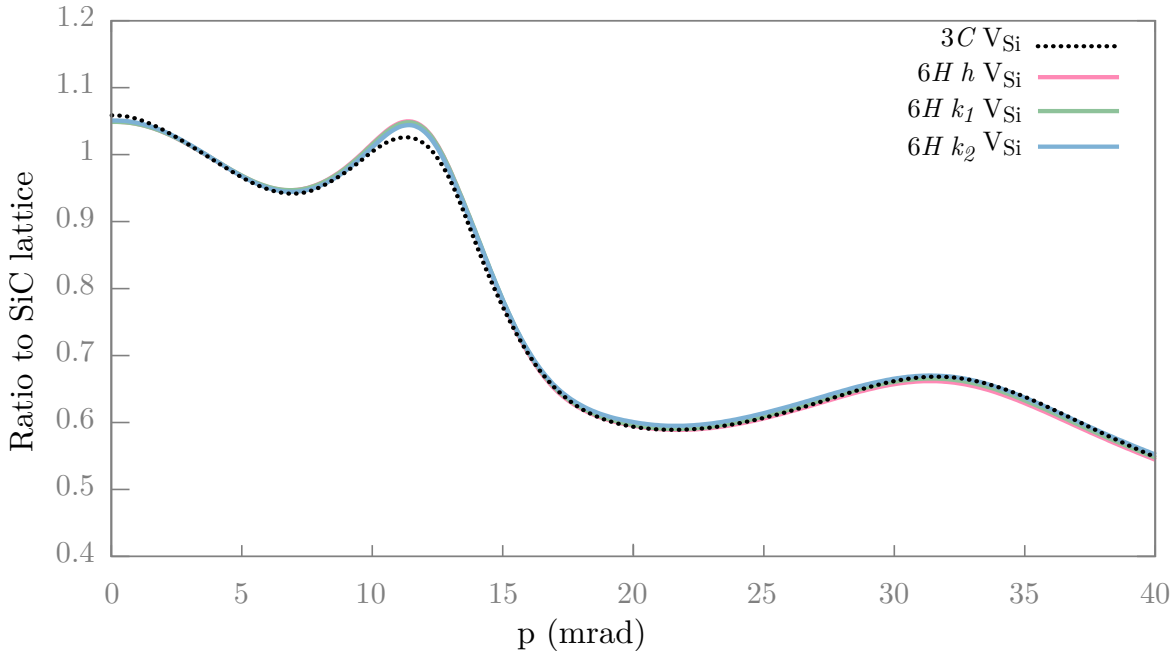

Figure 4.18: *Ratio curves of the calculated momentum distributions of annihilating electron-positron pairs in V_{Si} in 3C and 6H polytypes of silicon carbide. All spectra are convoluted with a Gaussian function with FWHM=4.7 mrad and divided by the lattice spectrum.*

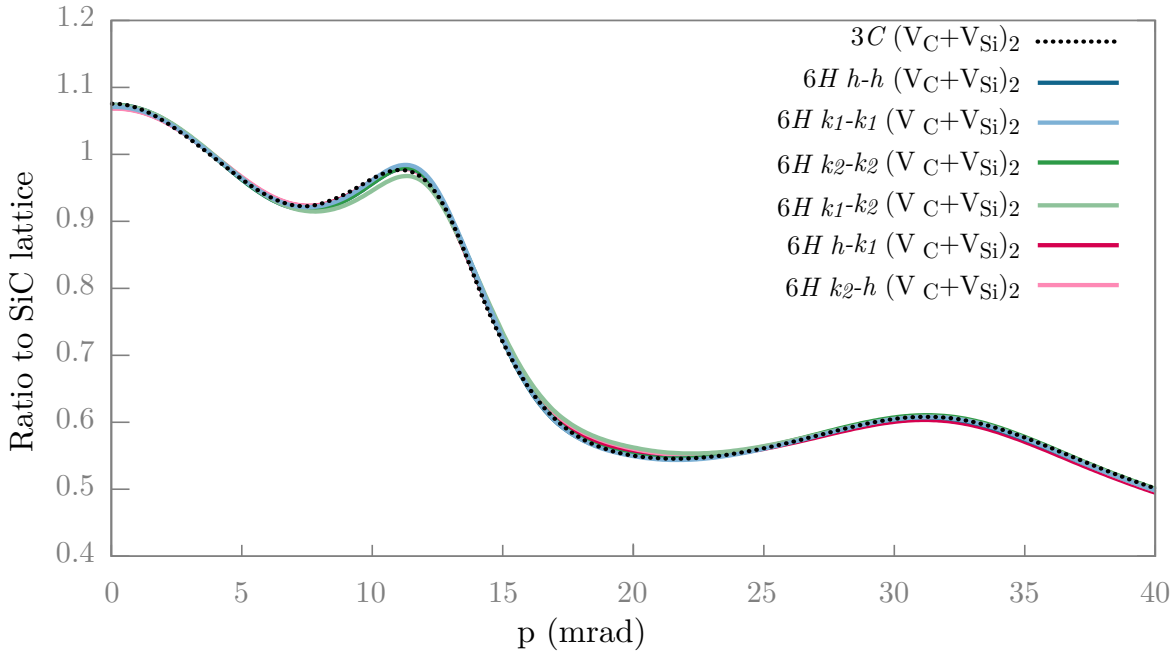

Figure 4.19: *Ratio curves of the calculated momentum distributions of annihilating electron-positron pairs in V_C+V_{Si} complexes in 3C and 6H polytypes of silicon carbide. All spectra are convoluted with a Gaussian function with FWHM=4.7 mrad and divided by the lattice spectrum.*

Table 4.13: *Relative S_{rel} and W_{rel} parameters calculated for various defects in 3C and 6H silicon carbide. The parameters were obtained using windows of 0–2.86 and 10.58–27.36 mrad for S and W, respectively. The spectra were convoluted with a Gaussian function with FWHM=4.7 mrad.*

Defect	Site	S_{rel}	W_{rel}
V_C	$3C$	1.058	0.840
V_C	$6H$, h	1.056	0.836
V_C	$6H$, k_1	1.029	0.938
V_C	$6H$, k_2	1.024	0.954
V_{Si}	$3C$	1.045	0.886
V_{Si}	$6H$, h	1.040	0.901
V_{Si}	$6H$, k_1	1.040	0.901
V_{Si}	$6H$, k_2	1.041	0.900
V_C+C_{Si}	$3C$	1.032	0.912
V_C+C_{Si}	$6H$, $h-h$	1.033	0.903
V_C+C_{Si}	$6H$, k_1-k_1	1.026	0.927
V_C+C_{Si}	$6H$, k_2-k_2	1.017	0.955
V_C+V_{Si}	$3C$	1.060	0.835
V_C+V_{Si}	$6H$, $h-h$	1.063	0.839
V_C+V_{Si}	$6H$, k_1-k_1	1.059	0.842
V_C+V_{Si}	$6H$, k_2-k_2	1.061	0.840
V_C+V_{Si}	$6H$, k_1-k_2	1.062	0.837
V_C+V_{Si}	$6H$, $h-k_1$	1.058	0.840
V_C+V_{Si}	$6H$, k_2-h	1.057	0.841

4.3.6 Effect of the nitrogen decoration of vacancies

In the majority of experimental studies on SiC discussed in this work, n-type samples were studies. In this case, the material is doped with nitrogen (with concentrations above 10^{17} cm^{-3}), which usually substitutes the carbon sites and can form complexes with vacancies. We studied the effect of the nitrogen decoration of silicon vacancies on the Doppler spectra and the S and W parameters. The calculated ratio curves are shown in Fig. 4.20. In Fig. 4.21 we present the S_{rel} and W_{rel} parameters, calculated using two sets of integration windows, $S \in (0, 2.5)$ mrad, $W \in (15.0, 27.36)$ mrad on the one hand and $S \in (0, 2.86)$ mrad, $W \in (10.58, 27.36)$ mrad on the second hand. In Fig. 4.20 we can observe that adding nitrogen atoms next to the silicon monovacancy leads to the decrease of the peak at $p = 0$ and to the increase of the ratio curve above around $p = 5$ mrad. The changes in the plot seem to be proportional to the number of nitrogen atoms surrounding the silicon vacancy.

As for the $S(W)$ plot (Fig. 4.21) we can observe that the decoration of the silicon monovacancy with nitrogen atoms leads to a clear shift of the corresponding points from the line connecting the lattice and V_{Si}. Moreover, the direction of that shift depends on the chosen integration windows.

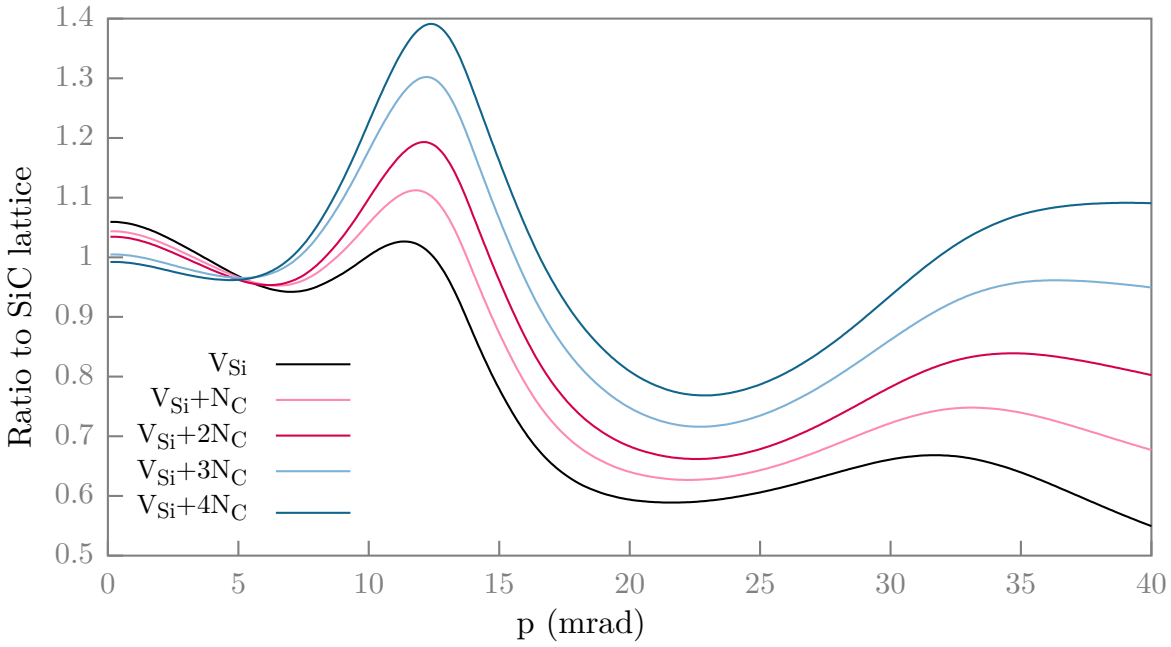

Figure 4.20: *Ratio curves of the calculated momentum distributions of annihilating electron-positron pairs in nitrogen-decorated silicon monovacancies. All spectra are convoluted with a Gaussian function with FWHM=4.7 mrad and divided by the lattice spectrum.*

For $S \in (0, 2.5)$ mrad, $W \in (15.0, 27.36)$ mrad the points corresponding to the complexes with nitrogen are on the left side of the line, while for $S \in (0, 2.86)$ mrad, $W \in (10.58, 27.36)$ mrad on its right side.

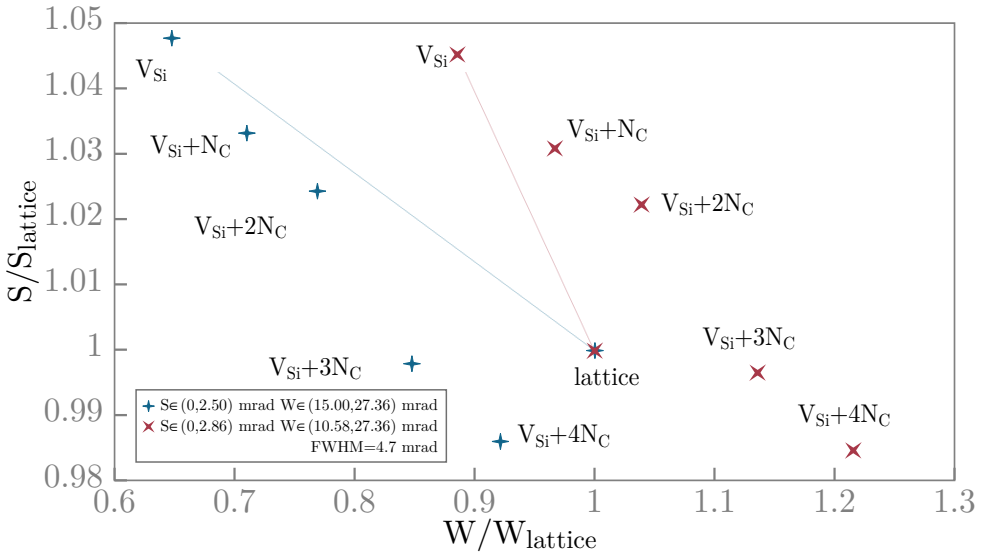

Figure 4.21: *S_{rel} parameter as a function of the W_{rel} parameter plotted for nitrogen-decorated silicon monovacancies calculated using two sets of integration windows. The results were obtained using spectra convoluted with a Gaussian function with FWHM=4.7 mrad.*

4.4 Discussion and contribution to interpretation of experimental results

4.4.1 Positron lifetimes

Our calculation results will be first used to discuss the positron lifetimes detected in silicon carbide presented in literature and to revisit the identifications of the signals proposed in the past. Most experimental results were already mentioned in the section on literature review (Sec. 1.3.1). For this comparison we use lifetimes scaled to the experimental lattice lifetime of 140 ps.

Kerbiriou *et al.* [32] observed a positron lifetime varying with temperature from 210 ps up to 220 ps in n-doped, irradiated 3*C*-SiC. The authors attributed the lifetimes to two vacancy-type defects - V_{Si} and V_C+V_{Si} based on the calculation results by Brauer *et al.* [58, 59]. The variation of the lifetime with temperature implies the presence of a defect that changes charge state, or at least two defects, among which one is negative or changes charge state. The EPR measurement on the same sample suggested that V_{Si}^{1-} [32, 35, 65, 66] was present. Considering the calculations results presented here, we firstly verified whether the defect corresponding to the experimental lifetime could be the silicon vacancy changing charge state. The shortest lifetime obtained for this defect in 3*C*-SiC is 222 ps (V_{Si}^{2-}). However, as the experimental lifetime for the lattice is shorter than the one we calculated (140 ps and 144 ps, respectively) we have to consider the lifetime relative to the experimental one. It yields 216 ps ($\frac{222\ \text{ps}*140\ \text{ps}}{144\ \text{ps}}$) for V_{Si}^{2-}. This lifetime is longer than the one of 210 ps observed by Kerbiriou *et al.* at low temperatures. Additionally, the change of the charge state of the silicon vacancy would result in a change in the EPR signal, while it was found to be the same for all the measurement temperatures. We propose, hence, a second interpretation: the positron lifetime observed by Kerbiriou *et al.* may come from both the neutral carbon monovacancy and the negative silicon vacancy. V_C could not be detected by EPR, as it is nonparamagnetic. As temperature increases, the electron chemical potential of the n-type material decreases, the carbon vacancies become positive and cannot be detected by PAS any longer. This induces an increase in the lifetime, which becomes closer to the 225 ps (218 ps when scaled to $\tau_{\text{lattice}}^{\text{exp.}}$) that was calculated for V_{Si}^{1-}.

Kawasuso *et al.* [56] detected a lifetime component of 188 ps in irradiated n-type 3*C*-SiC and attributed it to the silicon vacancy. The T1 signal, indicating the presence of V_{Si}, was detected using EPR in the same sample. The lifetime itself is close to the one we calculated for the carbon vacancy, but we cannot explain the simultaneous existence of these PAS and EPR signals. The

study of Kawasuso *et al.* was performed only at room temperature, hence the charge state of the observed defect is not known and it is not certain whether the signal comes from one or several defect types. Additionally, the experiment of Kawasuso *et al.* was carried out on a 30 μm 3C-SiC sample supported on unirradiated 6H-SiC. It is hence possible that even though the silicon vacancies were created in the 3C-SiC layer, the positron lifetime observed was also affected by the supporting material. In any case, since not many experimental data have been published for 3C-SiC it is rather difficult to draw definitive conclusions on the defects present based on the positron lifetimes alone. Moreover, we found that there is only a small region close to the conduction band where the carbon vacancy should be neutral and detected by PAS. The electron chemical potential changes with temperature and irradiation and is difficult to determine precisely. Thus, it is complicated to predict whether the carbon vacancies should be detected in a given 3C-SiC sample, therefore to interpret the PAS results in this polytype.

As for n-type 6H-SiC samples, several groups of lifetimes are observed, two of which are in the range of lifetimes that we calculated. Shorter experimental positron lifetimes, 176 ps [69], 183 ps [67], 174 ps and 176 ps [70], were observed and assigned to the silicon vacancy using the calculations of Brauer *et al.* These lifetimes are, however, much smaller than the lifetimes we calculated for both V_{Si}^{0} (226 ps or 221 ps when scaled to $\tau_{lattice}^{exp.}$) and V_{Si}^{-2} (222 ps and 223 ps or 217 ps and 218 ps scaled to $\tau_{lattice}^{exp.}$). These experimental lifetimes are on the contrary in a very good agreement with the lifetimes we calculated for the neutral carbon vacancy (175 ps, 173 ps and 193 ps or 171 ps, 169 ps and 189 ps when scaled to $\tau_{lattice}^{exp.}$).

The second group of signals observed in n-type 6H-SiC includes lifetimes of 210 ps [69], 202 ps [55], 210 ps and 220 ps [68]. These signals are between the values we calculated for V_C and V_{Si}. Since for vacancy complexes longer lifetimes are expected, we assume that these are mixed lifetimes of the carbon and silicon monovacancies.

As far as longer positron lifetimes are concerned, Barthe *et al.* [71] observed lifetimes of 257 ps and 281 ps lifetimes in n-type 6H-SiC implanted with low-energy protons (after 900°C and 1300°C annealing, respectively). These defects were identified as $(V_C{+}V_{Si})_2$ and $(V_C{+}V_{Si})_3$. Our calculations confirm this interpretation since we obtained lifetimes of 262 ps for the tetravacancy and 263 and 296 ps for the two configurations of the hexavacancy.

Aavikko *et al.* [72] studied undoped SiC samples annealed at 1600°C. They observed long lifetime components of 261, 283 and 284 ps, which were attributed to clusters containing four and five vacancies, respectively. This is consistent with our calculations, as these lifetimes are close to what we obtained for $(V_C{+}V_{Si})_2$ and $(V_C{+}V_{Si})_3$. It should be noted, however, that in the case of SiC, the number of silicon vacancies in the cluster has more influence on the positron lifetime than the total number of vacancies.

Finally, Brauer *et al.* [58] studied 6*H*-SiC samples irradiated with 200 keV Ge^+ ions, at fluences varying from 10^{16} to 10^{19} m^{-2}. For the lowest fluence, a long lifetime component of 235 ps was observed and attributed to the divacancy, even though it was longer than what Brauer *et al.* had calculated for this type of defect. The authors indicated that the discrepancy between the measured and calculated lifetimes could come from the fact that the relaxation effects were not taken into account. Our results confirm this, as our calculations yielded 235 ps for the relaxed V_C+V_{Si} cluster. For the 10^{19} m^{-2} fluence, Brauer *et al.* observed a lifetime component of 305 ps and attributed it to a defect containing six vacancies. We calculated a lifetime of 296 ps for the ring hexavacancy so this defect could be the one observed in this study.

4.4.1.1 Discussion of X. Kerbiriou measurements

We will now discuss the experimental results obtained during X. Kerbiriou's thesis at the CEMHTI Laboratory (Orléans, France). These results have been presented in Sec. 1.3.1.3. We recall the figures presenting the experimental measurements below to facilitate the discussion.

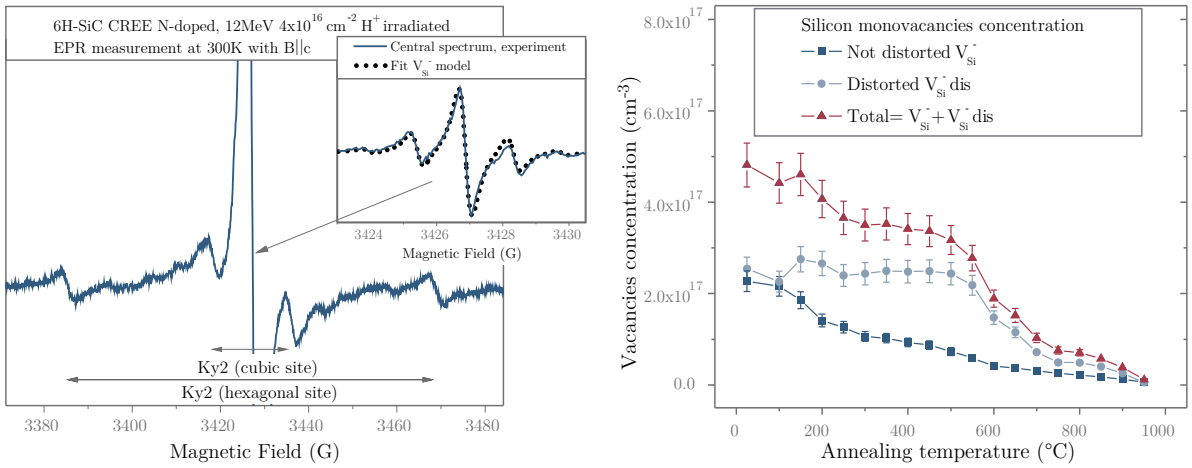

Figure 4.22: *(a) EPR spectrum obtained at 300 K in the proton irradiated 6H-SiC CREE crystal before annealing. The inset shows the central spectrum and its fit using the V_{Si}^{1-} model. (b) Silicon vacancies concentration (not distorted, distorted, sum) as a function of the annealing temperature in the 6H-SiC H^+ 12 MeV irradiated crystal.*

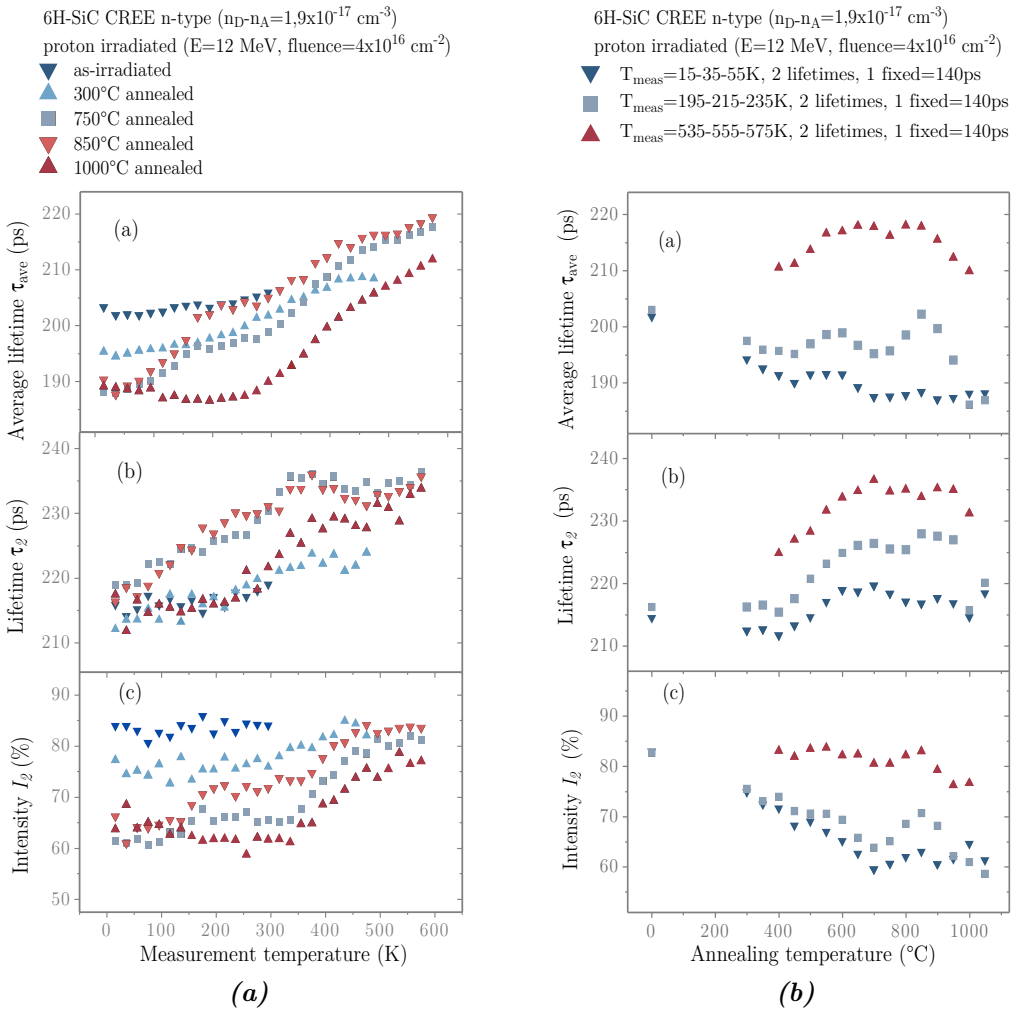

(a) ***(b)***

Figure 4.23: *(a) Measurement and annealing temperature dependence of the positron lifetime components obtained for the 12-MeV proton irradiated crystals. In both figures the average lifetime $\tau_{av.}$ (a), long lifetime component τ_2 (b) and its intensity I_2 (c), are shown.*

EPR experiments results Before annealing, measurements at 300 K show the presence of three main paramagnetic centers (see Fig. 4.22a). The first one resembles a center already detected after irradiation with various particles [34, 158, 159] and attributed to the isolated V_{Si}^{1-} with a spin $S = 3/2$. This signal is in fact a superposition of signals coming from hexagonal and quasicubic sites that cannot be distinguished. This signal is called V_{Si}^{1-} in the following. The V_{Si}^{1-} concentration in the as-irradiated crystals is $2.2(\pm 0.3)\times 10^{17}$ cm^{-3}.

The two other detected signals are similar to the ones detected after irradiation in various conditions in literature [34, 158, 159]. This signal is currently attributed to a distorted state of the negatively charged silicon vacancy [158]. This distortion may be due to the presence of an impurity or of another defect located at some distance along the c axis ([0001]) [158]. The signal is called V_{Si}^{1-}dis (as 'distorted') in the following. The V_{Si}^{1-}dis concentration in the as-irradiated crystals is $2.6(\pm 0.3)\times 10^{17}$ cm^{-3}.

From Fig. 4.22b we can observe that the concentration of V_{Si}^{1-}dis decreases from around 2.4×10^{17} cm^{-3} down to $1.6(\pm 0.3)\times 10^{16}$ cm^{-3} during annealing. The V_{Si}^{1-} concentration is first stable at $2.2(\pm 0.3)\times 10^{17}$ cm^{-3}, then decreases first to 1.4×10^{17} cm^{-3} and later to $6.7(\pm 1.0)\times 10^{15}$ cm^{-3}. The total silicon vacancy concentration [V_{Si}^{1-}tot] is first nearly constant around $4.5(\pm\ 0.6)\times 10^{17}$ cm^{-3} and then decreases down to $1.2(\pm 0.1)\times 10^{16}$ cm^{-3}. We can observe that all three concentrations become relatively low above approximately 600°C, which means that the silicon vacancies recombine or cluster in the sample.

Evidence for the detection of negatively charged non-vacancy defects For all annealing and measurement temperatures two components were obtained from the positron lifetime spectra decomposition (see Fig. 4.23 in Sec. 1.3.1.3). The long lifetime component τ_2 is much longer than the lattice lifetime for all measurement and annealing temperatures. This indicates trapping in vacancy defects. In that case, if some of the positrons had annihilated in a non-localized state (i.e. in the lattice), the short lifetime component τ_1 values would have been shorter than the lattice lifetime (the mean time spent in the lattice is shorter due to the trapping inside the defects). However, in the studied samples, the short lifetime component τ_1 was close to the 6H-SiC lattice lifetime (τ_L =140 ps [55]). This lifetime indicates the detection of negatively charged non-vacancy defects (also called 'negative ions'), as the electronic density around negative ions is close to the density observed around the atoms in the lattice [160]. As described in the paper related to the as-irradiated samples [55], two types of negative ions are in fact detected in the crystals. One of them was already detected in the as-grown crystals, and the other one was generated by irradiation. Moreover, the evolution of τ_1 as a function of the annealing temperature indicate a total trapping of the positrons in defects, both into vacancy defects and 'negative ions', even after 1050°C annealing.

Lifetime components as a function of the measurement temperature In the as-irradiated crystals only slight variations are observed in the positron characteristics when the measurement temperature changes. The average lifetime increases slightly from 202±1 ps to 205±1 ps between 15 K and 295 K. The long lifetime component τ_2 rises from 214±2 ps to 218±2 ps in the measurement temperature range and its intensity is stable at 83±2%.

After annealing at 300°C, $\tau_{\text{av.}}$ first increases slightly from 194±1 ps up to 198±1 ps and then reaches 208±1 ps at 415 K and remains stable. τ_2 increases from 212±2 ps up to 222±2 ps, while its intensity changes from 75±3% to 83±2%.

The average lifetime $\tau_{\text{av.}}$ measured in the crystals annealed at 300°C varies more strongly (from 194 ps to 208 ps) than in the as-irradiated crystals as a function of the measurement temperature. It indicates a modification of the distribution of the vacancy defects and/or of the 'negative ions' detected in the crystals. The long lifetime component τ_2 values are characteristic of the distribution of the vacancy defects detected in the crystals. For a given annealing temperature, EPR measurements show that the isolated silicon vacancy concentration remains constant for all measurement temperatures, which indicates that the Fermi level does not vary. We propose, therefore, that the modification of the trapping rate of the various defects is induced by a variation in their concentration, or by a change in the nature of the detected defects, but not by a modification of their charge states. The lifetime τ_2 measured in the 300°C annealed crystals varies from 212 ps to 222 ps when the measurement temperature changes from 15 K to 475 K. These values are close to the lifetimes measured in the as-irradiated crystals and the population of defects should be very similar to that in as-irradiated samples. However, the I_2 intensity is lower after annealing at 300°C. It suggests that the concentration of vacancy type defects has decreased during annealing.

After annealing at 750°C, the average positron lifetime first increases from 188±1 ps to 196±1 ps and is then stable between 175 K and 275 K. It then rises again and reaches 217±1 ps value at 575 K. τ_2 increases from 218±2 ps to 235±3 ps when the temperature increases. We can also observe an increase of the intensity I_2 around 350 K. A rather similar evolution of the three characteristics $\tau_{\text{av.}}$, τ_2 and I_2 is also observed after annealing at 850°C.

The average lifetime $\tau_{\text{av.}}$ measured in the 750°C annealed crystals increases very strongly, from 188 ps to 217 ps, in the 15–575 K measurement temperature range. It indicates a modification of the distribution of the vacancy defects detected in the samples. In addition, τ_2 increases from 218 ps to 235 ps when the measurement temperature increases from 15 K to 475 K. These values are very different from the lifetimes measured before and after annealing at 300°C. At higher temperatures, τ_2 values form a plateau at 235 ps. This lifetime is also observed at different annealing temperatures. These two points suggest that the 235 ps lifetime is characteristic of

a vacancy defect, which we will call V_A. The change of τ_2 with temperature indicates that at least one of the vacancy defects detected at low temperature is negatively charged, while the V_A defect detected at high temperatures is neutral. The negatively charged vacancy will be called V_B in the following.

After annealing at 750°C, I_2 is close to 60% in the 15–335 K measurement temperature range, while it is equal to 75% after annealing at 300°C. For higher measurement temperatures, I_2 values remain close to 80%. It indicates that the trapping rate at vacancy defects decreased at low measurement temperature, while it remained constant at high temperature. Two phenomena could explain the decrease of the trapping rate at vacancy defects in the low temperature range: an increase of the 'negative ions' concentration or a decrease of the V_B concentration. EPR measurements indicate that the isolated negative silicon monovacancy concentration has strongly decreased after annealings performed between 300°C and 600°C and is very small after annealing at 750°C. The I_2 decrease therefore probably results from the $[V_{Si}^{1-}]$ decrease. We propose, hence, that the negatively charged vacancy defect V_B is the silicon monovacancy.

After annealing at 850°C, $\tau_{av.}$ first increases from 188±1 ps up to 202±1 ps between 15 K and 175 K. It is then stable until 275 K and increases again until 575 K reaching 219±1 ps. τ_2 increases from 216±2 ps to 233±3 ps between 15 K and 375 K and it remains stable until 575 K. Its relative intensity I_2 is first stable at 64±2% between 15 K and 135 K, then it increases until 215 K and 72±2%. It is stable until 355 K, then increases again until 82±2% at 475 K and it finally remains stable until 575 K.

The values of the average lifetime $\tau_{av.}$, of the long lifetime component τ_2, and of its relative intensity I_2 measured in the samples annealed at 850°C are very close to the ones measured after annealing at 750°C, except in the 175–335 K measurement temperature range. In this range, $\tau_{av.}$ is 6 ps higher than the ones measured after annealing at 750°C. While the τ_2 lifetimes are almost identical, I_2 values are higher than the ones measured after annealing at 750°C. This indicates that the trapping rate in vacancy defects increases relatively to the trapping rate around the 'negative ions'. The I_2 increase can result from a change in the trapping rates coefficients or in the concentration of the negative ions or of the vacancy defects. The values of τ_2 are almost identical, even at low measurement temperature, where the trapping in the neutral defect called V_A is in competition with the trapping in V_{Si}^{1-}. It suggests that the nature (and therefore the trapping coefficient) and the concentration of the vacancy defects changed only slightly between annealing at 750°C and 850°C. Meanwhile, the silicon vacancies concentrations measured using EPR after annealing at 750°C and 850°C are close (respectively 8×10^{16}cm^{-3} and 6×10^{16}cm^{-3}). I_2 variations therefore result from a decrease in the negative ion concentration between 750°C and 850°C, while the vacancy defects distribution remains almost identical.

Finally, after annealing at 1000°C, $\tau_{\text{av.}}$ is first stable at 188±2 ps and then starts rising at around 300 K to finally reach 211±1 ps. The long lifetime component τ_2 varies between 216±2 ps and 231±3 ps. The intensity corresponding to this lifetime is firstly stable and then starts rising at around 350 K to reach 76±2% at 575 K.

The average lifetime $\tau_{\text{av.}}$ in the 1000°C annealed crystals is 6 ps to 15 ps shorter than after 850°C annealing. This suggests a change in the distribution of the vacancy defects detected in the samples. The τ_2 lifetime measured in these crystals is first stable around 215 ps for measurement temperatures lower than 235 K and then increases until 575 K reaching 231 ps. These values differ from the ones measured after annealing at 850°C. The 215 ps lifetime, measured at low temperature, probably corresponds to the positron trapping in negative silicon vacancies. At higher measurement temperatures, the values of τ_2 are around 231 ps, which is slightly shorter than the V_A characteristic lifetime is detected for lower annealing temperatures.

Lifetime components as a function of the annealing temperature For low measurement temperatures the average lifetime decreases from 202±1 ps to 188±1 ps as a function of annealing temperature. τ_2 is first stable at around 213±2 ps up to 450°C, then increases up to 700°C where it reaches 219±2 ps and then starts decreasing. The intensity corresponding to this lifetime component decreases up to 700°C and then remains stable at 60±2%.

For measurements performed at 215 K, the evolution of the average lifetime is more complex. The lifetime first decreases from 203±1 ps to 195±1 ps, then rises up to 199±1 ps and decreases again down to 195±1 ps. When the annealing temperature increases, it rises again to reach 202±1 ps and then it decreases abruptly to 186±1 ps. The long lifetime component is first stable at around 216±2 ps, then rises between 400°C and 700°C and becomes stable again at around 226±3 ps up to 950°C.

At high measurement temperatures $\tau_{\text{av.}}$ first increases from 211±1 ps up to 218±1 ps, then is stable between 700°C and 850°C and finally decreases to 210±1 ps. τ_2 first increases from 225±2 ps up to 235±3 ps between 400°C and 700°C and then remains stable at around 231±2 ps. Its relative intensity I_2 is high and remains stable at 82±2% between 400°C and 850°C and then decreases slightly to 76±2%.

Identification of defects The EPR measurements indicate the presence of V_{Si}^{1-} in the studied samples. This defect was especially observed in the as-irradiated samples and for low annealing temperatures. Meanwhile, the PAS measurements for the as-irradiated samples showed a lifetime of 214±2 to 218±2 ps. This lifetime is very close to the 219 ps lifetime we calculated for

the V_{Si}^{1-} in 6*H*-SiC, when scaled to the experimental lattice lifetime). The results of both the EPR and PAS measurements thus indicate that the silicon vacancy is probably the main defect observed by these methods before annealing and at low temperatures after annealing.

The PAS measurements at 215 K (see Fig. 4.23) show that the positron lifetime is stable for annealing temperatures lower than 400°C, then starts increasing and stabilizes around 650°C. For similar temperatures, the EPR signal (see Fig. 4.22b) attributed to the silicon vacancy decreases. This indicates that at these temperatures, the silicon vacancy is annealed and that a larger defect exhibiting a longer lifetime is created. This defect is probably neutral, because it is observed at high measurement temperatures, when the trapping coefficient depends more on the size of the defect than on its charge. Additionally, it has to contain at least part of the disappearing silicon vacancies.

At high measurement temperatures, the negative defect should not be predominant in the PAS signal any longer and the neutral cluster (called V_A) should be predominantly detected due to its larger volume. In Fig. 4.23 we can notice that τ_2 increases between the annealing temperatures of 400°C and 700°C for 555 K measurements. We propose that during this stage the silicon vacancy are annealed through clustering. The long lifetime component stabilizes at 235 ps. This lifetime is very close to the one we calculated for the neutral V_C+V_{Si} divacancy (235 ps in 3*C*-SiC and between 234 and 236 ps in 6*H*-SiC, when scaled to the experimental lattice lifetime). Additionally, our charge state calculations showed that the divacancy should be neutral in a wide range of electron chemical potentials (see Fig. 4.6b).

Therefore, we propose that the V_A defect is the neutral V_C+V_{Si} divacancy. This suggests that in the studied 6*H*-SiC samples silicon vacancies were created by irradiation and were then annealed between 400°C and 700°C. The annealing was probably due to formation of V_C+V_{Si}. This process requires migration of carbon or silicon vacancies. According to Zolnai *et al.* [39] the carbon monovacancies migration is only possible for annealing temperatures higher than 1100°C. Additionally, *ab initio* calculations of Bockstedte *et al.* [9] yielded a significantly higher migration barrier for the V_C^{2+} vacancy (5.2 eV) than for V_{Si}^{1-} (3.2 eV). Therefore, we propose that the process is related to silicon vacancies migration. This should, however, be confirmed by additional experimental and theoretical studies. We also assume that the carbon vacancies that are indispensable in the clusters formation were also created by irradiation, but that they could not be detected by the characterization methods used. Their most probable charge states, 0 and 2+ [143], are nonparamagnetic and cannot be observed in EPR. As for the PAS, the positive carbon vacancies do not trap positrons and the neutral ones would trap much less positrons than the negative silicon vacancies, inducing a very weak signal.

Our results can be compared with the EPR study of Carlsson *et al.* [154]. They observed a strong annealing of silicon vacancies in irradiated 4*H*-SiC up to 700°C and simultaneous increase in the

V_C+V_{Si} divacancy concentration. This behavior is in good agreement with what we observe in irradiated 6H-SiC samples. It is worth noting that in our study the divacancies were detected by PAS and not EPR. We suppose that the intensity of the $P6/P7$ center (V_C+V_{Si} divacancy) was too weak to identify it in the as-received samples and has not been tracked in the annealed crystals.

As for the behavior of the non-vacancy defects, we observe that the long lifetime component τ_2 measured at 215 K remains constant during annealing at temperatures between 700°C and 850°C. Meanwhile, its relative intensity I_2 increases. It indicates that in this annealing temperature range, the trapping rate of the vacancy defects increases. The increase in the I_2 values measured at 555 K is much smaller, because at this measurement temperature the positron trapping around negative ions is not dominant. We propose that the increase of the trapping in vacancies between 700°C and 850°C corresponds to the annealing of a part of the 'negative ions' detected by the positrons in the crystals. We suggest that the annealed defects might be the irradiation induced 'negative ions' rather than the native ones, because the annealing temperatures are much lower than the crystal growth temperature using the modified Lely method (>1800°C). This annealing phenomenon of the 'negative ions' has already been observed by Polity *et al.* [161] in 2 MeV electrons irradiated 6H-SiC crystals then annealed between 450°C and 900°C.

4.4.2 Doppler broadening

In this section we compare the Doppler spectra calculated for defects in silicon carbide with the experimental data obtained by F. Linez during her PhD thesis at the CEMHTI laboratory [162]. In this work n-type 6H-SiC samples were irradiated with 4 MeV Au ions with fluences from 10^{12} to 10^{15} cm^{-2}. These irradiations led to the creation of vacancies and vacancy clusters with various sizes. The samples were studied with a pulsed low energy positron beam with a varying energy, allowing measurement of both positron lifetime and momentum distributions.

In Tab. 4.14 we recall the positron lifetimes that were detected in the study of F. Linez in the cascade region of the irradiated SiC samples. In Fig. 4.24 we compare the measured and calculated S_{rel} and W_{rel} parameters. The calculated spectra were convoluted using a Gaussian function with FWHM=4.7 mrad, which should be close to the experimental resolution in the reference study. We observe that the calculated points are slightly below the experimental points. However, an overall good agreement is obtained in the evolution trends of the relative S_{rel} and W_{rel} values. The differences can be due to various approximations made in the calculations and to experimental uncertainties.

The experimental S_{rel} and W_{rel} parameters measured after irradiation at 10^{12} and 10^{13} cm^{-2} fluences do not align with any of the calculated values. However, they lay near the points calculated for V_{Si} and V_{Si}+V_C+C_{Si}. A long positron lifetime of 223–225 ps was measured after these irradiations, which is close to what was calculated for the silicon monovacancy. We suppose, hence, that a defect of a similar size was detected in these samples. It is worth noting that the experimental points measured after irradiation at 10^{12} and 10^{13} cm^{-2} fluences are above the line going through the (1,1) point and the data corresponding to samples irradiated at higher fluences (see dashed lines in Fig. 4.24). Meanwhile, for all the considered 'pure' defects in silicon carbide we calculated points that are aligned on the line going through the (1,1) point. We can suppose, hence, that the shift of the experimental points can be due to the presence of impurities. In Fig. 4.21 we show that the nitrogen decoration of the silicon monovacancy leads to a similar shift of the points on the $S(W)$ plot. We suppose hence that after irradiation at 10^{12} and 10^{13} cm^{-2} fluences vacancy complexes with impurities, such as nitrogen, are detected.

After irradiation at 10^{14} cm^{-2} fluence the S_{rel} increase and W_{rel} decrease. The experimental points corresponding to this irradiation are distributed along a line starting above the point calculated for V_C+V_{Si} and going in the direction of the $(V_C{+}V_{Si})_3^{\mathrm{ring}}$ complex. Several other complexes can correspond to the experimental points,V_C+V_C, V_C+V_{Si}+V_C, V_{Si}+V_C+V_{Si}, $(V_C{+}V_{Si})_2$ and $(V_C{+}V_{Si})_3^{\mathrm{chain}}$. The positron lifetimes measured in this sample vary from 239 to 289 ps as a function of the incident positron energy, corresponding to different depths which the positrons probe. It means that defects of different sizes, probably between divacancies and hexavacancies were created in this sample. However, in the region of the $S_{\mathrm{rel}}(W_{\mathrm{rel}})$ plot corresponding to the irradiation at 10^{14} cm^{-2} fluence, various theoretical points are close to each other and difficult to distinguish. It could be useful to have access to whole experimental ratio curves or to recalculate the experimental parameters using a different high-momentum integration region, since this can help in separating some of the points on the $S_{\mathrm{rel}}(W_{\mathrm{rel}})$ plot, as was showed in Fig. 4.14.

After irradiation at 10^{15} cm^{-2} fluence the experimental points move further towards the point calculated for the $(V_C{+}V_{Si})_3^{\mathrm{ring}}$ cluster. The measured S_{rel} and W_{rel} parameters are close to the value calculated for the 'ring' hexavacancy, but slightly shifted towards the points calculated for smaller defects. We suppose that several defects are detected at the same time, while $(V_C{+}V_{Si})_3^{\mathrm{ring}}$ is predominant. This is consistent with the positron lifetime measured in this sample. The value of around 284 ps, is lower than what we calculated for $(V_C{+}V_{Si})_3^{\mathrm{ring}}$ (296 ps when scaled to the experimental lattice lifetime), suggesting that some defects with smaller free volumes are also present in the sample.

Combining the information on the positron lifetimes and Doppler spectra can facilitate the defects identification. We can see, however, that in some cases it is still difficult to distin-

guish the defects. It would hence be useful to confirm our conclusions by coupling positron lifetime and Doppler broadening measurements with another type of experiment, for instance photoluminescence spectroscopy (PL), performed on the same samples.

Table 4.14: *Experimental positron lifetimes detected in 4 MeV Au irradiated 6H-SiC. Data were extracted from Ref. [162]. In the case of the irradiation at 10^{14} cm^{-2} the positron lifetime varied as a function of the incident positron energy (between 5 and 11 keV).*

Fluence (cm^{-2})	τ_1 (ps)	I_1 (%)	τ_2 (ps)	I_2 (%)
10^{12}	177±0	6±0.7	225±0	94±0.7
10^{13}	223±1	100	–	–
10^{14}	239±0	96↘56	289±0	4↗44
10^{15}	284±1	100	–	–

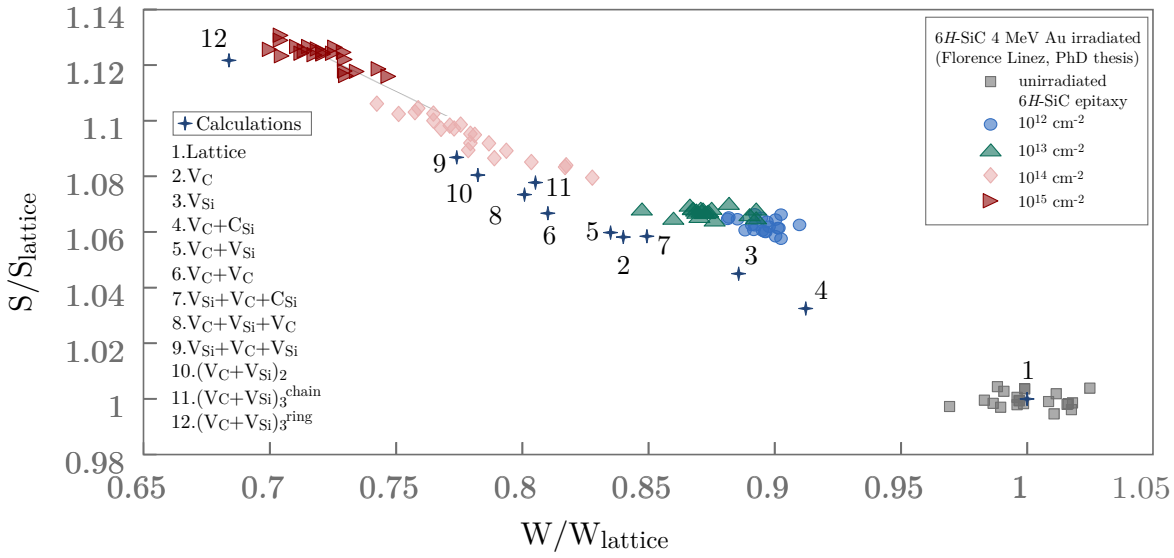

Figure 4.24: *Comparison between the calculated and experimental S_{rel} and W_{rel} parameters detected by F. Linez [162] in 4 MeV Au irradiated n-type 6H-SiC. The theoretical data were convoluted with a Gaussian function with FWHM=4.7 mrad.*

4.5 Conclusions

We calculated the positron lifetimes, Doppler spectra and formation energies for vacancy clusters containing from two to six vacancies. The calculated formation energies enabled us to predict the most stable charge states of these defects. We showed that the atomic relaxation effect affects strongly the calculated positron annihilation characteristics and should be taken into account in the calculations. We also showed that in silicon carbide the positron lifetime is mainly affected by the number of the silicon vacancies in the cluster. Additionally, in the case

of the large vacancy clusters, such as the hexavacancy, we observed that not only the number of vacancies but also their configuration strongly affects the positron lifetime.

In the Doppler broadening calculations we studied the effect of the experimental parameters on the S and W parameters that are commonly used to analyze the results. We showed the effect of the experimental resolution and the integration windows on the calculated S and W. We observed that an appropriate choice of the high-momentum integration region can facilitate the separation of the defects, especially on different sublattices.

We also studied the effect of the silicon carbide polytype on the calculated positron lifetimes and Doppler spectra. We observed that while the results obtained for the carbon vacancy depended strongly on the atomic site, the effect was much smaller for the silicon vacancy and V_C+V_{Si} complex. We concluded, hence, that the results obtained for clusters in 3C-SiC can also be used to analyze the experiments performed on other silicon carbide polytypes.

We compared our calculated results with the experimental lifetimes and Doppler broadening data reported in literature. The calculated positron lifetimes enabled us to confirm the identification of vacancy clusters done in previous studies by means of positron annihilation spectroscopy.

We also used the calculated positron lifetimes to analyze unpublished PAS and EPR results obtained on irradiated and annealed 6H-SiC crystals in the light of our positron and formation energies calculations. The combined characterization methods showed the presence of silicon vacancies in irradiated 6H-SiC, which was confirmed by the positron lifetime calculations. During annealing at temperatures starting at around 400–500°C the migration of the silicon vacancies and the formation of a larger defect were observed. This defect, exhibiting a positron lifetime of 235 ps, was identified as V_C+V_{Si} based both on the charge state and positron lifetime calculations.

The results of the Doppler spectra calculations were compared with experimental data obtained by F. Linez in n-type 6H-SiC samples irradiated with 4 MeV Au ions with fluences from 10^{12} to 10^{15} cm^{-2}. We observed a good general agreement between the measured and calculated points. However, it was shown that due to the choice of the integration windows in S and W parameters calculations, the points corresponding to different defects are aligned and difficult to distinguish, even when coupling the results with the information on positron lifetimes. We concluded that it could be useful to recalculate the experimental parameters using a different high-momentum integration region and to couple the positron lifetime and Doppler broadening measurements with another type of experiment, for instance photoluminescence spectroscopy (PL), performed on the same samples. The above mentioned activities are planned in the near future at the CEMHTI laboratory.

Chapter 5

Results on uranium dioxide

To support the identification of defects in uranium dioxide using positron annihilation spectroscopy, we calculated two types of properties: the formation energies to determine the most stable charges of defects and the positron annihilation characteristics. We present here the results of these calculations and the analysis of the experimental data based on them. The results described in this chapter have been partly published in Ref. [163], [164] and [165].

5.1 Formation energies of charged defects

We performed first principles calculations of the formation energies of various charged defects in UO_2 using the GGA+U method. We considered defects of different sizes, going up to the $2V_U$+$4V_O$ hexavacancy. This study was performed jointly with another PhD student, Emerson Vathonne, and partly presented in his thesis [22] and in Ref. [163] and [164]. The calculations of formation energies had two goals. First, it was done to study the clustering of defects and to provide a basis for a study of fission gas incorporation and migration. Second, the determination of the most stable charge states was necessary to predict if the given vacancy can be detected by PAS and to know which charge state can be expected in the examined samples. We will first describe the methods used in the calculations of the formation energies and then present the results.

5.1.1 Methods used in formation energy calculations

The formation energies of the charged defects can be calculated according to

$$E_{\mathrm{f}}(V_{\mathrm{X}}, q) = E_{\mathrm{tot}}(V_{\mathrm{X}}, q) - n_{\mathrm{O}}\mu_{\mathrm{O}}^{\mathrm{UO_2}} - n_{\mathrm{U}}\mu_{\mathrm{U}}^{\mathrm{UO_2}} + q\mu_{\mathrm{e}}, \tag{5.1.1}$$

where $E_{\mathrm{tot}}(V_{\mathrm{X}}, q)$ is the total energy of the supercell, n_{U} and n_{O} are the numbers of uranium and oxygen atoms in the cell, μ_{U} and μ_{O} are the chemical potentials of the uranium and the oxygen atom in UO_2, q is the charge of the defect and μ_{e} is the electron chemical potential, which varies from the bottom to the top of the band gap.

The chemical potentials of uranium and oxygen atoms in UO_2 cannot be directly retrieved from calculations. They can be, however, estimated considering the standard formation enthalpy and the energies of these atoms in their reference states (metallic uranium and oxygen molecule). Choice of the references will be described in Sec. 5.1.1.1.

As already mentioned in the study of charged defects in SiC (see Sec. 4.1), the classical supercell approach fails in providing accurate formation energies for charged supercells, thus approximations have to be made while calculating formation energies. We use a correction scheme proposed by Taylor and Bruneval [108]. We take, thus, the Madelung term $\Delta E_{\mathrm{el}}(q)$ [106, 107], that corrects the electrostatic interaction between the defect and its images and is given as

$$\Delta E_{\mathrm{el}} = \frac{\alpha q^2}{2\epsilon_0 L}, \tag{5.1.2}$$

where α is the Madelung lattice constant, ϵ is the static dielectric constant and L is the length of the supercell edge.

Additionally, we use a potential alignment ΔV, taking

$$\Delta V = \langle v_{\mathrm{KS}}^{\mathrm{bulk}} \rangle - \langle v_{\mathrm{KS}}^{\mathrm{defect}} \rangle, \tag{5.1.3}$$

where $\langle v_{\mathrm{KS}}^{\mathrm{bulk}} \rangle$ and $\langle v_{\mathrm{KS}}^{\mathrm{defect}} \rangle$ are the average Kohn-Sham potentials calculated for the cell without and with the defect, respectively.

Taking into account the previous equations, the final expression takes the form:

$$\begin{aligned} E_{\mathrm{f}}(V_{\mathrm{X}}, q) = \quad & E_{\mathrm{tot}}(V_{\mathrm{X}}, q) - n_{\mathrm{O}}\mu_{\mathrm{O}}^{\mathrm{UO_2}} - n_{\mathrm{U}}\mu_{\mathrm{U}}^{\mathrm{UO_2}} \\ & + q(E_{\mathrm{VBM}} + \mu_{\mathrm{e}} + \Delta V) + \Delta E_{\mathrm{el}}(q), \end{aligned} \tag{5.1.4}$$

where E_{tot} is the energy of the supercell with a defect.

5.1.1.1 Choice of the reference energies

To obtain formation energies using Equation (5.1.4) one needs to know the reference energies of U and O atoms in UO_2, i.e. their chemical potentials $\mu_{\mathrm{U}}^{\mathrm{UO_2}}$ and $\mu_{\mathrm{O}}^{\mathrm{UO_2}}$. These values, however, cannot be directly obtained from the calculations and they depend on the stoichiometry of the material. We can write two relations:

$$\mu_{\mathrm{UO_2}}^{\mathrm{bulk}} = \mu_{\mathrm{U}}^{\mathrm{UO_2}} + 2\mu_{\mathrm{O}}^{\mathrm{UO_2}} \tag{5.1.5}$$

and

$$\mu_{\mathrm{UO_2}}^{\mathrm{bulk}} - \mu_{\mathrm{U}}^{\mathrm{U\ met.}} - 2\mu_{\mathrm{O}}^{\mathrm{O_2}} = \Delta H_{\mathrm{f}}^{\mathrm{UO_2}}, \tag{5.1.6}$$

where $\mu_{\mathrm{U}}^{\mathrm{U\ met.}}$ is the energy of one uranium atom in metallic U and $\mu_{\mathrm{O}}^{\mathrm{O_2}}$ in the energy of one oxygen atom in the O_2 molecule. We will now consider differences between chemical potentials of the atoms in the UO_2 and in their standard states (metallic uranium and O_2 molecule),

$$\Delta\mu_{\mathrm{U}} = \mu_{\mathrm{U}}^{\mathrm{UO_2}} - \mu_{\mathrm{U}}^{\mathrm{U\ met.}} \tag{5.1.7}$$

$$\Delta\mu_{\mathrm{O}} = \mu_{\mathrm{O}}^{\mathrm{UO_2}} - \mu_{\mathrm{O}}^{\mathrm{O_2}}. \tag{5.1.8}$$

Introducing $\Delta\mu_{\mathrm{U}}$ and $\Delta\mu_{\mathrm{O}}$ to Eq. (5.1.4) we obtain

$$\begin{aligned} E_{\mathrm{f}}(V_{\mathrm{X}}, q) = \quad & E_{\mathrm{tot}}(V_{\mathrm{X}}, q) - n_{\mathrm{O}}(\mu_{\mathrm{O}}^{\mathrm{O_2}} + \Delta\mu_{\mathrm{O}}) \\ & -n_{\mathrm{U}}(\mu_{\mathrm{U}}^{\mathrm{U\ met.}} + \Delta\mu_{\mathrm{U}}) \\ & +q(E_{\mathrm{VBM}} + \mu_{\mathrm{e}} + \Delta V) + \Delta E_{\mathrm{el}}(q). \end{aligned} \tag{5.1.9}$$

The chemical potentials of both elements in UO_2 have to be smaller than in the standard states, otherwise the material would decompose. Both $\Delta\mu_{\mathrm{U}}$ and $\Delta\mu_{\mathrm{O}}$ have to be, thus, smaller than 0. The lower limit of these values is defined by the sum:

$$\Delta\mu_{\mathrm{U}} + 2\Delta\mu_{\mathrm{O}} = \Delta H_{\mathrm{f}}^{\mathrm{UO_2}}. \tag{5.1.10}$$

$$\Delta H_{\mathrm{f}}^{\mathrm{UO_2}} < \Delta\mu_{\mathrm{U}} < 0 \tag{5.1.11}$$

$$\frac{1}{2}\Delta H_{\mathrm{f}}^{\mathrm{UO_2}} < \Delta\mu_{\mathrm{O}} < 0 \tag{5.1.12}$$

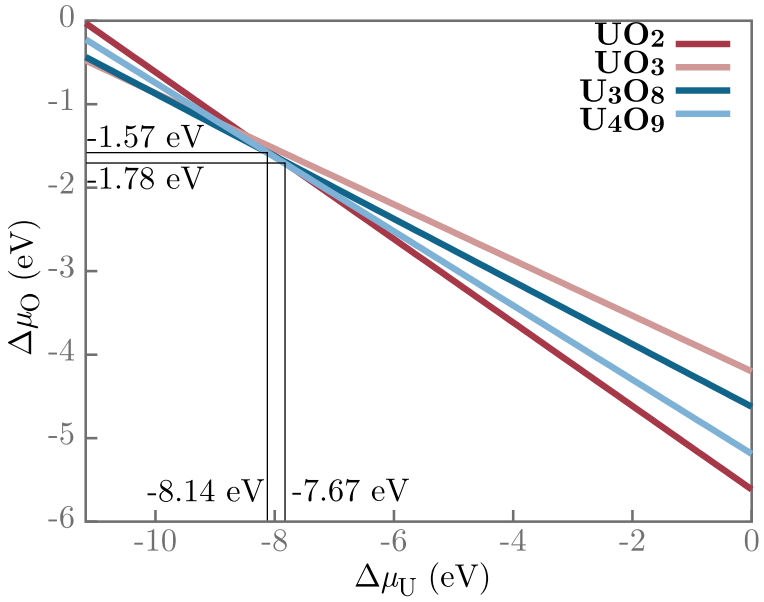

Figure 5.1: *$\Delta\mu_U$ as a function of $\Delta\mu_O$ for different phases of U-O systems.*

Taking the experimental value of the standard formation enthalpy (-11.23 eV [166]), these ranges are however very wide:

$$-11.23 \text{ eV} < \Delta\mu_{\mathrm{U}} < 0 \tag{5.1.13}$$

and

$$-5.62 \text{ eV} < \Delta\mu_{\mathrm{O}} < 0. \tag{5.1.14}$$

These ranges can be slightly narrowed by considering other phases of U-O systems. Following the reasoning of Na-Phattalung *et al.* [167], we trace $\Delta\mu_{\mathrm{U}}$ as a function of $\Delta\mu_{\mathrm{O}}$ (Fig. 5.1) for different phases, while keeping:

$$\Delta H_{\mathrm{f}}^{\mathrm{U}_x\mathrm{O}_y} = x\Delta\mu_{\mathrm{U}} + y\Delta\mu_{\mathrm{O}} \tag{5.1.15}$$

As the first principles calculations for U_3O_8 and U_4O_9 are quite complicated to perform, we took the experimental values of ΔH_{f} from Reference [166]. As our calculated value for UO_2 of 11.17 eV was very close to the experimental value of 11.23 eV, we suppose that this comparison is valid. In Fig. 5.1 it can be seen that UO_2 is stable ($\Delta\mu_{\mathrm{U}}$ and $\Delta\mu_{\mathrm{O}}$ are minimized for this phase) when $\Delta\mu_{\mathrm{O}}$ is lower than -1.78 eV and $\Delta\mu_{\mathrm{U}}$ is larger than -7.67 eV. For higher $\Delta\mu_{\mathrm{O}}$, what is equivalent to more O-rich conditions, U_4O_9 and U_3O_8 would precipitate. We have, hence, new ranges for the differences in chemical potentials:

$$-7.67 \text{ eV} < \Delta\mu_{\mathrm{U}} < 0 \tag{5.1.16}$$

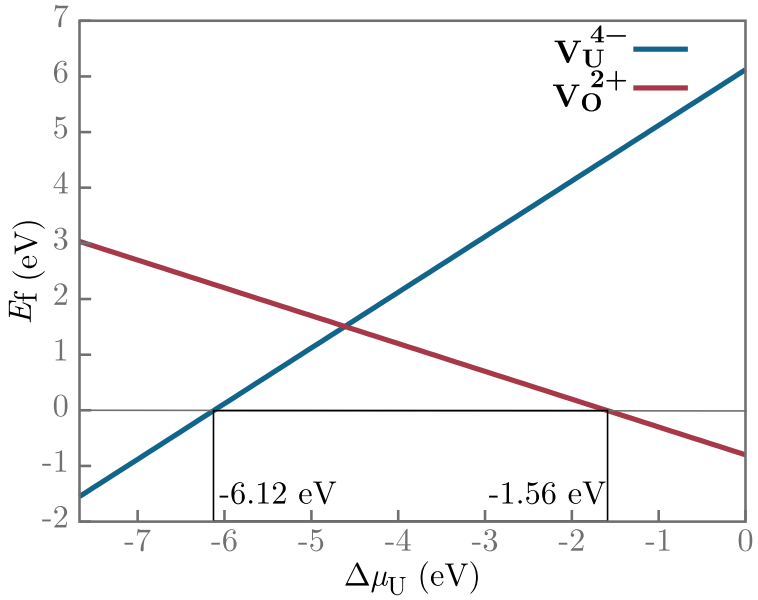

Figure 5.2: *Formation energies of V_U^{4-} and V_O^{2+} as a function of $\Delta\mu_U$. Energies are taken for the Fermi level in the middle of the band gap.*

and

$$-5.62 \text{ eV} < \Delta\mu_O < -1.78 \text{ eV}. \tag{5.1.17}$$

This range is still wide. We further narrow it by putting a constraint on the formation energies of the vacancies, in a similar way to what was done for ZrN by Pukari *et al.* [168]. In their study, they imposed chemical potentials of Zr and N so that the formation energies of the vacancies is positive. They studied, however, neutral defects only. In our case, formation energies depend not only on the chemical potentials of the atoms, but also on μ_e. We will impose reference energies for which all the vacancies have positive formation energies for the Fermi level in the middle of the gap, i.e. for $\mu_e = 1.2$ eV, since we have calculated a gap of 2.4 eV. The O-rich conditions are defined by E_f of V_U^{4-} and the U-rich conditions by E_f of V_O^{2+} (for more details on the formation energies of these defects see Sec. 5.1.5). The positive formation energy of the uranium vacancy is assured by $\Delta\mu_U$ larger than -6.12 eV (see Fig. 5.2). The constraint on oxygen vacancy formation energy implies $\Delta\mu_U$ smaller than -1.56 eV. Finally, we have

$$-6.12 \text{ eV} < \Delta\mu_U < -1.56 \text{ eV} \tag{5.1.18}$$

and

$$-4.80 \text{ eV} < \Delta\mu_O < -2.52 \text{ eV}. \tag{5.1.19}$$

We will consider three cases in our further study: O-rich with $\Delta\mu_O = -2.52$ eV and $\Delta\mu_U = -6.12$ eV, U-rich with $\Delta\mu_O = -4.80$ eV and $\Delta\mu_U = -1.56$ eV and a near-stoichiometric case,

where we take the mean values, $\Delta\mu_O = -3.66$ eV and $\Delta\mu_U = -3.84$ eV. It is worth keeping in mind that the values for the various regimes can differ slightly from the ones in the real stoichiometric material, and an approximation is made here.

5.1.2 Previous studies on defects in UO_2

Defects in UO_2 have already been widely studied within the density functional theory (see for instance Ref. [21] and [22]). However, there are some inconsistencies in the formation energies of the defects in UO_2 obtained in previous theoretical study. This is mainly due to the different methods used in these studies. First, various methods can be chosen for description of interactions between the electron, for example: LDA, GGA, LDA+U, GGA+U and hybrid functionals. Second, if the DFT+U method is chosen, one can deal with the convergence to the metastable states (through occupation matrix control or U-ramping) or not. Third, charge states of the defects have been taken into account in some of the studies and not in the others. Finally, the choice of the reference energies of O and U atoms, used in formation energies calculations, differs between the studies. Some authors choose O-rich conditions, where oxygen atom energy is set to its energy in a O_2 molecule, other authors change references from one defect to another. We will briefly recall conditions of previous studies on defects in UO_2.

Freyss *et al.* [27] performed calculations for neutral point defects and Frenkel pairs in GGA. They used 24 atom supercells. Iwasawa *et al.* [169], studied neutral point defects in the GGA+U framework in 96 atom supercells. In this study the influence of the metastable states was not taken into account. Dorado *et al.* [28, 30] also used the GGA+U method to study neutral defects up to the V_U+$2V_O$ trivacancy in 96 atom supercells. However, in the studies of Dorado *et al.* occupation matrices were controlled to avoid the convergence to the metastable states. In all the calculations above, the O-rich conditions were used for O-related defects and U-rich conditions for U-related defects.

There are also several studies that were performed for charged defects in 96 atom supercells, in which O-rich conditions were used for all the defects. Crocombette *et al.* used the GGA+LHFCE (pseudo-hybrid) [29] and GGA+U [170] methods, with U-ramping, to study various charged defects up to the V_U+$2V_O$ trivacancy. Nerikar *et al.* [171] also used GGA+U to study similar defects. However, in this study, no metastable state control was used.

In our study, we use the GGA+U method and we control the occupation matrices. We performed calculations for charged point defects and defects clusters up to the $2V_U$+$4V_O$ hexavacancy. We used supercells containing 96, 144 and 324 atoms. We also narrowed the range of possible

reference energies for O and U atoms, as presented in Sec. 5.1.1.1, and considered three cases: the O-rich, stoichiometric and U-rich regimes.

5.1.3 Computational details

The formation energy calculations were performed using the projector augmented wave method (PAW) [102, 103] as implemented in the Vienna Ab initio Simulation Package (VASP) [172–174]. The generalized gradient approximation (GGA) as parametrized by Perdew, Burke, Ernzerhof (PBE) [175] is used to describe the exchange-correlation interactions. Moreover, a Hubbard-like term (U) is added in order to take into account the strong correlations between the $5f$ electrons of the uranium atoms. The Liechtenstein scheme [101] of the DFT+U method is used. The values of the U and J parameters were set to 4.5 eV and 0.51 eV respectively, in agreement with earlier DFT+U calculations [97] and the values extracted from experiments [176]. In order to avoid the convergence to one of the numerous metastable states yielded by the DFT+U method and ensure that the ground state is reached, we used the occupation matrix control scheme [31, 177, 178].

Uranium dioxide is paramagnetic above 30.8 K and below this temperature it has a noncollinear 3**k** antiferromagnetic order [179]. These systems can be, however, only modeled using large numbers of atoms. We consider, therefore, a 1**k** antiferromagnetic ordering, which is an approximation of the noncollinear 3**k** order, since the two exhibit only small differences in energy [180].

Two types of supercells were used in our study. Calculations for monovacancies, monointerstitials, oxygen di-interstitials, U-O divacancy and bound Schottky defects were performed in supercells containing 96 atomic sites (2×2×2 repetitions of the fluorite unit cell). In this case we used a 2×2×2 Monkhorst-Pack **k**-point mesh [181]. For larger defects, we use supercells containing 144 atomic sites (2×2×3 repetitions of the unit cell) with a 2×2×1 Monkhorst-Pack **k**-point mesh [181]. A Gaussian smearing of 0.1 eV is used in all the calculations. The lattice parameters and atomic positions are relaxed and all initial point symmetries are removed during calculations. A plane wave cutoff energy of 500 eV is used, in agreement with cutoff convergence tests and previous studies. We relax the structures until the Hellmann-Feynman forces are converged to less than 0.01 eV/Å. In addition, we make sure that the total energy of the system is converged to less than 10^{-5} meV/atom. With these conditions we find lattice parameters $a = b = 5.57$ Å and $c = 5.49$ Å for perfect UO_2, compared to 5.47 Å measured experimentally [14]. The distortion in the z axis is due to the 1**k** antiferromagnetic order.

5.1.4 Considered defects

We study the various point defects and defects clusters that can be formed in UO_2. These defects are divided in three groups. First, we consider 'small defects' i.e. oxygen and uranium monovacancies (V_O and V_U), oxygen and uranium interstitials (I_O and I_U), an oxygen di-interstitial ($2I_O$) and a divacancy containing one oxygen vacancy and one uranium vacancy (V_U+V_O). The second type of defects are the bound Schottky defect (BDS) containing one uranium vacancy and two oxygen vacancies (V_U+$2V_O$). Three configurations of this defect are possible, with the two oxygen vacancies aligned along [100], [110] and [111] directions called BSD1, BSD2 and BSD3, respectively. Finally, we study various large clusters, containing two uranium vacancies: a $2V_U$ divacancy, a $2V_U$+V_O trivacancy, a $2V_U$+$2V_O$ tetravacancy and a $2V_U$+$4V_O$ hexavacancy (di-Schottky).

We considered various charge states of the defects listed above. To do that we add or remove electrons from the supercell taking into account the charges of uranium and oxygen ions in UO_2: O^{2-} and U^{4+}. For all the defects we consider at least all the charges between +2 and −2. In some cases we investigate additionally the charge states up to the ones based on the formal charges of oxygen and uranium ions in uranium dioxide, 2− and 4+, respectively. For instance, in the case of the uranium vacancy, one U^{4+} is removed from the system, along with four electrons taking part in the ionic bonds. To compensate the loss of these four electrons, we add up to four electrons to the system. The formation energies of the charged defects depend on the electron chemical potential (μ_e), which is equivalent to the Fermi level. μ_e changes between the top of the valence band and the bottom of the conduction band. Thus, we present our results across the band gap of the material which was found to be 2.4 eV.

It is worth noting that for some defects the charge states corresponding to the formal charges of oxygen and uranium ions are very high, e.g. −8 for V_U+V_U. In these cases, even after applying corrections, the errors related to the finite size of the cells used in calculations can be significant. Nevertheless, we decided to perform and present the calculations also for high charge states as a first attempt of modeling such defects.

5.1.5 Small defects

The formation energies of the small defects are presented in Fig. 5.3. Three different cases are considered: O-rich (Fig. 5.3a), stoichiometric (Fig. 5.3b) and U-rich conditions (Fig. 5.3c).

It is worth noting that stoichiometry does not affect the charge state stability regions. For all the growth conditions, in the undoped material (Fermi level in the middle of the gap) the

stable charges for all these defects are in agreement with the formal charges of ions except for the uranium interstitial. In the middle of the gap, we find defects with charge states as follows: V_O^{2+}, I_O^{2-}, $2I_O^{4-}$, V_U^{4-}, I_U^{3+} and V_O+V_U^{2-}. The disagreement on I_U can be due to the errors connected to using finite supercells sizes in charged defects calculations. Our results show that all of the 'small defects' in UO_2 are charged, which is in agreement with results of Crocombette [170] and confirms the very ionic nature of UO_2. Charge states cannot be, thus, neglected in studies on defects in this material.

In the case of the hyperstoichiometric UO_2 (Fig. 5.3a) we found that the V_U^{4-} vacancy has the lowest formation energy when the Fermi level lays in the middle of the gap. There are also two defects with slightly higher E_f, I_O^{2-} and V_O+V_U^{2-} (difference of 0.37 eV). These three defects should be, therefore, the most stable ones in UO_{2+x}.

When the oxygen chemical potential decreases and moves towards stoichiometric conditions, the formation energies of these three defects rise and become higher than the one of the oxygen vacancy. V_O^{2+} is the most stable defect in both stoichiometric and hypostoichiometric UO_2 (Fig. 5.3b and 5.3c). It is worth noting that for the Fermi levels above the middle of the gap we find that the oxygen vacancy is negative, with a -2 charge. In previous studies this charge state was not predicted for the oxygen vacancy at all, probably mainly because it was not taken into account [170]. What is also interesting in the stoichiometric and hypostoichiometric conditions is that the V_O+V_U divacancy has a lower formation energy than the uranium monovacancy. Therefore, this complex should be highly stable.

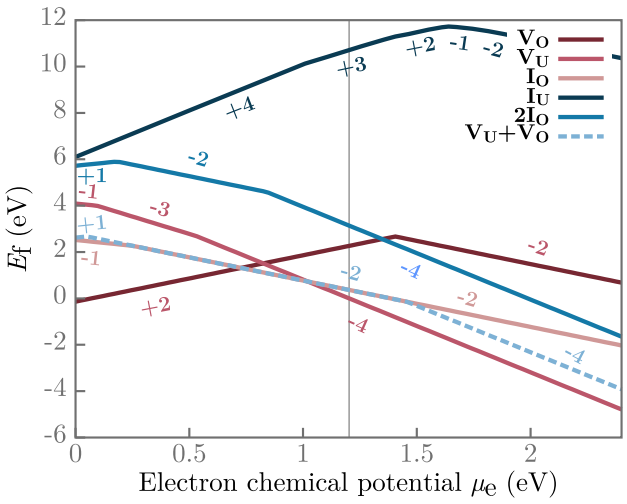

(a) O-rich

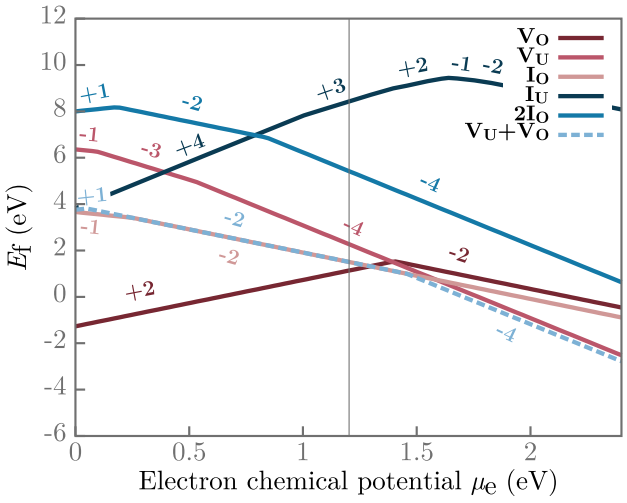

(b) Stoichiometric

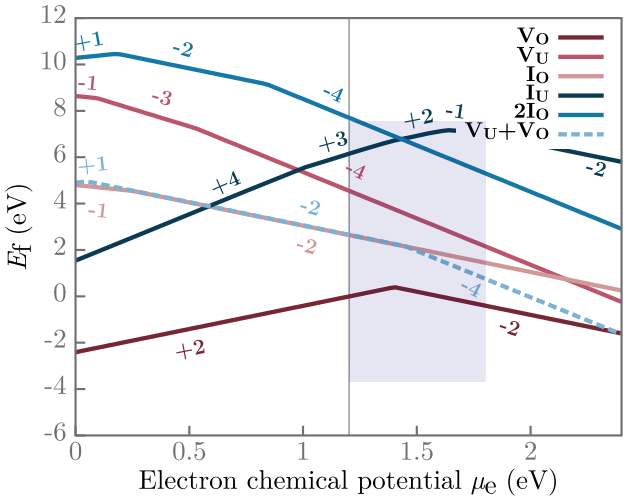

(c) U-rich

Figure 5.3: *Formation energies of the small defects in UO_2 for O-rich, stoichiometric and U-rich conditions.*

5.1.6 Bound Schottky defects

In Fig. 5.4 we present the formation energies of the bound Schottky defects. Since this is a stoichiometric defect, its formation energy does not depend on the choice of the reference energies. The formal charges of ions are also respected in this case, since the neutral charge state is stable for a wide range of the Fermi levels for the three Schottky defects. However, for Fermi levels above the middle of the gap, the three trivacancies become negative.

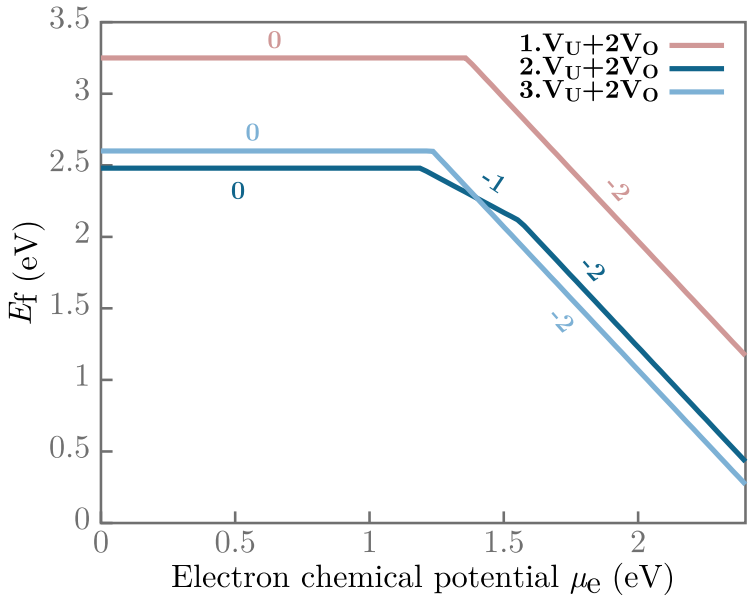

Figure 5.4: *Formation energies of the three configurations of the V_U+2V_O*

The BSD2 is the most stable one for the Fermi level laying in the middle of the band gap, in agreement with the study of Crocombette [170]. However, for higher Fermi levels we find that the BSD3 has the lowest formation energy. This is in disagreement with the study of Crocombette [170], who found that the BSD2 is the most stable in the whole gap. This difference can be due to the choice of the method used to avoid metastable states. In our study we used the occupation matrix control scheme, while Crocombette used the U-ramping method.

5.1.7 Large defects

The formation energies calculated for the vacancy clusters containing two uranium vacancies are presented in Fig. 5.5. Three regimes are taken into account: the hyperstoichiometric (Fig. 5.5a), stoichiometric (Fig. 5.5b) and hypostoichiometric (Fig. 5.5c) regimes. First of all, we can observe that the charge states of almost all the vacancy clusters are again in agreement with the formal

charges of point defects. In the middle of the band gap we find the charge states of -8 for $2V_U$, -6 for $2V_U{+}V_O$ and -4 for $2V_U{+}2V_O$. In the case of the $2V_U{+}4V_O$ (di-Schottky) it is the neutral charge that is expected. However, we observe that this defects ins neutral only for Fermi levels laying below the band gap middle and then becomes negative.

Additionally, we can observe that the formation energies of the clusters are quite small, especially in the case of the O-rich UO_2. It means that their presence should be expected in the material. However, it is worth noting that for some of these large clusters high charge states are expected. The errors due to the finite cells sizes increase with the defects charge state, hence the formation energies of defects with charge states of e.g. -4, -6 or -8 can be encumbered with rather large errors.

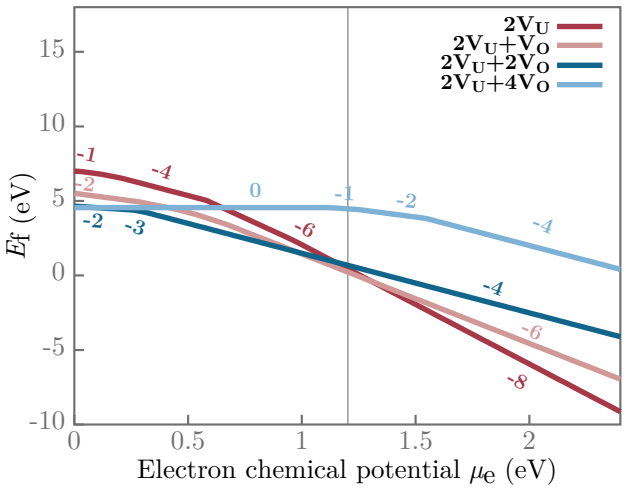

(a) O-rich

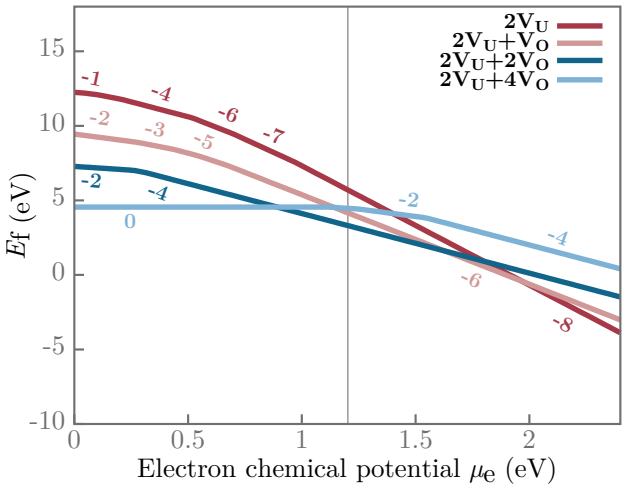

(b) Stoichiometric

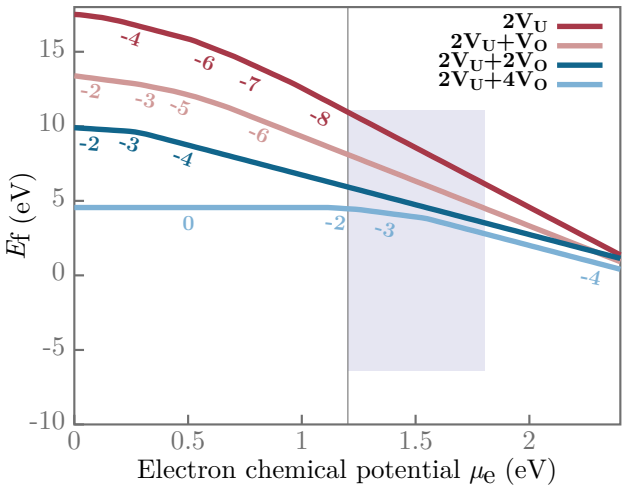

(c) U-rich

Figure 5.5: *Formation energies of the large defects in UO_2 for O-rich, stoichiometric and U-rich conditions.*

5.1.7.1 Comparison with previous studies

In the literature, the results are spread within a few eV for the formation energies of point defects due to the use of various calculation methods (LDA, GGA, LDA+U, GGA+U), the method to avoid the apparition of metastable states in DFT+U (occupation matrix control scheme or U-ramping) but also due to different references in energies for chemical potential of oxygen and uranium. Moreover, the majority of the studies dealt with neutral defects only even if currently authors take into account the various possible charges for the defects.

In the studies of Freyss *et al.* [27] (standard DFT) and Dorado *et al.* [28] (DFT+U with occupation matrices), a chemical potential of $\Delta\mu_{\mathrm{O}} = 0$ for the oxygen defects and a chemical potential of $\Delta\mu_{\mathrm{U}} = 0$ for the uranium defects have been used. These studies of neutral defects show the oxygen interstital to be the most stable defect in UO_2 whereas the uranium vacancy is unstable, which is not consistent with our results. This difference is due to the fact that they compared a result for the oxygen interstitial in the O-rich conditions with a result for the uranium vacancy for U-rich conditions.

Crocombette *et al.* [29, 170] used the O-rich conditions ($\Delta\mu_{\mathrm{O}} = 0$ and $\Delta\mu_{\mathrm{U}} = \Delta H_{\mathrm{f}}^{\mathrm{UO_2}}$) in their calculations. They found that the uranium vacancy is the most stable defect, which is consistent with our results for hyperstoichiometric UO_2. However, they found very low, negative formation energies for this defect. It would mean that this vacancies is formed spontaneously in the material. It is due to the fact that for $\Delta\mu_{\mathrm{O}} = 0$, the condition used in the studies of Crocombette *et al.*, UO_2 is not stable and it is rather U_3O_8 that is formed for this oxygen chemical potential.

Finally, in the study of Nerikar *et al.* [171] two cases were considered, the U-rich case with α-uranium chosen as the reference state, and the O-rich case with the oxygen molecule chosen as a reference. In both cases, $\mathrm{I}_{\mathrm{O}}^{2-}$ is found to be the most stable defect and $\mathrm{V}_{\mathrm{U}}^{4-}$ is approximately 2 eV higher in energy in undoped UO_2. This result is very different from the one obtained by Crocombette [29, 170] and by us. This difference is certainly due to the fact that no control of the occupation matrices was applied in the work of Nerikar *et al.* A different treatment of the Dudarev scheme, as well as a different definition of the O-rich and U-rich conditions, can also explain the discrepancies.

5.2 Positron lifetimes

5.2.1 Computational details

The positron lifetimes of defects in UO_2 were calculated using the ABINIT code. The atomic datasets used in this study were generated by the ATOMPAW code [104]. The methods and parameters used in the positron lifetime calculations were the same as in the study on the formation energies of defects (see Sec. 5.1.3).

5.2.2 Calculation results

We performed positron lifetime calculations for fully relaxed defects in UO_2 containing between one and six vacancies in both the GGGC+GC and PSN+GC schemes (see Sec. 3.1.4.2 for explanations of the schemes). The results are presented in Tab. 5.1. For almost all types of defects we considered two charge states. First, we performed positron lifetime calculations for neutral defects. Second, we calculated the lifetimes for vacancies in the charge states that were determined as the most stable ones in the stoichiometric material [163, 164]. Considering the oxygen vacancy, its formal charge (2+) cannot be detected by PAS. The 2− charge, however, was found to be stable for Fermi levels lying close to the middle of the band gap [163, 164], so we studied it as well. In Fig. 5.6 to 5.9 we present the positron isodensities calculated for the stable charge states of defect using the GGGC+GC and PSN+GC schemes.

As can be seen in Tab. 5.1, the differences between the positron lifetimes obtained in the two calculation schemes are lower than 10 ps for almost all considered defects. The biggest differences are found for two large defects, the neutral $2V_U+2V_O$ tetravacancy (difference of 15 ps) and the 2− charged $2V_U+4V_O$ hexavacancy (difference of 24 ps). It is also worth noting that similar results are yielded by the PSN+GC and GGGC+GC schemes for the stable charge states of the defects up to the $2V_U$ divacancy, i.e. defects which can most likely be observed in the PAS measurements.

For both schemes, we can observe that the lifetimes of the negative defects are almost always shorter than for the neutral ones. It is due to both a smaller relaxation and a higher electronic density in negative defects. However, in the case of the $2V_U+4V_O$ hexavacancy, the lifetime of the negative charge state is longer than the one of the neutral defect in both calculation schemes. This is due to the fact that the positron is localized differently in these two defects. In the GGGC scheme (Fig 5.8 (c) and (d)), in neutral $2V_U+4V_O$ the positron is localized inside

Table 5.1: *Positron lifetimes calculated in GGGC+GC and PSN+GC schemes for fully relaxed neutral and charged defects in UO_2. The lifetimes obtained for the most stable charge state of each defects are marked in bold.*

	Charge	Lifetime GGGC+GC (ps)	Lifetime PSN+GC (ps)
Lattice		168	167
V_O	0	206	199
V_O	2−	203	195
V_U	0	295	304
V_U	4−	**289**	**293**
V_U+V_O	0	303	306
V_U+V_O	2−	**299**	**301**
V_U+2V_O[100]	0	**301**	**304**
V_U+2V_O[110]	0	**310**	**313**
V_U+2V_O[111]	0	**314**	**316**
2V_U	0	313	318
2V_U	8−	**290**	**289**
2V_U+2V_O	0	324	339
2V_U+2V_O	4−	**309**	**319**
2V_U+4V_O	0	323	329
2V_U+4V_O	2−	**341**	**365**

one of the uranium vacancies, while in 2− charged 2V_U+4V_O the majority of its density can be found between two V_U. In the PSN scheme (Fig 5.9 (c) and (d)) we find a similar localization between two uranium vacancies in 2− charged 2V_U+4V_O. In the case of the neutral hexavacancy, however, the positron density has two maxima, one in each uranium vacancy.

In both schemes, it can be observed that different defects have similar positron lifetimes. For example, in GGGC+GC, the uranium monovacancy V_U^{4-} and divacancy $2V_U^{8-}$ have lifetimes of 289 and 290 ps, respectively. The PSN+GC scheme yields lifetimes of 293 and 289 ps, respectively. The lifetimes obtained for the $(V_U+V_O)^{2-}$ divacancy, 299 ps in GGGC+GC and 301 ps in PSN+GC, are also close to these values. Moreover, using the two methods we calculated positron lifetimes between 301 and 316 ps for the three configurations of the V_U+2V_O trivacancy and lifetimes of 309 ps (GGGC+GC) and 319 ps (PSN+SC) for $(2V_U+2V_O)^{4-}$. This can lead to difficulties in the defect identification in the positron lifetime spectroscopy studies on UO_2. The positron lifetimes can be, however, coupled with additional information on the defect properties, in particular their charge (through studying the temperature dependence of the PAS signals) or its chemical environment (through the Doppler spectra measurements).

To understand why different defects have similar positron lifetimes, we plotted the isodensities of the positron localized in these systems. We plot the results obtained in the GGGC+GC

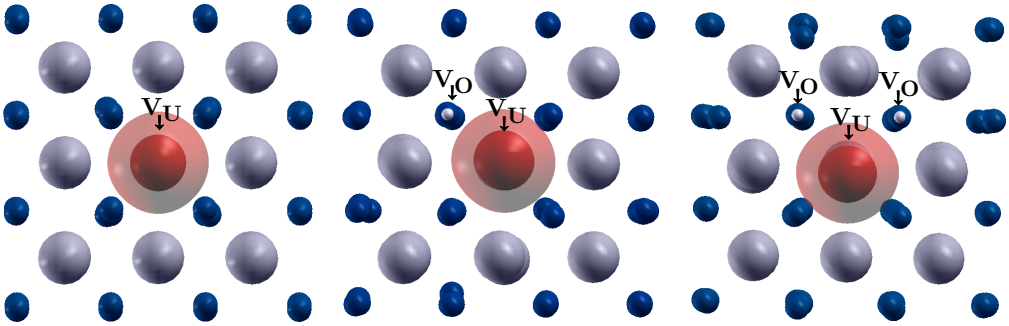

(a) $(V_U)^{4-}$ **(b)** $(V_U{+}V_O)^{2-}$ **(c)** $(V_U{+}2V_O)^0(110)$

Figure 5.6: *Positron isodensities found in the GGGC+GC scheme (70% of the maximum density – solid and 30% – transparent), in red, in defects containing one uranium vacancy. Uranium atoms are presented in gray, oxygen atoms in blue. White spheres represent the oxygen vacancies. Figures were generated using the* XCRYSDEN *[182, 183] program.*

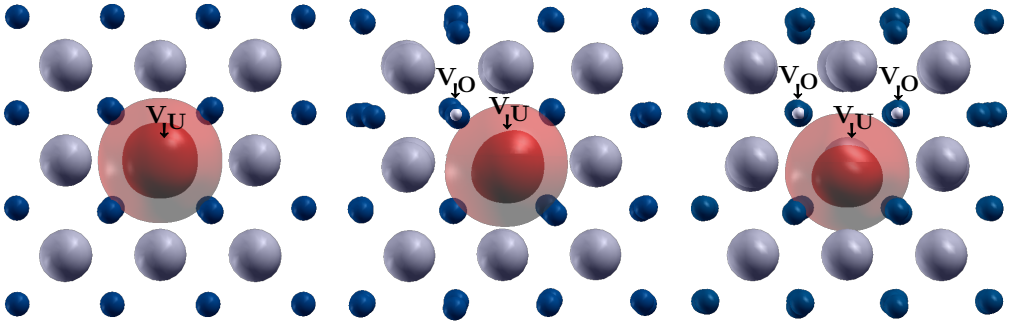

(a) $(V_U)^{4-}$ **(b)** $(V_U{+}V_O)^{2-}$ **(c)** $(V_U{+}2V_O)^0(110)$

Figure 5.7: *Positron isodensities found in the PSN+GC scheme (70% of the maximum density – solid and 30% – transparent), in red, in defects containing one uranium vacancy. Uranium atoms are presented in gray, oxygen atoms in blue. White spheres represent the oxygen vacancies. Figures were generated using the* XCRYSDEN *[182, 183] program.*

scheme in Fig. 5.6 and 5.8 and in the PSN+GC scheme in Fig. 5.7 and 5.9. It is worth noting that in the PSN+GC scheme we applied the gradient correction on the enhancement factor only, hence there is no effect of this correction on the calculated densities.

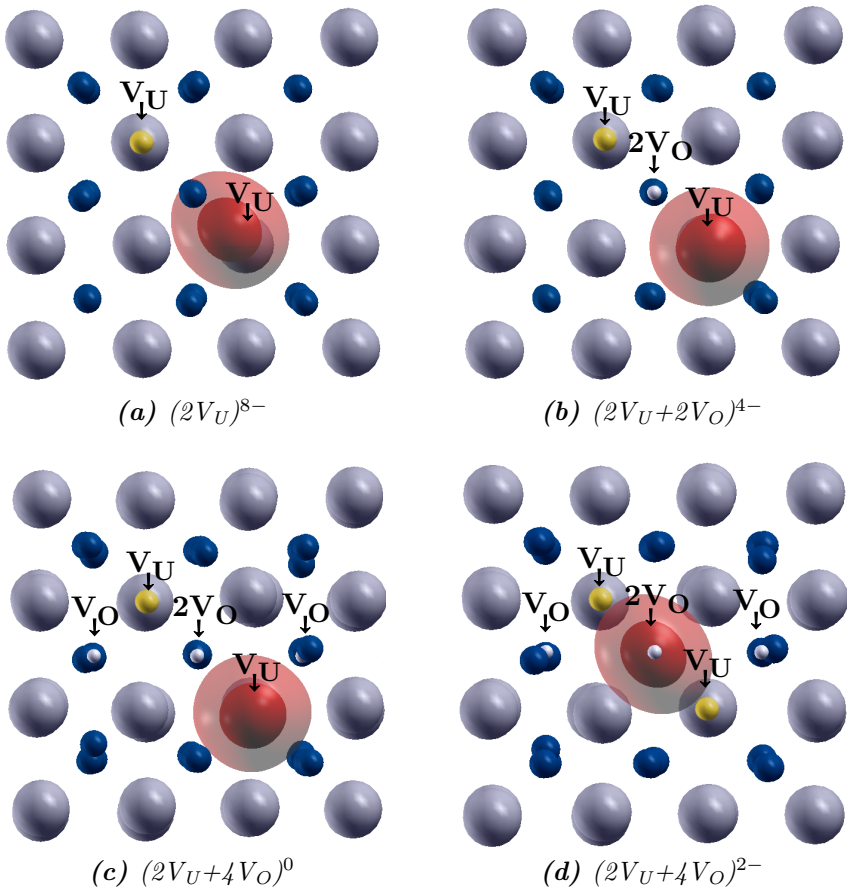

Figure 5.8: *Positron isodensities found in the GGGC+GC scheme (70% of the maximum density – solid and 30% – transparent), in red, in defects containing two uranium vacancies. Uranium atoms are presented in gray, oxygen atoms in blue. White and yellow spheres represent oxygen and uranium vacancies, respectively. Figures were generated using the* XCRYSDEN *[182, 183] program.*

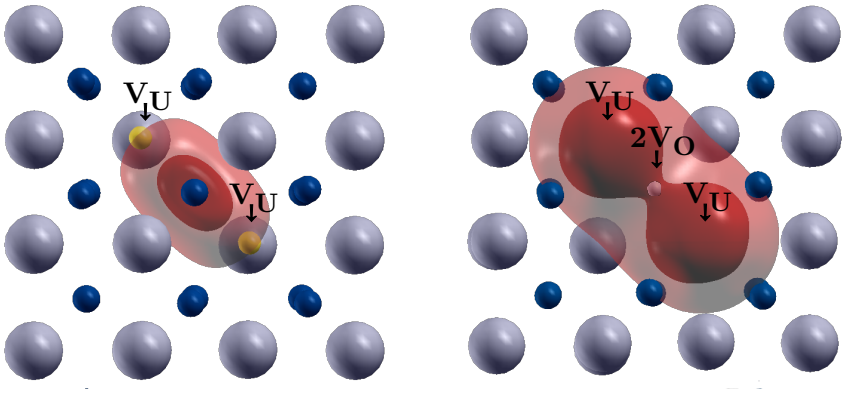

(a) $(2V_U)^{8-}$ ***(b)*** $(2V_U{+}2V_O)^{4-}$

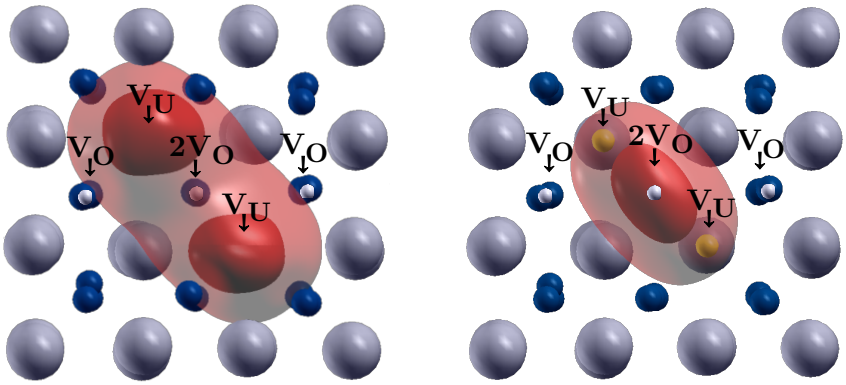

(c) $(2V_U{+}4V_O)^{0}$ ***(d)*** $(2V_U{+}4V_O)^{2-}$

Figure 5.9: *Positron isodensities found in the PSN+GC scheme (70% of the maximum density – solid and 30% – transparent), in red, in defects containing two uranium vacancies. Uranium atoms are presented in gray, oxygen atoms in blue. White and yellow spheres represent oxygen and uranium vacancies, respectively. Figures were generated using the* XCRYSDEN *[182, 183] program.*

First, we can observe that for all defects the GGGC+GC scheme yields more localized positron densities than the PSN scheme, which was expected [119, 120]. In all defects presented in Fig. 5.6 and 5.8 except the negative hexavacancy, the GGGC scheme finds the positron localized inside one uranium vacancy. In these defects, the positron density is only slightly affected by the presence of the other vacancies. The fact that the positron 'senses' similar volumes and geometries in these defects explains why similar lifetimes are obtained in these cases. The $(2V_U{+}4V_O)^{2-}$ hexavacancy is the only defect in which the positron localizes between the two uranium vacancies. It is reflected in the longer lifetime of 341 ps calculated for this cluster in the GGGC+GC scheme.

In the PSN scheme, however, we obtain a different positron localization for the clusters containing two uranium vacancies (see Fig. 5.9). In $(2V_U)^{8-}$ and $(2V_U{+}4V_O)^{2-}$ the positron is localized between the two uranium vacancies. However, in the 2− charged hexavacancy the free volume that the positron occupies is much larger than in $(2V_U)^{8-}$ and we observe a significantly longer lifetime for this defect. In both $(2V_U{+}2V_O)^{4-}$ and $(2V_U{+}4V_O)^{0}$ defects, we observe two maxima of the positron density, one in each uranium vacancy.

5.3 Doppler broadening of annihilation radiation

Beside the positron lifetime, the momentum distribution of electron-positron pairs can be measured through the Doppler broadening of the annihilation line using a Dopper broadening spectrometer [112]. This distribution is also a valuable source of information on the nature and chemical environment of vacancy defects and is complementary to the lifetime. In this section we present the calculations of the momentum distributions of the annihilation radiation calculated for various defects in uranium dioxide.

5.3.1 Computational details

The momentum distribution calculations have been performed using 96 atom supercells using the state-dependent scheme and geometries relaxed according to both the electronic and positronic forces. In these calculations the positron wavefuntion has been calculated at two **k**-points, the Γ point and another one chosen to lie on the edge of the Brillouin zone, as proposed by Korhonen *et al.* [157], to avoid the delocalization of the positron due to the small supercell. The momentum distributions have been calculated using the wavefunctions corresponding to the Γ point only. We used a cut-off energy of 680 eV, since we found it was enough to obtain Doppler

spectra converged up to 40 mrad. The atomic datasets used in this study were generated by a modified version of the ATOMPAW code [104]. They contained 14 valence electrons with $5s$ and $5p$ states added in the positron wavefunction basis set for uranium and 8 valence electron for oxygen. The other methods and parameters used in the momentum distribution calculations are the same as for the calculations of the formation energies of defects (see Sec. 5.1.3).

5.3.2 Comparison of calculation schemes

In Fig. 5.10 we compare the ratio curves calculated for the uranium monovacancy using the CONV, GGGC and PSN schemes. The vacancy was relaxed using the PSN and GGGC schemes. In the case of the CONV method we compare results calculated first for unrelaxed atomic positions and then taking the relaxed positions from the GGGC calculation. We can observe that the general shapes of the ratio curves calculated using different schemes are similar. For all methods a peak at p=0 is observed, with GGGC yielding the largest amplitude and the CONV method with unrelaxed positions the lowest. A second peak can be observed around $p = 15$ mrad, while around $p = 27$ mrad a shoulder or a peak, depending on the method used, appears.

The effect of the atomic relaxation on the calculated ratio curve can be analyzed by comparing the results obtained using the CONV method for two different geometries (blue lines in Fig. 5.10). We can observe that when the uranium vacancy relaxes outwards, the low-momentum contribution increases, since the electronic density moves further from the positron. At the same time, the ratio curve at higher momenta decreases.

The localized shape of the ratio curve calculated using the GGGC scheme is consistent with the overestimation of the positron localization yielded by this method, which was already discussed in the sections dedicated to positron lifetimes. As for the PSN scheme, the ratio curve obtained using this method is the flattest. Additionally, we can see that at low momenta the results yielded by this method are in good agreement with the ones calculated using the CONV scheme in the relaxed geometry. The agreement is, however, not as good above $p = 10$ mrad. In the calculations presented below, we use the PSN scheme since this method yields the best description of the positron localization in the defect.

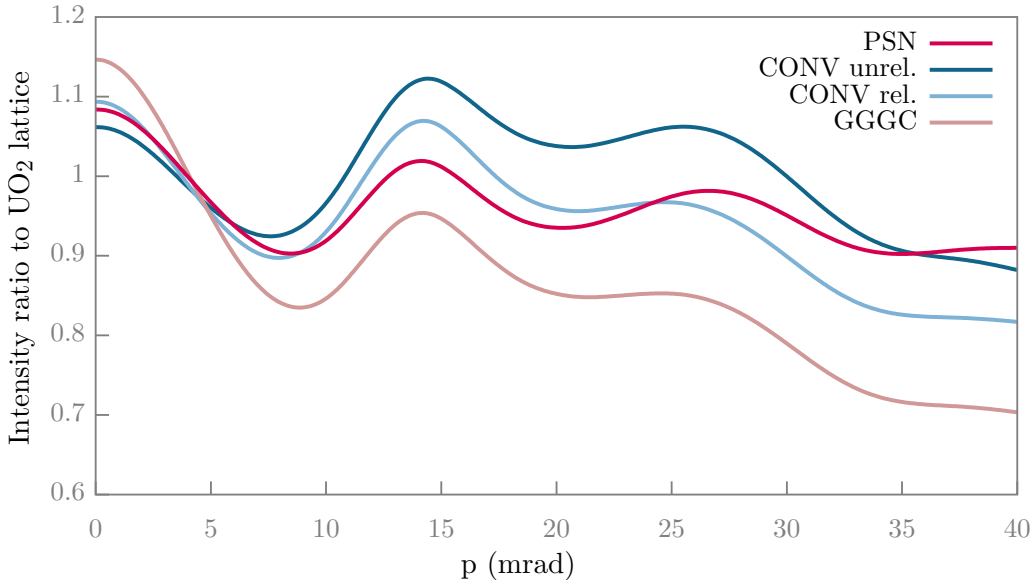

Figure 5.10: *Ratio curves of the calculated momentum distributions of annihilating electron-positron pairs in V_U using different schemes. All spectra are convoluted with a Gaussian function with FWHM=4.7 mrad and divided by the lattice spectrum.*

5.3.3 Vacancies in UO_2

We performed calculations of the momentum distributions for several vacancy defects in UO_2. The ratio curves found for neutral V_U, V_U+V_O, the three configurations of V_U+2V_O and one configuration of 2V_U+4V_O vacancies are presented in Fig. 5.11. We can see that all the calculated ratio curves are rather similar, with a maximum at $p = 0$ and two peaks, one around $p = 15$ mrad and one around around $p = 27$ mrad. The result calculated for the neutral 2V_U+4V_O complex is the most distinct from the others, it is more flat and has much lower values at high moments. The similarity between for instance the monovacancy and the trivacancies can be explained by the fact, that while oxygen 2− ions are removed from the neighborhood of V_U, the remaining ones can attract the positron and shift its density toward them. This shift can be observed for example in Fig. 5.7c. As a result, even though there are less oxygen atoms surrounding the positron, the annihilation rate with the remaining ones increases and the two effects cancel each other out, leading to rather small changes in the ratio curves. As a result, even though these changes will be probably possible to observe in the S and W parameters, it could be difficult to distinguish defects based on them.

In the study of the positron lifetimes we observed that the positron localization in the hexavacancy depends on the charge state of this defect. In the 2V_U+4V_O^{2-} complex the positron density was centered between the uranium sites and not inside it, as in the other defects (see Fig. 5.9). We performed, therefore, a momentum distribution calculation for this defect and

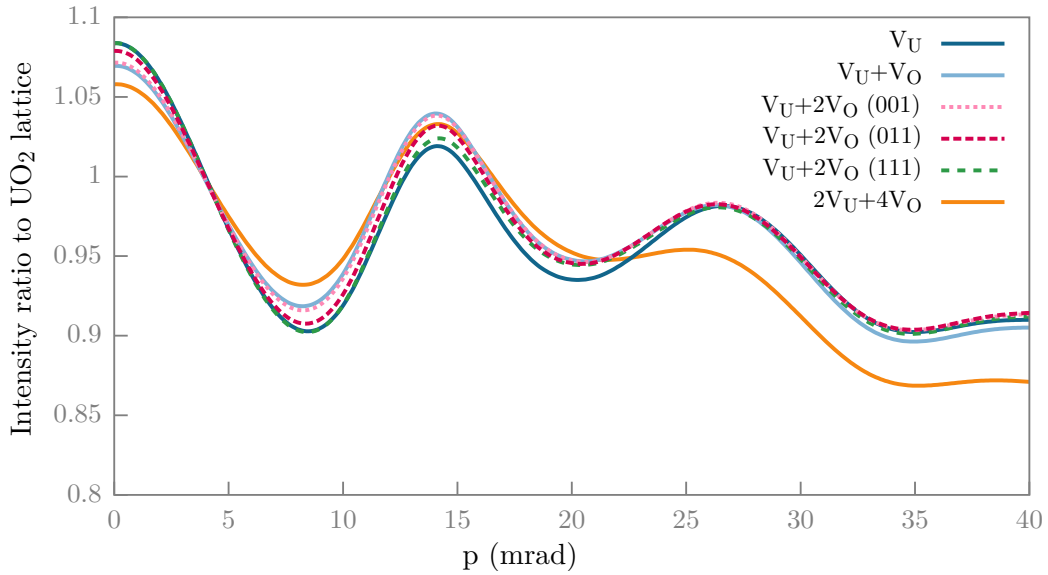

Figure 5.11: *Ratio curves of the calculated momentum distributions of annihilating electron-positron pairs in various defects in UO_2. All spectra are convoluted with a Gaussian function with FWHM=4.7 mrad and divided by the lattice spectrum.*

present it in Fig. 5.12d, along with the ratio curves of the V_O and V_U monovacancies. In the negative hexavacancy, the positron occupies a large open volume, which is reflected in the high value of the maximum at $p = 0$, around 1.2. This is consistent with the long positron lifetime (365 ps) calculated for this defect. The curve at higher momenta has a shape similar to that of V_U–peaks are observed around $p = 15$ and $p = 27$ mrad. However, the absolute values at high momenta between 10 and 30 mrad are closer to those calculated for V_O.

5.3.4 Effect of the charge state

We verified the effect of the charge state on the momentum distribution for the uranium monovacancy. In Fig. 5.13 we present the ratio curves calculated for V_U and V_U^{4-}. There are only slight differences between the two charge states. For the negative monovacancy we can observe a slight increase in the maximum at $p = 0$ and a decrease for momenta above $p = 5$ mrad. These results suggest that the change in charge state has an almost negligible effect on the ratio curves, unless it changes the site at which the positron is localized, like in the case of the hexavacancy discussed before.

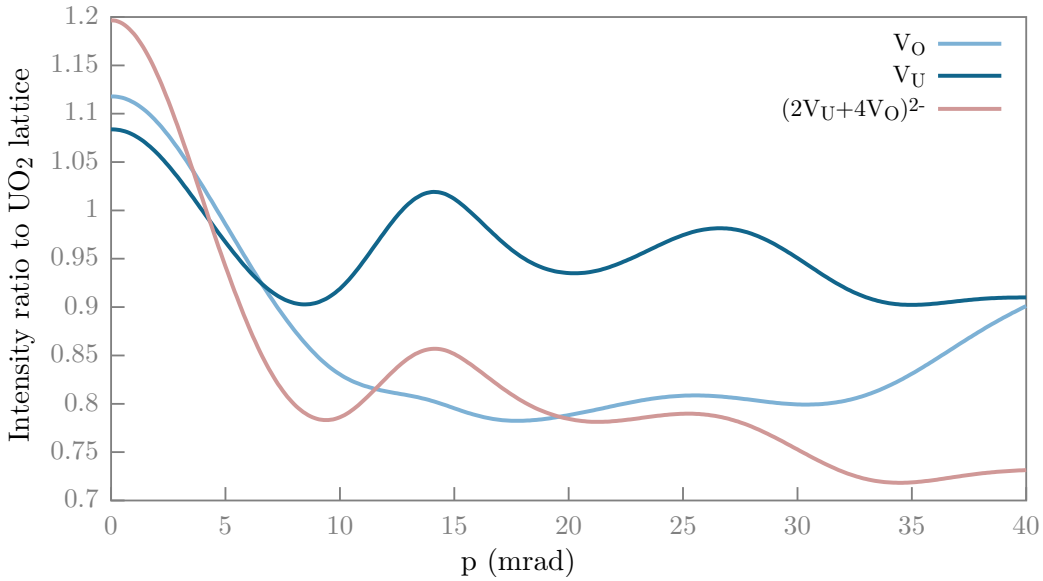

Figure 5.12: *Ratio curves of the calculated momentum distributions of annihilating electron-positron pairs in various defects in UO_2. All spectra are convoluted with a Gaussian function with FWHM=4.7 mrad and divided by the lattice spectrum.*

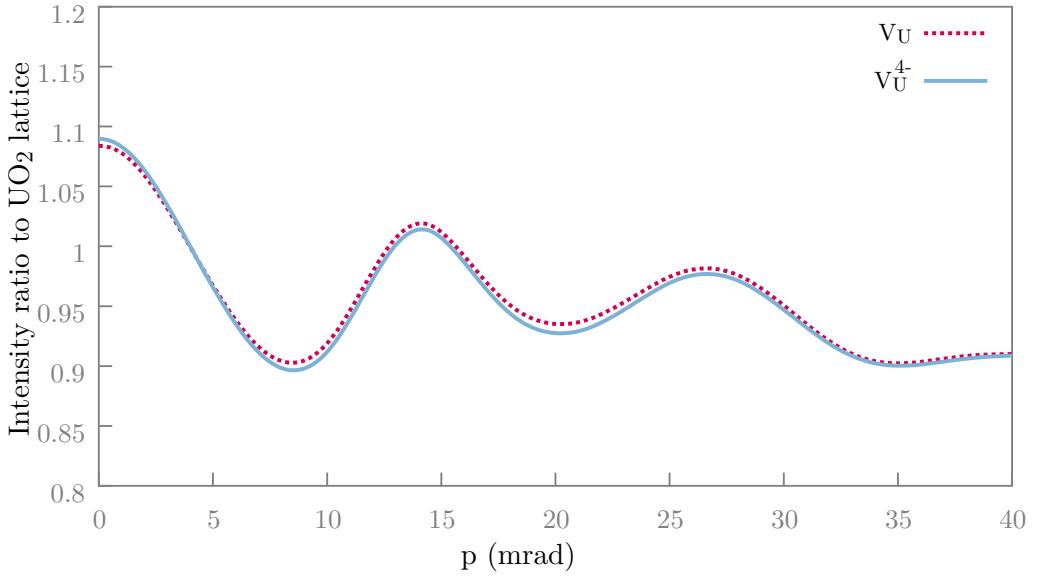

Figure 5.13: *Ratio curves of the calculated momentum distributions of annihilating electron-positron pairs in V_U and V_U^{4-}. All spectra are convoluted with a Gaussian function with FWHM=4.7 mrad and divided by the lattice spectrum.*

5.3.5 Krypton incorporation

The incorporation of the gaseous fission products in the vacancies in UO_2 is an important issue in the studies of the fuel behavior under irradiation. The momentum distribution of the

annihilation radiation is especially sensitive to the chemical environment of the defect. We have studied, therefore, the effect of a Kr atom on the Doppler spectrum of V_U+2V_O(110). The calculated ratio curve is presented in Fig. 5.14 and the positron isodensity in this defect in Fig. 5.15. We can see that the Kr incorporation has a significant effect on the ratio curve. The maximum at $p = 0$ is decreased, since krypton increases the electron density and decreases the free volume available to the positron, as seen in Fig. 5.14. Additionally, the peak around $p = 15$ mrad decreases and the one around $p = 27$ mrad increases. This is only a preliminary calculation, but the high sensitivity of the momentum distribution of the annihilation radiation to the presence of krypton atoms suggests that its measurement can be very useful in studies of fission products incorporation in UO_2. Therefore, it would be interesting to continue the calculations for other defects and for other fission gases, such as xenon, but also for helium or non-gaseous volatile fission products, such as iodine or cesium.

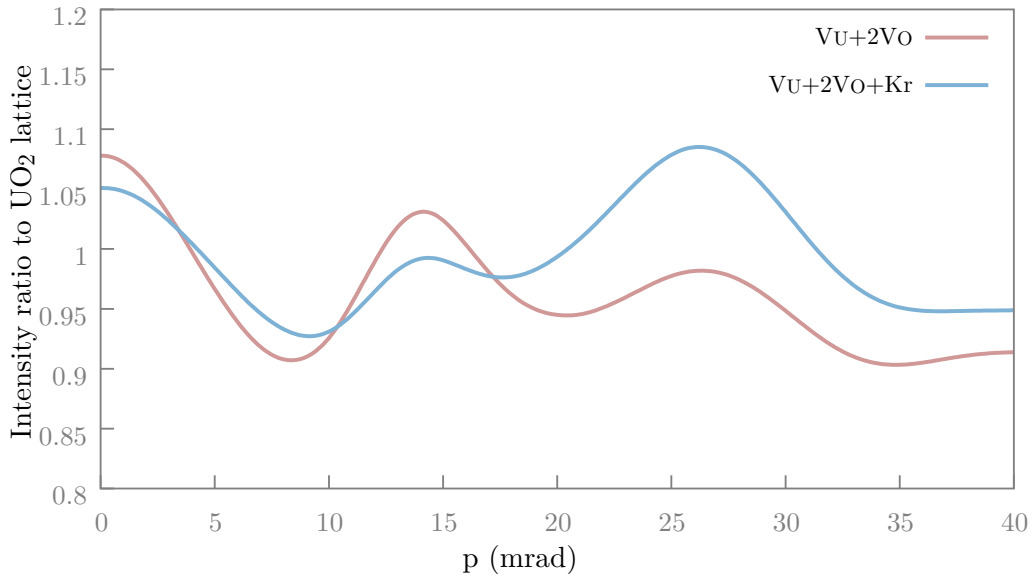

Figure 5.14: *Ratio curves of the calculated momentum distributions of annihilating electron-positron pairs in the V_U+2V_O(110) trivacancy (Bound Schottky Defect), empty and containing one Kr atom. All spectra are convoluted with a Gaussian function with FWHM=4.7 mrad and divided by the lattice spectrum.*

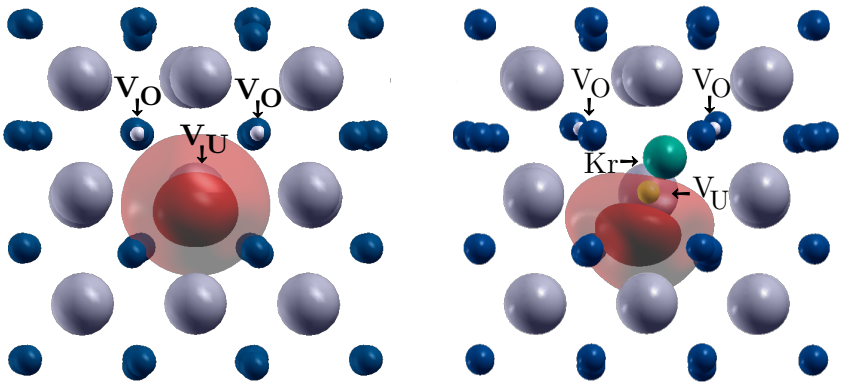

Figure 5.15: *Positron isodensities (70% of the maximum density – solid and 30% – transparent), in red, found in the V_U+2V_O(110) defect, empty (a) and containing a Kr atom (b). Uranium atoms are presented in gray, oxygen atoms in blue and krypton in green. White and yellow spheres represent oxygen and uranium vacancies, respectively. Figures were generated using the* XCRYSDEN *[182, 183] program.*

5.3.6 S and W parameters

We calculated the relative S_{rel} and W_{rel} parameters, determined as:

$$S_{\text{rel}} = \frac{S_{\text{defect}}}{S_{\text{lattice}}} \tag{5.3.1}$$

and

$$W_{\text{rel}} = \frac{W_{\text{defect}}}{W_{\text{lattice}}}, \tag{5.3.2}$$

for the vacancies considered in UO_2. These parameters were calculated using the integration windows of $S \in (0, 2.8)$ mrad and $W \in (10.61, 26.35)$ mrad, as in Ref. [81], and are shown in Fig. 5.16. We can see that the points corresponding to V_U, V_U+V_O, the three configurations of V_U+2V_O and neutral 2V_U+4V_O are close to each other. However, they could probably be distinguished in high precision experimental measurements. The points corresponding to V_O and to negative 2V_U+4V_O lay far from the other points, hence could be easily identified if detected in Doppler broadening measurements. By comparing the S_{rel} and W_{rel} parameters calculated for the empty V_U+2V_O(110) defect and when containing a Kr atom, we can conclude that for the set of integration windows used, the krypton incorporation leads to a clear shift in the measured signal, which could be observed.

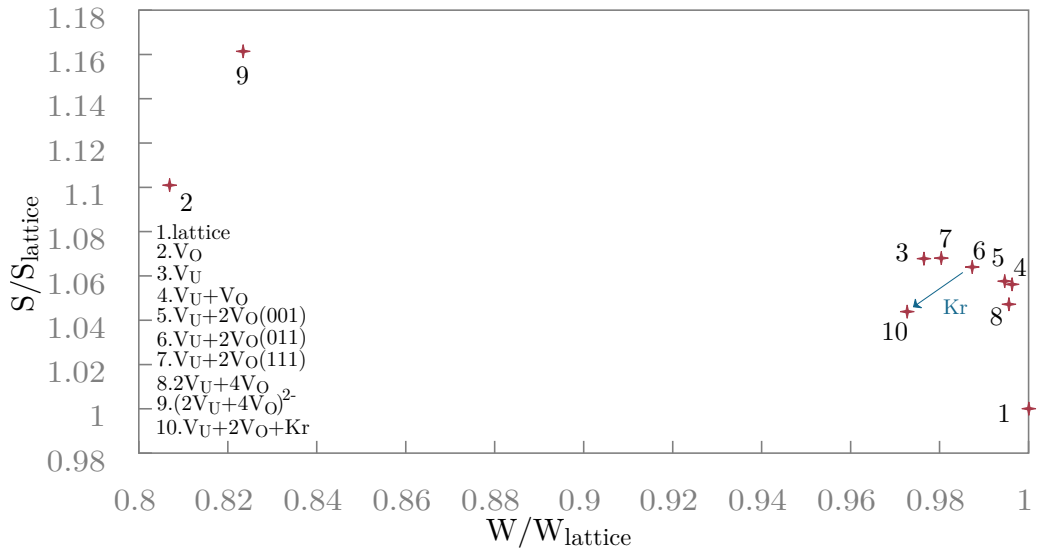

Figure 5.16: *S_{rel} parameter as a function of the W_{rel} parameter plotted for various defects in UO_2, using windows $S \in (0, 2.8)$ mrad and $W \in (10.61, 26.35)$ mrad. The results were obtained using spectra convoluted with a Gaussian function with FWHM=4.7 mrad.*

5.4 Discussion and contribution to interpretation of experimental results

The theoretical calculations of the positron lifetimes in UO_2 presented above were used to interpret experimental results obtained at the CEMHTI Laboratory (Orléans, France). The evolution of the annihilation characteristics as a function of the measurement temperature in 45 MeV α irradiated UO_2 disks was presented in Fig. 1.8, Sec. 1.3.2.

It can be seen that $\tau_{\text{av.}}$ increases slightly from approximately 220±5 ps to 235±5 ps when the temperature rises, while τ_1 and τ_2 remain stable at about 170±5 ps and 310±5 ps, respectively. The I_2 intensity increases when the measurement temperature rises, similarly to the average positron lifetime $\tau_{\text{av.}}$

For all measurement temperatures, the values of τ_2 are much larger than the lattice lifetime, already determined in unirradiated UO_2 disks [81] (169±1 ps). This indicates positron trapping in vacancy defects. In addition, the short lifetime component τ_1 remains close to the experimental lattice lifetime of UO_2. In the case of materials containing only vacancy defects, if some of the positrons had annihilated in a delocalized state (in the lattice), the short lifetime component would have been shorter than the perfect lattice lifetime since the average time spent by the positron in the lattice would be shorter due to the trapping in defects. Thus, the values of τ_1 indicate that the positrons were also trapped in negative non-vacancy defects. The short

lifetime component is still equal to the experimental lattice lifetime at 300 K which means that the non-vacancy traps are still effective at this temperature. The nature of these non-vacancy defects will be discussed further in Sec. 5.4.1.

The long lifetime component τ_2 changes only slightly as a function of measurement temperature and remains stable at 310±5 ps. This positron lifetime is close to the long positron lifetime components ranging from 300±10 to 310±5 ps observed in the previous study on the same samples [81] and 313±19 ps detected in UO_2 with 0.2% plutonium weight content [82]. The intensity I_2 corresponding to the long lifetime component increases slightly when temperature rises, which means that its trapping rate changes only slightly.

To determine the nature of the vacancy-type defects detected in the samples, we used a positron trapping model (see Sec. 1.2.1.1). First, we considered models with only two types of positron traps (negative non-vacancy defects and neutral or negative vacancies). Both of them, however, failed to reproduce the experimental data. We concluded, therefore, that at least three types of traps were present in the studied samples – negative non-vacancy defects, neutral and negative vacancies – and that a corresponding model should be used. The solutions of the rate equations used in the model containing three different defect types were obtained by Krause-Rehberg and Leipner [50].

The fits to the experimental data obtained using the positron trapping model are presented in Fig. 5.17 (solid lines). Several parameters are needed in the model, some of which must be deduced or estimated. For the lattice and the non-vacancy defects we used the same annihilation rate, $\lambda_L = \lambda_{NV} = 1/\tau_L$, with $\tau_L = 170$ ps. We considered the positron binding energy of the non-vacancy defects to be at least 0.3 eV, as these traps were still efficient at 300 K. Since the lifetime spectra decomposition returned only two lifetime components (even when three components decomposition was tested) and we do not observe strong variations of the τ_2 lifetime, we suppose that the lifetimes of the neutral and negative vacancies are indistinguishable. We considered $\tau = 310$ ps for both of them. As for the trapping coefficients, we used $\mu_V = 1 \times 10^{15}$ s^{-1} for the neutral vacancies, $\mu_{V^-} = 4 \times 10^{16}$ s^{-1} at 20 K for the negative vacancies and $\mu_{NV} = 4 \times 10^{16}$ s^{-1} at 20 K for the non-vacancy defects. The choice of the trapping coefficients was based on the values gathered in Ref. [54] and the predicted charge states of the negative defects.

The fits presented in Fig. 5.17 were obtained using concentrations $c_V = 6.5 \times 10^{19}$ cm^{-3}, $c_{V^-} = 2 \times 10^{18}$ cm^{-3} and $c_{NV} = 1 \times 10^{19}$ cm^{-3}. It is worth noting that some of the parameters used in the trapping model were only estimated, hence the absolute values of the concentrations cannot be considered as certain. However, conclusions can be drawn on the proportions between the defects concentrations. The best fits of the present experimental data were obtained for the neutral vacancies concentration c_V at least 30 times larger than c_{V^-} and over 6 times larger

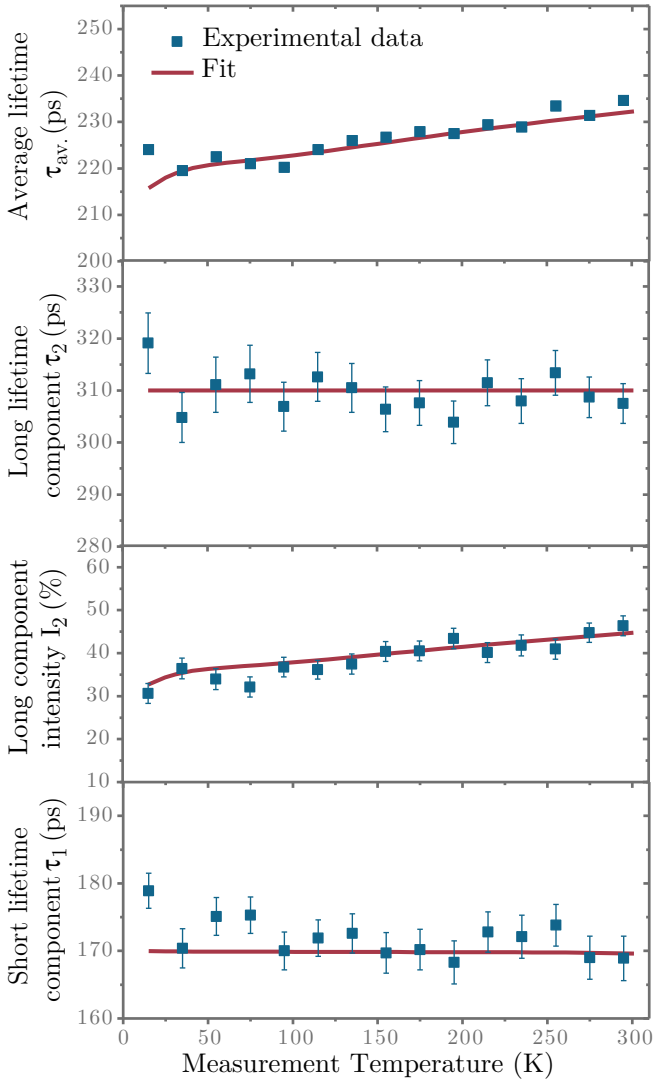

Figure 5.17: *Fit to the experimental PAS data obtained for UO_2 crystals irradiated with 45 MeV α particles.*

than c_{NV}, which suggests that the neutral vacancies are the predominant positron traps in the examined UO_2 samples. Smaller, but not negligible, concentrations of negative non-vacancy defects and vacancies are also present in the material.

5.4.1 Identification of defects in irradiated UO_2

In this section we combine the calculation and experimental results to interpret the signals observed by PAS in the UO_2 samples in the present and previous studies.

The short lifetime component τ_1 detected in the studied UO_2 disks remains close to the experimental lattice lifetime of UO_2 of 170±5 ps for all measurement temperatures (see Fig. 5.17). This suggests that part of the positrons annihilate around negative non-vacancy defects in the samples, as mentioned before. The samples analyzed in this study were slightly hyper-stoichiometric with $O/U = 2.0051 \pm 0.0001$, which means that excess oxygen atoms were already present in the lattice before irradiation. The nature of the point defects in slightly hyperstoichiometric UO_2 and their local configurations have been the object of extensive studies, both experimental [184–187] and theoretical [27–29, 164, 170, 188, 189]. Depending on the study, various types of defects containing additional oxygen atoms, such as monointerstitials, di-interstitials, split-interstitials or Willis clusters, are proposed as the most stable ones. All these possible defects structures were found to be stable in negative charge states due to the oxygen ions formal charge state of −2. Recently, Wang *et al.* [189] suggested that the average structure of UO_{2+x} can be represented as a combination of all of these defects structures. Therefore, we suppose that the short lifetime component detected in the studied samples corresponds to mixed signals coming from the positron annihilation around negatively charged monointerstitials and interstitial clusters. These could be defects already present in the unirradiated UO_2 discs or created by irradiation.

The long lifetime component of 310±5 ps detected in the samples is close to what we calculated for the neutral V_U+$2V_O$ trivacancy (301–314 ps in GGGC+GC and 304–316 ps in PSN+GC, depending on the configuration) and the $2V_U$+$2V_O$ with the −4 charge state (309 ps in GGGC+GC and 319 ps in PSN+GC). The analysis of the evolution of the positron annihilation characteristics as a function of the measurement temperature based on the trapping model indicates that two types of vacancy defects are present in the sample, the neutral one being predominant. The theoretical studies on the charge states of the defects clusters in UO_2 [163, 164, 170] suggest that the only neutral defect in the material close to the stoichiometry for the Fermi level near the middle of the band gap is the V_U+$2V_O$ trivacancy. We propose, hence, that the bound Schottky defects are the neutral vacancies observed in the samples. The analysis

of the experimental data based on the positron trapping model implies that negative vacancies are also detected in the UO_2 samples. They should have a positron lifetime close to 310 ps, since only one long component was obtained from the lifetime spectra decompositions. The formation energy calculations of defects in UO_2 [164] suggest that several types of negatively charged vacancies can be present in the material. The positron lifetime calculations presented in this work yield values slightly shorter or longer than 310 ps for various negative defects (from 293 ps for V_U^{4-} to 319 ps for $2V_U{+}2V_O$ with the -4 charge state in the PSN+GC scheme). We suppose, hence, that negative uranium monovacancies, U-O divacancies and $2V_U{+}2V_O$ tetravacancies are present in the examined samples. However, the concentrations of all these defects are much smaller than the concentration of Schottky defects.

Our results can be compared with the classical molecular dynamics (CMD) simulation of 10 keV displacement cascades in UO_2 by Martin *et al.* [190]. The authors found that even though initially mostly monovacancies and monointerstitials were created, they quickly started to form stoichiometric clusters, such as bound Schottky defects, because of the high oxygen mobility. It is worth noting that the empirical potentials used in this study favored the neutral defects over the charged ones and that the simulations corresponded to a physical time of approximately 25 ps. Nevertheless, the present results confirm the general conclusion of the CMD study.

In addition to the studies of positron lifetimes in UO_2, measurements of the Doppler broadening of annihilation radiation have also been performed [81, 83–87]. We did not, however, observe any clear agreement between the experimental S and W parameters and the values calculated in this work. In our calculations the values of the W_{rel} parameters of for instance neutral V_U, $V_U{+}V_O$, three configuration of $V_U{+}2V_O$ and $2V_U{+}4V_O$ defects are close to 1. Meanwhile, in Ref. [81], where a long positron lifetime component of around 310±5 ps was detected, much lower values of W_{rel} are observed. This inconsistency may be related to the fact that the measurements reported in literature were very probably performed on hyper-stoichiometric samples. As a consequence, the reference samples may contain significant concentrations of negative oxygen interstitials, which can affect the reference spectra and, therefore, also the relative S_{rel} and W_{rel} parameters. The inconsistencies between the calculations and the experiments need to be further investigated and measurements on UO_2 samples with controlled stoichiometry (stoichiometric and hypo-stoichiometric) should be performed.

5.5 Conclusions

First, we performed electronic structure calculations of the formation energies of various neutral and charged defects in UO_2 using the GGA+U method. The occupation matrix control scheme

was used to overcome the problem of the convergence to multiple metastable states. We presented a physically justified formalism for the calculation of defect formation energies in UO_2. This is especially important since the chemical potentials of the two components oxygen and uranium vary strongly in UO_2. Additionally, we showed the importance of the choice of the reference energies. The accessible ranges of U and O chemical potentials are calculated using the U-O experimental phase diagram and a constraint on the formation energies of vacancies. This enables a more consistent comparison between the various defects in UO_2, as well as a function of its stoichiometry.

We then calculated the positron lifetimes of neutral and charged fully relaxed vacancies and vacancy clusters in UO_2 using two different fully self-consistent calculation schemes, GGGC and PSN, in the DFT+U formalism. We observed that the parameters used in the electronic calculations do not affect directly the positron lifetime. However, since the positron lifetime is highly sensitive to the free volume, there is an effect of the equilibrium volume corresponding to the method and the parameters used on the lifetimes obtained. We showed that the gradient correction describes better the absolute values of the positron lifetimes in this material. We showed that the PSN and GGGC schemes yielded similar positron lifetimes for the majority of studied defects, especially for the stable charge states of defects up to trivacancies. Therefore, similar general conclusions could be drawn by comparing results obtained using both schemes with the experimental values. However, the choice of calculation scheme can affect the experiment interpretation if larger defects are present in the material.

For several defects, in particular 2− charged V_U+V_O, neutral V_U+2V_O and 4− charged 2V_U+2V_O, similar positron lifetimes were obtained. It is due to the fact that for almost all the studied vacancy clusters the positron is localized in one uranium vacancy and is only slightly affected by the presence of the oxygen vacancies or of the second uranium vacancy. The only cluster having a significantly longer positron lifetime (341 ps) is the 2− charged 2V_U+4V_O hexavacancy, where the positron is localized between the two uranium vacancies.

The calculations of the momentum distribution of the annihilation radiation yielded rather similar results for the majority of defects containing uranium vacancies. We found, however, very distinct ratio curves for the oxygen monovacancy and the negative hexavacancy. Additionally, the results of preliminary calculations showed that it should be possible to observe the incorporation of Kr in vacancy defects using PAS.

We analyzed PAS measurements performed on UO_2 sintered disks irradiated with 45 MeV α particles at a fluence of 2×10^{16} cm^{-2}. The positron lifetime was measured as function of temperature in the 15–300 K range. Two lifetime components, τ_1 (170±5 ps) and τ_2 (310±5 ps) were observed in the experiments. The short lifetime component is close to the lattice lifetime

for all measurement temperatures. It means that all positrons annihilated in vacancy defects or around negative non-vacancy defects. These non-vacancy defects are assumed to be negatively charged oxygen monointerstitials and interstitials clusters. We used a positron trapping model with three types of positron traps to analyze the evolution of the positron annihilation characteristics as a function of measurement temperature. We concluded that a neutral vacancy was the most predominant positron trap, while smaller, but not negligible, concentrations of negative vacancies were also present in the material.

The comparison of the results obtained experimentally with the calculated positron lifetimes and the most stable charge states of the defects in UO_2 allowed us to identify the predominant neutral vacancy as the V_U+2V_O trivacancy (bound Schottky defect). This result shows that the coupling of precise experimental studies and calculations using carefully chosen assumptions is an effective method to bring further insight into the defects created by irradiation in UO_2.

As far as the momentum distribution measurements are concerned, we suggest that further analyses based on the calculation results should be performed, as well as experiments on UO_2 samples with controlled stoichiometry.

Conclusions and perspectives

The goal of the present thesis was to support the identification of the experimental signals observed in positron annihilation spectroscopy in nuclear ceramics using first-principles calculations. To achieve this, we first implemented the methods allowing one to calculate the momentum distribution of annihilating electron-positron pairs in the ABINIT code. Then, we performed electronic structure calculations of the energetic properties and positron annihilation characteristics of various vacancy defects in uranium dioxide and silicon carbide. The calculation results were used to contribute to the interpretation of various PAS experiments performed at the CEMHTI laboratory.

The first part of the study was dedicated to code tests and development. We performed tests to validate the implementation of the positron lifetime calculations in the ABINIT code. Then, we determined the optimal parameters for the calculations of positron annihilation characteristics of defects in SiC and UO_2. We then implemented the methods necessary for the calculation of the second positron annihilation characteristic, the momentum distribution of annihilating electron-positron pairs, since they were not available in the electronic structure codes. The development was done fully within the projector augmented-wave (PAW) formalism and was tested on several materials. The comparison of results yielded by our implementation with reference data confirmed the validity of the methods used and the implementation itself. It is worth noting that the PAW method does not improve the description of the positron wavefunctions, as compared, for instance, to the pseudopotential method, and can even lead to some difficulties in this task. We showed, however, that when the PAW dataset is carefully chosen and tested, a good description of the positron can be obtained along with positron lifetimes and momentum distributions in good agreement with experimental data.

The second part of this work was dedicated to silicon carbide. First, to determine the most stable charge states of defects, we investigated their formation energies. This gave us an indication of whether a defect can be detected using positrons in a material with a given doping level. Then, we performed calculations of positron lifetimes in various vacancies in silicon carbide. We

showed the importance of using fully self-consistent TCDFT schemes and taking into account the relaxation effects due to both the electronic and positronic forces in the positron lifetime calculations. The calculation results were used to revisit the identification of the experimental PAS signals presented in literature. We suggested that the omission of the atomic relaxation effect in the previous calculations, which were used to interpret the PAS measurements on SiC, might have led to misidentification of defects. We also analyzed the experimental data obtained at the CEMHTI laboratory on 12 MeV proton irradiated n-type 6H-SiC samples. In the as-irradiated samples we identified negative silicon monovacancies with the positron lifetime of 218 ps. We observed that during annealing at temperatures starting at around 400–500°C the silicon vacancies migrated and formed a larger defect. This defect, exhibiting a positron lifetime of 235 ps, was identified as V_C+V_{Si} based both on the charge state and positron lifetime calculations. Finally, we performed calculations of the Doppler spectra of various defects in SiC. We studied the effect of the polytype on the spectra and found that for the silicon vacancy and clusters involving this defect similar results were found in 3C and 6H-SiC. We also calculated the S and W parameters, which are usually considered in the experimental studies. We investigated the effect of the experimental resolution and the choice of the integration windows on these parameters, suggesting that for some windows the defects can be easier to distinguish than for others.

The last part of this study was dedicated to defects in uranium oxide. In this case, we first developed a physically justified formalism for the calculation of defect formation energies in this material. We emphasized the influence of the choice of the reference energies on the results. This choice is especially important in UO_2 since the chemical potentials of the oxygen and uranium atoms vary strongly in this material. We calculated the accessible ranges of U and O chemical potentials using the U-O experimental phase diagram and applying a constraint on the formation energies of vacancies, to define the hypo- and hyperstoichiometric regimes. Second, the formation energies of various neutral and charged defects in UO_2 were calculated using the GGA+U method. We used the occupation matrix control scheme to overcome the problem of the convergence to the multiple metastable states. The formation energy calculations allowed us to determine the most stable charge states of the defects that can be expected in a material with a given stoichiometry. Third, we performed first principles calculations of the positron lifetimes of neutral and charged fully relaxed vacancies and vacancy clusters using two different calculation schemes, GGGC and PSN, in the DFT+U formalism. Using the calculated results, we analyzed the experimental PAS measurements on α irradiated UO_2 samples. The observed positron lifetime of 310±5 ps was similar to lifetimes calculated for several defects. However, using the information on the most stable charge states of the defects and the positron trapping model, we showed that the neutral V_U+2V_O trivacancy (bound Schottky defect) predominated in the studied samples. Finally, we performed Doppler spectra calculations for various defects

in UO_2. We obtained similar spectra for different defects. This suggests that their identification in the momentum distribution of the annihilation radiation measurements can be difficult. On the other hand, we showed that krypton incorporation leads to significant changes in the Doppler spectra of the defects, hence can be successfully studied using momentum distribution measurements.

There are various perspectives stemming from this work. First, further analyses of experimental measurements must be performed, especially using the most recently calculated Doppler spectra. In the case of silicon carbide, defect investigations combining theoretical predictions and experimental measurements of positron lifetime and Doppler broadening with additional photoluminescence experiments are planned. Additionally, analyses of the existing experimental data using different integration windows for S and W parameters determination have been started. In the case of uranium dioxide we did not observe a clear agreement between the calculated and measured S_{rel} and W_{rel} parameters. We suppose that this can be related to the fact that the reference samples may contain nonnegligible concentrations of negative oxygen interstitials. Additional experiments on samples with controlled stoichiometry (stoichiometric and hypo-stoichiometric UO_2) are proposed to verify the influence of the reference data on the $S(W)$ plots. Also, our first calculations of momentum distribution of annihilation radiation in the trivacancy in UO_2 containing krypton showed that the Doppler broadening measurements can be especially useful in studying fission products incorporation. The calculations should be continued for other defects and for other fission gases, such as xenon, but also for helium and non-gaseous volatile fission products, such as iodine or cesium. The momentum distribution calculations should also be interesting for the study of doped UO_2 and of mixed actinide oxides, in particular to determine the influence of the presence of several types of cations on the defect and fission product behavior. Additionally, this study is part of the joint experimental and modeling approach taken by the Fuel behavior law laboratory (LLCC) at CEA Cadarache. The present and future interpretations of the PAS measurements will therefore contribute to a comprehensive understanding of the defect behavior in nuclear ceramics and will yield fundamental data and mechanisms for larger scale models, for instance cluster dynamics. Finally, since our implementation of the momentum distribution of annihilation radiation is freely available in the ABINIT code, we hope that it will be used in studies of other materials by other groups.

Publications

The following manuscripts involving results described in this work have already been published or submitted:

1. J. Wiktor, G. Jomard, M. Torrent and M. Bertolus. Electronic structure investigation of energetics and positron lifetimes of fully relaxed monovacancies with various charge states in $3C$-SiC and $6H$-SiC, *Phys. Rev. B*, **87**, 235207 (2013).

2. J. Wiktor, E. Vathonne, M. Freyss, G. Jomard and M. Bertolus. Calculation of defect formation energies in UO_2, *MRS Proceedings*, **1645** (2014).

3. J. Wiktor, G. Jomard and M. Bertolus. Electronic structure calculations of positron lifetimes in SiC: Self-consistent schemes and relaxation effect, *Nucl. Instrum. Meth. B*, **327**, 63 (2014).

4. J. Wiktor, X. Kerbiriou, G. Jomard, S. Esnouf, M.-F. Barthe and M. Bertolus. Positron annihilation spectroscopy investigation of vacancy clusters in silicon carbide: Combining experiments and electronic structure calculations, *Phys. Rev. B*, **89**, 155203 (2014).

5. E. Vathonne, J. Wiktor, M. Freyss, G. Jomard and M. Bertolus. DFT+U investigation of charged defects in UO_2, *J. Phys.: Condens. Matter.*, **26**, 325501 (2014).

6. J. Wiktor, M.-F. Barthe, G. Jomard, M. Torrent, M. Freyss and M. Bertolus. Coupled experimental and DFT+U investigation of positron lifetimes in UO_2, *Phys. Rev. B*, **90**, 184101 (2014).

7. J. Wiktor, G. Jomard and M. Torrent. Two-component density functional theory within the projector augmented-wave approach: accurate and self-consistent computations of positron lifetimes and momentum distributions, *Phys. Rev. B*, **92**, 125113 (2015).

List of Abbreviations

AE	All electron
BSD	Bound Schottky defect
CONV	Conventional
DFT	Density functional theory
EPR	Electron paramagnetic resonance
FFT	Fast Fourier transform
GC	Gradient correction
GGA	Generalized gradient approximation
GGGC	Gilgien, Galli, Gygi and Car
IPM	Independent particle model
LDA	Local density approximation
PAS	Positron annihilation spectroscopy
PAW	Projector augmented-wave
PS	Pseudo
PSN	Puska, Seitsonen and Nieminen
SC	Semiconductor correction
TCDFT	Two-component density functional theory
XC	Exchange-correlation

List of Figures

List of Tables

Bibliography

[1] P. Yvon and F. Carré. Structural materials challenges for advanced reactor systems. *J. Nucl. Mater.*, **385**, 217, 2009.

[2] H. Feinroth, M. Ales, E. Barringer, G. Kohse, D. Carpenter, and R. Jaramillo. Mechanical strength of CTP Triplex SiC fuel clad tubes after irradiation in MIT research reactor under PWR coolant conditions. In *Ceram. Eng. Sci. Proc.*, volume 30, page 47, 2009.

[3] H. Feinroth. Silicon Carbide TRIPLEXTM Fuel Clad and SiC Channel Boxes for Accident Resistance and Durability. *E-Journal of Advanced Maintenance*, **5**, 128, 2013.

[4] N. P. Bansal and J. Lamon. *Ceramic Matrix Composites: Materials, Modeling and Technology.* John Wiley & Sons, 2014.

[5] M. Willander, M. Friesel, Q. Wahab, and B. Straumal. Silicon carbide and diamond for high temperature device applications. *J. Mater. Sci. - Mater. Electron.*, **17**, 1, 2006.

[6] M. E. Levinshtein, S. L. Rumyantsev, and M. S. Shur. *Properties of Advanced Semiconductor Materials: GaN, AIN, InN, BN, SiC, SiGe.* John Wiley & Sons, 2001.

[7] A. Mattausch. *Ab initio-Theory of Point Defects and Defect Complexes in SiC.* PhD thesis, University of Erlangen-Nuremberg, 2005.

[8] G. Roma, F. Bruneval, L. A. Ting, O. N. Bedoya Martínez, and J. P. Crocombette. Formation and migration energy of native defects in silicon carbide from first principles: an overview. In *Defect and Diffus, Forum*, volume 323, page 11. Trans Tech Publ, 2012.

[9] M. Bockstedte, A. Mattausch, and O. Pankratov. *Ab initio* study of the migration of intrinsic defects in 3C-SiC. *Phys. Rev. B*, **68**, 205201, 2003.

[10] A. Zywietz, J. Furthmüller, and F. Bechstedt. Vacancies in SiC: Influence of Jahn-Teller distortions, spin effects, and crystal structure. *Phys. Rev. B*, **59**, 15166, 1999.

[11] Q. Yin, A. Kutepov, K. Haule, G. Kotliar, S. Y. Savrasov, and W. E. Pickett. Electronic correlation and transport properties of nuclear fuel materials. *Phys. Rev. B*, **84**, 195111, 2011.

[12] B. T. M. Willis. Neutron diffraction studies of the actinide oxides. II. Thermal motions of the atoms in uranium dioxide and thorium dioxide between room temperature and 1100°. *P. Roy. Soc. Lond. A. Mat.*, **274**, 134, 1963.

[13] Y. Q. An, A. J. Taylor, S. D. Conradson, S. A. Trugman, T. Durakiewicz, and G. Rodriguez. Ultrafast hopping dynamics of $5f$ electrons in the Mott insulator UO_2 studied by femtosecond pump-probe spectroscopy. *Phys. Rev. Lett.*, **106**, 207402, 2011.

[14] M. Idiri, T. Le Bihan, S. Heathman, and J. Rebizant. Behavior of actinide dioxides under pressure: UO_2 and ThO_2. *Phys. Rev. B*, **70**, 014113, 2004.

[15] H. P. Myers, T. Jonsson, and R. Westin. Intrinsic semiconduction in uranium dioxide. *Solid State Commun.*, **2**, 321, 1964.

[16] J. L. Bates, C. A. Hinman, and T. Kawada. Electrical conductivity of uranium dioxide. *J. Am. Ceram. Soc.*, **50**, 652, 1967.

[17] J. C. Killeen. The effect of niobium oxide additions on the electrical conductivity of UO_2. *J. Nucl. Mater.*, **88**, 185, 1980.

[18] Y. Baer and J. Schoenes. Electronic structure and coulomb correlation energy in UO_2 single crystal. *Solid State Commun.*, **33**, 885, 1980.

[19] G. C. Allen, P. M. Tucker, and J. W. Tyler. Electronic structure of some binary uranium and thorium oxides and halides. *Philos. Mag. B*, **48**, 63, 1983.

[20] W. P. Cox, L. Ellis, R. D. Cowan, J. W. Allen, S.-J. Oh, I. Lindau, B. B. Pate, and A. J. Arko. Valence-band photoemission in UO_2 (111) near the $5d$ resonant photon energy. *Phys. Rev. B*, **35**, 5761, 1987.

[21] B. Dorado. *Étude des propriétés de transport atomique dans le dioxyde d'uranium par le calcul de structure électronique : influence des fortes corrélations.* PhD thesis, Aix Marseille 2, 2010.

[22] E. Vathonne. *Étude par calcul de structure électronique des dégâts d'irradiation dans le combustible nucléaire UO_2 : comportement des défauts ponctuels et gaz de fission.* PhD thesis, University Aix-Marseille, 2014.

[23] F. Bruneval. Methodological aspects of the GW calculation of the carbon vacancy in $3C$-SiC. *Nucl. Instrum. Meth. B*, **277**, 77, 2012.

[24] F. Bruneval and G. Roma. Energetics and metastability of the silicon vacancy in cubic SiC. *Phys. Rev. B*, **83**, 144116, 2011.

[25] L. Torpo, T. E. M. Staab, and R. M. Nieminen. Divacancy in $3C$- and $4H$-SiC: an extremely stable defect. *Phys. Rev. B*, **65**, 085202, 2002.

[26] L. Torpo, M. Marlo, T. E. M. Staab, and R. M. Nieminen. Comprehensive ab initio study of properties of monovacancies and antisites in $4H$-SiC. *J. Phys.: Condens. Mat.*, **13**, 6203, 2001.

[27] M. Freyss, T. Petit, and J.-P. Crocombette. Point defects in uranium dioxide: Ab initio pseudopotential approach in the generalized gradient approximation. *J. Nucl. Mater.*, **347**, 44, 2005.

[28] B. Dorado, G. Jomard, M. Freyss, and M. Bertolus. Stability of oxygen point defects in UO_2 by first-principles DFT+U calculations: Occupation matrix control and Jahn-Teller distortion. *Phys. Rev. B*, **82**, 035114, 2010.

[29] J.-P. Crocombette, D. Torumba, and A. Chartier. Charge states of point defects in uranium oxide calculated with a local hybrid functional for correlated electrons. *Phys. Rev. B*, **83**, 184107, 2011.

[30] B. Dorado, D. A. Andersson, C. R. Stanek, M. Bertolus, B. P. Uberuaga, G. Martin, M. Freyss, and P. Garcia. First-principles calculations of uranium diffusion in uranium dioxide. *Phys. Rev. B*, **86**, 035110, 2012.

[31] B. Dorado, B. Amadon, M. Freyss, and M. Bertolus. DFT + U calculations of the ground state and metastable states of uranium dioxide. *Phys. Rev. B*, **79**, 235125, 2009.

[32] X. Kerbiriou, M.-F. Barthe, S. Esnouf, P. Desgardin, G. Blondiaux, and G. Petite. Silicon displacement threshold energy determined by electron paramagnetic resonance and positron annihilation spectroscopy in cubic and hexagonal polytypes of silicon carbide. *J. Nucl. Mater.*, **362**, 202, 2007.

[33] X. Kerbiriou, M.-F. Barthe, S. Esnouf, P. Desgardin, G. Blondiaux, and G. Petite. Silicon displacement threshold energy determined by electron paramagnetic resonance and positron annihilation spectroscopy in cubic and hexagonal polytypes of silicon carbide. *J. Nucl. Mater.*, **362**, 202, 2007.

[34] H. J. von Bardeleben, J. L. Cantin, L. Henry, and M.-F. Barthe. Vacancy defects in p-type $6H$-SiC created by low-energy electron irradiation. *Phys. Rev. B*, **62**, 10841, 2000.

[35] J. Lefèvre, J.-M. Costantini, D. Gourier, S. Esnouf, and G. Petite. Characterization of a silicon-related defect detected by its excited triplet state in electron-irradiated $3C$-SiC. *Phys. Rev. B*, **83**, 075201, 2011.

[36] P. G. Baranov, A. P. Bundakova, A. A. Soltamova, S. B. Orlinskii, I. V. Borovykh, R. Zondervan, R. Verberk, and J. Schmidt. Silicon vacancy in SiC as a promising quantum system for single-defect and single-photon spectroscopy. *Phys. Rev. B*, **83**, 125203, 2011.

[37] N. T. Son, P. N. Hai, and E. Janzén. Carbon vacancy-related defect in $4H$ and $6H$-SiC. *Phys. Rev. B*, **63**, 201201, 2001.

[38] N. T. Son, X. T. Trinh, L. S. Løvlie, B. G. Svensson, K. Kawahara, J. Suda, T. Kimoto, T. Umeda, J. Isoya, T. Makino, T. Ohshima, and E. Janzén. Negative-U system of carbon vacancy in $4H$-SiC. *Phys. Rev. Lett.*, **109**, 187603, 2012.

[39] Z. Zolnai, N. T. Son, C. Hallin, and E. Janzén. Annealing behavior of the carbon vacancy in electron-irradiated 4H-SiC. *J. of Appl. Phys.*, **96**, 2406, 2004.

[40] H. He and D. Shoesmith. Raman spectroscopic studies of defect structures and phase transition in hyper-stoichiometric UO_{2+x}. *Phys. Chem. Chem. Phys.*, **12**, 8109, 2010.

[41] R. Bès, P. Martin, E. Vathonne, R. Delorme, C. Sabathier, M. Freyss, M. Bertolus, and P. Glatzel. Experimental evidence of Xe incorporation in Schottky defects in UO_2. *Appl. Phys. Lett.*, **106**, 114102, 2015.

[42] L. Patrick and W. J. Choyke. Photoluminescence of radiation defects in ion-implanted $6H$-SiC. *Phys. Rev. B*, **5**, 3253, 1972.

[43] E. Sörman, N. T. Son, W. M. Chen, O. Kordina, C. Hallin, and E. Janzén. Silicon vacancy related defect in $4H$ and $6H$-SiC. *Phys. Rev. B*, **61**, 2613, 2000.

[44] M. J. Puska and R. M. Nieminen. Theory of positrons in solids and on solid surfaces. *Rev. Mod. Phys.*, **66**, 841, 1994.

[45] C.H. Lam and C.C. Ling. Decomposition of positron lifetime spectra generated by Monte Carlo method: The case study of $6H$ silicon carbide. *Nucl. Instrum. Meth. B*, **251**, 479, 2006.

[46] M. J. Puska, C. Corbel, and R. M. Nieminen. Positron trapping in semiconductors. *Phys. Rev. B*, **41**, 9980, 1990.

[47] C. Corbel, F. Pierre, K. Saarinen, P. Hautojärvi, and P. Moser. Gallium vacancies and gallium antisites as acceptors in electron-irradiated semi-insulating GaAs. *Phys. Rev. B*, **45**, 3386, 1992.

[48] K Saarinen, AP Seitsonen, P Hautojärvi, and C Corbel. Introduction and recovery of point defects in electron-irradiated Te-and Si-doped GaAs studied by positron lifetime spectroscopy. *Phys. Rev. B*, **52**, 10932, 1995.

[49] K. Saarinen, T. Laine, S. Kuisma, J. Nissilä, P. Hautojärvi, L. Dobrzynski, J. M. Baranowski, K. Pakula, R. Stepniewski, M. Wojdak, A. Wysmolek, T. Suski, M. Leszczynski, I. Grzegory, and S. Porowski. Observation of native Ga vacancies in GaN by positron annihilation. *Phys. Rev. Lett.*, **79**, 3030, 1997.

[50] R. Krause-Rehberg and H. S. Leipner. *Positron annihilation in semiconductors: defect studies*, volume 127. Springer, 1999.

[51] A. Zubiaga, F. Plazaola, J. A. Garcia, F. Tuomisto, V. Muñoz Sanjosé, and R. Tena-Zaera. Positron annihilation lifetime spectroscopy of ZnO bulk samples. *Phys. Rev. B*, **76**, 085202, 2007.

[52] F. Tuomisto, K. Saarinen, D. C. Look, and G. C. Farlow. Introduction and recovery of point defects in electron-irradiated ZnO. *Phys. Rev. B*, **72**, 085206, 2005.

[53] F. Tuomisto, V. Ranki, D. C. Look, and G. C. Farlow. Introduction and recovery of Ga and N sublattice defects in electron-irradiated GaN. *Phys. Rev. B*, **76**, 165207, 2007.

[54] F. Tuomisto and I. Makkonen. Defect identification in semiconductors with positron annihilation: Experiment and theory. *Rev. Mod. Phys.*, **85**, 1583, 2013.

[55] L. Henry, M.-F. Barthe, C. Corbel, P. Desgardin, G. Blondiaux, S. Arpiainen, and L. Liszkay. Silicon vacancy-type defects in as-received and 12-mev proton-irradiated 6H-SiC studied by positron annihilation spectroscopy. *Phys. Rev. B*, **67**, 115210, 2003.

[56] A. Kawasuso, H. Itoh, N. Morishita, M. Yoshikawa, T. Ohshima, I. Nashiyama, S. Okada, H. Okumura, and S. Yoshida. Silicon vacancies in 3C-SiC observed by positron lifetime and electron spin resonance. *Appl. Phys. A*, **67**, 209, 1998.

[57] M. J. Puska, S. Mäkinen, M. Manninen, and R. M. Nieminen. Screening of positrons in semiconductors and insulators. *Phys. Rev. B*, **39**, 7666, 1989.

[58] G. Brauer, W. Anwand, P. G. Coleman, A. P. Knights, F. Plazaola, Y. Pacaud, W. Skorupa, J. Störmer, and P. Willutzki. Positron studies of defects in ion-implanted SiC. *Phys. Rev. B*, **54**, 3084, 1996.

[59] G. Brauer, W. Anwand, E.-M. Nicht, J. Kuriplach, M. Šob, N. Wagner, P. G. Coleman, M. J. Puska, and T. Korhonen. Evaluation of some basic positron-related characteristics of SiC. *Phys. Rev. B*, **54**, 2512, 1996.

[60] B. Barbiellini, M. J. Puska, T. Korhonen, A. Harju, T. Torsti, and R. M. Nieminen. Calculation of positron states and annihilation in solids: A density-gradient-correction scheme. *Phys. Rev. B*, **53**, 16201, 1996.

[61] B. K. Panda, W. LiMing, S. Fung, and C. D. Beling. Electron-positron momentum distributions and positron lifetime in semiconductors in the generalized gradient approximation. *Phys. Rev. B*, **56**, 7356, 1997.

[62] B. K. Panda, G. Brauer, W. Skorupa, and J. Kuriplach. Positron energy levels in semiconductors. *Phys. Rev. B*, **61**, 15848, 2000.

[63] A. Kawasuso, M. Yoshikawa, H. Itoh, R. Krause-Rehberg, F. Redmann, T. Higuchi, and K. Betsuyaku. Positron study of electron irradiation-induced vacancy defects in SiC. *Physica B*, **376–377**, 350, 2006.

[64] T. E. M. Staab, L. M. Torpo, M. J. Puska, and R. M. Nieminen. Calculated positron annihilation parameters for defects in SiC. *Mater. Sci. Forum*, **353**, 533, 2000.

[65] H. Itoh, M. Yoshikawa, I. Nashiyama, S. Misawa, H. Okumura, and S. Yoshida. Radiation induced defects in CVD-grown 3C-SiC. *IEEE Trans. Nucl. Sci.*, **37**, 1732, 1990.

[66] X. Kerbiriou, M.-F. Barthe, S. Esnouf, P. Desgardin, G. Blondiaux, and E. Balanzat. Vacancy defects induced in the track region of 132 MeV ^{12}C irradiated SiC. *Nucl. Instrm. Meth. B*, **250**, 259, 2006.

[67] A. Kawasuso, H. Itoh, S. Okada, and H. Okumura. Annealing processes of vacancy-type defects in electron-irradiated and as-grown 6H-SiC studied by positron lifetime spectroscopy. *J. Appl. Phys.*, **80**, 5639, 1996.

[68] S. Arpiainen, K. Saarinen, P. Hautojärvi, L. Henry, M.-F. Barthe, and C. Corbel. Optical transitions of the silicon vacancy in 6$H-$SiC studied by positron annihilation spectroscopy. *Phys. Rev. B*, **66**, 075206, 2002.

[69] A. A. Rempel, W. Sprengel, K. Blaurock, K. J. Reichle, J. Major, and H.-E. Schaefer. Identification of lattice vacancies on the two sublattices of SiC. *Phys. Rev. Lett.*, **89**, 185501, 2002.

[70] S. Dannefaer and D. Kerr. Positron annihilation investigation of electron irradiation-produced defects in 6H-SiC. *Diamond Relat. Mater.*, **13**, 157, 2004.

[71] M.-F. Barthe, D. T. Britton, C. Corbel, A. Hempel, L. Henry, P. Desgardin, W. Bauer-Kugelmann, G. Kögel, P. Sperr, and W. Triftshäuser. Negatively charged vacancy defects

in 6H-SiC after low-energy proton implantation and annealing. *Physica B*, **308**–**310**, 668, 2001.

[72] R. Aavikko, K. Saarinen, F. Tuomisto, B. Magnusson, N. T. Son, and E. Janzén. Clustering of vacancy defects in high-purity semi-insulating SiC. *Phys. Rev. B*, **75**, 085208, 2007.

[73] T. Ohshima, A. Uedono, K. Abe, H. Itoh, Y. Aoki, M. Yoshikawa, S. Tanigawa, and I. Nashiyama. Characterization of vacancy-type defects and phosphorus donors introduced in 6H-SiC by ion implantation. *Appl. Phys. A: Mater.*, **67**, 407, 1998.

[74] A. Kawasuso, F. Redmann, R. Krause-Rehberg, M. Yoshikawa, K. Kojima, and H. Itoh. Positron annihilation due to silicon vacancies in 3C and 6H-SiC epitaxial layers induced by 1 MeV electron irradiation. *Phys. Status Solidi B*, **223**, R8, 2001.

[75] A. Kawasuso, F. Redmann, R. Krause-Rehberg, M. Weidner, T. Frank, G. Pensl, P. Sperr, W. Triftshauser, and H. Itoh. Annealing behavior of vacancies and Z1/2 levels in electron-irradiated 4H-SiC studied by positron annihilation and deep-level transient spectroscopy. *Appl. Phys. Lett.*, **79**, 3950, 2001.

[76] A. Kawasuso, F. Redmann, R. Krause-Rehberg, T. Frank, M. Weidner, G. Pensl, P. Sperr, and H. Itoh. Vacancies and deep levels in electron-irradiated 6H-SiC epilayers studied by positron annihilation and deep level transient spectroscopy. *J. Appl. Phys.*, **90**, 3377, 2001.

[77] L. Henry. *Structure atomique et activité électrique des défauts natifs et induits par irradiation dans le carbure de silicium 6H-SiC déterminées par annihilation de positions.* PhD thesis, University of Orléans, 2002.

[78] Q. Xu, T. Yoshiie, and M. Okada. Positron annihilation of vacancy-type defects in neutron-irradiated 4H-SiC. *J. Nucl. Mater.*, **386**, 169, 2009.

[79] J. Wiktor, X. Kerbiriou, G. Jomard, S. Esnouf, M.-F. Barthe, and M. Bertolus. Positron annihilation spectroscopy investigation of vacancy clusters in silicon carbide: Combining experiments and electronic structure calculations. *Phys. Rev. B*, **89**, 155203, 2014.

[80] http://www.srim.org/SRIM/SRIMINTRO.htm.

[81] M.-F. Barthe, H. Labrim, A. Gentils, P. Desgardin, C. Corbel, S. Esnouf, and J. P. Piron. Positron annihilation characteristics in UO_2: for lattice and vacancy defects induced by electron irradiation. *Phys. Status Solidi C*, **4**, 3627, 2007.

[82] D. Roudil, M.-F. Barthe, C. Jégou, A. Gavazzi, and F. Vella. Investigation of defects in actinide-doped UO_2 by positron annihilation spectroscopy. *J. Nucl. Mater.*, **420**, 63, 2012.

[83] M.-F. Barthe, P. Desgardin, G. Blondiaux, S. Guilbert, H. Labrim, T. Sauvage, G. Carlot, P. Garcia, and J. P. Piron. Near surface vacancy defects in sintered polished UO_2 disks. In *Mater. Sci. Forum*, volume 445, page 48, 2004.

[84] H. Labrim, M.-F. Barthe, P. Desgardin, T. Sauvage, G. Blondiaux, C. Corbel, and J. P. Piron. Vacancy defects induced in sintered polished UO_2 disks by helium implantation. *App. Surf. Sci.*, **252**, 3256, 2006.

[85] H. Labrim, M.-F. Barthe, P. Desgardin, T. Sauvage, C. Corbel, G. Blondiaux, and J. P. Piron. Thermal evolution of the vacancy defects distribution in 1MeV helium implanted sintered UO_2. *Nucl. Instrum. Meth. B*, **261**, 883, 2007.

[86] N. Djourelov, B. Marchand, H. Marinov, N. Moncoffre, Y. Pipon, P. Nédélec, N. Toulhoat, and D. Sillou. Variable energy positron beam study of Xe-implanted uranium oxide. *J. Nucl. Mater.*, 2012.

[87] N. Djourelov, B. Marchand, H. Marinov, N. Moncoffre, Y. Pipon, N. Bérerd, P. Nédélec, L. Raimbault, and T. Epicier. Study of temperature and radiation induced microstructural changes in Xe-implanted UO_2 by TEM, STEM, SIMS and positron spectroscopy. *J. Nucl. Mater.*, **443**, 562, 2013.

[88] P. Hohenberg and W. Kohn. Inhomogeneous Electron Gas. *Phys. Rev.*, **136**, B864, 1964.

[89] L. H. Thomas. The calculation of atomic fields. *Math. Proc. Cambridge Philos. Soc.*, **23**, 542, 1927.

[90] E. Fermi. Un metodo statistico per la determinazione di alcune proprietà dell'atomo. *Rend. Accad. Naz. Lincei*, **6**, 602, 1927.

[91] J. M. Born and R. Oppenheimer. Zur Quantentheorie der Molekeln. *Ann. Physik (Leipzig)*, **84**, 457, 1927.

[92] E. Wigner. Effects of the electron interaction on the energy levels of electrons in metals. *Trans. Faraday Soc.*, **34**, 678, 1938.

[93] D. M. Ceperley and B. J. Alder. Ground state of the electron gas by a stochastic method. *Phys. Rev. Lett.*, **45**, 566, 1980.

[94] J. P. Perdew and A. Zunger. Self-interaction correction to density-functional approximations for many-electron systems. *Phys. Rev. B*, **23**, 5048, 1981.

[95] J. P. Perdew, K. Burke, and M. Ernzerhof. Generalized gradient approximation made simple. *Phys. Rev. Lett.*, **77**, 3865, 1996.

[96] J. P. Perdew and Y. Wang. Accurate and simple analytic representation of the electron-gas correlation energy. *Phys. Rev. B*, **45**, 13244, 1992.

[97] S. L. Dudarev, D. Nguyen Manh, and A. P. Sutton. Effect of Mott-Hubbard correlations on the electronic structure and structural stability of uranium dioxide. *Phil. Mag. B*, **75**, 613, 1997.

[98] L. Petit, A. Svane, Z. Szotek, and W. M. Temmerman. First-principles calculations of $PuO_{2\pm x}$. *Science*, **301**, 498, 2003.

[99] I. D. Prodan, G. E. Scuseria, and R. L. Martin. Covalency in the actinide dioxides: Systematic study of the electronic properties using screened hybrid density functional theory. *Phys. Rev. B*, **76**, 033101, 2007.

[100] A. Georges, G. Kotliar, W. Krauth, and M. J. Rozenberg. Dynamical mean-field theory of strongly correlated fermion systems and the limit of infinite dimensions. *Rev. Mod. Phys.*, **68**, 13, 1996.

[101] A. I. Liechtenstein, V. I. Anisimov, and J. Zaanen. Density-functional theory and strong interactions: Orbital ordering in Mott-Hubbard insulators. *Phys. Rev. B*, **52**, R5467, 1995.

[102] P. E. Blöchl. Projector augmented-wave method. *Phys. Rev. B*, **50**, 17953, 1994.

[103] G. Kresse and D. Joubert. From ultrasoft pseudopotentials to the projector augmented-wave method. *Phys. Rev. B*, **59**, 1758, 1999.

[104] N. A. W. Holzwarth, A. R. Tackett, and G. E. Matthews. A Projector Augmented Wave (PAW) code for electronic structure calculations, Part I: atompaw for generating atom-centered functions. *Comput. Phys. Commun.*, **135**, 329, 2001.

[105] M. Torrent, F. Jollet, F. Bottin, G. Zérah, and X. Gonze. Implementation of the projector augmented-wave method in the ABINIT code: Application to the study of iron under pressure. *Comp. Mater. Sci.*, **42**, 337, 2008.

[106] M. Leslie and N. J. Gillan. The energy and elastic dipole tensor of defects in ionic crystals calculated by the supercell method. *J. Phys. C*, **18**, 973, 1985.

[107] S. Lany and A. Zunger. Accurate prediction of defect properties in density functional supercell calculations. *Model. Simul. Matter. Sci. Eng.*, **17**, 084002, 2009.

[108] S. E. Taylor and F. Bruneval. Understanding and correcting the spurious interactions in charged supercells. *Phys. Rev. B*, **84**, 075155, 2011.

[109] R. M. Nieminen, E. Boroński, and L. J. Lantto. Two-component density-functional theory: Application to positron states. *Phys. Rev. B*, **32**, 1377, 1985.

[110] E. Boroński and R. M. Nieminen. Electron-positron density-functional theory. *Phys. Rev. B*, **34**, 3820, 1986.

[111] S. Daniuk, G. Kontrym-Sznajd, A. Rubaszek, H. Stachowiak, J. Mayers, P. A. Walters, and R. N. West. Selective enhancement of different electron populations by electron-positron attraction: application to zinc. *J. Phys. F: Met. Phys.*, **17**, 1365, 1987.

[112] M. Alatalo, B. Barbiellini, M. Hakala, H. Kauppinen, T. Korhonen, M. J. Puska, K. Saarinen, P. Hautojärvi, and R. M. Nieminen. Theoretical and experimental study of positron annihilation with core electrons in solids. *Phys. Rev. B*, **54**, 2397, 1996.

[113] I. Makkonen, M. Hakala, and M. J. Puska. Modeling the momentum distributions of annihilating electron-positron pairs in solids. *Phys. Rev. B*, **73**, 035103, 2006.

[114] J. Arponen and E. Pajanne. Angular correlation in positron annihilation. *J. Phys. F: Met. Phys.*, **9**, 2359, 1979.

[115] I. Makkonen and M. J. Puska. Energetics of positron states trapped at vacancies in solids. *Phys. Rev. B*, **76**, 054119, 2007.

[116] A Calloni, A Dupasquier, R Ferragut, P Folegati, MM Iglesias, I Makkonen, and MJ Puska. Positron localization effects on the doppler broadening of the annihilation line: Aluminum as a case study. *Phys. Rev. B*, **72**, 054112, 2005.

[117] P. Folegati, I. Makkonen, R. Ferragut, and M. J. Puska. Analysis of electron-positron momentum spectra of metallic alloys as supported by first-principles calculations. *Phys. Rev. B*, **75**, 054201, 2007.

[118] C. Rauch, I. Makkonen, and F. Tuomisto. Identifying vacancy complexes in compound semiconductors with positron annihilation spectroscopy: A case study of inn. *Phys. Rev. B*, **84**, 125201, 2011.

[119] L. Gilgien, G. Galli, F. Gygi, and R. Car. *Ab initio* study of positron trapping at a vacancy in GaAs. *Phys. Rev. Lett.*, **72**, 3214, 1994.

[120] M. J. Puska, A. P. Seitsonen, and R. M. Nieminen. Electron-positron Car-Parrinello methods: Self-consistent treatment of charge densities and ionic relaxations. *Phys. Rev. B*, **52**, 10947, 1995.

[121] L. J. Lantto. Variational theory of multicomponent quantum fluids: An application to positron-electron plasmas at *T=0*. *Phys. Rev. B*, **36**, 5160, 1987.

[122] M. J. Puska. Ab-initio calculation of positron annihilation rates in solids. *J. Phys.: Condens. Matter*, **3**, 3455, 1991.

[123] B. Barbiellini, M. J. Puska, T. Torsti, and R. M. Nieminen. Gradient correction for positron states in solids. *Phys. Rev. B*, **51**, 7341, 1995.

[124] H. Stachowiak and J. Lach. Positron-annihilation characteristics in an electron gas from low to high densities. *Phys. Rev. B*, **48**, 9828, 1993.

[125] E. Boroński. Positron lifetime calculations for some elements on the base of the GGA-PHNC approximation. *Nukleonika*, **55**, 9, 2010.

[126] J. Kuriplach and B. Barbiellini. Improved generalized gradient approximation for positron states in solids. *Phys. Rev. B*, **89**, 155111, 2014.

[127] N. D. Drummond, P. López Ríos, R. J. Needs, and C. J. Pickard. Quantum monte carlo study of a positron in an electron gas. *Phys. Rev. Lett.*, **107**, 207402, 2011.

[128] W. Zhang, L. Jiandang, Z. Jie, H. Shijuan, L. Jun, and Y. Bangjiao. Assessment of several calculation methods for positron lifetime. In *JJAP Conference Proceedings*, volume 2. The Japan Society of Applied Physics, 2014.

[129] X. Gonze, B. Amadon, P.-M. Anglade, J.-M. Beuken, F. Bottin, P. Boulanger, F. Bruneval, D. Caliste, R. Caracas, M. Côté, T. Deutsch, L. Genovese, Ph. Ghosez, M. Giantomassi, S. Goedecker, D. R. Hamann, P. Hermet, F. Jollet, G. Jomard, S. Leroux, M. Mancini, S. Mazevet, M. J. T. Oliveira, G. Onida, Y. Pouillon, T. Rangel, G.-M. Rignanese, D. Sangalli, R. Shaltaf, M. Torrent, M. J. Verstraete, G. Zerah, and J. W. Zwanziger. ABINIT: First-principles approach to material and nanosystem properties. *Comput. Phys. Commun.*, **180**, 2582, 2009.

[130] X. Gonze, J.-M. Beuken, R. Caracas, F. Detraux, M. Fuchs, G.-M. Rignanese, L. Sindic, M. Verstraete, G. Zérah, F. Jollet, M. Torrent, A. Roy, M. Mikami, Ph. Ghosez, J.-Y. Raty, and D. C. Allan. First-principles computation of material properties: the ABINIT software project. *Comp. Mater. Sci.*, **25**, 478, 2002.

[131] X. Gonze, G.-M. Rignanese, M. Verstraete, J.-M. Beuke, Y. Pouillon, R. Caracas, F. Jollet, M. Torrent, G. Zérah, M. Mikami, Ph. Ghosez, M. Veithen, J.-Y. Raty, V. Olevano, F. Bruneval, L. Reining, R. Godby, G. Onida, D. R. Hamann, and D. C. Allan. A brief introduction to the ABINIT software package. *Zeit. Kristallogr.*, **220**, 558, 2005.

[132] H. Takenaka and D. J. Singh. Full-potential all-electron positron lifetime calculations: Assessment of local enhancement factors. *Phys. Rev. B*, **77**, 155132, 2008.

[133] W. Koch and M. C. Holthausen. *A chemist's guide to density functional theory.* Wiley-VCH, 2000.

[134] M. Saito and A. Oshiyama. Lifetimes of positrons trapped at si vacancies. *Phys. Rev. B*, **53**, 7810, 1996.

[135] J. Schoenes. Optical properties and electronic structure of UO_2. *J. Appl. Phys.*, **49**, 1463, 1978.

[136] F. Bottin, S. Leroux, A. Knyazev, and G. Zérah. Large-scale ab initio calculations based on three levels of parallelization. *Comp. Mater. Sci.*, **42**, 329, 2008.

[137] A. Levitt and M. Torrent. Parallel eigensolvers in plane-wave density functional theory. *Comput. Phys. Commun.*, **187**, 98, 2015.

[138] V. Ranki, A. Pelli, and K. Saarinen. Formation of vacancy-impurity complexes by annealing elementary vacancies introduced by electron irradiation of As-, P-, and Sb-doped Si. *Phys. Rev. B*, **69**, 115205, 2004.

[139] I. Makkonen. Calculation of valence electron momentum distributions in solids. Master's thesis, Helsinki University of Technology, Espoo, Finland, 2004.

[140] Y. Nagai, Z. Tang, and M. Hasegawa. Chemical analysis of precipitates in metallic alloys using coincidence Doppler broadening of positron annihilation radiation. *Radiat. Phys. Chem.*, **58**, 737, 2000.

[141] Y. Nagai, T. Honma, Z. Tang, K. Hono, and M. Hasegawa. Coincidence Doppler broadening study of the pre-precipitation stage of an Al-Cu-Mg-Ag alloy. *Philos. Mag. A*, **82**, 1559, 2002.

[142] H. Kauppinen, C. Corbel, K. Skog, K. Saarinen, T. Laine, P. Hautojärvi, P. Desgardin, and E. Ntsoenzok. Divacancy and resistivity profiles in n-type Si implanted with 1.15-MeV protons. *Phys. Rev. B*, **55**, 9598, 1997.

[143] J. Wiktor, G. Jomard, M. Torrent, and M. Bertolus. Electronic structure investigation of energetics and positron lifetimes of fully relaxed monovacancies with various charge states in $3C$-SiC and $6H$-SiC. *Phys. Rev. B*, **87**, 235207, 2013.

[144] J. Wiktor, G. Jomard, and M. Bertolus. Electronic structure calculations of positron lifetimes in SiC: Self-consistent schemes and relaxation effect. *Nucl. Instrum. Meth. B*, **327**, 63, 2014.

[145] S. B. Zhang and John E. Northrup. Chemical potential dependence of defect formation energies in GaAs: Application to Ga self-diffusion. *Phys. Rev. Lett.*, **67**, 2339, 1991.

[146] C. G. Broyden. The convergence of a class of double-rank minimization algorithms 2. The new algorithm. *J. Inst. Math. Appl.*, **6**, 221, 1970.

[147] R. Fletcher. A new approach to variable metric algorithms. *Comput. J.*, **13**, 317, 1970.

[148] D. Goldfarb. A family of variable-metric methods derived by variational means. *Math. Comput.*, **24**, 23, 1970.

[149] D. F. Shanno. Conditioning of quasi-newton methods for function minimization. *Math. Comput.*, **24**, 647, 1970.

[150] L. Patrick and W. J. Choyke. Static dielectric constant of SiC. *Phys. Rev. B*, **2**, 2255, 1970.

[151] L. Torpo, R. M. Nieminen, K. E. Laasonen, and S. Poykko. Silicon vacancy in SiC: A high-spin state defect. *Appl. Phys. Lett.*, **74**, 221, 1999.

[152] T. Wimbauer, B. K. Meyer, A. Hofstaetter, A. Scharmann, and H. Overhof. Negatively charged Si vacancy in 4*H*-SiC: A comparison between theory and experiment. *Phys. Rev.B*, **56**, 7384, 1997.

[153] N. T. Son, P. Carlsson, J. ul Hassan, E. Janzén, T. Umeda, J. Isoya, A. Gali, M. Bockstedte, N. Morishita, T. Ohshima, and H. Itoh. Divacancy in 4*H*-SiC. *Phys. Rev. Lett.*, **96**, 055501, 2006.

[154] P. Carlsson, N. T. Son, A. Gali, J. Isoya, N. Morishita, T. Ohshima, B. Magnusson, and E. Janzén. EPR and *ab initio* calculation study on the EI4 center in 4H- and 6H-SiC. *Phys. Rev. B*, **82**, 235203, 2010.

[155] T. E. M. Staab, M. Haugk, Th. Frauenheim, and H. S. Leipner. Magic number vacancy aggregates in GaAs: Structure and positron lifetime studies. *Phys. Rev. Lett.*, **83**, 5519, 1999.

[156] D. V. Makhov and L. J. Lewis. Two-component density functional theory calculations of positron lifetimes for small vacancy clusters in silicon. *Phys. Rev. B*, **71**, 205215, 2005.

[157] T. Korhonen, M. J. Puska, and R. M. Nieminen. First-principles calculation of positron annihilation characteristics at metal vacancies. *Phys. Rev. B*, **54**, 15016, 1996.

[158] N. Mizuochi, S. Yamasaki, H. Takizawa, N. Morishita, T. Ohshima, H. Itoh, and J. Isoya. Continuous-wave and pulsed EPR study of the negatively charged silicon vacancy with $s = \frac{3}{2}$ and C_{3v} symmetry in n-type $4H$-SiC. *Phys. Rev. B*, **66**, 235202, 2002.

[159] S. B. Orlinski, J. Schmidt, E. N. Mokhov, and P. G. Baranov. Silicon and carbon vacancies in neutron-irradiated SiC: A high-field electron paramagnetic resonance study. *Phys. Rev. B*, **67**, 125207, 2003.

[160] C. Corbel, M. Stucky, P. Hautojärvi, K. Saarinen, and P. Moser. Positron-annihilation spectroscopy of native vacancies in as-grown GaAs. *Phys. Rev. B*, **38**, 8192, 1988.

[161] A. Polity, S. Huth, and M. Lausmann. Defect characterization in electron-irradiated $6H$-SiC by positron annihilation. *Phys. Rev. B*, **59**, 10603, 1999.

[162] Florence Linez. *Propriété des défauts lacunaires dans le carbure de silicium: évolution de leur nature en fonction des conditions d'irradiation et intéraction avec l'hélium.* PhD thesis, Université d'Orléans, 2012.

[163] J. Wiktor, E. Vathonne, M. Freyss, G. Jomard, and M. Bertolus. Calculation of defect formation energies in UO_2. In *MRS Proceedings*, volume 1645, page mrsf13. Cambridge Univ Press, 2014.

[164] E. Vathonne, J. Wiktor, M. Freyss, G. Jomard, and M. Bertolus. DFT+U investigation of charged point defects and clusters in UO_2. *J. Phys.: Condens. Mat.*, **26**, 325501, 2014.

[165] J. Wiktor, M.-F. Barthe, G. Jomard, M. Torrent, M. Freyss, and M. Bertolus. Coupled experimental and DFT+u investigation of positron lifetimes in UO_2. *Phys. Rev. B*, **90**, 184101, 2014.

[166] C. Guéneau, M. Baichi, D. Labroche, C. Chatillon, and B. Sundman. Thermodynamic assessment of the uranium-oxygen system. *J. Nucl. Mater.*, **304**, 161, 2002.

[167] S. Na-Phattalung, M. F. Smith, K. Kim, M.-H. Du, S.-H. Wei, S. B. Zhang, and S. Limpijumnong. First-principles study of native defects in anatase TiO_2. *Phys. Rev. B*, **73**, 125205, 2006.

[168] M. Pukari, P. Olsson, and N. Sandberg. He, Kr and Xe diffusion in ZrN - An atomic scale study. *J. Nucl. Mater.*, **438**, 7, 2013.

[169] M. Iwasawa, Y. Chen, Y. Kaneta, T. Ohnuma, H. Geng, and M. Kinoshita. First-principles calculation of point defects in uranium dioxide. *Mater. Trans.*, **47**, 2651, 2006.

[170] J.-P. Crocombette. Influence of charge states on energies of point defects and clusters in uranium dioxide. *Phys. Rev. B*, **85**, 144101, 2012.

[171] P. Nerikar, T. Watanabe, J. S. Tulenko, S. R. Phillpot, and S. B. Sinnott. Energetics of intrinsic point defects in uranium dioxide from electronic-structure calculations. *J. Nucl. Mater.*, **384**, 61, 2009.

[172] G. Kresse and J. Furthmüller. Efficient iterative schemes for *ab initio* total-energy calculations using a plane-wave basis set. *Phys. Rev. B*, **54**, 11169, 1996.

[173] G. Kresse and J. Hafner. *Ab initio* molecular dynamics for liquid metals. *Phys. Rev. B*, **47**, 558, 1993.

[174] G. Kresse and J. Furthmüller. Efficiency of *Ab initio* total energy calculations for metals and semiconductors using a plane-wave basis set. *Comput. Mater. Sci.*, **6**, 15, 1996.

[175] J. P. Perdew, K. Burke, and M. Ernzerhof. Generalized gradient approximation made simple. *Phys. Rev. Lett.*, **77**, 3865, 1996.

[176] A. Kotani and T. Yamazaki. Systematic analysis of core photoemission spectra for actinide di-oxides and rare-earth sesqui-oxides. *Prog. Theor. Phys. Suppl.*, **108**, 117, 1992.

[177] G. Jomard, B. Amadon, F. Bottin, and M. Torrent. Structural, thermodynamic, and electronic properties of plutonium oxides from first principles. *Phys. Rev. B*, **78**, 075125, 2008.

[178] B. Amadon, F. Jollet, and M. Torrent. γ and β cerium: LDA$+U$ calculations of ground-state parameters. *Phys. Rev. B*, **77**, 155104, 2008.

[179] K. Ikushima, S. Tsutsui, Y. Haga, H. Yasuoka, R. E. Walstedt, N. M. Masaki, A. Nakamura, S. Nasu, and Y. Ōnuki. First-order phase transition in uo_2 : ^{235}U and ^{17}O nmr study. *Phys. Rev. B*, **63**, 104404, 2001.

[180] R. Laskowski, G. K. H. Madsen, P. Blaha, and K. Schwarz. Magnetic structure and electric-field gradients of uranium dioxide: An *ab initio* study. *Phys. Rev. B*, **69**, 140408, 2004.

[181] H. J. Monkhorst and J. D. Pack. Special points for brillouin-zone integrations. *Phys. Rev. B*, **13**, 5188, 1976.

[182] A. Kokalj. XCrySDen-a new program for displaying crystalline structures and electron densities. *J. Mol. Graph. Model.*, **17**, 176, 1999.

[183] A. Kokalj. Computer graphics and graphical user interfaces as tools in simulations of matter at the atomic scale. *Comput. Mat. Sci.*, **28**, 155, 2003.

[184] G. C. Allen, P. M. Tucker, and J. W. Tyler. Oxidation of uranium dioxide at 298 K studied by using X-ray photoelectron spectroscopy. *J. Phys. Chem.*, **86**, 224, 1982.

[185] G. C. Allen and P. A. Tempest. Ordered defects in the oxides of uranium. *Proc. R. Soc. Lond. A*, **406**, 325, 1986.

[186] K. Clausen, W. Hayes, J. E. Macdonald, R. Osborn, and M. T. Hutchings. Observation of oxygen frenkel disorder in uranium dioxide above 2000 K by use of neutron-scattering techniques. *Phys. Rev. Lett.*, **52**, 1238, 1984.

[187] L. Desgranges, M. Gramond, C. Petot, G. Petot-Ervas, P. Ruello, and B. Saadi. Characterisation of uranium vacancies in hyper stoichiometric uranium dioxide. *J. Eur. Cera. Soc.*, **25**, 2683, 2005.

[188] B. T. M. Willis. The defect structure of hyper-stoichiometric uranium dioxide. *Acta Cristallogr.*, **A34**, 88, 1978.

[189] J. Wang, R. C. Ewing, and U. Becker. Average structure and local configuration of excess oxygen in UO_{2+x}. *Scientific reports*, **4**, 2014.

[190] G. Martin, P. Garcia, C. Sabathier, L. Van Brutzel, B. Dorado, F. Garrido, and S. Maillard. Irradiation-induced heterogeneous nucleation in uranium dioxide. *Phys. Lett. A*, **374**, 3038, 2010.

Résumé en français

Introduction

La connaissance du comportement des matériaux utilisés dans les réacteurs nucléaires est essentielle pour la sécurité et l'efficacité des centrales nucléaires. Lors de l'irradiation en réacteur la fission des atomes d'actinides entraîne la création de grandes quantités de défauts et de produits de fission, qui affectent les propriétés physiques et chimiques des matériaux. Un champ actif de recherche est l'amélioration de la connaissance des mécanismes élémentaires gouvernant la modification des matériaux sous irradiation. Cela peut être fait par simulation expérimentale permettant de découpler les différents effets de l'irradiation ainsi que par modélisation numérique à différentes échelles. Les approches de simulation expérimentales et de modélisation, ainsi que leur couplage, sont mises en ouvre au Laboratoire de Loi de Comportement des Combustibles (LLCC) au CEA Cadarache, en France, où cette thèse a été réalisée.

Une question importante pour comprendre le comportement des matériaux nucléaires sous irradiation est le début de la formation des bulles de gaz rares formées par la fission de l'uranium. Les petits agrégats de défauts lacunaires, qui peuvent piéger les atomes de gaz rares, comme le krypton ou le xenon, sont donc particulièrement intéressants pour l'investigation des mécanismes de formation des bulles. De plus, les défauts ponctuels eux-mêmes, vides ou contenant des produits de fission, peuvent affecter les propriétés thermochimiques et thermomécaniques des matériaux.

Une des méthodes non destructives pouvant être utilisées pour caractériser les défauts induits par irradiation, vides ou contenant des produits de fission, est la spectroscopie d'annihilation de positons (SAP). Cette technique expérimentale consiste à détecter le rayonnement généré lors de l'annihilation des paires électron-positon dans un échantillon et à en déduire les propriétés de la matière étudiée. La SAP est basée sur le fait que quand un positon diffuse dans un

échantillon il peut être piégé dans les défauts de type lacunaire, ce qui modifie ses caractéristiques d'annihilation. La SAP permet de détecter les défauts neutres et négatifs. Les défauts positifs ne peuvent pas être observés, parce qu'ils repoussent les positons ayant la même charge. Il y a deux caractéristiques d'annihilation de positons qui permettent de détecter les défauts dans les matériaux : le premier, le temps de vie de positon, est principalement sensible au volume ouvert des défauts. Le deuxième, l'élargissement Doppler du rayonnement d'annihilation, apporte des informations sur l'environnement chimique dans lequel le positon s'annihile.

Cependant, les résultats de la spectroscopie d'annihilation de positons ne fournissent pas un lien direct entre le signal et le type du défaut. L'interprétation des données expérimentales nécessite souvent des comparaisons avec d'autres techniques expérimentales ou avec des calculs de structure électronique. Les caractéristiques d'annihilation de positons peuvent être calculées en utilisant la théorie de la fonctionnelle de la densité à deux composants (two-component density functional theory, TCDFT). Cette technique est une généralisation de la théorie de la fonctionnelle de la densité (density functional theory, DFT).

Ce travail est consacré à la modélisation à l'échelle atomique des matériaux nucléaires contenant des défauts et au calcul de leurs caractéristiques d'annihilation pour contribuer à l'interprétation des résultats expérimentaux obtenus par la SAP et à l'identification des défauts. Les matériaux considérés dans cette thèse sont le carbure de silicium (SiC) et le dioxyde d'uranium (UO_2). Deux sortes de propriétés peuvent être calculées pour contribuer à l'identification des défauts dans les deux matériaux étudiés : les caractéristiques d'annihilation des défauts elles-mêmes, mais également les énergies de formation de défauts (chargés ou neutres). La spectroscopie d'annihilation de positons est en effet sensible aux états de charge des défauts et leur prédiction peut, par conséquent, faciliter l'identification de défauts. De plus la prédiction des défauts les plus stables peut permettre de discriminer entre différents défauts avec des caractéristiques similaires.

Dans ce travail, les calculs de temps de vie de positon ont été effectués en utilisant la théorie de la fonctionnelle de la densité à deux composants déjà implémentée dans le code ABINIT. Les méthodes nécessaires pour le calcul de la deuxième caractéristique de l'annihilation de positons, l'élargissement Doppler des paires électron-positon, ont ensuite été implémentées dans le code. Cette partie a été réalisée en collaboration avec Marc Torrent du CEA DAM/DIF.

La deuxième partie de cette thèse a été consacrée aux calculs des caractéristiques d'annihilation de positons et des énergies de formation de défauts pour le carbure de silicium et dioxyde d'uranium. Des efforts ont été faits pour effectuer les meilleures calculs possibles pour les caractéristiques d'annihilation, c'est-à-dire en utilisant des calculs complètement auto-cohérents et en prenant en compte l'effet des changements des positions atomiques dans les défauts. Les résultats combinés des calculs des énergies de formation, du temps de vie et de l'élargissement Doppler ont été ensuite utilisés pour identifier les défauts détectés expérimentalement dans le carbure de silicium et le dioxyde d'uranium au laboratoire CNRS-CEMHTI à Orléans, France.

Matériaux considérés

Dans cette thèse nous avons considéré deux céramiques nucléaires, le carbure de silicium (SiC) et le dioxyde d'uranium (UO_2).

Le carbure de silicium est une céramique ayant un point de fusion élevé, une bonne stabilité chimique et absorbant faiblement les neutrons. Ces propriétés en font un matériau de gaine potentiel dans les réacteurs nucléaires de génération IV et pour les combustibles nucléaires ATF (accident tolerant fuel) dans les réacteurs de génération II et III. De plus, ses propriétés mécaniques en tant que un système composite en font un matériau intéressant pour les enveloppes d'assemblages de combustible. Le carbure de silicium peut exister sous environ 250 formes cristallines, qui diffèrent par le mode d'empilement des couches atomiques. Dans ce travail, les polytypes $3C$-SiC et $6H$-SiC ont été étudiés. $6H$-SiC, qui a une structure hexagonale et est formé à des températures supérieures à 1700°C, est le polytype le plus fréquent du carbure de silicium. À des températures inférieures à 1700°C, une structure cubique, $3C$-SiC, est formée.

Le deuxième matériau étudié, le dioxyde d'uranium (UO_2), est actuellement le combustible le plus largement utilisé dans les réacteurs à eau pressurisée (REP). Il a été choisi comme matériau combustible à cause de sa température de fusion élevée (3120 K) et de sa stabilité chimique, en particulier grâce à sa faible réactivité chimique avec l'eau. Lors de l'irradiation dans le réacteur les propriétés de l'UO_2 évoluent de façon importante, en particulier en raison de la création de défauts et de produits de fission dans le réseau, il est important d'être capable de prédire quels types de défauts sont produits et quelle est leur influence sur le matériau.

À pression atmosphérique et température ambiante l'UO_2 est un isolant de Mott paramagnétique avec une structure cristalline fluorine cubique et un paramètre de maille de 5.473 Å. Le dioxyde d'uranium est un matériau ionique, dans lequel les cations de l'uranium (U^{4+}) forment une structure cubique face centrée (FCC) dont les ions oxygène (O^{2-}) occupent les sites tétraédriques. Les électrons $5f$ de l'uranium en UO_2 sont fortement corrélés et localisés à proximité des noyaux. En conséquence, les méthodes théoriques qui doivent être utilisées pour modéliser le dioxyde d'uranium doivent être choisies avec précaution.

Méthodes

L'objectif de cette thèse est de contribuer à l'identification des signaux observés par SAP dans le dioxyde d'uranium et le carbure de silicium en utilisant les calculs de structure électronique qui permettent de décrire la matière à l'échelle atomique. À cette échelle, les systèmes sont constitués d'électrons et noyaux qui interagissent entre eux. L'équation de base pour décrire ce type de problème est l'équation de Schrödinger, qui est impossible à résoudre analytiquement pour un système contenant plus d'un électron et des approximations complexes et des méthodes numériques sont nécessaires.

La théorie de la fonctionnelle de la densité (DFT) est une des méthodes de la mécanique quantique permettant de modéliser la structure électronique de systèmes contenant un grand nombre d'électrons, tels que atomes, molécules et la matière condensée en utilisant plusieurs simplifications. Cette méthode a été formulée par Hohenberg et Kohn et est basée sur le modèle de Thomas-Fermi. En DFT, la densité électronique est le paramètre fondamental décrivant le système, ce qui veut dire que toutes les propriétés du système peuvent être exprimées comme fonctionnelles de la densité. Cette approche simplifie les calculs en remplaçant le problème de N électrons avec $3N$ coordonnées par un problème de densité de charge globale avec 3 coordonnées spatiales seulement.

La théorie de la fonctionnelle de la densité peut être généralisée afin d'étudier les systèmes d'électrons interagissant avec un positon. Cette généralisation conduit à la théorie de la fonctionnelle densité à deux composantes (TCDFT) développée notamment par Chakraborty, Siegel, Boroński et Nieminen. La TCDFT permet de calculer les fonctions d'onde et les densités de positons et d'électrons interagissant entre eux. Ces quantités permettent de déterminer les temps de vie des positons et des distributions des moments dans un système donné.

Tests et développement du code ABINIT

La première partie de l'étude a été consacrée à des tests et développements de code. Nous avons effectué des tests pour valider l'implémentation des calculs de temps de vie de positons dans le code ABINIT. Ensuite, nous avons déterminé les paramètres optimaux pour les calculs des caractéristiques d'annihilation de positons dans les défauts dans le SiC et l'UO_2. Puis, nous avons implémenté les méthodes nécessaires pour le calcul de la deuxième caractéristique d'annihilation de positons, la distribution de moments de paires électron-positon, qui n'étaient pas disponibles dans le code. Le développement a été réalisé dans le formalisme des ondes augmentées par projecteurs (projector augmented-wave, PAW) et a été testé sur plusieurs matériaux. La comparaison entre les résultats obtenus en utilisant notre implémentation et les données de référence a confirmé la validité des méthodes utilisées et l'implémentation elle-même. Il est important de noter que la méthode PAW n'améliore pas la description des fonctions d'onde du positon, par rapport, par exemple, à la méthode des pseudopotentiels. Elle peut même rendre cette description plus difficile. Nous avons montré, cependant, que lorsque les données PAW sont choisies et testées avec précaution, une bonne description du positon peut être obtenue avec des temps de vie et des distributions de moment en bon accord avec les données expérimentales.

Résultats sur le SiC

La deuxième partie de cette thèse a été consacrée à l'étude de défauts dans le carbure de silicium. Tout d'abord, pour déterminer des états de charge les plus stables de défauts, nous avons étudié leurs énergies de formation. À ce stade, nous sommes déjà capable de prédire les défauts qui seront visibles ou non dans les expériences de SAP en fonction du niveau de dopage de l'échantillon (les défauts positifs ne peuvent pas piéger les positons). Ensuite, nous avons effectué des calculs de temps de vie des positons pour les différents défauts lacunaires dans le carbure de silicium. Nous avons montré l'importance de l'utilisation de méthodes de TCDFT entièrement auto-cohérentes et de tenir compte des effets de relaxation dus aux forces électroniques et positroniques dans les calculs de temps de vie de positons. Les résultats de calcul ont été utilisés pour vérifier les identifications des signaux expérimentaux SAP publiés dans la littérature. Nous avons suggéré que la non prise en compte de l'effet de la relaxation atomique dans les calculs précédents, qui ont été utilisés pour interpréter les mesures de la SAP dans SiC, pouvait conduire à une mauvaise identification des défauts. Les monolacunes

de carbone, en particulier, avaient très probablement été confondues avec les monolacunes de silicium.

Nous avons également analysé les nouvelles données expérimentales obtenues au laboratoire CEMHTI dans les échantillons de $6H$-SiC de type n irradiés avec des protons ayant une énergie de 12 MeV. Dans ces échantillons irradiés nous avons identifié des monolacunes de silicium négatives avec un temps de vie de positons de 218 ps. Nous avons observé que pendant le recuit à des températures à partir de 400–500°C les lacunes de silicium migrent et forment un défaut plus grand. Ce défaut, présentant un temps de vie de positons de 235 ps, a été identifié comme la bilacune V_C+V_{Si}, en se basent à la fois sur les calculs de l'état de charge et des temps de vie.

Enfin, nous avons effectué des calculs des spectres Doppler de différents défauts dans SiC. Le carbure de silicium peut exister sous plusieurs géométries différentes, appelées 'polytypes'. Nous avons donc étudié l'effet du polytype sur les spectres. Nous avons obtenu des résultats très similaires pour la lacune de silicium et les complexes contenant ce défaut dans les deux polytypes étudiés, le polytype cubique $3C$ et hexagonal $6H$. Cela veut dire que les résultats obtenus dans $3C$-SiC, qui est plus simple à modéliser, peuvent être utilisés pour l'identification de défauts dans les autres structures. Nous avons également calculé les paramètres S et W, représentant les contributions de faibles moments et de moments élevés du spectre Doppler, qui sont généralement considérés dans les études expérimentales. Nous avons étudié l'effet de la résolution expérimentale et le choix des fenêtres d'intégration de ces paramètres, et montré que pour certaines fenêtres les défauts peuvent être plus faciles à distinguer que pour les autres.

Résultats sur l'UO_2

La dernière partie de cette étude a été consacrée à des défauts dans le dioxyde d'uranium. Nous avons d'abord développé un formalisme physiquement justifié pour le calcul des énergies de formation de défauts dans ce matériau. Dans les études précédentes sur les défauts dans UO_2, une formule simplifiée a été utilisée pour les calculs des énergies de formation, en approximant les potentiels chimiques de l'uranium et de l'oxygène dans l'UO_2 par leurs valeurs soit dans la molécule O_2 soit dans l'uranium métallique U-α. Nous avons insisté sur l'influence du choix des ces énergies de référence sur les énergies de formation de défauts ponctuels. Ce choix est particulièrement important dans UO_2 parce que les potentiels chimiques des atomes d'oxygène et d'uranium peuvent fortement varier. Nous avons calculé les intervalles de potentiels chimiques de

l'uranium et de l'oxygène accessibles en utilisant le diagramme de phase de l'UO_2 expérimental. Puis, nous avons appliqué une contrainte sur les énergies de formation de lacunes, afin de définir les régimes hypo- et hyperstoechiométriques.

Les énergies de formation de différents défauts neutres et chargés dans UO_2 ont été calculées en utilisant la méthode GGA+U. Cette méthode a été choisie pour bien décrire les fortes corrélations entre les électrons $5f$ dans l'UO_2. Nous avons utilisé la méthode de contrôle des matrices d'occupation pour résoudre le problème de la convergence vers les multiples états métastables. Les calculs de l'énergie de formation nous ont permis de déterminer les défauts le plus stables et les états de charge les plus stables dans un matériau de stœchiométrie et de niveau de dopage donnés.

Troisièmement, nous avons effectué des calculs de temps de vie de positons de lacunes neutres et chargées complètement relaxées dans le formalisme DFT+U. Nous avons utilisé en deux méthodes de calcul de temps de vie différentes, GGGC et PSN. La première, proposée par Gilgien, Galli, Gygi et Car, exprime l'interaction électron-positon considèrent la densité de positon négligeable, qui est pas le cas par exemple pour le positon localisé dans un défaut. La deuxième, PSN, proposée par Puska, Seitsonen, and Nieminen, utilise une description plus complète de l'énergie d'interaction entre les particules en prenant en compte la densité de positon. En utilisant les résultats de calculs, nous avons analysé les mesures de la SAP obtenues sur des échantillons d'UO_2 irradiés. Le temps de vie de positons de 310±5 ps observé était similaire aux temps de vie calculées pour plusieurs défauts. Cependant, en utilisant les informations sur les états de charge les plus stables des défauts et le modèle de piégeage de positons, nous avons montré que les trilacunes V_U+$2V_O$ neutre (défauts de Schottky liés) prédominaient dans les échantillons étudiés.

Enfin, nous avons effectué des calculs de spectres Doppler pour différents défauts dans UO_2. Nous avons obtenu des spectres similaires pour certains défauts. Cela suggère que leur identification dans les mesures de distribution de moments du rayonnement d'annihilation peut être difficile. D'autre part, nous avons montré que l'incorporation du krypton conduit à des changements significatifs dans les spectres Doppler des défauts. Celle-ci peut donc être étudiée avec succès en utilisant des mesures de distributions de moments.

Perspectives

Il y a de nombreuses perspectives issues de ce travail. Premièrement, d'autres mesures expérimentales doivent être analysées, en particulier en utilisant les spectres Doppler calculés le plus récemment. Dans le cas du carbure de silicium, des études supplémentaires des défauts combinant les résultats de calcul et les mesures expérimentales de temps de vie de positons et d'élargissement Doppler avec les expériences de photoluminescence supplémentaires sont prévues. En outre, des nouvelles analyses des données expérimentales existantes en utilisant des fenêtres d'intégration différentes pour la détermination de paramètres S et W ont été lancées. Dans le cas du dioxyde d'uranium, nous n'avons pas observé un accord clair entre les paramètres S et W calculés et mesurés. Cela pouvait être lié au fait que les échantillons de référence contenant des concentrations non négligeables d'interstitiels négatifs d'oxygène. Des expériences complémentaires sur des échantillons avec stœchiométrie contrôlée (UO_2 stoechiométrique et hypo-stoechiométrique) sont proposées afin de vérifier l'influence des données de référence sur les paramètres S et W. De plus, nos premiers calculs de la distribution des moments du rayonnement d'annihilation de la trilacune contenant un atome de krypton ont montré que les mesures de l'élargissement Doppler peuvent être particulièrement utiles pour étudier l'incorporation des produits de fission. Les calculs doivent être étendus aux autres défauts et à d'autres gaz de fission, tels que le xénon, mais aussi pour l'hélium et à d'autres produits de fission volatils non ga zeux, tels que l'iode ou le césium. Les calculs de distribution des moments devraient également être intéressants pour l'étude de l'UO_2 dopé et d'oxydes mixtes d'actinides, en particulier pour déterminer l'influence de la présence de plusieurs types de cations sur le défaut et le comportement des produits de fission.

De plus, cette étude fait partie de l'approche couplant simulation expérimentale et de modélisation développée au Laboratoire de Loi de Comportement des Combustibles (LLCC) au CEA Cadarache. Les interprétations actuelles et futures des mesures de la SAP contribueront à une compréhension approfondie du comportement des défauts dans les céramiques nucléaires et permettront d'obtenir les données fondamentales et les mécanismes nécessaires pour les modèles de plus grande échelle, par exemple pour la dynamique des amas. Enfin, comme notre implémentation de méthodes de calcul de la distribution des moments du rayonnement d'annihilation est disponible librement dans le code ABINIT, nous espérons qu'elle sera utilisée par d'autres groupes pour des études sur d'autres matériaux.

Calcul de structure électronique des propriétés des défauts et caractéristiques d'annihilation de positons dans les céramiques nucléaires : identification des défauts d'équilibre et créés par l'irradiation

Durant l'irradiation en réacteur la fission des atomes d'actinides entraine la création de grandes quantités de défauts, qui affectent les propriétés physiques et chimiques des matériaux dans le réacteur, en particulier les matériaux combustibles ou de structure. Une des méthodes non destructives pouvant être utilisées pour caractériser les défauts induits par irradiation, vides ou contenant les produits de fission, est la spectroscopie d'annihilation de positons (SAP). Cette technique expérimentale consiste à détecter le rayonnement généré lors de l'annihilation de la paire électron-positon dans un échantillon et à en déduire les propriétés de la matière étudiée. Les positons peuvent être piégés dans les défauts de type lacunaire dans les solides, et en mesurant leur temps de vie et les distribution de moment de rayonnement d'annihilation, on peut obtenir des informations sur les volumes libres et les environnements chimiques des défauts. Dans ce travail, des calculs de structure électronique des caractéristiques d'annihilation de positons ont été effectués en utilisant la théorie de la fonctionnelle de la densité à deux composants (TCDFT). Pour calculer les distributions de moment rayonnement d'annihilation, nous avons implementé les méthodes nécessaires dans le code de calcul libre ABINIT. Les résultats théoriques ont été utilisés pour contribuer à l'identification des défauts d'irradiation dans deux céramiques nucléaires, le carbure de silicium (SiC) et le dioxyde d'uranium (UO_2).

Mots-clés : calcul de structure électronique, spectroscopie d'annihilation de positons, UO_2, SiC, défauts lacunaires

Identification of equilibrium and irradiation-induced defects in nuclear ceramics: electronic structure calculations of defect properties and positron annihilation characteristics

During in-pile irradiation the fission of actinide nuclei causes the creation of large amounts of defects, which affect the physical and chemical properties of materials inside the reactor, in particular the fuel and structural materials. Positron annihilation spectroscopy (PAS) can be used to characterize irradiation induced defects, empty or containing fission products. This non-destructive experimental technique involves detecting the radiation generated during electron-positron annihilation in a sample and deducing the properties of the material studied. As positrons get trapped in open volume defects in solids, by measuring their lifetime and momentum distributions of the annihilation radiation, one can obtain information on the open and the chemical environments of the defects. In this work electronic structure calculations of positron annihilation characteristics were performed using two-component density functional theory (TCDFT). To calculate the momentum distributions of the annihilation radiation, we implemented the necessary methods in the open-source ABINIT program. The theoretical results have been used to contribute to the identification of the vacancy defects in two nuclear ceramics, silicon carbide (SiC) and uranium dioxide (UO_2).

Keywords: electronic structure calculations, positron annihilation spectroscopy, UO_2, SiC, vacancy defects